

**VARIABLE TEMPERATURE RATE COEFFICIENT STUDIES
THROUGH A COAXIAL MOLECULAR BEAM
RADIOFREQUENCY RING ELECTRODE ION TRAP**

By

Bing Yuan

A Dissertation Submitted to the Faculty of the
DEPARTMENT OF CHEMISTRY AND BIOCHEMISTRY

In Partial Fulfillment of the Requirements
For the Degree of

DOCTOR OF PHILOSOPHY
WITH A MAJOR IN CHEMISTRY

In the Graduate College
THE UNIVERSITY OF ARIZONA

2012

THE UNIVERSITY OF ARIZONA
GRADUATE COLLEGE

As members of the Dissertation Committee, we certify that we have read the dissertation
prepared by Bing Yuan

entitled Variable Temperature Rate Coefficient studies Through a Coaxial Molecular
Beam Radiofrequency Ring Electrode Ion Trap

and recommend that it be accepted as fulfilling the dissertation requirement for the
Degree of Doctor of Philosophy

Mark A. Smith Date: 07/16/2012

Andrei A. Sanov Date: 07/16/2012

Lucy M. Ziurys Date: 07/16/2012

Stephen G. Kukolich Date: 07/16/2012

Date:

Final approval and acceptance of this dissertation is contingent upon the candidate's
submission of the final copies of the dissertation to the Graduate College.

I hereby certify that I have read this dissertation prepared under my direction and
recommend that it be accepted as fulfilling the dissertation requirement.

Dissertation Director: Mark A. Smith Date: 07/16/2012

STATEMENT BY AUTHOR

This dissertation has been submitted in partial fulfillment of requirements for an advanced degree at the University of Arizona and is deposited in the University Library to be made available to borrowers under rules of the Library.

Brief quotations from this dissertation are allowable without special permission, provided that accurate acknowledgment of source is made. Requests for permission for extended quotation from or reproduction of this manuscript in whole or in part may be granted by the head of the major department or the Dean of the Graduate College when in his or her judgment the proposed use of the material is in the interests of scholarship. In all other instances, however, permission must be obtained from the author.

SIGNED: Bing Yuan

ACKNOWLEDGEMENTS

I would like to thank all the people who help me in my research in the past five years. Firstly I want to thank my research director, Prof. Mark Smith. Prof. Smith taught me the basic knowledge of vacuum technique and the chemical kinetics of reactions in the interstellar medium. He also provided me lots of guide in my research whenever I met significant problems, for example, the explanation of the unusual rate coefficient data and the troubleshooting of the instrument. All of these made great contribution in my study.

Next I want to thank my committee members: Prof. Andrei Sanov, Prof. Stephen Kukolich and Prof. Lucy Ziurys. All of them provided me lots of assistance in my research as there is plenty of overlap among my research and their studies. They are always very helpful and enthusiastic. Especially, I want to thank everyone in Prof. Sanov's group who helped me a lot when Prof. Smith is in the University of Huston.

Then I want to thank Prof. Dieter Gerlich. The information of our instrument designation is mostly from Prof. Gerlich's studies. He came to Tucson several times to help us solving the important problems we met in the instrument operation. Meanwhile, I want to thank Dr. George Tikhonov, the instrument is mainly built by him as well as the LabVIEW controlling program. What's more, Mr. Mike Read, Dr. Marcus and Dr. Kevin Bao in the electronic workshop, Mr. Ed Autz and Mr. Lee Macomber in the machine workshop also made lots of contribution for the troubleshooting and improvement of the instrument.

On a personal level I'd like to single out Mr. Zachary Scott. He is my research partner in the first four years. He taught me step and step how to use the instrument and helped me to improve my English. We discussed research problems, repaired the instrument and studied the chemical kinetics of the reactions altogether. I really appreciate for all his assistance these years and I'm glad he found a good job after graduation.

I would like to thank all my friends here, especially Boying Liang, Jie Min, Dr. Chao He and his wife Yanqing Zhang. They helped me a lot for my research and my life in Tucson. Without their help, my study here would be more difficult. Also I want to thank my two cats, Ron and Jick, they have lived with me for two years and they brought me a lot of happiness.

Finally I want to thank my parents in China also our dog Kexijin. Without their supporting, I might give up my study in the middle. I wish they have a happy and wonderful life forever.

TABLE OF CONTENTS

LIST OF FIGURES.....	8
LIST OF TABLES.....	11
ABSTRACT.....	12
CHAPTER 1 INTRODUCTION.....	14
1.1 Interstellar chemistry.....	14
1.2 Techniques of rate coefficient measurement.....	18
1.3 Multipoles and ring electrode ion trap.....	26
1.4 Reaction Mechanism.....	38
1.4.1 Collision theory.....	38
1.4.2 Statistical theory.....	41
CHAPTER 2 EXPERIMENTAL.....	45
2.1 General description of the instrument.....	45
2.2 Ion cloud apparatus.....	47
2.2.1 Ion source.....	47
2.2.2 Quadrupole ion guide/mass selector.....	49
2.2.3 Ring electrode trap (RET).....	54
2.2.4 Detector (MCP + Amplifier/Discriminator + Counter).....	58
2.3 Molecular beam.....	61
2.3.1 Molecular beam nozzle.....	61
2.3.2 Shutter.....	65
2.3.3 Closed ion source residual gas analyzer (CIS-RGA).....	67
2.4 Vacuum system.....	71
2.5 Potential control of electronic lenses through labview program.....	77

CHAPTER 3 TEMPERATURE CONTROLLING.....	83
3.1 Cold head.....	83
3.2 Ions cooling by buffer collisions.....	84
3.3 Molecular beam temperature.....	87
CHAPTER 4 $\text{N}_2^+ + \text{H}_2\text{O}$ REACTION SYSTEM.....	88
4.1 Introduction.....	88
4.2 Experimental.....	90
4.3 Results and Discussion.....	92
4.4 Conclusion.....	100
CHAPTER 5 $\text{C}_2\text{H}_4 + \text{H}_3\text{O}^+ \leftrightarrow \text{C}_2\text{H}_5^+ + \text{H}_2\text{O}$ PROTON TRANSFER EQUILIBRIUM REACTION.....	101
5.1 Introduction.....	101
5.2 Experimental.....	102
5.3 Result and discussion.....	104
5.3.1 Beam number density calibration.....	104
5.3.2 Measurement of forward rate coefficient $\text{H}_3\text{O}^+ + \text{C}_2\text{H}_4$	105
5.3.3 Measurement of reverse reaction $\text{C}_2\text{H}_5^+ + \text{H}_2\text{O}$ and the Van Hoff plot of equilibrium reaction.....	109
5.4 Conclusion.....	111
CHAPTER 6 $\text{H}_3\text{O}^+ + (\text{C}_2\text{H}_2)_2$ REACTION.....	113
6.1 Introduction.....	113
6.2 Experimental.....	116

6.3 Result and discussion.....	118
6.3.1 Calibration reaction: $\text{N}_2^+ + \text{C}_2\text{H}_2$	118
6.3.2 $\text{H}_3\text{O}^+ + \text{C}_2\text{H}_2$ and $\text{H}_3\text{O}^+ + (\text{C}_2\text{H}_2)_2$ reactions.....	121
6.3.3 Radiative association of H_3O^+ and C_2H_2	128
6.4 Conclusion.....	130
CHAPTER 7 CONCLUSION.....	131
APPENDIX.....	134
REFERENCES.....	207

LIST OF FIGURES

Figure 1.1 Scheme of the flowing afterflow apparatus.....	19
Figure 1.2 Scheme of the drift tube apparatus.....	20
Figure 1.3 Scheme of the SIFT instrument.....	21
Figure 1.4 Scheme of the CRESU apparatus.....	22
Figure 1.5 The schematic diagram of the free jet flow reactor.....	24
Figure 1.6 Scheme of the ICR apparatus.....	25
Figure 1.7 Various design of ion traps.....	27
Figure 1.8 Ion movement in homogeneous and inhomogeneous electric field.....	28
Figure 1.9 Maximum relative velocity change $\Delta v/v$ of ions as a function of nominal stability parameter η over 5000rf period.....	30
Figure 1.10 Parameters r_0 and z_0 in the ring electrode ion trap.....	32
Figure 1.11 Effective potential in the multipole and ring electrode ion trap.....	32
Figure 1.12 Time dependant ion kinetic energy of one reflection from V^* wall in the octupole trap.....	34
Figure 1.13 Typical trajectory of an ion in octupole when $\eta=0.3$	35
Figure 1.14 Effective potential and trajectory of ions in octupole with static voltage U_0	36
Figure 1.15 Ion trajectories in the octupole trap at different stability η value and different initial kinetic energy.....	37
Figure 1.16 Schematic ion molecule collisions.....	38
Figure 1.17 Schematic energy levels of unimolecular reaction system.....	43
Figure 2.1 The scheme of CoMB-RET instrument.....	45
Figure 2.2 Picture of ion source trap and U-shaped Rf plate.....	48

Figure 2.3 Mathieu (a_2 , q_2) stability diagram.....	51
Figure 2.4 Interconnection between HIGH-Q HEAD and quadrupole.....	52
Figure 2.5 Mass spectroscopy of N_2^+ ions in the third quadrupole (resolution value tuned at 0.050).....	54
Figure 2.6 Ion counts in the ion flow and number of ions stored in the RET at different trap DC potentials.....	55
Figure 2.7 Two phases of Rf potential in the RET.....	57
Figure 2.8 The circuit of MCP power supply.....	59
Figure 2.9 Ions signal and systematic noise in the MCP.....	59
Figure 2.10 Ions signal from the output of Amplifier/Discriminator.....	60
Figure 2.11 The beam pressure in RGA at different x, y and z positions.....	62-63
Figure 2.12 The circuit of shutter power supply.....	65-66
Figure 2.13 The voltage across the shutter and the trigger signal while shutter is working.....	66
Figure 2.14 The structure of CIS probe.....	68
Figure 2.15 The fraction of reactant and product ions at different trapping times.....	70
Figure 2.16 Second order rate of H_2O^+ formation.....	70
Figure 2.17 Pumping system of the instrument.....	73
Figure 2.18 Gas inlet system to the CoMB-RET instrument.....	76
Figure 2.19 Ion counts in the ion flow at different potentials on some electronic lenses.....	78
Figure 2.20 Labview screen for the controlling of the potentials on the electronic lenses in the CoMB-RET instrument (N_2^+ ions).....	79
Figure 3.1 Time profile of buffer cooling for single buffer pulse.....	85
Figure 4.1 Electronic energy levels for $N_2^+ + H_2O$ reaction.....	89

Figure 4.2 Observed rate coefficients in various buffer densities.....	95
Figure 4.3 Rate coefficient measurement at constant He buffer in the RET and variable ion source N ₂ pressure.....	96
Figure 4.4 Rate coefficient of N ₂ ⁺ + H ₂ O reaction as a function of collision temperature in equation (4.7).....	97
Figure 5.1 Reactant and product ions varied with reaction time with and without H ₂ O ⁺ impurity in the system.....	105
Figure 5.2 The observed rate coefficient for H ₃ O ⁺ + C ₂ H ₄ forward reaction at different collision temperatures.....	106
Figure 5.3 The observed rate coefficient for H ₃ O ⁺ + C ₂ H ₄ forward reaction at defined statistical temperatures.....	108
Figure 5.4 Rate coefficient of H ₃ O ⁺ + C ₂ H ₄ reverse reaction.....	109
Figure 5.5 The Van Hoff plot for C ₂ H ₄ + H ₃ O ⁺ ↔ C ₂ H ₅ ⁺ + H ₂ O equilibrium reaction...	110
Figure 6.1 Rate coefficient of N ₂ ⁺ + C ₂ H ₂ reaction at different statistical reaction.....	120
Figure 6.2 The reactant and product ions at different trapping time for H ₃ O ⁺ + C ₂ H ₂ component reaction.....	122
Figure 6.3 Second order rate coefficient measurements based upon acetylene monomer density k'(T _{react}) for C ₂ H ₅ O ⁺ product formation in reaction of H ₃ O ⁺ with the components of the acetylene beam.....	122
Figure 6.4 The rate coefficient defined in (6.19) of H ₃ O ⁺ + (C ₂ H ₂) ₂ reaction versus statistical temperature with the expression of (6.20).....	128

LIST OF TABLES

Table 1.1 Gas-phase reactions in the ISM.....	17
Table 2.1 Pressures of each vacuum chamber and the RGA under different molecular beam stagnation pressure (N ₂ gas).....	64
Table 2.2 Pumps and ion gauges used in the vacuum system of ions.....	74
Table 2.3 Pressures in vacuum chambers and backing system under the pumping system.....	75
Table 2.4 Maximum ion counts and current with related explanation for potentials on electronic lenses.....	80-81
Table 4.1 Rate coefficients for N ₂ ⁺ + H ₂ O reaction measured at H ₂ O nozzle temperatures between 300 K and 450 K.....	97
Table 5.1 Comparison of the experimental enthalpy ΔH , entropy ΔS and free standard energy ΔG at 300 K for equilibrium reaction $H_3O^+ + C_2H_4 \leftrightarrow C_2H_5^+ + H_2O$..	111
Table 6.1 The calculated dimer/monomer equilibrium constant $K_p(T)$, dimer fraction P_d/P_m values at binding energy D_0 equals 404 cm ⁻¹ while parameter z is 0.32.....	127

ABSTRACT

The dissertation focuses on the temperature dependent rate coefficient measurement of reactions in the interstellar medium using a coaxial molecular beam ring electrode ion trap apparatus. The first chapter introduces the previous studies of ion-molecule reactions in the ISM, the types of instruments mainly used in the reaction rate coefficient study, the former research on the ring electrode ion trap and the gas phase reaction mechanisms. Compare to other instruments, our molecular beam - ring electrode ion trap is extremely good at ion cooling and temperature control for both ions and neutral molecules. Chapter two describes each part of the instrument used in detail. Ions produced by electron impact in the ion source chamber, are mass filtered and then reach the ring electrode ion trap. In the trap, ions collide with molecules in the molecular beam where reaction takes place. When the reaction is done, all the ions remained in the trap (the reactant and product ions) come out and move to the detector. The molecular beam terminates at residual gas analyzer which is used for the number density calibration.

The third chapter shows how the temperature of ions and molecules are controlled separately in order to find the reaction mechanism. Ions are cooled by the pulsed He buffer in the ring electrode trap and a chopped beam is used to make sure the ions are cooled to the desired low temperature when the reaction takes place.

Chapters four to six describe the three reactions being studied using this instrument: $\text{N}_2^+ + \text{H}_2\text{O}$ charge transfer reaction, $\text{H}_3\text{O}^+ + \text{C}_2\text{H}_4$ proton transfer reaction and $\text{H}_3\text{O}^+ + (\text{C}_2\text{H}_2)_2/\text{C}_2\text{H}_2$ dimer reaction. The temperature dependent rate coefficient data of these reactions are explained by the average dipole orientation theory, statistical theory and

Colussi's acetylene dimer model, respectively. Two temperatures are defined and applied in the experimental rate coefficients analysis: ion-molecule center of mass collision temperature and the reaction statistical temperature which is based on the numbers of degrees of freedom of both reactants.

CHAPTER 1 INTRODUCTION

1.1 Interstellar chemistry

Interstellar chemistry is the study of chemistry in the environment of the interstellar medium (ISM) which focuses on the existence and synthesis of gaseous molecules in the ISM. Interstellar chemistry has made significant contributions in the research subjects like: matter distribution in the universe, the origin of star and galaxy, cosmic isotopic ratios and its direct relationship to the origin of universe, the oxygenated molecules in the ISM and its assistance in the study of the origin of life, etc.¹

Interstellar chemistry starts since the 1930s with the discovery of simple molecules from molecular absorption spectra, like CH, CH⁺ and CN.² It becomes truly important to researchers since 1963 from the observation of Λ doubling transition of OH at 18 cm.³ Radio-millimeter telescope is generally applied nowadays and more and more polyatomic substances including molecular ions are discovered in the ISM. The observation of microwave emission from the ISM creates a significant revolution in the understanding of the ISM from homogeneous atomic condition to heterogeneous environment with non-uniform density.² Most of the universal space is close to empty with a molecular number density below 0.1 cm⁻³ and substances in the ISM accumulate in clouds.¹ There are disparate interstellar clouds in the ISM as a result of different temperatures and densities.

The simplest clouds are diffuse clouds. The total gas density is 10² cm⁻³ with temperature ranges from 50 K to 100 K. Galactic starlight and cosmic rays can penetrate

diffuse clouds because of its low density which are the main external energy sources within the diffuse clouds. Gas and dust in this region are mainly neutral molecules; however, most of the carbon related substances in this area are ionized by ultra-violet radiation from stars. The most abundant elements (>99%) in the diffuse clouds are hydrogen and helium with high ionization energy which can only be ionized by cosmic rays. Most of the chemicals in diffuse clouds are diatomic, like H_2 , HD, OH, CO, CH, CH^+ , N_2 , NO, CN, O_2 , etc.⁴

Dense clouds are more complicated compared to diffuse clouds. The density of dense clouds is 10^4 cm^{-3} and the temperature is only 10 K. This area is opaque to ultraviolet starlight and cosmic ray is the only external energy source.⁴ The initial ionization step of hydrogen and helium by cosmic rays (γ) can be written as



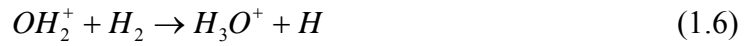
Then the created H_2^+ and He^+ ions will continue to produce highly reactive ions and neutral molecules in the ISM.¹

Ions play a significant role for reactions in the ISM, especially in the cold regions. Although the great majority of chemicals identified in the ISM are unsaturated neutral molecules or free radicals, reactions between neutral and neutral molecules are often ignored in the models of the ISM as these reactions always has big activation energy which makes the rate coefficient in pretty low level.³ As most of the ion-molecule reactions are exothermic with low activation energy, therefore, ion-molecule reactions are more popular in the ISM. In addition, the chemical reaction in the cold region of the ISM

is often a kinetically process, not thermodynamically controlled. H_3^+ ions in the ISM is made from H_2^+ in equation (1.1) through

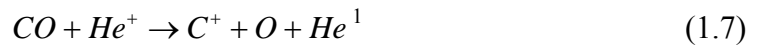


and it is the precursor for the formation of more complex species.¹ For example, H_3^+ can react with oxygen atom producing hydrogenated molecules⁴

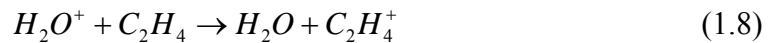


and the product ions H_3O^+ are one of the most popular ions studied in the rate coefficient measurements.

He^+ ions in equation (1.2) can dissociate molecules to atomic ions, which is the main way to produce atomic ions in the dense clouds. For example, C^+ can be produced from He^+ by



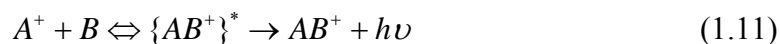
The three major types of ion-molecule reactions in the ISM are charge transfer reaction, atomic transfer reaction and radiative association reaction.¹ In charge transfer reaction, electron moves from the reactant to product, for instance,



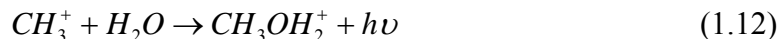
Atom or group transfer reaction is similar. In an atom transfer reaction, the atom transfers from one molecule to the other. The most predominant reactions in this area are carbon insertion reaction and condensation reaction.⁴ For example,



Radiative association reaction is a process in which two reactants A and B combine together to form a new complex product. The complex is stabilized by infrared light emission. The mechanism of radiative association reaction³ can be written as



Radiative association reaction is one of the fundamental methods in the ISM for producing oxygenated organic molecules, for example,



Gas phase reaction types in the ISM are summarized in Table 1.1.¹

Table 1.1 Gas-phase reactions in the ISM

Ion – Molecule Reaction	Charge transfer	$A^+ + B \rightarrow B^+ + A$
	Radiative association	$A^+ + B \rightarrow AB^+ + h\nu$
Electron recombination	Atom transfer	$A^+ + BC \rightarrow AB^+ + C$ or $AB^+ + C \rightarrow A^+ + BC$
	Radiative	$A^+ + e^- \rightarrow A + h\nu$
Photochemical	Dissociative	$AB^+ + e^- \rightarrow A + B$
	Photodissociation	$AB^+ + h\nu \rightarrow A^+ + B$
Neutral-neutral	Photoionization	$A + h\nu \rightarrow A^+ + e^-$
	Atom transfer	$A + BC \rightarrow AB + C$
	Radiative association	$A + B \rightarrow AB + h\nu$
Other	Chemionization	$A + B \rightarrow AB^+ + e^-$
	Ion-ion neutralization	$A^+ + B^- \rightarrow C + D$
	Negative ion-neutral	$A^- + B \rightarrow AB + e^-$ or $A^- + BC \rightarrow AB^- + C$

To improve the understanding of how the observed molecules are being produced in the ISM, fundamental chemical and physical processes in the ISM are studied experimentally and theoretically. This is done in order to build chemical models using large networks of these processes.³ Rate coefficient measurement is one of the most

important methods for obtaining information in the network building. Assuming a simple reaction, $A + B \rightarrow C + D$, the reaction rate can be written as

$$- \frac{d[A]}{dt} = k[A] \cdot [B] \quad (1.13)$$

where k is the rate coefficient and $[A]$ and $[B]$ are the instantaneous concentrations of the two reactants. The rate coefficient k is usually temperature dependant and for chemical reactions in the ISM, the expression of temperature dependent rate coefficient $k(T)$ can be written as

$$k(T) = \alpha \cdot (T/300)^\beta \cdot \exp(-\gamma/T) \quad (1.14)$$

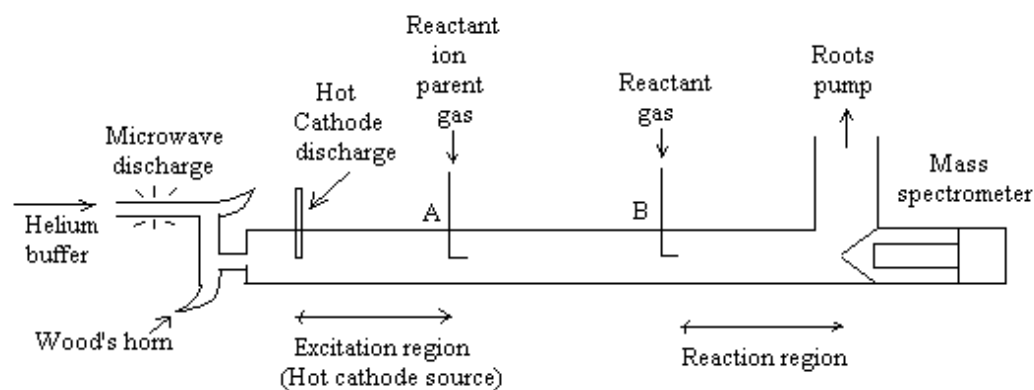
where α , β and γ are parameters.³ In this study, the rate coefficients of three reactions in the ISM are measured at different temperatures in order to provide useful information of chemical network building. Meanwhile the reaction mechanisms are studied.

1.2 Techniques of rate coefficient measurement

There are several generally applied techniques for rate coefficient measurement of reactions in the ISM including flowing afterflow, drift flow tube, selected ion flow tube, expanding jet technique (CRESU), free jet flow reactor, ion cyclotron resonance and electronic ion trap. These methods, under their own study limits, provide large amount of rate coefficient information ranges from $10^{-15} \text{ cm}^3 \cdot \text{s}^{-1}$ to $10^{-8} \text{ cm}^3 \cdot \text{s}^{-1}$.

Flowing afterflow is the technique for rate coefficient studies in a flow tube. The scheme of the apparatus is shown in figure 1.1.

Figure 1.1 Scheme of the flowing afterflow apparatus⁵

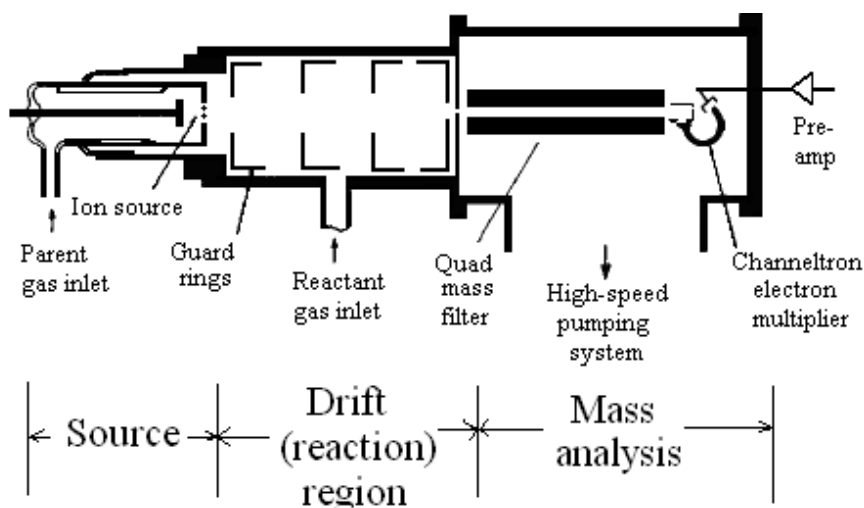


Pure helium is injected at the beginning of the flow tube. The gas flow rate is about $100 \text{ m}\cdot\text{s}^{-1}$. The system is evacuated by a roots pump at the end of the flow tube to keep the internal pressure usually from 0.2 torr to 2.0 torr. Ions and excited substances are produced by electron impact in the excitation region and are carried down through the flow tube by He buffer gas. Ions formed in the excited states can be stabilized to the ground electronic state through buffer gas collision as the concentration of the ions are five orders of magnitude lower than He neutral buffer. When the neutral reactant is introduced into the flow tube from the tubular entry inlet B, the reactant concentration will become uniform quickly and the product ions will be formed in this area by ion-neutral collisions. The reaction time equals the effective length of reaction region divided by the average velocity of gas flow.^{5,6} The reaction temperature in the flowing afterflow method ranges from 80 K to 900 K.⁷

Drift flow tube is the technique for ion-molecule reaction study as a function of ion energy in a drift mobility tube with a differentially pumped mass spectrometer to detect

the reactant and product ions. The simplified drawing of drift flow tube is shown in figure 1.2.

Figure 1.2 Scheme of the drift tube apparatus⁸



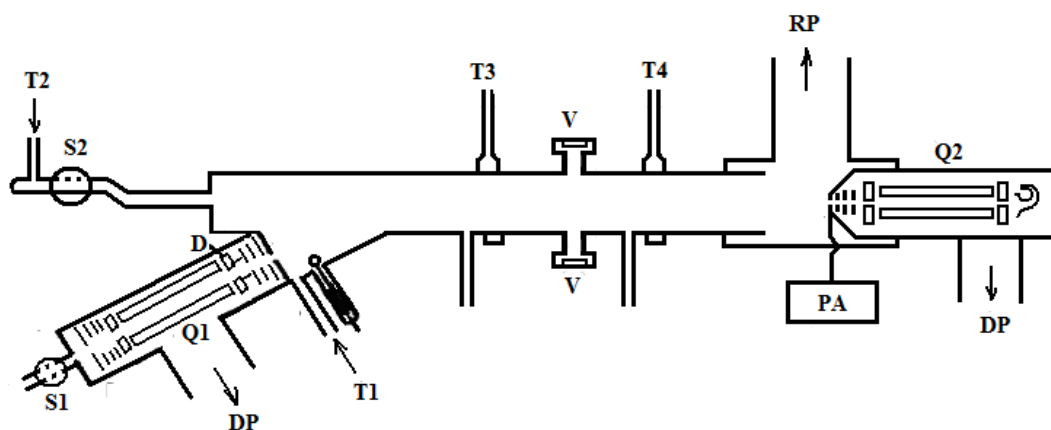
Pulsed ions generated in the source region are admitted into the drift reaction region. An electric field is applied as ions travel through this area. Neutral reactant gas is admitted in the drift region where the reaction takes place. Reactant ions and product ions formed in the drift region will finally go through a small orifice at the collector end of the tube to do mass analysis. The rate coefficient k is determined by the translational energy of ions which depends on both gas temperature and the applied electric field in the drift tube. The drift tube contains 1 torr helium buffer gas to inhibit diffusion and establish the equilibrium of ions temperature by collision. The expression of ions mean energy E_{ion} in the drift tube can be written as

$$E_{ion} = \frac{3}{2}kT_{gas} + \frac{1}{2}(m_{ion} + m_{gas}) \cdot v_d^2 \quad (1.15)$$

where v_d is drift velocity and the last term $m_{\text{gas}}v_d^2/2$ means that the amount of energy picked up from the electric field is converted into random motion of ions.⁸

The main problem in the flowing afterflow tube and the drift tube methods is that all the ions produced in the ion source can be injected into the reaction region without mass selection which makes the rate coefficient analysis complicated as there will be unwanted parallel reactions in the system. For example, assume N_2^+ is the supposed reactant ions in the system. However, as helium buffer is also in the ion source area, He^+ , N^+ and excited neutral species can also be produced, together with the electrons and energetic photons, will strongly affect the rate coefficient result. This problem has been solved by selected ion flow tube (SIFT) method in which quadrupole mass filter is used to select the single ion specie from a remote ion source. The scheme of the SIFT instrument is shown in figure 1.3.

Figure 1.3 Scheme of the SIFT instrument⁹

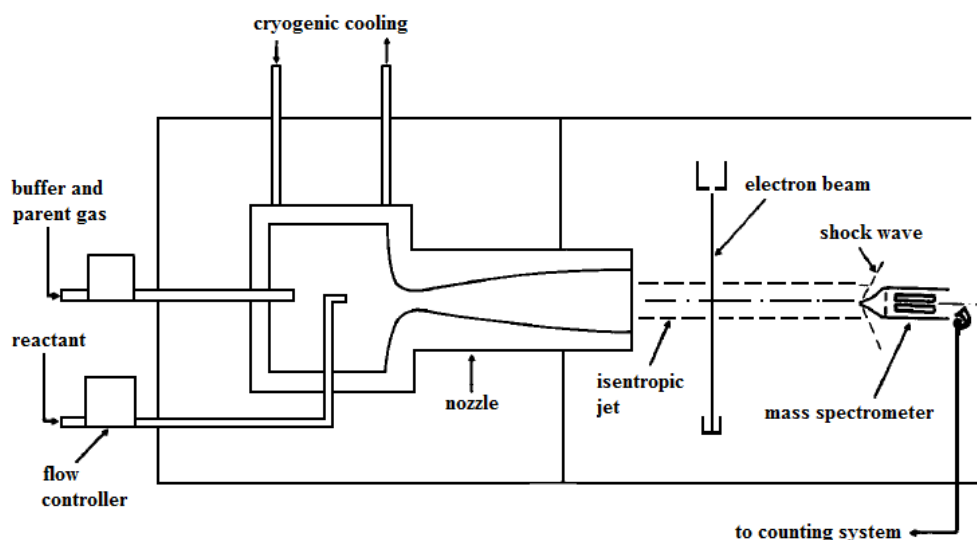


Ions produced by microwave discharge in quartz tube S_1 are mass selected in quadrupole Q_1 and then admitted into the flow tube after passing through deflecting plate

D. In the flow tube, ions are transported by buffer gas flow which is admitted from port T_1 . The pressure ranges from 0.1 torr to 1.0 torr. Under buffer collisions, ions are relaxed and finally move into a field free region with temperature equilibrium to the buffer gas. Neutral reactant gas is introduced into the flow tube through port T_3 or T_4 and then the reaction takes place. The decay rate of reactant ions and the growth rate of product ions are observed by downstream mass spectrometer Q_2 . The reaction time is determined by the mean velocity of ions moving along the flow tube.^{9,10}

CRESU is the technique of studying the reaction kinetics through uniform supersonic flow. The temperature range of SIFT method is usually between 80 K and 600 K, but in the CRESU technique, the temperature is in the lower range from 8 K to 169 K.¹¹ The scheme of CRESU is shown in figure 1.4.

Figure 1.4 Scheme of the CRESU apparatus¹¹



The nozzle generates a supersonic jet and its flow temperature, T , and pressure, p , can be calculated using isentropic relationships

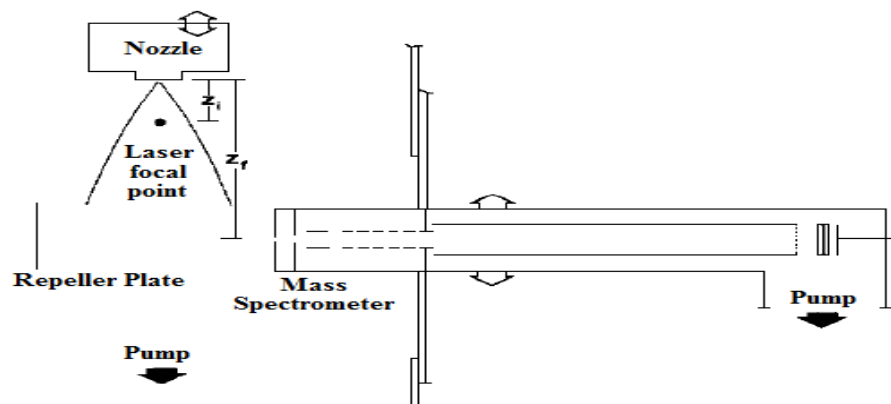
$$\frac{T_0}{T} = 1 + M^2 \cdot \frac{(\gamma - 1)}{2} \quad (1.16)$$

$$\frac{p_0}{p} = \left(\frac{T_0}{T} \right)^{\gamma/(\gamma-1)} \quad (1.17)$$

where T_0 and p_0 are the stagnation temperature and pressure, respectively, γ is the heat ratio of buffer gas and M is the Mach number. The nozzle reservoir is cooled by liquid N_2 or He in order to get low reaction temperature. Ions are created by a 20 keV electron beam directly across the jet and the vibrationally excited ions can be quickly quenched by charge exchange. Neutral reactant gas is translationally thermalized while it is mixed with buffer gas. The reactant and product ions are monitored as a function of the flow rate of neutral reactant gas through a quadrupole mass analyzer and counting system. The ions detection system is located behind a skimmer to avoid the shock wave.¹¹

Similarly as CRESU, the pulsed supersonic free jet is another useful technique for the study of reaction kinetics. With much smaller nozzle orifice (nozzle diameter 0.03 cm)¹² and pulsed flows, the gas consumption is four orders of magnitude lower compared to CRESU (nozzle diameter 16 cm)¹¹. The schematic diagram of the free jet flow reactor is shown in figure 1.5.

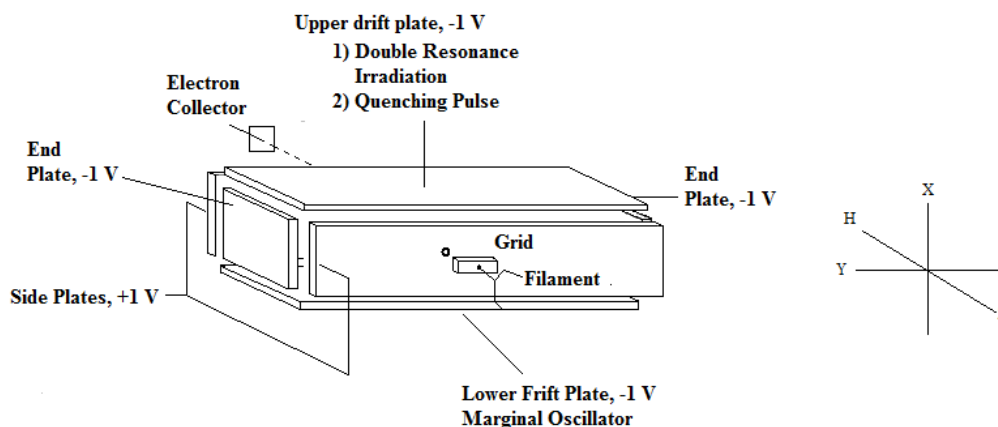
Figure 1.5 The schematic diagram of the free jet flow reactor¹²



Ions are produced a short distance from the nozzle where the velocity of the flow reaches a constant value. Resonantly enhanced multiphoton ionization is used to selectively produce the ions of interest. Ions are allowed to flow in the field-free area until they are repelled into the time of flight mass analyzer. The reaction takes place in the jet between ions and neighboring neutral molecules.¹²

Ion cyclotron resonance (ICR) is another significant technique for ion-molecule reaction study. Different from flow tube in which ions are carried by buffer gas moving through a long tube, in ICR ions are trapped in a cell under the electromagnetic field. The buffer gas pressure in the cell is 10^{-5} torr which is orders of magnitude lower than flow tube method. The scheme of ICR is shown in figure 1.6.¹³

Figure 1.6 Scheme of the ICR apparatus¹³



In the ICR method, a pulsed electron beam is emitted from the filament and moves in the parallel direction of magnetic field. As electrons pass through the analyzer cell, ions are formed by electron impact and electrons are finally captured by the collector mounted on the other side of the cell. The motion of ions is constrained in the cell in circular orbits. The angular frequency of this motion equals $\omega_c = qH/mc$, where q/m is charge to mass ratio, H is magnetic field strength and c is the speed of light. The motion of trapped ions inside the cell is also controlled by the low DC voltages on each of the six metal plates of the cell. Proper trapping conditions are attained for a wide variety of voltage values on the cell plates. The lower drift plate of the cell is incorporated as a capacitive element in the resonant circuit of a marginal oscillator. The marginal oscillator strengthens an Rf electric field with frequency ω_1 which is perpendicular to the direction of magnetic field. After certain reaction time, ions are ejected to the detector only when the cyclotron motion frequency ω_c in the magnetic field equals to the frequency ω_1 of marginal oscillator.^{13,14}

Besides these techniques, other methods like cooled hyperbolic Penning ion trap are also widely used for rate coefficient studies at low temperatures and low pressures. Our instrument is a coaxial molecular beam radiofrequency ring electrode ion trap which can sufficiently trapped the ions in the small space and can control reaction temperatures well. Details of this instrument are in chapter two.

1.3 Multipoles and ring electrode ion trap

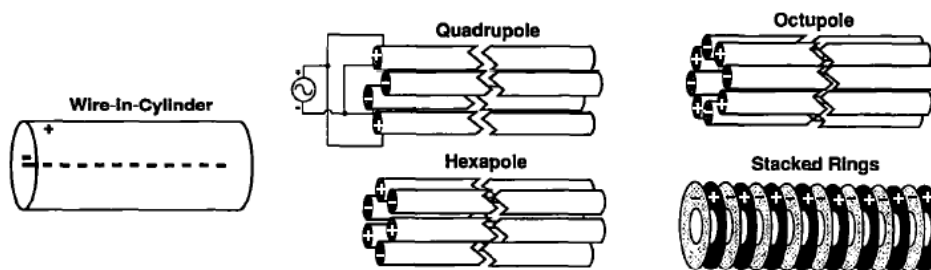
The instrument we are using is a coaxial molecular beam-radiofrequency ring electrode ion trap (CoMB-RET). Compared to other techniques, this technique provides several obvious advantages for rate coefficient studies in the ISM.

Firstly, ions are produced by electron impact in the ion source chamber which is separated from the trap chamber where the reaction takes place by two quadrupole mass filters, two DC quadrupole benders and several electrostatic lenses. In the ion source area, the ions are cooled to ground electronic states by neutral molecule collisions. Secondly, ions are mass selected by quadrupole mass selector before they reach the ring electrode trap. The resolution of the quadrupole mass selector is smaller than 1 amu. Thirdly, ions in the ring electrode trap can stay for at least 50 s and both the translational and internal energy of ions can be cooled by pulsed buffer gas before the reaction starts. When the reaction takes place, the pressure in the trap is pumped down to 10^{-8} torr which is much lower than flow tube technique and in this case, there is no three-body association

reaction in the system. Fourthly, the temperatures of ions and neutral molecules can be controlled separately which is quite useful for the study of reaction mechanism.

Ion trap technique is the core of our instrument and it is the application of inhomogeneous oscillatory electronic fields on multi-pole electrode trap or ring electrode trap in which the reaction takes place. Figure 1.7 shows the structures of multipole electrode (quadrupole, hexapole and octupole) and ring electrode ion traps.

Figure 1.7 Multipole and ring electrode ion traps¹⁵



Take quadrupole for example, it has two electrode pairs as shown in figure 1.7. One is labeled as (+), the other is (-). The potential voltage on the positive electrodes is

$$\Phi_0 = U_0 - V_0 \cos(\Omega t + \delta) \quad (1.18)$$

while on negative electrodes it becomes

$$\Phi_0 = -U_0 + V_0 \cos(\Omega t + \delta) \quad (1.19)$$

where U_0 is DC voltage, V_0 is AC potential and Ω is AC frequency, so the potential difference between the two electrode pairs is $2U_0 - 2V_0 \cos(\Omega t)$.¹⁶ Potentials applied on other multipole electrode ion traps are similar to the quadrupole. In the ring electrode ion trap, appearing like multipole trap, it has two electrode terms as shown in figure 1.7 and the voltage applied on each term is the same as equation (1.18) and (1.19).

The electronic field in the ion trap composes two parts: a static field $E_s(r)$ and a time dependent field $E_0(r) \cdot \cos(\Omega t + \delta)$. The ion motion in the inhomogeneous electronic field can be written as

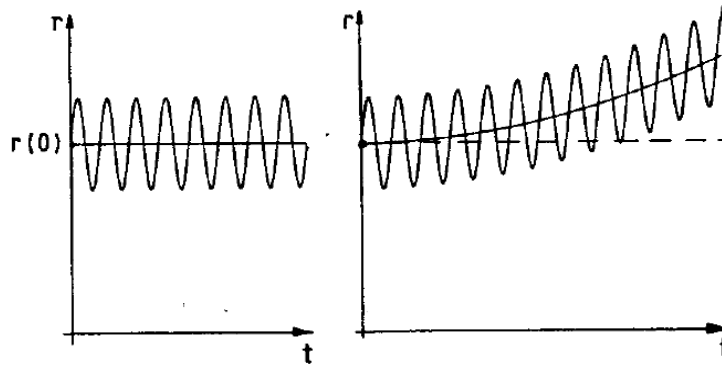
$$m \frac{d^2 r}{dt^2} = qE_0(r) \cdot \cos(\Omega t + \delta) + qE_s(r) \quad (1.20)$$

and the solution of (1.20) is

$$r(t) = R_0(t) + R_1(t) = R_0(t) - \frac{qE_0(r)}{m\Omega^2} \cos(\Omega t) \quad (1.21)$$

From ion trajectory solution (1.21), it is found that there are two kinds of ion motions: the smooth drift motion $R_0(t)$ and fast oscillating motion $R_1(t)$.¹⁶ The difference of ions motion in homogeneous oscillatory electronic field and inhomogeneous oscillatory electronic field is shown in figure 1.8.

Figure 1.8 Ions motion in homogeneous and inhomogeneous electric field¹⁶



In figure 1.8, the left one represents ions motion in the homogeneous electric field which shows the particle oscillation as a function of time without changing the direction

of its initial mean position $r(0)$. The right one is in the inhomogeneous electric field and shows the drift motion of ions towards to the weaker field region.

The smooth drift motion of ions in the first order approximation as be written as

$$m \frac{d^2 r_0}{dt^2} = -q^2 \nabla_0 E_0^2(r_0) / 4m\omega^2 + qE_s(r_0) \quad (1.22)$$

and it describes the time-averaged effect of the oscillatory electronic field with static field on the smooth drift motion.¹⁴ When the static electric field E_s equals zero, equation (1.22) shows that ions in the trap experience the electric field gradient force caused by the inhomogeneous filed which proves the ions trajectory in figure 1.7. Defined a time-independent mechanical effective potential V^* as

$$V^*(R_0) = \frac{q^2 E_0^2(R_0)}{4m\Omega^2} + q\Phi_s \quad (1.23)$$

where Φ_s is the negative gradient of electrostatic potential E_s . Under this definition, the smooth drift motion of ions in (1.22) can be simplified as

$$m \frac{d^2 R_0}{dt^2} = -\nabla V^*(R_0). \quad (1.24)$$

Equation (1.24) indicates that the kinetic energy of ions smooth drift motion can be transferred to effective potential energy V^* . Integrating (1.24), we get

$$\frac{1}{2} \cdot m \left(\frac{dR_0}{dt} \right)^2 + \frac{q^2 E_0^2}{4m\Omega^2} + q\Phi_s = E_m \quad (1.25)$$

which demonstrates that the total energy E_m of ions motion is an adiabatic constant value.¹⁶ What's more, the time dependent oscillatory motion of ions can be written using effective potential V^* as

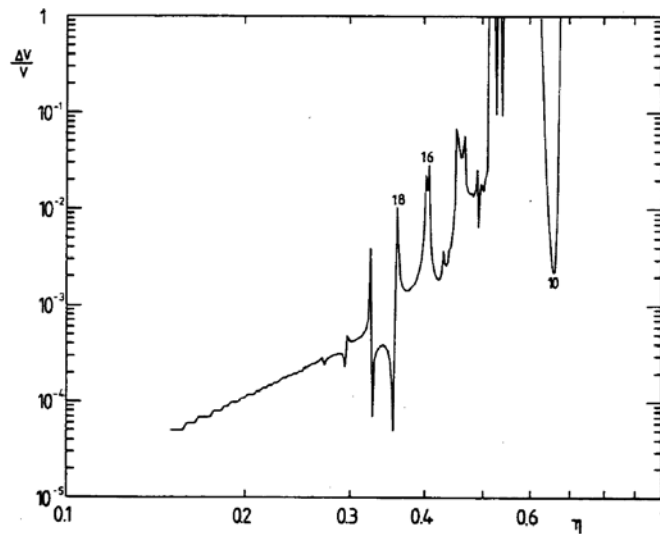
$$\frac{1}{2} \cdot m \left(\frac{dR_1}{dt} \right)^2 = 2V^* \sin^2(\Omega t) \quad (1.26)$$

The conclusion from equation (1.25) that the average total energy of ions motion is an adiabatic constant only works under the safety limit of the ion trap. If the electric condition is out of the safety limit, the kinetic energy of ions will continuously accumulate by increasing the amplitude of the smooth motion. Adiabatic parameter η is defined as

$$\eta = \frac{2q|\nabla E_0|}{m\Omega^2} \quad (1.27)$$

the value of which varies from the center of the ion trap to the electrode surface. The maximum η value $\eta_{\max} < 0.3$ guarantees the adiabaticity of most ion trap practical application.^{16,17} Figure 1.9 describes the relative velocity change $\Delta v/v$ of ions in different stability parameter η .

Figure 1.9 Maximum relative velocity change $\Delta v/v$ of ions as a function of nominal stability parameter η over 5000 rf period¹⁶



As shown in figure 1.9, when $\eta < 0.3$, the $\Delta v/v$ value is always smaller than 10^{-3} , so $\eta_{\max} < 0.3$ is the condition of the conservation of ions kinetic energy in the ion trap.

To avoid ions collision with electrodes, effective potential V^* near the electrodes in the ion trap must be higher than ion total energy E_m which means

$$\frac{q^2 E_0(r_m)^2}{4m\Omega^2} + q\Phi_s(r_m) > E_m \quad (1.28)$$

where r_m is the closest allowed approach of ions to the electrode surface. So the expression of effective potential V^* in the form of AC voltage V_0 (Rf amplitude), AC frequency Ω and DC voltage U_0 can be written as

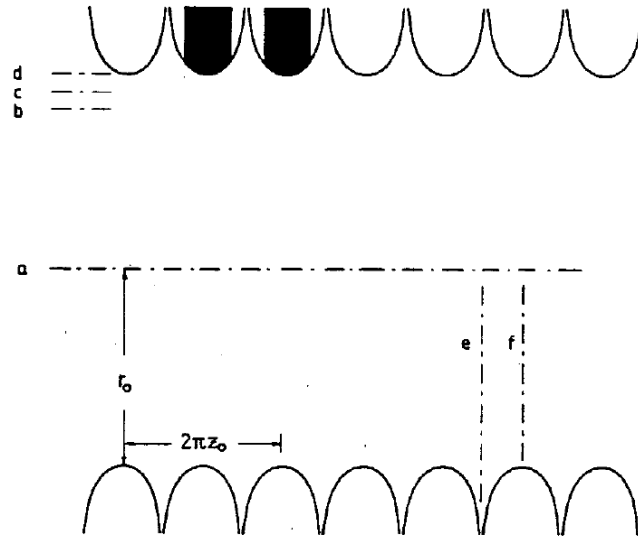
$$V^* = \frac{n^2}{4} \frac{q^2}{m\Omega^2} \frac{V_0^2}{r_0^2} \hat{r}^{2n-2} + qU_0 \hat{r}^n \cos(n\varphi) \quad (1.29)$$

where \hat{r} is the reduced variable equals r/r_0 (r_0 is the diameter of ion trap) and n is the number of electrode pairs in the multipole ion trap.¹⁶ For ring electrode ion trap, equation (1.29) becomes

$$V^* = \frac{q^2 V_0^2}{4m\Omega^2 z_0^2} \cdot \frac{I_1^2(\hat{r}) \cdot \cos^2 \hat{z} + I_0^2(\hat{r}) \cdot \sin^2 \hat{z}}{I_0^2(\hat{r}_0)} \quad (1.30)$$

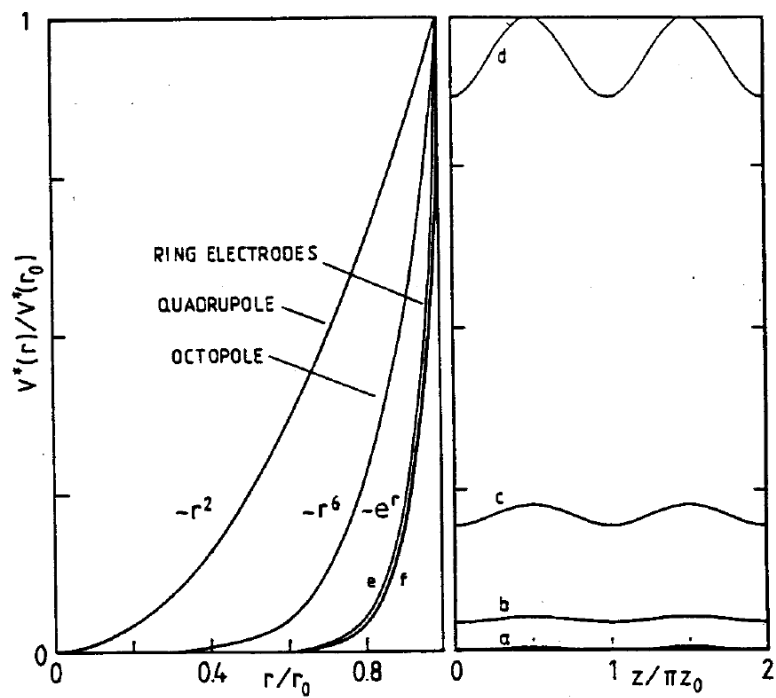
where \hat{z} is the reduced variable equals z/z_0 , $I_0(x)$ is the zero-order modified Bessel function and $I_1(x) = dI_0(x)/dx$.¹⁵ The structure of the ring electrode ion trap and related parameters are shown in figure 1.10.

Figure 1.10 Parameters r_0 and z_0 in the ring electrode ion trap¹⁶



The effective potential in the multipole ion trap (1.29) and the ring electrode trap (1.30) from trap center to the electrode surface is shown in figure 1.11.

Figure 1.11 Effective potential in the multipole and ring electrode ion trap¹⁶



The left one shows the effective potential in the quadrupole, octupole and ring electrode ion trap which varies from the trap center to the electrode surface and e^r is a first order approximation to equation (1.30). For the two potential lines e and f of the ring electrode trap labeled in figure 1.11, e means the potential from trap center to the space between two electrodes and f is the potential from trap center to the electrode surface. The right figure shows the effective potential of ring electrode trap at positions a, b, c and d, the positions of which are labeled in figure 1.10.

The effective potential is near zero at the center area of the ion trap and it becomes higher and higher as it goes closer to the electrode surface. Compared to quadrupole and octupole trap, the ring electrode trap has a boarder field free area near the trap center with a steeper effective potential wall. What's more, for multipole traps, the weak field region in the trap center becomes larger and larger with the increase of the electrode pairs number. In this case, it can be concluded that the ring electrode ion trap and high multipole ion trap are more suitable for chemical reaction studies than the quadruple and octupole trap as there is more field free space for the motion of ions and the ions temperature can be easily cooled down by buffer gas collisions. In quadrupole trap, ions are too easy to touch the effective potential wall and the kinetic energy of ions will be heat up and coupled from micro-motion into secular motion.

When ions move in the ion trap, there is a continuous exchange between the two different forms of translational energy: smooth drift motion $R_0(t)$ and oscillating motion $R_1(t)$. The total instantaneous kinetic energy of ions is

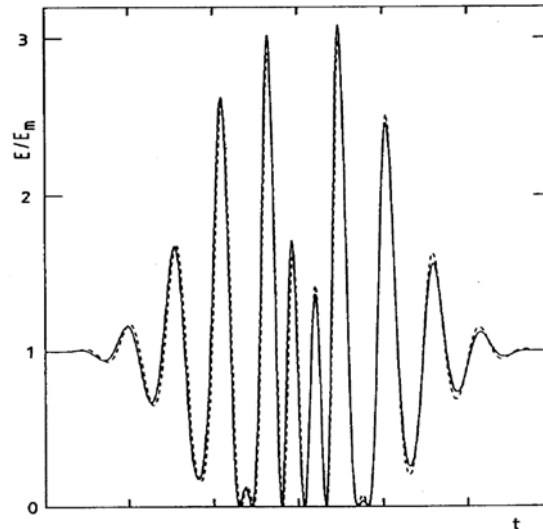
$$E_{kin}(t) = \frac{1}{2} m \cdot [\dot{R}_0(t) + \dot{R}_1(t)]^2 \quad (1.31)$$

and the expression can be also written in the form of effective potential V^* as

$$E_{kin}(t) = [(E_m - V^*)^{1/2} + (2V^*)^{1/2} \cdot \sin(\Omega t)]^2 \quad (1.32)$$

Assume ions movement starts from the center of the ion trap with initial kinetic energy E_m , the total instantaneous energy of ions is identical to E_m in the field free region where V^* is zero. As ions move closer to the electrode surface, the effective energy V^* goes up and at the turning point of ions smooth drift motion where $V^* = E_m$, the kinetic energy of ions becomes $2E_m \times \sin(\Omega t)$ in equation (1.32). Equation (1.32) also shows that the maximum value of E_{kin} is $3E_m$ at the position in the trap where two thirds of the total energy is converted into oscillatory motion and one third remains in smooth motion.¹⁶ Thus, the kinetic energy of ions fluctuates between 0 and $3E_m$ at the ion reflection point from the V^* wall. Figure 1.12 describes the instantaneous kinetic energy of ions during one reflection from the Rf wall.

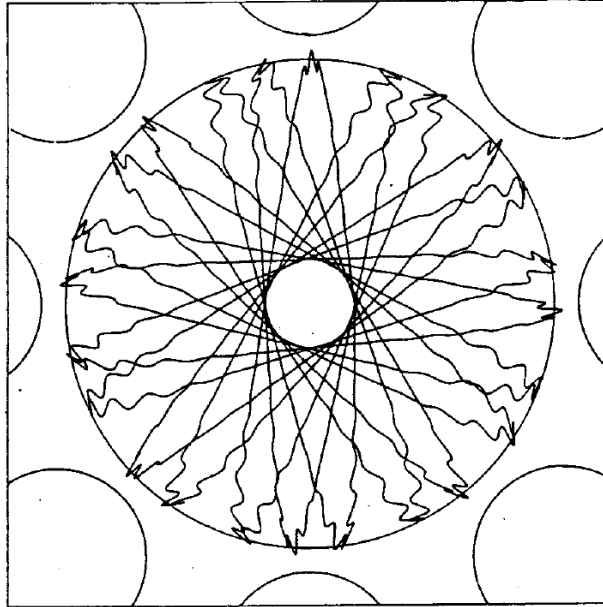
Figure 1.12 Time dependant ion kinetic energy of one reflection from V^* wall in the octupole trap¹⁶



Though the kinetic energy of ions varied from 0 to $3E_m$ in figure 1.12, the average energy stays at E_m . Therefore, at the stability limit $\eta_{\max} < 0.3$, the conservation of ions kinetic energy means that the average kinetic energy stays at initial value E_m , but it keeps oscillating all the time.¹⁶

The trajectory of ions movement under the stability limit in the octupole trap is shown in figure 1.13 which combines the smooth drift motion and the oscillatory motion. The oscillatory motion can be seen more clearly during the reflection turning point. The trajectory in figure 1.13 is in the absence of a superimposed static field U_0 . The interaction between ions and the Rf field results in a pure central force. The hole in the center of figure 1.13 is due to the conservation of the angular momentum of ions motion.¹⁶

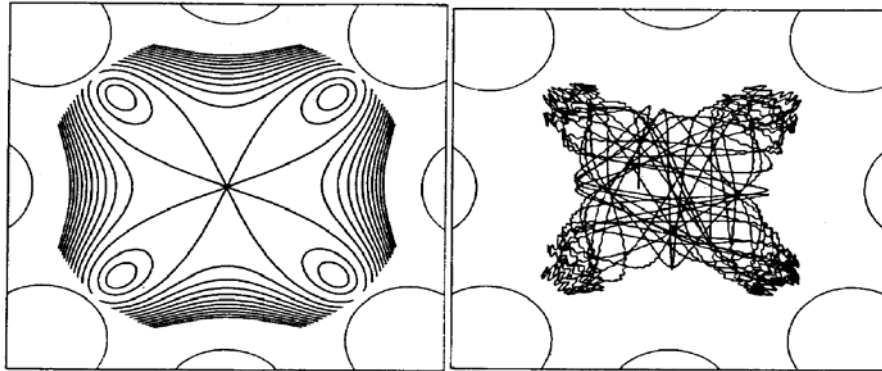
Figure 1.13 Typical trajectory of an ion in octopole when $\eta=0.3$ ¹⁴



When η is greater than 0.3, the angular momentum of ions is no longer consistent and the ions trajectory in this case will change its closest approach to the center, so the blank space in the center of figure 1.13 will not be seen and after a few more reflections, ions will be lost.

The effective potential with superimposed DC voltage and the ion trajectory when static DC potential U_0 is applied to the multipole or ring electrode trap are shown in figure 1.14.

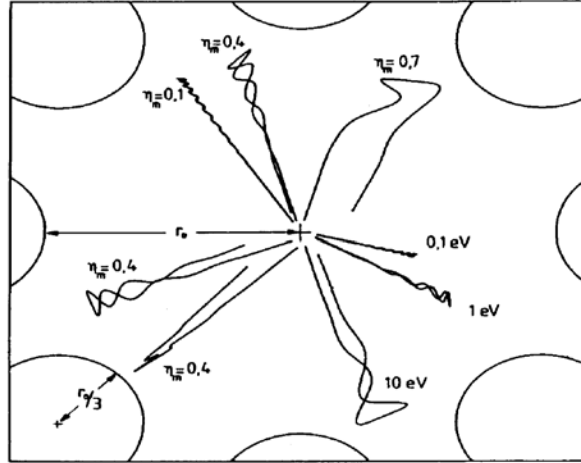
Figure 1.14 The effective potential and the ion trajectory in octupole with static voltage U_0 ¹⁶



The left one is the effective potential and the one on the right is the ion trajectory which shows that when the DC voltage is superimposed, ions spend most of the time in the four potential minima locations which are close to the surface negative biased electrodes.

The trajectory of ions in the same inhomogeneous electric field condition with different initial kinetic energy and η values are shown in figure 1.15.

Figure 1.15 Ion trajectories in the octupole trap at different stability η values and different initial kinetic energy¹⁶



The three trajectories in the lower right corner of figure 1.15 are ions with initial kinetic energy 0.1 eV, 1 eV and 10 eV, respectively, while the stability limit η value equals 0.4. The figure shows that if the initial energy of ions is too high (for example 10 eV), it is pretty easy for them to hit the electrodes and lost in the trap.

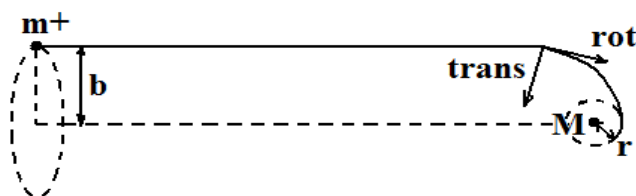
In summary, an ion trap applied with inhomogeneous electric field can store ions sufficiently. When the electric condition is under stability limit ($\eta_{\max} < 0.3$), the average kinetic energy of trapped ions stays constant though the instantaneous kinetic energy changed from 0 to $3E_m$. Multipole ion trap and ring electrode trap are selected for chemical reaction studies as there is more field free region in the trap center and in this case, ions temperature can be easily controlled by buffer collision. What's more, to effectively store ions for a long time (about 50 s) in the ion trap, the initial kinetic energy of ions cannot be too high.

1.4 Reaction Mechanism

1.4.1 Collision theory

Ion-molecule collision theory is used to study low energy ion-molecule reactions in the ISM and it successfully explains many rate coefficient experimental results. In collision theory, both ion and neutral molecule are assumed to be point particles with no internal energy. The basic idea of the collision theory is shown in figure 1.16 which describes the process that ion m^+ and neutral molecule M approaches to each other with relative velocity v and impact parameter b .

Figure 1.16 Schematic ion molecule collisions¹⁸



If the separation distance between ion and neutral molecule equals r , the relative total energy E_r of the system is a sum of the instantaneous kinetic energy $E_{kin}(r)$ and potential energy $V(r)$ which can be written as

$$E_r = \frac{1}{2} \mu v^2 = E_{kin}(r) + V(r) = E_{kin}(r) - \frac{\alpha q^2}{2r^4} \quad (1.33)$$

where μ is the reduced mass, α is the polarizability of a neutral molecule and q is the ion charge.¹⁸ There are two components in E_{kin} . One is the translational energy $E_{trans}(r)$ along the center line of the collision and the other is the relative rotational energy $E_{rot}(r)$ which can be written in the expression

$$E_{rot}(r) = L^2 / 2\mu r^2 = E_r b^2 / r^2 \quad (1.34)$$

where L is the classical orbiting angular momentum of the two particles.¹⁸ Defining the effective potential $V_{eff}(r)$ of the ion-molecule reaction system as the sum of the central potential $V(r)$ and the centrifugal barrier energy $E_{rot}(r)$. Thus, the relative total energy of the reaction system equals

$$E_r = E_{trans}(r) + E_{rot}(r) + V(r) = E_{trans}(r) + V_{eff}(r) \quad (1.35)$$

The Gedankenexperiment of varying the impact parameter b shows the following: when $b=0$, $E_{rot}(r)$ is zero and $V_{eff}(r)$ is attractive in all values of r , so the system passes through the scattering center with $r=0$ in figure 1.16. When $b>0$, there is a special case in the collision system which is $E_{rot}(r)=E_r$ at $b=b_c$ and in this case, $V_{eff}(r)=E_r$ at $r=r_c$. Therefore, it can be concluded that $E_{trans}=0$ at $r=r_c$ from equation (1.35) and ion will orbit the scattering center with a constant radius r_c as shown in figure 1.16. For all impact parameters smaller than b_c , a capture collision (particle with proper energy and impact parameters to pass through $r=0$) will occur. However, if $b>b_c$, the centrifugal barrier prevents capture and particles are scattered at $r>r_c$. The cross section σ for the collision system is defined as

$$\sigma(v) = \pi b_c^2(v) = \pi q (2\alpha / E_r)^{1/2} \quad (1.36)$$

and then the rate coefficient can be written as

$$k_c = v \sigma_c = 2\pi q \cdot (\alpha / \mu)^{1/2} \quad (1.37)$$

which is independent of the relative velocity v .¹⁸

The rate coefficient in equation (1.37) which is called the Langevin rate coefficient works well in simple low energy ion non-polar molecule reaction. However, it underestimates the rate coefficient value for polar molecules with a permanent dipole moment as it ignores the contribution of ion-dipole potential to the collision cross section. Several theories are made to deduce the rate coefficient value of ion dipole molecule reaction and among these theoretical calculations, average dipole orientation (ADO) theory is the most popular one which well explains the experimental result. In ADO theory, the effective potential V_{eff} between ion and neutral molecule is written as

$$V_{\text{eff}}(r) = \frac{L^2}{2\mu r^2} - \frac{\alpha q^2}{2r^4} - \frac{\mu_D q}{r^2} \cdot \cos \bar{\theta}(r) \quad (1.38)$$

where μ_D is the dipole moment of molecule and $\cos \bar{\theta}$ is the average angle between the dipole axis and the line of collision.¹⁸ ADO theory assumes that there is no net angular momentum transfer between the rotating polar molecule and the whole system meanwhile the rotation of the polar molecule is approximated by a two-dimensional rotor in the collision plane. The assumption causes less than 5% error in polyatomic molecules. $\cos \bar{\theta}$ in (1.38) can also be calculated as the average of the whole $\cos \theta$ term and the two theoretical results are very close to each other.¹⁵ In ADO theory, the rate coefficient is deduced as

$$k = \frac{2\pi q}{\mu^{1/2}} \left[\alpha^{1/2} + c\mu_D \left(\frac{2}{\pi kT} \right)^{1/2} \right] \quad (1.39)$$

where c represents the average position between the dipole moment and the collision line and the value of c ranges from 0 to 1.¹⁸ From (1.39), it is found that the rate coefficient k for ion-dipole molecule reaction is varied with the reaction temperature.

1.4.2 Statistical theory

Statistical theory plays an important role in low energy ion-molecule reaction mechanism studies and there are three major categories in the statistical theory: transition state theory, unimolecular theory and complex formation theory. Statistical theory describes the direct bimolecular reaction and is called the transition state theory. There are three basic assumptions in the transition state theory: (1) Born-Oppenheimer approximation is used to separate electron and nuclear motion. (2) The motion of nuclei can be described by classical mechanics. (3) There is a surface in the reaction process which can completely separate the reactants and products. If the reaction system crosses this surface originated as reactants will terminate to be products as the surface can be crossed only once. The surface in the transition state theory is located at a saddle point of the potential barrier.¹⁸

For a general bimolecular reaction



the well known rate coefficient of the canonical transition state theory is

$$k(T) = \frac{k_B T}{h} \frac{Q^*}{Q} \exp(-E_0 / k_B T) \quad (1.41)$$

where h is Planck constant, E_0 is the activation energy and Q^* and Q are the internal partition functions of the transition state complex and reactants, respectively.¹⁸ Equation (1.41) can be written in the micro-canonical version as

$$k(E) = W^*(E - E_0) / h\rho(E) \quad (1.42)$$

where $W^*(E-E_0)$ is the sum of all the vibrational and rotational states of the reaction transition state with energy less than or equal to $(E-E_0)$ and E is the total energy of the system. $\rho(E)$ is the state density for the reactants. The transition state theory provides an upper limit for the true classical dynamical rate coefficient and it sometimes fails because of its third assumption as the system may pass through the transition surface several times before reacting.^{18,19}

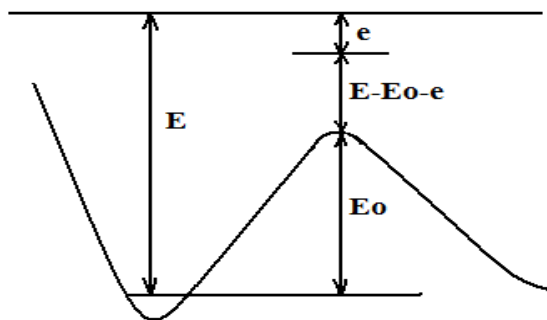
Variation theory is the derivative of the transition state theory which defines that the best choice of the dividing surface in the third assumption of the transition state theory is the one between reactants and products that produces the lowest rate coefficient in the transition state theory.^{18,20} Considering a micro-canonical system with s center of mass degrees of freedom and one of the degrees of freedom is a separable reaction coordinates r . The best surface location in the variation theory is

$$\frac{\partial}{\partial r} W_{s-1}(E - V(r); r) = 0 \quad (1.43)$$

where $W_{s-1}(E-V(r);r)$ is the sum of states of $(s-1)$ numbers of degrees of freedom perpendicular to coordinates r at energy less than or equal to $E-V(r)$ and $V(r)$ is the potential energy at r .¹⁸

A popular statistical theory for unimolecular reaction is called RRKM (Rice/Ramsperger/ Kassel/Marcus)-QET (quasi-equilibrium) theory. The assumptions in the transition state theory also work in RRKM-QET theory.^{18,21} The micro-canonical version of the rate coefficient for the RRKM-QET theory is similar as equation (1.42) and the schematic energy levels in the unimolecular system is shown in figure 1.17.

Figure 1.17 Schematic energy levels of unimolecular reaction system²¹



E_0 is the activation energy, E is the reaction total energy, e is translational energy in the reaction coordinates and $E - E_0 - e$ is internal energy available to be statistically distribution.

Statistical theory for reactions with a long-lived intermediate complex has also been developed under the assumption that the complex undergoes quasi-equilibrium and it decays into each available channel at the reaction rate proportional to the flux through the transition state for that channel. The rate coefficient can be written as

$$k = \int \frac{\partial k_c}{\partial \wp} P(\wp) d\wp \quad (1.44)$$

where $\partial k_c / \partial \wp$ is the differential collision rate coefficient and $P(\wp)$ is the decomposition probability of that complex.¹⁸

Statistical theory has been used a lot in low energy reaction studies in the ISM. Combined the statistical theory and collision theory, more reaction rate coefficient models are obtained²², and among them the Su-Chesnavich formula³ is one of most popular ones.

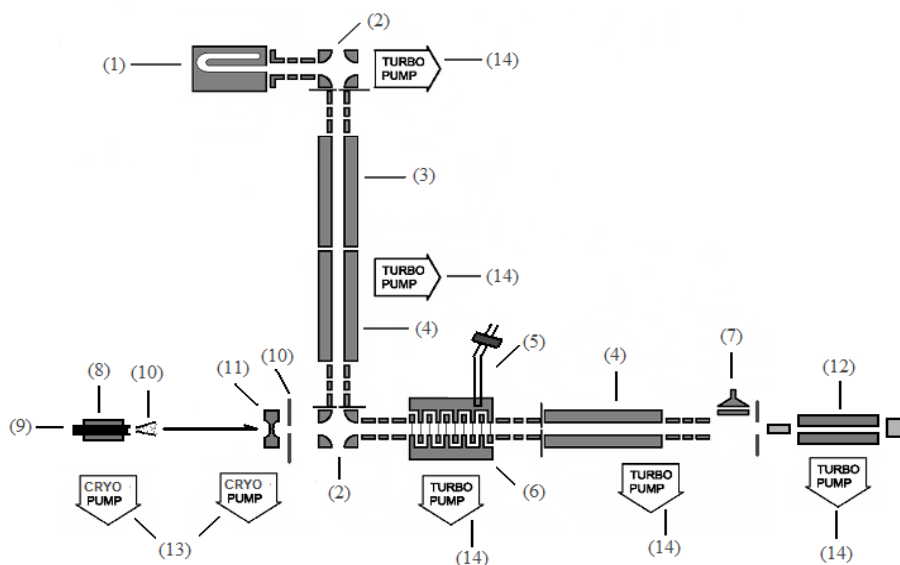
In this study, rate coefficients of ion-molecule reactions in the ISM are measured using a coaxial molecular beam radiofrequency ring electrode ion trap. The temperatures of both ions and neutral molecules are controlled separately. By measuring the reaction rate coefficients at different ion and molecule temperatures, the reaction mechanisms were studied which are mainly based on the collision theory and statistical theory.

CHAPTER 2 EXPERIMENTAL

2.1 General description of the instrument

The instrument applied in our rate coefficient study is a coaxial molecular beam – ring electrode trap (CoMB-RET) which has been specifically designed to minimize trap interactions with the ion source gas and background beam molecule contaminations. The instrument is shown schematically in Figure 2.1.

Figure 2.1 The scheme of CoMB-RET instrument. (1) U-shaped radio-frequency trap/electron bombardment ion source. (2) quadrupole bender. (3) quadrupole ion guide. (4) mass selection quadrupole. (5) gas inlet and pulsed valve. (6) ring electrode trap. (7) multi-channel plate detector. (8) cryostat. (9) effusive nozzle. (10) skimmer. (11) shutter. (12) RGA detector. (13) cryo-pump. (14) turbo-pump.



Ions produced by electron impact with neutral molecules in the source trap, pass through three electronic lenses, turn 90° by a DC quadrupole bender, and then focus into a double quadrupole mass filter. The first quadrupole is operated in the RF only mode working as an ion guide and the second one operates in mass selection mode. Next, the mass-selected ion beam passes an electronic lens set, bends another 90° in a second DC quadrupole bender which brings it coaxial with both the RET axis and the axis of the molecular beam.

Ions are injected into the RET at low energy (<0.1 eV) by lowering the entrance guard ring potential for a 1 ms ion loading period. The RET is mounted on the end of a thermally regulated liquid He cryostat to vary the trap temperature between 25 K and 450 K. Pulsed buffer gas admitted to the RET equilibrates to the defined wall temperature, as do the ions through buffer gas collisions.

The cooled ions stored in the trap are then exposed to a pulsed molecular beam and the reaction takes place. The ion-molecule reaction period is typically regulated from several hundred milliseconds to several seconds. After the reaction, the electrostatic potential on the trap exit gate lens is dropped, so the reactant and product ions in the trap enter the third quadrupole, where they are accelerated, mass-selectively filtered and finally detected through a fast micro-channel plate (MCP) ion counting system.

The molecular beam source nozzle is mounted onto the end of a second thermally regulated cryostat for temperature variation. The molecular beam is skimmed twice before it reaches the ring electrode ion trap which lies 450 mm away from the beam nozzle. A regulated shutter is placed in the beam path in front of the second aperture

which can block better than 99.9% of the molecular gas flow when the shutter is closed. The shutter is open after the ions in the trap are in equilibrium with the trap wall temperature and the He buffer gas is pumped out which allows the ions to collide with the neutral beam molecules under the desired low temperatures without the three-body association affection. The shutter is kept open until the ions in the trap come out the trap and the reaction is done. The molecular beam terminates at the residual gas analyzer (RGA) in the beam dump chamber. The RGA is used to determine the molecular beam flux which is then calibrated to the number density of molecular beam in the RET.

The dimensions of all the vacuum chambers, all the electronic plates used in the ion-molecule reaction and the holders and supporters mounted in the vacuum system for the electronic lenses and quadrupoles are summarized in the Appendix.

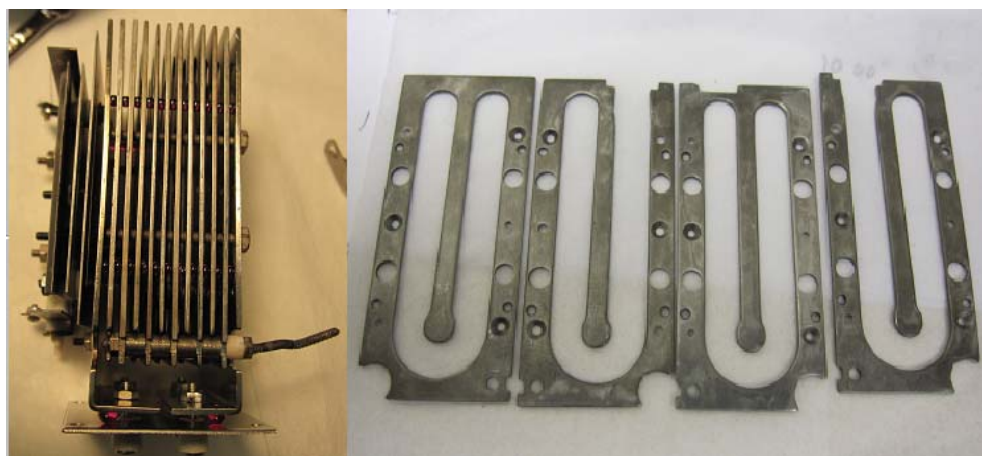
2.2 Ion cloud apparatus

2.2.1 Ion source

Ions are produced in the radiofrequency storage ion source by electron impact with neutral molecules. The gas pressure in the ion source chamber is between 10^{-5} torr and 10^{-3} torr depends on different gases. For example, to produce N_2^+ ions, the pressure of N_2 is usually set around 10^{-3} torr for better ions cooling but for H_3O^+ ions, the H_2O vapor pressure is set around 5×10^{-5} torr as H_2O consumes the filament pretty fast at higher pressures. Ions being produced in the source trap are relaxed to the ground electronic

state by ion-molecule collisions. The structure of the ion source trap is shown in figure 2.2.

Figure 2.2 Picture of ion source trap and U-shaped Rf plate

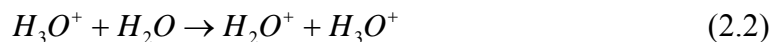


The filament being used is thoriated tungsten (W 99/Th 1, 0.15 mm) which is supported by two filament holders. The voltage across the filament is 4.9 V with 2.20 A current. The plate in front of the filament is the repeller and the voltage applied is -80.0 V. The plate right behind the filament is called the electron extraction plate and the voltage on which is usually set around -50 V. This voltage can be tuned by a potentiometer (precision series K/RV 4). There is a slot on the electron extraction for electron beam passing through. The U-shaped storage volume in the ion source trap is made by a stack of 10 molybdenum plates separated by ruby balls which are alternately connected to the two phases of an 3.33 MHz Rf generator (AC amplitude is 70 V with static DC voltage around 3-4 V). The structure of each U-shaped plate is shown in figure 2.2. The front and back of the U-shaped storage volume are limited by two L-shaped endplates, each containing a small slot for electron beam passing. The DC voltage applied on the endplates is around 6 to 7 V to inhibit the positive ions leaving the storage volume. The

whole storage volume part with the two endplates is right behind the electron extraction plate. Electrons being created by the filament are accelerated into one leg of the U-shaped hole of the storage volume and the ion exit plate is at the end of the other leg. So ions being created in the ion source must move through the whole U-shaped area and during this process, ions can be relaxed to the temperature of the ion source which is around 400 K. Ions being formed by electron impact can create secondary ions by neutral molecules collision and there are plenty of ions being produced in this way, for example, H_3O^+ ions are formed by reaction²³



and ions are cooled in the source by



This is why we use an RF ion source. Some of the unwanted ions are also quenched in this way. The potential of the exit lens which is at the end of the other leg of the U-shaped hole is pulsed to ground (1 ms duration) to produce an ion packet of maximal density when the ion loading in the RET starts. In summary, ions can be created by electron impact and relaxed to ground electronic states by neutral molecule collisions.

2.2.2 Quadrupole ion guide/mass selector

In this instrument, two quadrupole mass filters are used, one is in ion guide mode and the other is in mass selected mode. Ions being created in the ion source, pass through three electronic lenses, turn 90° after a quadrupole DC bender (Ardara Technologies,

PB_2701A) and then reach the mass filter. The diameter of the four quadrupole rods in the instrument is 0.935 cm while the radius of the inner circle formed by the four rods is 0.415 cm.

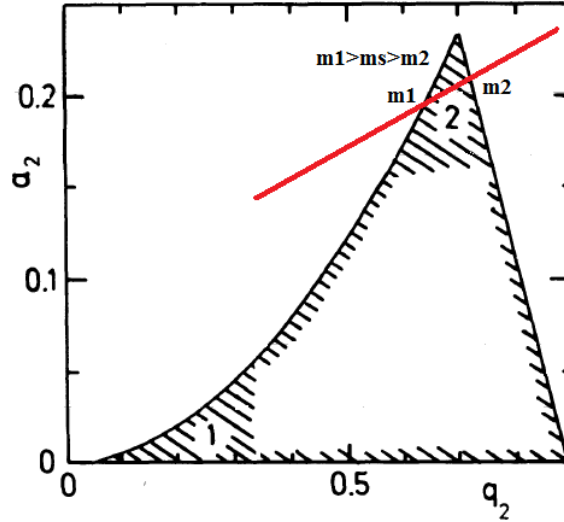
The Rf and DC potential applied on the four electrode rods are perpendicular to the z-axis in the quadrupole which causes ions to undergo transverse motion and the differential equation describes the ions motion in the x-y plane (the cross section of the quadrupole) is called the Mathieu equation. Stability parameters a_2 and q_2 defined by Mathieu equation are

$$a_2 = \frac{8 \cdot U_0 \cdot q}{m \cdot \Omega^2 \cdot r_0^2} \quad (2.3)$$

$$q_2 = \frac{4 \cdot V_0 \cdot q}{m \cdot \Omega^2 \cdot r_0^2} \quad (2.4)$$

where Ω is the radio-frequency, r_0 is the radius of the quadrupole, U_0 and V_0 are the DC voltage and AC amplitude applied on the four electrodes, and q/m is the charge to mass ratio of ions.¹⁶ In quadrupole, r_0 is a fixed value, by varying U_0 , V_0 and Ω , different (a_2 , q_2) coordinates in Mathieu stability diagram are obtained which determines ions with what q/m ratios can pass through the quadrupole safely. The Mathieu stability diagram (a_2 , q_2) is shown in figure 2.3.

Figure 2.3 Mathieu (a_2, q_2) stability diagram¹⁶



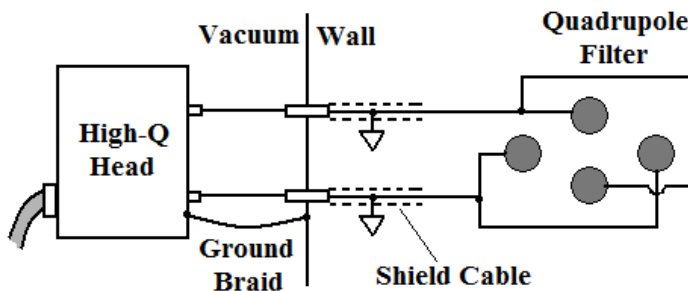
The triangularly shaped area in figure 2.3 restricts the conditions in which ions motion is simultaneously stable in the x and y directions in the quadrupole. Most of the time the operation conditions of the quadrupole are focused in region (1) and (2) in figure 2.3. Region (1) is the area where $q_2 < 0.3$ and, as discussed in the introduction, it is the limitation of the conservation of ions kinetic energy in the quadrupole. If the quadrupole operates in the condition of region (1), it is in what is called ion guide mode. In this mode, the DC voltage on electrode rods is near zero and ions with mass lower than a certain limiting value will pass the quadruple with a narrow kinetic energy distribution. The cut-off mass in this mode equals¹⁶

$$m_c = \frac{q \cdot V_0^2}{\Omega^2 \cdot r_0^2 \cdot U_0} \quad (2.5)$$

Region (2) is the top area of the triangle and the tip point is $(a_2, q_2) = (0.237, 0.706)$. If the quadrupole operated in region (2), it is called mass selection mode and high mass resolution can be obtained.

The power supply of the quadrupole is made from an Extranuclear Laboratories Inc. mass spectrometer system which contains (1) RADIO FREQUENCY POWER SOURCE, (2) HIGH-Q HEAD model #13 and (3) QUADRUPOLE CONTROL. The RADIO FREQUENCY POWER SOURCE produces the Rf potential and the operating frequency is generated by a pentode tube in the electron-coupled oscillator with highest generated frequency around 6 MHz. The HIGH-Q HEAD is a high-Q tuned transformer which steps up the rf potential in order to make the mass filter driving properly. As a result, the operating frequency of the oscillator in the RADIO FREQUENCY POWER SOURCE matches to the frequency of the resonant circuit in the HIGH-Q HEAD inductor and the frequency on the capacitance of the quadrupole mass filter. The slight differences on the quadrupole electrodes are balanced out through Rf balance control on the HIGH-Q HEAD, meanwhile, all the connections and cables should be as identical as possible. The interconnection between the HIGH-Q HEAD and quadrupole is shown in figure 2.4.

Figure 2.4 Interconnection between HIGH-Q HEAD and quadrupole



The maximum mass that can be selected by our quadrupole mass filter is

$$m_{\max} = \frac{V_{\max}}{7.219 \times r_0^2 f^2} \quad (2.6)$$

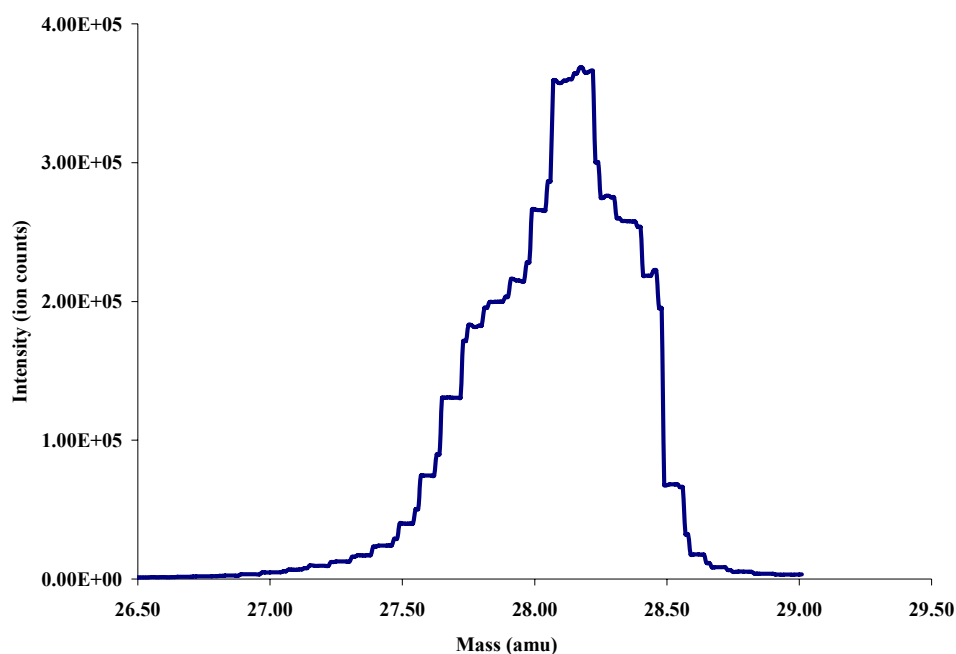
where V_{\max} is the upper limit of the AC amplitude, r_0 is the radius of the quadrupole and f is the AC frequency. In the HIGH-Q HEAD model #13, the radio frequency is around 2.1 MHz with the peak of rf amplitude at 2800 V, therefore, this mass filter can operate up to mass 350 amu.

The QUADRUPOLE CONTROL unit is the center of system controlling and monitoring. On the QUADRUPOLE CONTROL, by setting on the value of the manual mass dial, the mass selection is made to transmit ions with the single determined mass. As there is a linear relationship between the applied pole potential and the transmitted mass, so an electrical current is programmed to command the mass to which the quadrupole is tuned. The resolution of the quadrupole can be operated in either a constant $m/\Delta m$ mode, or a constant Δm mode. The potential along the z-axis of the quadrupole determines the ion energy during the transmission. This voltage is tuned through zero adjust on QUADRUPOLE CONTROL to no more than 0.1 V off ground.

There is a third quadrupole mass filter right after the ring electrode ion trap which is used to analyze the reactant and product ions after the reaction. The DC and Rf potentials are applied by a homemade power supply while the mass and resolution can be tuned through the Labview program. The resolution of mass on the Labview program is usually set at a value higher than 0.050 and in this case a mass peak with width less than 1 amu

can be obtained. The mass spectroscopy of N_2^+ ions for the third quadrupole is shown in figure 2.5.

Figure 2.5 Mass spectroscopy of N_2^+ ions in the third quadrupole (resolution value tuned at 0.050)

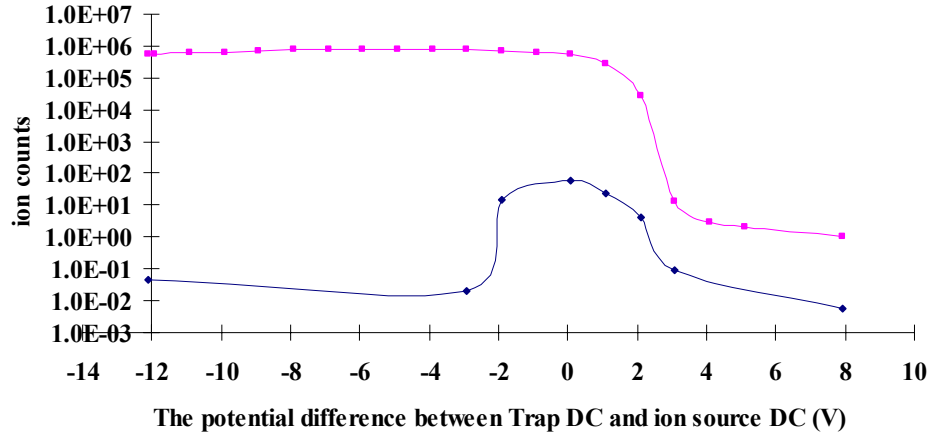


2.2.3 Ring electrode trap (RET)

Ring electrode ion trap is used for ions trapping in the ion-molecule reaction studies. The trapping area is formed by 20 ring electrodes alternatively connected to two metal plates which are connected to the Rf two phases power supply. The distance between the two neighboring electrodes on one metal plate is 1.5 mm and the thickness of the single electrode is 1 mm. The radius of the circular hole on each electrode is 5 mm. The scheme of the RET structure is shown in figure 1.7. Stored ions should move with conserved kinetic energy in a field free region when the stability limit η defined in equation (1.25) is smaller than 0.3. As shown in figure 1.11, the edge of ions field free transverse motion is around $0.7r_0$ which means that ions are allowed to move safely in a 3.5 mm radius

cylindrical area. The trap DC potential is set at a value in the range 0 to 0.3 V higher than the DC potential in the ion source in order to store slow ions in the RET as in this case the kinetic energy of ions is near thermal. What's more, sometimes the potential used in the trap DC is not exactly the potential to obtain the highest ion counts in the ion flow to the detector. This does not affect the trapping efficiency as the ions being purged are the fast ions which cannot be trapped in the RET for a long time. Details of the ion counts in the ion flow and number of ions could be stored in the RET at different trap DC potentials is shown in figure 2.6.

Figure 2.6 Ion counts in the ion flow and number of ions stored in the RET at different trap DC potentials. (♦) Number of ions stored in the RET (■) Ion counts in the ion flow reach the detector



The axial direction of the RET can be opened and closed by changing the potentials on the trap entrance and exit lens. When loading ions into the RET, the voltage on the trap entrance drops from 2 V higher than the trap DC potential to 3 V lower for 1 ms and during the loading time, the trap exit stays at high potential (2 V greater than trap DC potential). For ion ejection, the potential of trap exit decreases to 4 V below trap DC

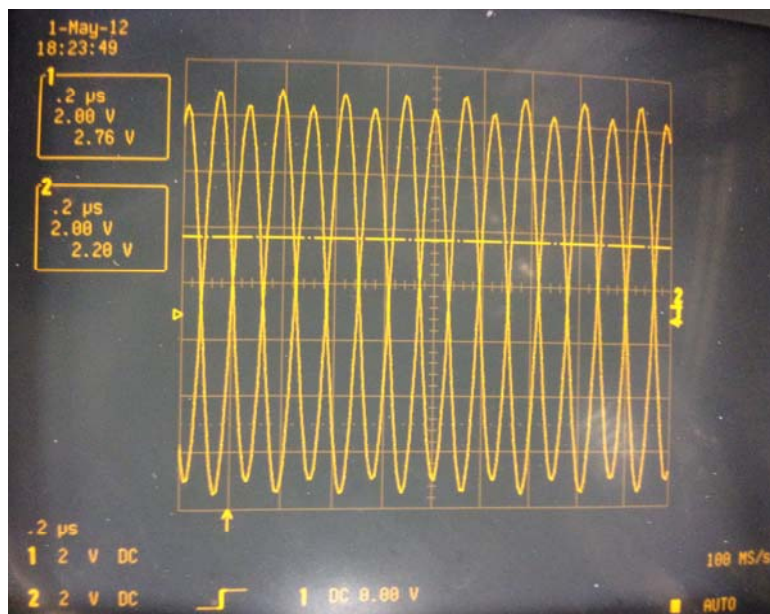
potential while trap entrance keeps at the high potential value. If the ions in the RET are totally relaxed by the buffer collision, 100 meV higher than the trap DC voltage on both trap entrance and exit are good enough to store ions in the RET. However, in actual experiment, this value is set at 2 V higher to make sure there are enough ions being trapped during the reaction. The time of ions motion in the field free area in the RET without any acceleration by the Rf field is about 50 s which is much longer compared to the time period of chemical reaction.

The ion loading time for ion-molecule reaction in the system is usually set between 1 ms to 3ms. There is no apparent difference for the number of ions stored in the RET at longer loading time. If the loading time is smaller than 0.5 ms, the number of trapped ions in the RET is 10% to 20% lower. The ion detection time is usually set to be 2 ms. When the detection time is between 1 ms and 10 ms, there is no difference for the number of ions being detected in the detector which means 2 ms is long enough for ions detection. If the detection time is longer than 10 ms, the noise signal starts to accumulate which can ruin the experimental data.

The Rf potentials on the two metal plates are $\pm (U_0 - V_0 \cdot \cos(\Omega t))$, respectively, where U_0 is DC potential, V_0 is AC amplitude and Ω is AC frequency. The Rf potential is provided by a homemade power supply with AC amplitude 76 V and AC frequency 20 MHz. In this condition, the stability limit η is smaller than 0.3, so ions won't be heat up by the Rf field while they are stored in the RET. The Rf potential in the RET is shown in figure 2.7 and in this figure the voltage value multiply by 10 is the real AC potential. To

trap more ions, the two phases of the Rf potential should be balanced as equally as possible.

Figure 2.7 Two phases of Rf potential in the RET



The ring electrode trap is surrounded by copper walls mounted on the end of a thermally regulated liquid N_2/He cryostat (Janis Model ST-400). The temperature of RET in our instrument can be varied from 20 K to 450 K. The translational and internal energy of ions can be cooled by pulsed buffer gas collision and finally these energies will be equilibrium with the trap wall temperature. Details of temperature controlling and buffer gas collision are described in chapter 3.

The position of the RET can be varied in the x, y and z directions by the xyz manipulator (Lesker, LSMXYZT64) in order to get the maximum ion counts in the detector and to ensure the RET does not contact with other electronic parts in the vacuum chamber. As the trap temperature is varied, the x direction of the manipulator which

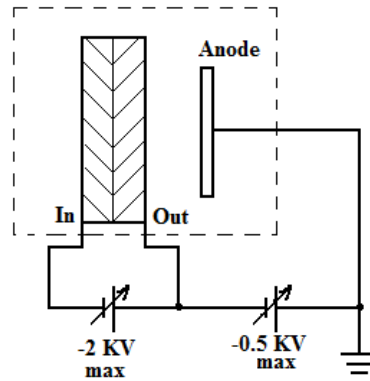
controls the up and down position of the RET should be changed. Usually, if the trap temperature drops about 50 K, the x direction of the RET should go up about 10 to 20 of the lowest graduations in the xyz manipulator. When doing the ion-molecular beam reaction, the position of the RET should fulfill the two requirements: (1) Maximum ion counts in the ion flow should be obtained in the detector. (2) Maximum pressure reading of the molecular beam in the RGA should be obtained which will be discussed in section 2.3. The y and z positions of the RET are totally the same under these two requirements but the x direction sometimes are different. In this case, the maximum pressure reading of the molecular beam in the RGA is the most significant one to be considered as the high ion counts in the detector can be obtained by varying the potentials on the electronic lenses especially the voltages on the DC quadrupole benders.

2.2.4 Detector (MCP + Amplifier/Discriminator + Counter)

When the ion-molecule reaction is done, ions are extracted from the RET through trap exit lens and then are mass selected to the detection area. Firstly, the mass selected ions are projected onto the multi-channel plates (MCP; Hamamatsu Photonics, F4655-13) where the signal is amplified by secondary electrons. The potential on the input side of MCP is -2150 V while on the output side is -300 V, so the potential gradient is formed along the channels. Positive ions, coming out of the quadrupole, accelerate to the input side of the MCP and strike the inner wall of the channel. During this process, electrons are emitted in the channel and are accelerated to the output side of the MCP by the potential gradient which causes more secondary electrons coming out repeatedly.

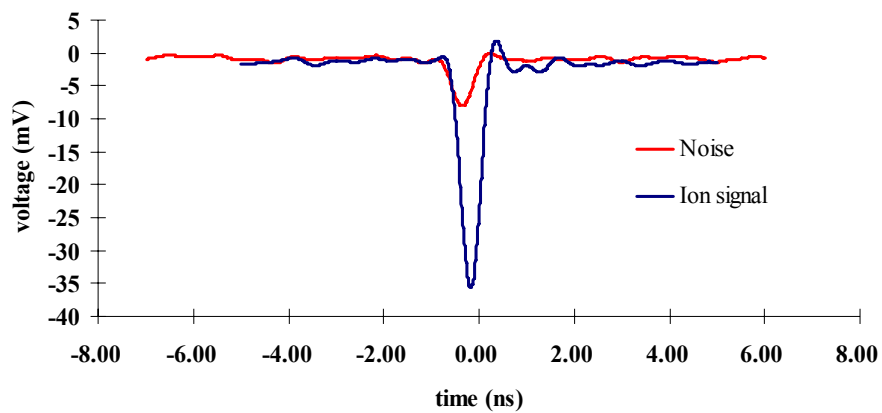
Therefore, the ion signal is exponentially increased. The circuit of the MCP power supply is shown in figure 2.8.

Figure 2.8 The circuit of MCP power supply



The potential on the MCP anode is grounded and the BNC connector is used to send the ion signal to the 300 MHz Amplifier/Discriminator (Phillips Scientific, Model #6908). Connect the BNC connector from the MCP anode to the oscilloscope, the ions signal and systematic noise on the MCP are shown in figure 2.9.

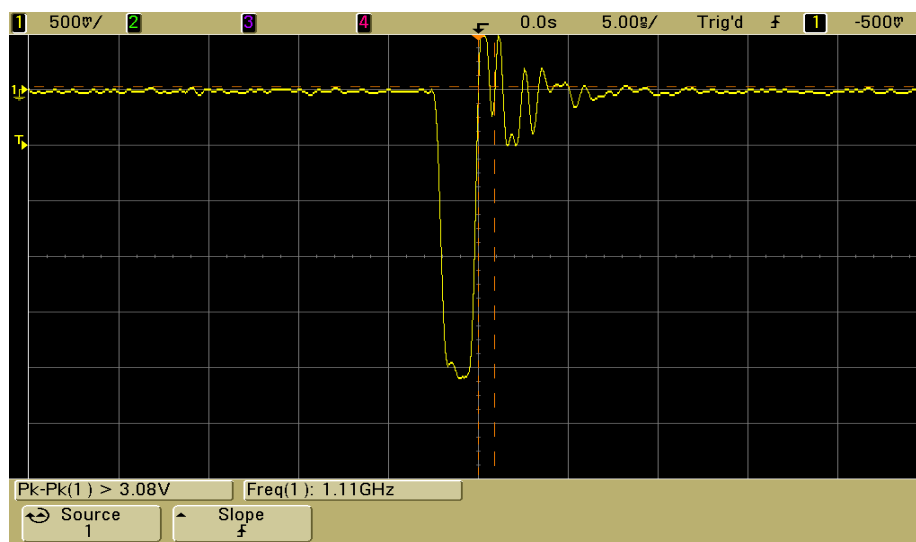
Figure 2.9 Ions signal and systematic noise in the MCP



The noise is detected by setting the trap exit potential at 10 V which blocks all the positive ions. As shown in figure 2.9, the ions signal is about 4 times higher than the noise (the noise is caused by using 50 Ω input impedance of the oscilloscope) and when

setting the threshold potential of the discriminator, the absolute value should be higher than the noise level but lower than the ion signal peak. Before the 300 MHz Amplifier/Discriminator, there is a surge protector (Philips Scientific, Model #450) in the circuit which is designed to protect the Amplifier/Discriminator from voltage spikes. The Amplifier/Discriminator owns a 300 MHz continuous repetition rate capability which is good enough for our system as the ions counts in the continuous ion flow are around 1 to 10 MHz. The threshold can be varied in the range from -1 mV to -100 mV by a 15-turn screwdriver adjustment which is in our experimental range as shown in figure 2.8. There are 6 outputs in the Amplifier/Discriminator, two pairs of bridged outputs and two complements. The one being used is the output from a bridged pair. When only one output of a bridged pair is used, the double-amplitude NIM pulse is generated in order to ensure the narrow pulse width through long cables. The ion signal from the Amplifier/Discriminator output is shown in figure 2.10.

Figure 2.10 Ions signal from the output of Amplifier/Discriminator



In this figure, the pulse width is 2.5 ns with the signal peak 2.6 V.

The Amplitude/Discriminator output is connected to the input 1 of the counter (Stanford Research systems, Model # SR400) and the output of the counter is connect to the Labview program of the laboratory computer. The final discrimination potential on the Labview program is set to be 0.5 V. Under this condition when the ion signal is around 1,000,000 Hz, the background noise is below 50 Hz. The signal to noise ratio is low enough for the rate coefficient measurement of the ion-molecule reaction.

2.3 Molecular beam

2.3.1 Molecular beam nozzle

The molecular beam source nozzle consists of a 56 mm long, 0.3 mm internal-diameter (ID) tube mounted onto the end of a second thermally regulated liquid He cryostat, and is backed with 20 to 60 torr neutral gas which depends on what gas is chosen in the reaction system. The beam pressure in the aperture area of the nozzle can be estimated in the simple equation

$$P = \frac{P_c \cdot S}{C_{mol}} \quad (2.7)$$

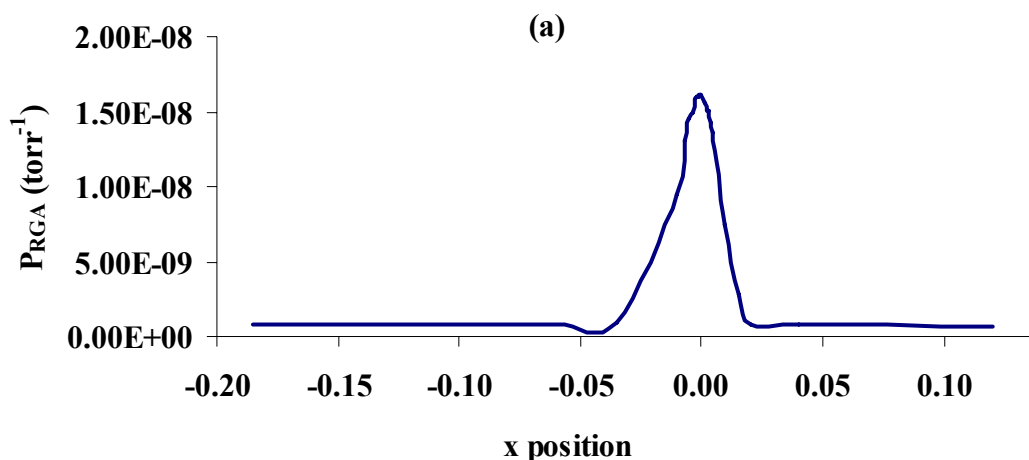
where P_c is the pressure in the beam chamber which is 2×10^{-4} torr, S is the pumping speed of the cryo-pump which equals 2000 l/s. C_{mol} is the conductance of the molecular flow and the expression²⁴ is

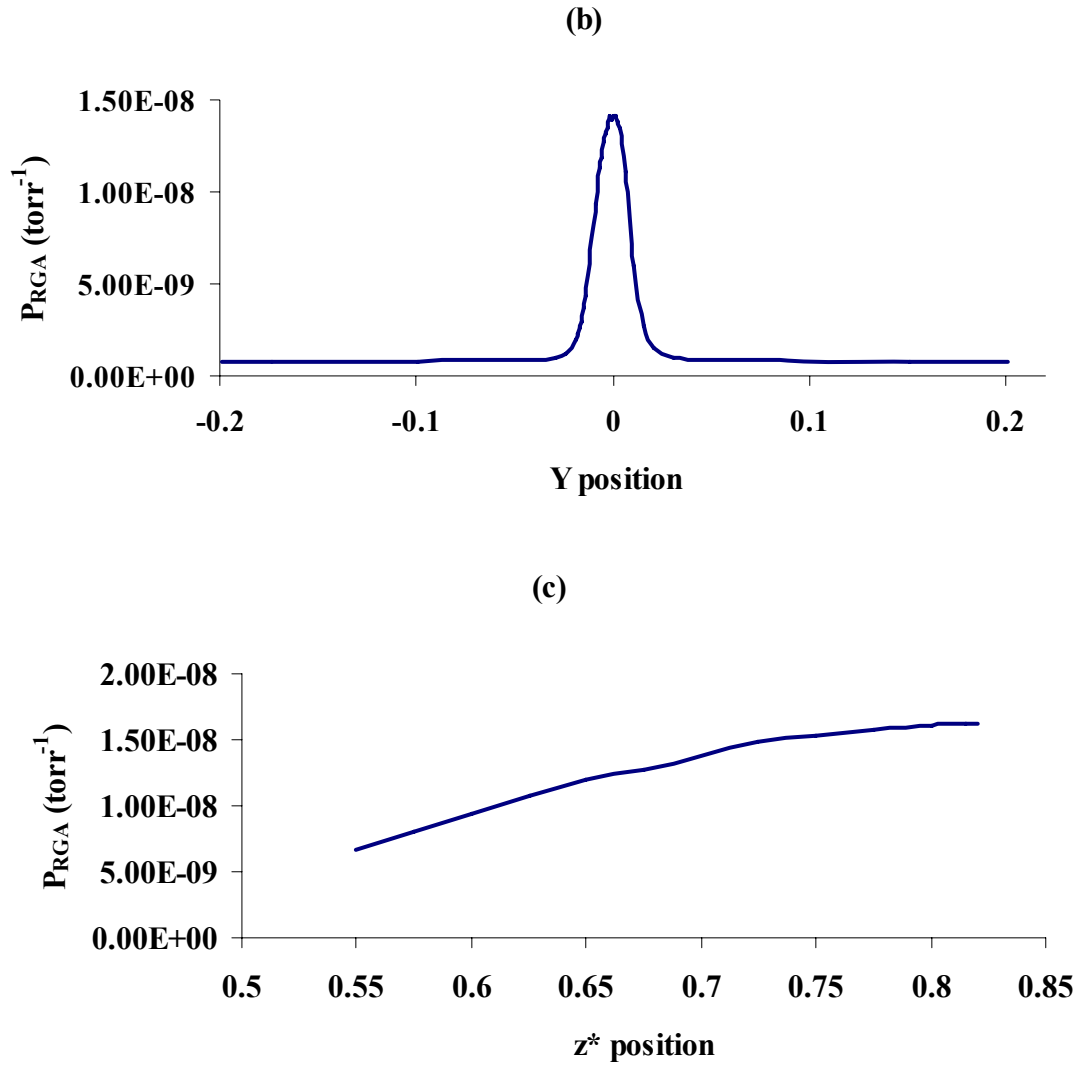
$$C_{mol}(l/s) = 11.6 \cdot \pi r^2 \quad (2.8)$$

Thus, the pressure around the nozzle aperture is about 1 torr and under this condition, the mean free path of the gas molecules is 1 cm which is much longer than the nozzle diameter, so our molecular beam is effusive beam and the velocity distribution follows the Maxwell-Boltzmann function.

The temperature of the molecular beam can be controlled by the liquid He cryo-stat and the temperature is varied from 20 K to 450 K. The beam passes through a 0.5 mm orifice conical skimmer (Beam Dynamics, Inc.) mounted 20 mm downstream and enters a differentially pumped buffer chamber. The position of the nozzle can be varied in the x, y and z directions by the xyz manipulator (Lesker, LSMXYZT64). As the molecular beam passes through the nozzle, by varying the x, y and z positions the maximum pressure value can be found in the RGA which corresponds to the best experimental condition for ion-molecule reactions as in this case the maximum number density of molecular beam can be obtained in the RET. The figure of RGA beam pressure values under different x, y and z positions are shown in figure 2.11 (a), (b) and (c).

Figure 2.11 The beam pressure in the RGA at different x, y and z positions





As shown in figure 2.11, the z direction is the line between the nozzle and skimmer and z^* means the x -axis in 2.11(c) is not the really distance between the nozzle and skimmer, but a meaningful effective value. As the nozzle moves closer to the skimmer, the beam number density in the trap becomes higher and finally the beam number density starts to keep constant. The z value is set at 0.775 to make sure the beam number density

in the trap is high enough while the nozzle and the skimmer are not too close so as to touch each other.

If the nozzle temperature is varied, the x position which controls the up and down of the nozzle should be changed. The x position is tried at different places until the maximum pressure reading in the RGA is obtained. Usually if the nozzle temperature drops 20 K, the x position of the nozzle will move down about 3 to 5 of the smallest graduation in the x direction of the xyz manipulator.

When the molecular beam with different stagnation pressures (20 torr to 50 torr) is loaded to the system, the pressure readings in the instrumental vacuum system for different chambers (beam source chamber, buffer chamber, trap chamber) in the beam pass way and the RGA in the beam dump chamber are shown in Table 2.1. The molecular beam is placed at the best x, y and z positions to get the maximum number density in the RET.

Table 2.1 Pressures of each vacuum chamber and the RGA under different molecular beam stagnation pressure (N_2 gas)

Pressure (torr)				
stagnation	beam source	buffer	trap	RGA
$< 10^{-4}$	2×10^{-9}	2×10^{-9}	2×10^{-9}	$< 10^{-10}$
17.3	3.83×10^{-6}	8.25×10^{-8}	2.25×10^{-9}	9.90×10^{-9}
32.6	1.13×10^{-5}	2.70×10^{-7}	3.00×10^{-9}	2.40×10^{-8}
51.1	2.63×10^{-5}	6.30×10^{-7}	3.75×10^{-9}	4.77×10^{-8}
66.6	4.35×10^{-5}	1.05×10^{-6}	4.50×10^{-9}	6.62×10^{-8}
72.7	5.18×10^{-5}	1.28×10^{-6}	5.25×10^{-9}	7.36×10^{-8}
86.5	7.20×10^{-5}	1.80×10^{-6}	6.00×10^{-9}	8.79×10^{-8}

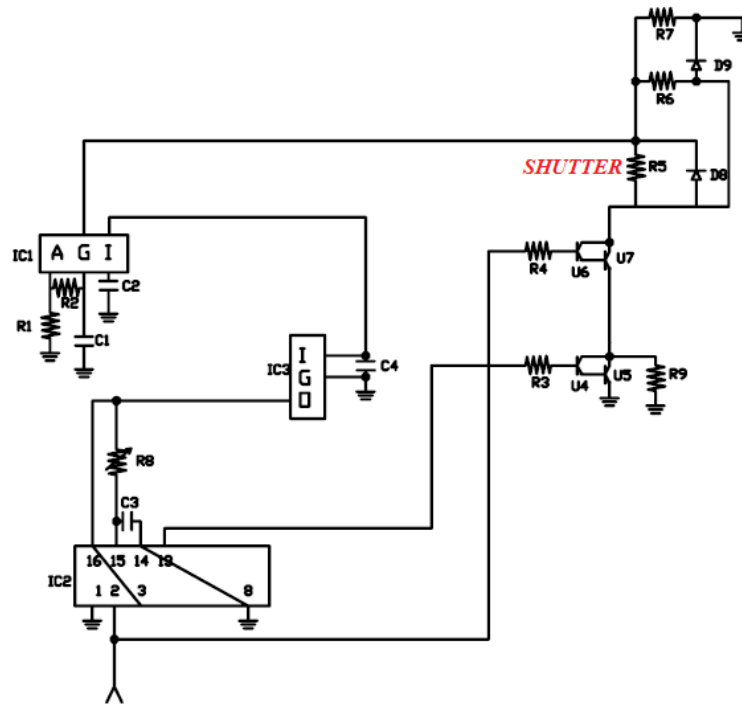
To do the molecular dimer reaction, the dimensions of the nozzle is changed to be a 40 mm long, 3.2 mm ID tube terminates at a 1 mm thick wall with a 0.3 mm diameter

aperture. This design is to make sure the molecular cluster pass the nozzle quick enough without dissociation and the details of this nozzle is discussed in chapter 6.

2.3.2 Shutter

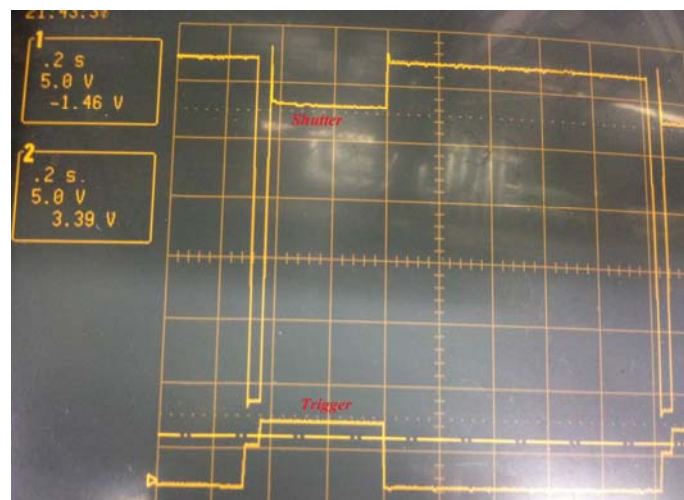
As the molecular beam passes the first skimmer and enters the buffer chamber, it is then skimmed a second time, 300 mm downstream from the nozzle, using a 2 mm diameter flat aperture, and becomes coaxial with the trap. A regulated shutter (Schneider optics, prontor magnetic shutter #0) is placed in the beam path right in front of the second aperture. The shutter is opened after the ions stored in the trap have been totally cooled by He buffer collision and the buffer gas has been pumped in the RET (pressure in the RET 10^{-8} torr). The shutter is kept open for a time defining the reaction period in the trap. The power supply to the shutter is home designed. The circuit is shown in figure 2.12.

Figure 2.12 The circuit of shutter power supply. c_1 to c_4 are 10 uf, 1 uf, 1 uf and 4.7 uf capacitors, respectively. R_1 to R_9 are resistors and the values of which are 5 k Ω , 220 Ω , 100 Ω , 100 Ω , 50 Ω , 30 k Ω , 2.66 k Ω , 10 k Ω and 130 Ω , respectively. Among them, R_5 represents the resistance of the shutter which is 50 Ω . IC_1 is a three-terminal positive adjustable regulator (LM317T), IC_2 is a dual re-triggerable mono-stable multi-vibrator which is capable of generating pulses from a few nano-seconds to 100% duty cycle, and IC_3 (DM74LS123N) is a positive voltage regulator (L7805CV1). U_4 to U_7 are transistors: U_4 and U_6 are small signal NPN transistors (2N3904) while U_5 and U_7 are base island technology power transistors (TIP31C). D_8 is the diode (IN4007) and D_9 is the LED which flashes on and off when the shutter is triggered by the pulsed wave.



When the shutter is working, the voltage across the shutter and the trigger signal is shown in figure 2.13

Figure 2.13 The voltage across the shutter and the trigger signal while the shutter is working



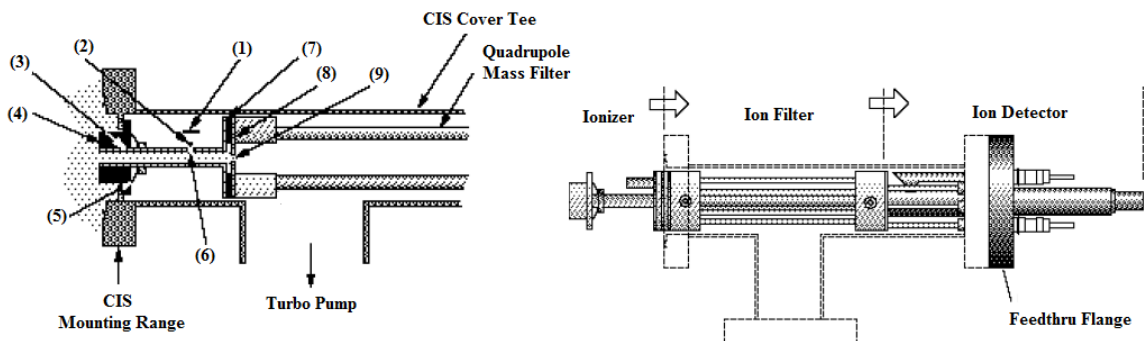
As shown in figure 2.13, to force the shutter open, 30 V DC potential should be applied across the shutter for at least 30 ms and to keep the shutter open only 3 V is required. When the voltage across the shutter drops to zero, the shutter is closed. In order not to decrease the lifetime of the shutter, the initial 30 V across the shutter should not last for more than 60 ms. The shutter is triggered by the wave-function and the amplitude of which is 5 V. The trigger signal is controlled by the labview program. When the ions in the RET are cooled by pulsed He buffer and the pressure in the RET is pumped down to 10^{-8} torr, the trigger wave is on and the shutter is open. The shutter is closed when the reaction period is done.

2.3.3 Closed ion source residual gas analyzer (CIS-RGA)

After the molecular beam traverses the RET and exits without wall interactions through the 4 mm aperture exit gate lens, it is followed by a 6 mm aperture differential wall, a differentially pumped ($210 \text{ L}\cdot\text{s}^{-1}$) quadrupole filter/ion detector, and a final 10 mm internal diameter, 100 mm long tube directing the molecular beam into a beam dump chamber (pumped by a $70 \text{ L}\cdot\text{s}^{-1}$ turbo pump). Finally, the molecular beam terminates at the closed ion source residual gas analyzer (RGA; Stanford Research Systems 200) in the end of the beam dump. The CIS-RGA is used to detect the neutral molecules in the molecular beam and the background environment, meanwhile, to calibrate the number density of molecular beam in the RET.

The CIS-RGA consists of a CIS probe and an electronics control unit. The structure of the CIS probe is shown in figure 2.14.

Figure 2.14 The structure of CIS probe²⁵. (1) Repellar (2) Filament (3) Ionization tube (4) Alumina insulator and seal (5) Spring washer (6) Emission slit (7) Alumina insulator and seal (8) Extraction Plate (9) Exit aperture.



The closed ion source contains the filament, repeller, electron emission slit, ionization tube and ion exit aperture. As the molecular beam reaches the closed ion source of the RGA, ions are produced by electron impact and then enter into the quadrupole through the small aperture. The sensitivity of the closed ion source is two orders of magnitude higher than the open ion source because it has lower background affection. The kinetic energy of ions as they move along the quadrupole filter equals to the voltage biasing on the ionization tube which determines the time ions spent in the quadrupole and is related to the intensity of ions signal and the mass resolution. There are two settings of ions energy which equals 4 V and 8 V, and the resolutions for each setting equals 0.2 amu and 0.3 amu, respectively. CIS-RGA has two types of detectors: the faraday cup and the optional electron multiplier detector. In our study, the latter one is used as it can improve the instrumental sensitivity by three orders of magnitude.

The CIS-RGA can perform both analog scan and histogram scan over the whole mass range. In the analog scan, the mass spectrometer is stepped at the fixed mass

increment through the pre-settled mass range. This mode is used in our instrument to check whether there are gas contaminations in the vacuum system. The histogram scan consists of a succession of individual peak-height measurement over pre-settled masses. This mode is used in the calibration of molecular beam number density. There is also a leak checking mode in the CIS-RGA and He is always used for leak test.

The molecular beam number density can be calibrated by the reaction with known rate coefficient. Assume a reaction



the rate of the reaction can be written as

$$-\frac{d[A]}{dt} = \frac{d[C]}{dt} = k[A] \cdot [B] \quad (2.10)$$

Integrate equation (2.9), it becomes

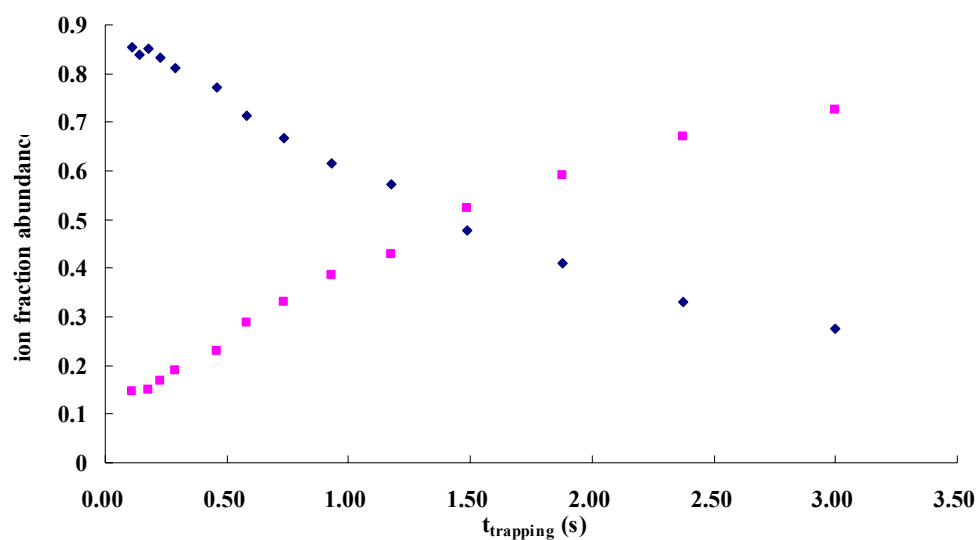
$$\text{Ln}\left(\frac{[A]}{[A]_0}\right) = -k[B] \cdot t \quad (2.11)$$

Plot $\text{Ln}([A]/[A]_0)$ versus trapping time t , a straight line is obtained and the slope equals $-k[B]$ where $[B]$ is the number density of molecular beam and k is the rate coefficient. For calibration reaction, the rate coefficient k is known, so the beam number density equals the slope divided by the rate coefficient. As soon as the beam number density is known, the unknown rate coefficient can be easily calculated in the similar way. Take reaction



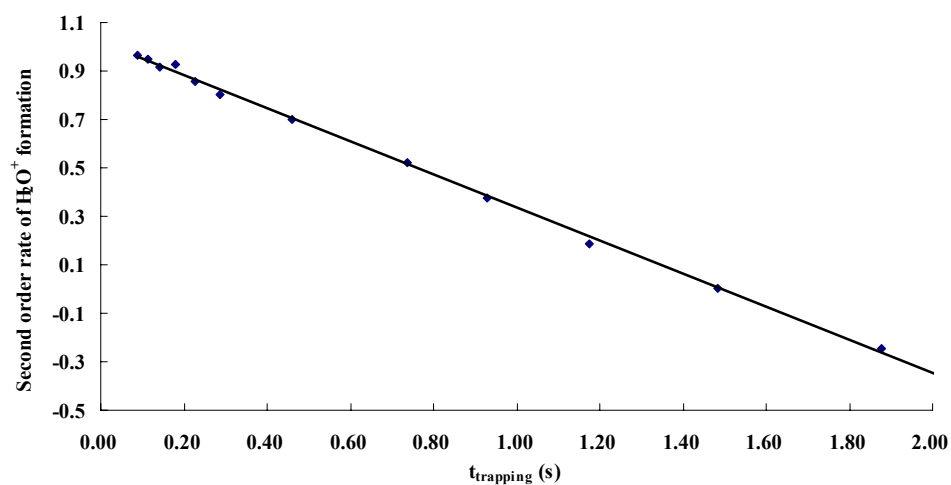
for example, as the reaction time becomes longer and longer, the fraction of reactant ions N_2^+ decreases together with the increase of the product H_2O^+ ions. Details are shown in figure 2.15.

Figure 2.15 The fractions of reactant and product ions at different trapping times (♦) represent H_3O^+ ions and (■) is the H_2O^+ ions.



Plot the second order rate of product H_2O^+ formation which is $\text{Ln}([\text{N}_2^+]/([\text{N}_2^+]+[\text{H}_2\text{O}^+]))$ versus trapping time, as shown in Figure 2.16, a straight line is obtained and the slope of the line equals the beam number density multiply the rate coefficient.

Figure 2.16 Second order rate of H_2O^+ formation



When doing calibration reaction, the molecular beam partial pressure reading from the RGA maintained at $(1.10 \pm 0.20) \times 10^{-8}$ torr, indicating that the flux of the molecular beam remained constant. The number density of molecular beam is inversely proportional to the square root of beam temperature.

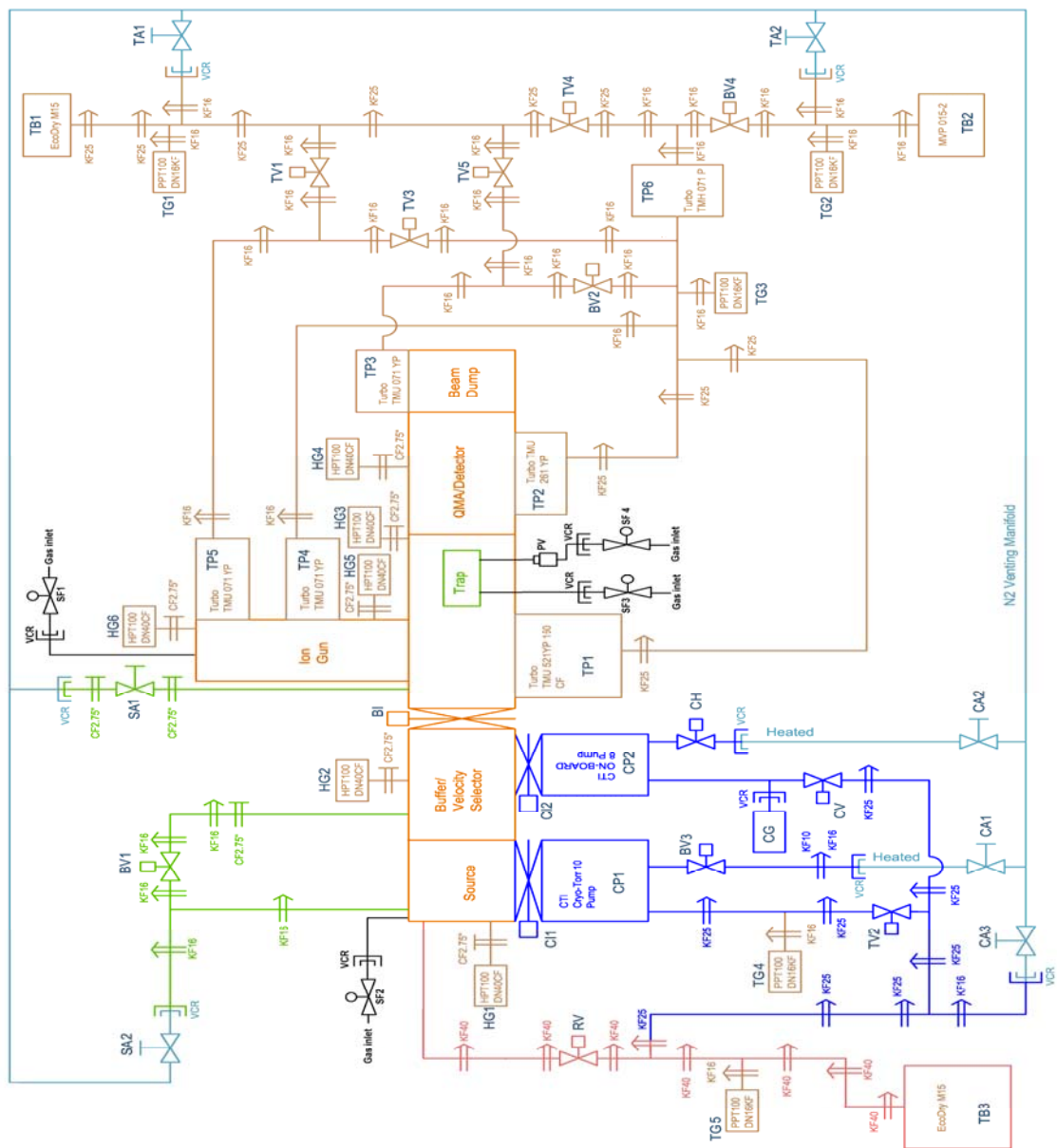
2.4 Vacuum system

A good ultra high vacuum system is the most fundamental requirement for ion-molecule rate coefficient study in the ISM. In order to best simulate the environment of the ISM, the pressure in the reaction system should be lower than 10^{-15} torr. However, under the technical limit nowadays, the pressure of the vacuum for ion-molecule reaction is normally between 10^{-8} and 10^{-10} torr. If there is too much background gas in the system, ions will collide with these molecules producing by-products which will strongly affect the rate coefficient measurements. For example, usually before the rate coefficient studies, the whole instrument should be baked for a few days in order to get rid of the H_2O impurities in the system as H_2O always consumes reactant ions pretty fast.

The vacuum system is based on the standard UHV stainless steel chambers with flanges and separated by differential walls. The ion source, quadrupole, trap, detector and beam dump chambers are pumped by turbo-molecular pumps. These turbo pumps are backed with the scroll pump, diaphragm pump and drag pump in order to get enough compression for H_2 molecules and avoid oil contamination in the vacuum system. To pump the instrument from the atmosphere to ultra high vacuum, the turbo pumps are

turned on only when the pressure of the instrument is lower than 10^{-3} torr. The molecular beam chamber and beam buffer chamber are pumped by cryo-pumps backed with the scroll pump which can pump the H_2O molecules and other impurities out of the chamber with high efficiency. To operate the cryo-pump, the pressure in the cryo-pump system should be pumped down by the scroll pump until it is lower than 10^{-2} torr and then the compressor and the cold head of the cryo-pump can be turned on. The cryo-pump is ready to use until the pressure in the cryo-pump system is 7.5×10^{-5} torr and the temperature in the second stage of the cryo-pump is below 15 K meanwhile the pressure in the vacuum system is lower than 10^{-3} torr. It takes for about 2 to 3 hours for the temperature of the cryo-pump to cool down. To shut down the cryo-pump, the compressor and the cold head need to be turned off first and it takes for about 4 hours for the cryo-pump system to warm up to room temperature and the pressure in the pump increases as the pump temperature goes up. The cryo-pump cannot open to atmosphere until it has been warm up to 298 K in order to get rid of water contamination. There is a gate valve between the molecular buffer chamber and the trap chamber which can separate the two vacuum systems with the leaking rate lower than 10^{-9} torr·L·s⁻¹. Details of our vacuum pumping system are shown in figure 2.17.

Figure 2.17 Pumping system of the instrument



The description of all the pumps, ion gauges and valves used in the vacuum system are summarized in Table 2.2.

Table 2.2 Pumps and ion gauges used in the vacuum system of ions

Pump				
Symbol	TYPE	Model	Pumping Speed	Location
TP 3-5	Turbo	TMU 071 YP	60 L/s	Ion Gun/ Beam Dump
TP 1	Turbo	TMU 521 YP	520 L/s	Trap
TP 2	Turbo	TMU 261 YP	210 L/s	Detector
TP 6	Drag	TMH 071 P	60 L/s	Back pump
TB 1/3	Scroll	EcoDry M15	11.1 m ³ /hr	Back pump
TB 2	Diaphragm	MVP 015-2	4.4 L/min	Back pump
CP 1	Cryo	Cryo-torr 10	3000 L/s	Beam
CP 2	Cryo	On-board 8	1500 L/s	Buffer
Ion Gauge				
Symbol	Type	Detection range	Location	
HG 1-6	HPT 100	10 ⁻⁹ -1000 mbar	Ion Source/ Trap/ Beam/ Beam Dump	
TG 1-5	PPT 100	10 ⁻⁴ -1000 mbar	Measure back pressure	
CG	AUX TC	10 ⁻³ -1 torr	Cryo pump CP2	
Valve				
Symbol	Type	Description		
TV 1-5	Electro-pneumatic	Pfeiffer Vacuum, EVB 025 PX, flange (in) DN-25-ISO KF		
BV 1-4	Electro-pneumatic	Pfeiffer Vacuum, EVB 016 PX, flange (in) DN-16-ISO KF		
RV	Electro-pneumatic	Pfeiffer Vacuum, EVB 040 PX, flange (in) DN-40-ISO KF		
Cl 1-2	gate	between the cryo-pump and vacuum chamber		
CH	purge	Between cryo-pump CP2 and purge gas supply line		
CV	roughing	Between cryo-pump CP2 and roughing pump system		
Bl	gate	Lesker SG0400PCCF, CF 6" OD flanged, Connect the molecular beam buffer chamber and ion trap chambers		
PV	pulsed	Parker, series 9, admitted pulsed buffer into the RET for ions cooling		
CA 1-3	Quantum-turn	ss-4P4T2, for nitrogen venting		
SA 1-2	Nupro BK	ss-4BK VCR, for nitrogen venting		
TA 1-2	Ball	ss-43GVCR4, for nitrogen venting		
SF 1-4	solenoid	3-way, #8320P184, for vacuum safety		

Under all these pumping conditions, the pressure in each chamber and the backing system for the CoMB-RET reaction system with no gas loading in the ion source chamber and trap chamber to the instrument are shown in table 2.3.

Table 2.3 Pressures in vacuum chambers and backing system under the pumping system

Location	Pressure (torr)
Ion source chamber	2.0×10^{-8}
RET chamber	2.0×10^{-9}
Beam dump	2.0×10^{-9}
Molecular beam source chamber	7.5×10^{-10}
Beam buffer chamber	7.5×10^{-10}
Back pressue of ion train system (scroll pump)	10^{-3} to 10^{-4}
Back pressure of ion train system (drag pump)	7.5×10^{-5}
Back pressure of ion train system (diaphragm pump)	1.0 to 2.0
Back pressure of molecular beam system	10^{-3} to 10^{-4}

As described in table 2.2, the whole system is under a good vacuum environment. When doing the ion-molecule reaction, the pressure in the ion source chamber is usually around 10^{-3} torr and in this case, the pressure in the trap chamber goes up to 2×10^{-8} torr. Though the pressure in the RET goes up to 10^{-8} torr, it is still low enough for the study of the temperature dependent ion-molecule reaction. For some of the testing reactions, instead of using molecular beam, continuous buffer gas is injected into the RET and the real buffer pressure in the RET equals the pressure reading from the HPT ion gauge of the trap chamber (TP1 in figure 2.17) times a calibration factor 70. The calibration factor is obtained from calibration reaction

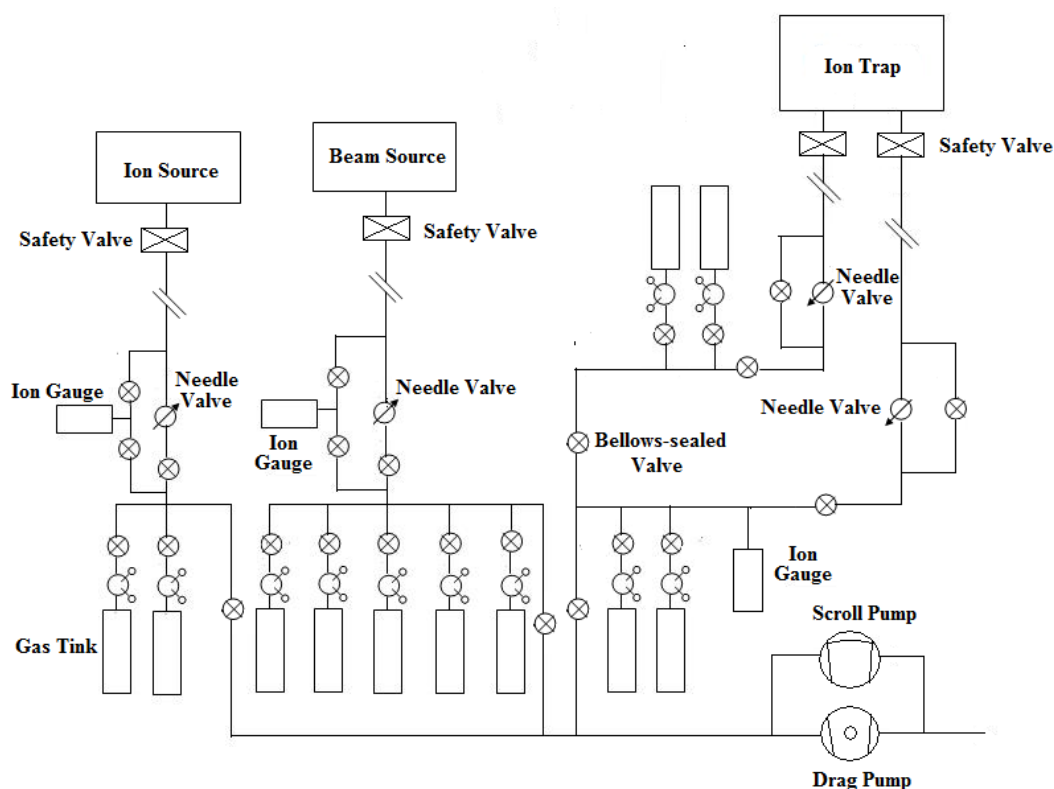


with known rate coefficient $2.7 \times 10^{-10} \text{ cm}^3\text{s}^{-1}$ and $3.2 \times 10^{-10} \text{ cm}^3\text{s}^{-1}$, respectively. The pulsed buffer gas in the RET and the related pressure changing are described in chapter 3. In order to protect the MCP detector, the maximum continuous buffer pressure can be

loaded into the trap chamber is 4.5×10^{-6} torr and the pressure of the beam dump chamber in this case is 10^{-8} torr meanwhile the pressures in the other chambers do not have obvious change.

The gas inlet system to the CoMB-RET instrument is shown in figure 2.18 which contains three main parts: (1) gas inlet to ion source chamber, (2) gas inlet to molecular beam nozzle and (3) gas inlet to the RET. The third one has two gas lines, one is for the continuous buffer gas and the other is for pulsed buffer gas.

Figure 2.18 Gas inlet system to the CoMB-RET instrument



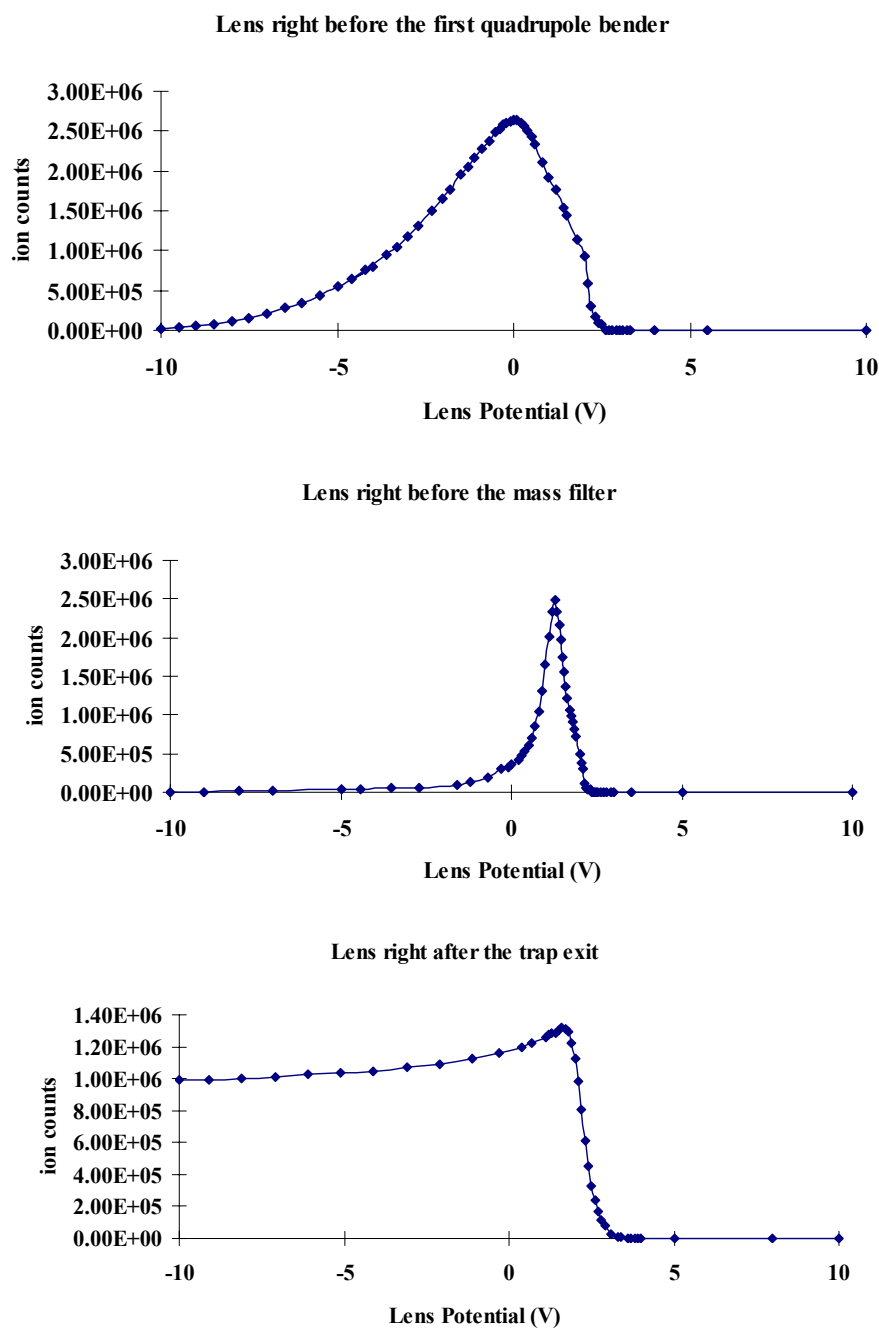
Needle valves (precision valve # 315010, MDC) are used in each gas line to control the gas flow to the vacuum system. In the rate coefficient study, the gas pressure before the needle value is usually from 400 to 760 torr and after the needle value the pressure in

the gas line which goes directly to the vacuum system is below 1 torr. The pressure range of the ion gauge (Teledyne hastings instrument, model 2002) used in the system is from 10^{-4} torr to 1000 torr. To pump the gas inlet system, the valve connected to the scroll pump is open first to pump the system pressure to 10^{-2} torr and then the drag pump line is open to pump the whole system to 10^{-4} torr. Right before the gas in the four gas lines flows into the vacuum system, safety valves (solenoid valve, 3-way, #8320P184) are placed in each gas lines to protect the vacuum environment of the CoMB-RET instrument. When the pressure in the vacuum chambers is higher than 10^{-5} torr, the four safety valves will close altogether automatically mainly to protect the MCP detector, quadrupole mass filter and the turbo-pumps.

2.5 Potential control of electronic lenses through labview program

The voltage on each electronic lens can be controlled totally by the Labview program to get the maximum ion counts in the ion flow to the detector or the maximum ions stored in the RET. To keep the ions movement in the relative low kinetic energy, the potentials on each electronic lens in the labview program ranges from -10 V to 10 V. To choose the proper potentials for the electronic lenses, there are three things need to be considered: (1) Obtain maximum ion counts in the ion flow. (2) The RET can store the maximum number of ions. (3) The potential applied on the electronic lens should close to the DC potential in the ion source. Figure 2.19 shows some examples of the ion counts in the ion flow at different potentials on some of the electronic lenses.

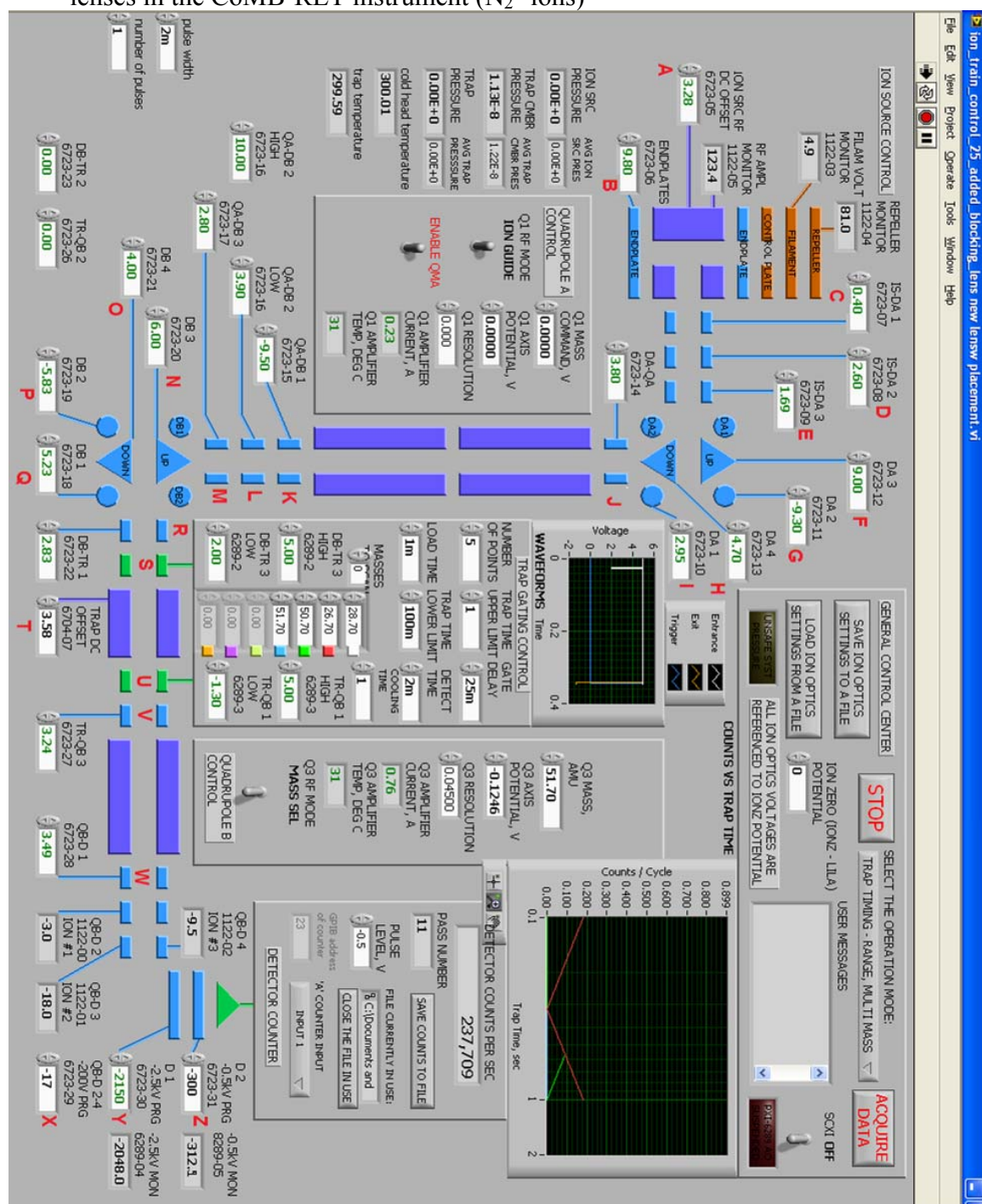
Figure 2.19 Ion counts in the ion flow at different potentials on some electronic lenses



From these figures, it is easy to tell at which potential the maximum ion counts are obtained. Figure 2.20 is the screen of the labview program for ions flow and ion-molecule

reaction controlling. The potential value beside each electronic lens shows an example to get the maximum ion counts stored in the RET.

Figure 2.20 Labview screen for the controlling of the potentials on the electronic lenses in the CoMB-RET instrument (N_2^+ ions)



The maximum ion counts in the ion flow reaching the MCP detector in these potential settings is 2.0 MHz and the number of N_2^+ ions can be stored in the RET is between 80 to 100. The maximum current on each electronic lens measured by the pico-meter (Keithley, model #6485) in this example and the explanation of the potentials on each electronic lens is summarized in Table 2.4.

Table 2.4 The current and the related explanation of potentials on electronic lenses

Label	Location	Current (nA)	Description
A	DC potential in the ion source		Determines the ground kinetic energy of ions
B	Endplate		Hold the ions in the storage volume of the ion source
C	Ion exit lens of the ion source	12	To get the maximum ion counts in the ion flow, this value should be set at -10V. But to make sure the ions energy is as low as possible, so this value stays around 0 V in order to get rid of fast ions. Though the ion counts in the ion flow is lower in this case, it doesn't affect the number of ions stored in the RET.
D	First lens in front of the first DC bender	0.16	Make sure the potential is close to the DC potential in the ion source in order to get slow ions
E	Second lens in front of the first DC bender	1.1	
F	First DC quadrupole bender		Though it is better to make the potentials as close to the DC potential in the ion source as possible, to bend the ions 90°, on some of the electronic poles, -9 V should be applied.
G			
H			
I			
J	Lens before the mass filter	0.46	Same as D & E (K is -9.5 V in order to obtained more ions after the mass filter)
K	Lens out of the mass filter	0.04	
L	First lens in front of the second DC bender	0.012	

M	First lens in front of the second DC bender	0.005	
N	Second DC quadrupole bender		Same as F to I
O			
P			
Q			
R	Lens after the second DC bender	0.002	Same as D & E
S	trap entrance	0.001	For ion loading before the reaction, the potential is 2.0 V in order to make sure ions can flow into the RET with low energy. For holding ions in the RET during the reaction, the potential is 5 V.
T	Trap DC potential		To get the maximum ion counts in the ion flow, the value should be 1-2 V lower, but to trap ions in the RET the potential should ranges 0 to 0.3 V higher than the DC potential in the ion source as in this case the kinetic energy of ions is close to ground.
U	Trap exit	0.001	For ions exit after the reaction, the potential is -1.3 V in order to make sure all the ions stored in the RET move to the mass analyzer. For holding ions in the RET during the reaction, the potential is 5 V.
V	Lens before the mass analyzer	0.001	Same as D & E
W	Lens after the mass analyzer		
X	Control the potentials of the three lenses before the MCP		Ranges between 0 and -190 V
Y	MCP in		Usually set between -2150 V to -2190 V, the maximum value is -2250 V.
Z	MCP out		Always set at -300 V.

In summary, the ion current is lower and lower as the ion flow goes further in the ion train which is because lots of fast ions lost each time they pass through the electronic

lens, DC quadrupole bender and the quadrupole mass filter and finally only ions with low kinetic energy can reach the RET. The potentials on the electronic lenses should be close to the DC potential of the ion source in order to get slow ions. To store ions in the RET, the DC potential in the RET ranges 0 to 0.3 V higher than the one in the ion source.

CHAPTER 3 TEMPERATURE CONTROLLING

In this study, rate coefficients are measured at different temperatures in order to find the temperature dependent rate coefficients of reactions in the ISM. Trap and beam temperatures are controlled separately in order to find more details of chemical kinetics and reaction mechanism behind the experimental data. Cryostats (ST-400) are mounted on both the wall of the RET and the molecular beam nozzle, together with the temperature controller (Lakeshore, Model 331) to control the temperatures of ions and molecular beam.

3.1 Cold head

The Janis Research SuperTran (ST) system includes a continuous flow cryostat which can perform a wide variety of experimental temperatures ranges from 5 K to 450 K. The cryostat includes a 25 Ω heater and a silicon diode thermometer for monitoring and regulating the temperature. For our study, the temperature range we obtained in the RET is from 20 K to 450 K. Besides the thermometer on the cryostat, there is a second silicon thermometer contact directly to the wall of the RET and the temperature of which is displayed by the same temperature controller through a parallel input channel. Usually there is a 2 K to 5 K temperature difference between the two thermometers and the reading from the one directly connected to the trap wall is used as trap temperature in the study. In the molecular beam, temperature ranges from 160 K to 450 K and the lowest

temperature reached in our study depends on the condensation point of the neutral molecules used in the reactions. Liquid Helium or nitrogen stored in the cryogen storage container is continuously transferred through a high efficiency super-insulated line to the copper sample mounted inside the cryostat vacuum jacket. For temperatures above 80 K, liquid nitrogen is transferred for the cooling of the RET and for temperatures below 80 K, liquid helium has to be used. A needle valve flow regulator is in the transfer line to regulate the liquid Helium/nitrogen flow. The vent valve of the storage dewar is adjusted to maintain the pressure of the storage dewar between 4.5-5.0 psi and for nitrogen cooling, sometimes nitrogen need to be added in the dewar. For liquid He cooling, besides the initial copper walls mounted around the RET, there is another copper shielding walls outside the former one in order to get rid of the blackbody radiation in the vacuum system and cool the trap temperature to a much lower value. The dimensions of the second copper shielding wall are shown in appendix.

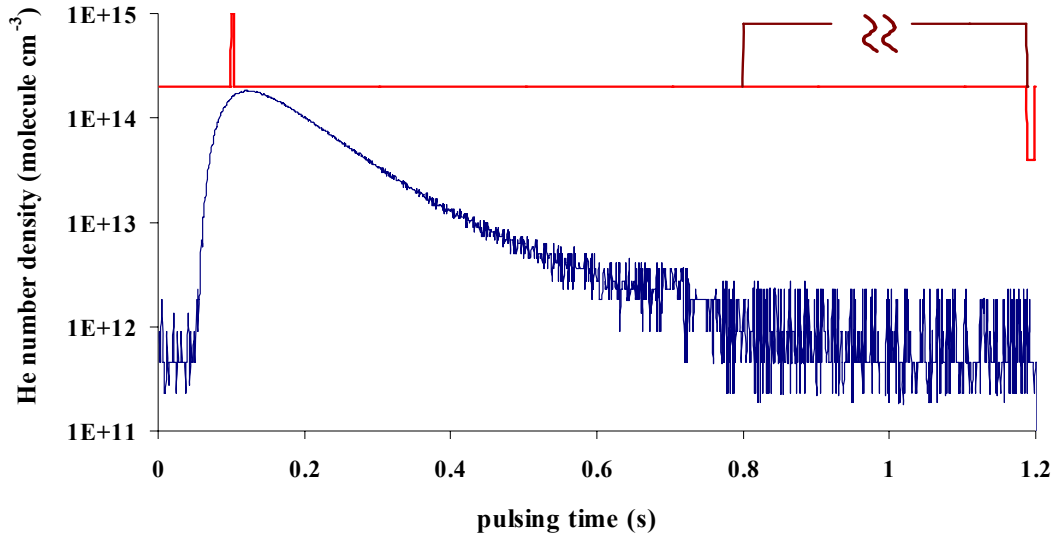
3.2 Ions cooling by buffer collisions

In order to get cold ions in the chemical studies of the ISM, the translational energy of ions has to be low; meanwhile, the internal degrees of freedom of ions also need to be frozen. The internal temperature of ions is unaffected by the Coulomb interaction. For ions stored in the RET, the internal temperature will finally equilibrates with the temperature of the RET wall by blackbody radiation. Buffer cooling is the most sufficient way to cool both the translational temperature and internal temperature of ions in a short

time window through elastic and inelastic collisions between buffer molecules and ions.²⁶ The only requirement of buffer cooling is that ions can be survived by multiply collisions.

In our study, a pulsed valve is employed in one of the buffer gas inlet lines to the RET, which opens 100 ms prior to ions loading for a 3 ms period and He buffer is admitted. A typical time profile of the trap pressure after single He buffer pulse is shown in Figure 3.1. The time scale of ion loading, beam pulsing and ion sampling are also labeled in this figure.

Figure 3.1 Time profile of buffer cooling for single buffer pulse



The highest number density of He in the RET is $2 \times 10^{14} \text{ cm}^{-3}$, the width of the density profile is approximately 150 ms, and it takes 800 ms to exhaust the majority of the He buffer. These conditions correspond to a maximum collision frequency between trapped ions and He buffer of $3 \times 10^5 \text{ s}^{-1}$ and an average number of collisions per ion experienced of approximately $2 \times 10^4 \text{ s}^{-1}$ integrated across the buffer pulse. The ions and

the buffer gas can be approximated by two Maxwellians with different temperatures T_1 and T_2 , so the collision temperature can be written as

$$T = \frac{m_1 T_2 + m_2 T_1}{m_1 + m_2} \quad (3.1)$$

After sufficient numbers of collisions and under the safety limit of the RET, in the ideal situation, the ions in the trap with the buffer gas ultimately reach thermal equilibrium at a temperature (both translational and internal) which is defined by the temperature of the trap wall.

The pulsed valve used for buffer gas is ultra low leak extreme performance valve (Parker, series 9) and the power supply to the pulsed valve is homemade and the principle of which is similar to the one used for the shutter. The ion gauge for the measurement of pulsed buffer pressure is powered from the gauge controller (Granville Philips, series 260). Electrons created by the filament are accelerated to the grid and ions are formed by electron impact. These ions are then accelerated to the collector electrode and the ion current is measured by the high resolution pico-meter (Keithley, model #6485). The current signal can be converted to the pressure value from the calibration function $4 \times 10^{-5} I + 6 \times 10^{-10}$ through labview program, where I is the current reading from the pico-meter and the units of pressure is torr.

3.3 Molecular beam temperature

The temperature of the molecular beam is controlled by the cryostat on the nozzle. The average pressure in the nozzle for ion-molecule reaction experiments is about 30 torr, so the average conductance in the nozzle is calculated to be $0.007 \text{ L}\cdot\text{s}^{-1}$ using the expression²⁴

$$C = 135 \cdot \frac{d^4}{l} \cdot \bar{p} \quad (3.2)$$

Therefore it takes about 5 ms for the neutral molecules passing through the nozzle and the average collision frequency of molecules in the nozzle is 10^7 s^{-1} . As a result, the number of collisions one molecule experienced in the nozzle is 5×10^4 which is good enough to cool to molecules to low temperatures.

In conclusion, the temperatures of ions and neutral molecules are controlled separately by cryostats with liquid He/N₂ and heater in order to find the reaction mechanisms. Ions are cooled efficiently by pulsed He buffer collisions in the RET to relax both the translational and internal energies of ions. Neutral molecules are cooled because of its high collision efficiency in the beam nozzle.

CHAPTER 4 $N_2^+ + H_2O$ REACTION SYSTEM

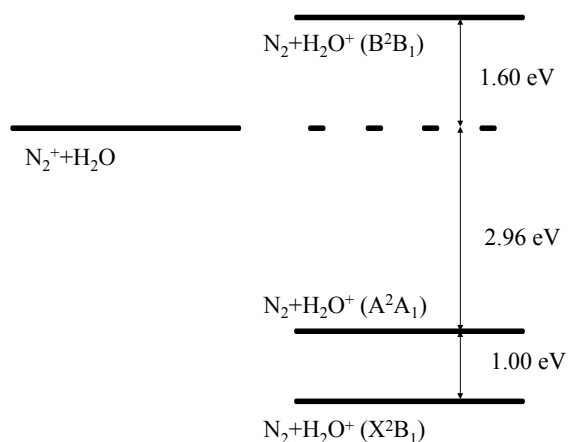
4.1 Introduction

In low-Earth orbit, water is one of the major components in the artificial atmosphere around spacecraft.^{27,28,29} The charge transfer reaction between nitrogen in the atmosphere and water molecules,



is one of the most important ion-molecule reactions observed in low-Earth orbit associated with shuttle glow. That this reaction is occurring in a highly perturbed non-equilibrium environment regarding both velocity and internal energy distribution is equally intriguing. Meanwhile, ion- H_2O reactions are ubiquitous in all studies of ion chemistry and mass spectrometry and therefore a thorough understanding of the dynamics of this reaction is warranted.

There have been a multitude of studies of the rate coefficient for Reaction (4.1) under equilibrium conditions over the years. The kinetic energy dependence of the cross section for this reaction has been studied in the 1960's and more recently by Dressler and co-workers in the 1990's. The relevant electronic energy levels of the electron exchange process for $N_2^+ + H_2O$ reaction are shown in figure 4.1.

Figure 4.1 Electronic energy levels for $\text{N}_2^+ + \text{H}_2\text{O}$ reaction

If the H_2O^+ product of the reaction is in the A^2A_1 electronic state, there is an exothermicity of 2.96 eV while production of the B^2B_2 state of H_2O^+ is 1.60 eV endothermic. The energy difference between the A^2A_1 state and the ground state (X^2B_1) of water ions is 1.00 eV.^{28,29} Turner and Rutherford in the 1960's found that for incident ion energy in the range from 1 to 400 eV using beam techniques, the cross section decreases with increasing collision energy from 30×10^{-16} to $7 \times 10^{-16} \text{ cm}^2$ and the large cross section demonstrates that the reaction takes place at long range.²⁷ Using a guided ion beam-gas cell technique, Dressler and his co-workers have shown that the excited product A^2A_1 state of H_2O^+ is populated at low collision energies while the B^2B_2 state is populated as soon as it becomes energetically accessible which is above 1.60 eV. At low collision energy, a long-lived complex is formed which is governed by the long-range ion-dipole interaction and that at collision energies above 4 eV, a long-lived complex is not involved.²⁸ The agreement between the Average Dipole Orientation (ADO) model

and the $\text{N}_2^+ + \text{H}_2\text{O}$ cross section is good at the lowest meaningful energy (about 0.4-0.8 eV) of their work while at higher energies, the cross section becomes less dependent on the collision energy because of a direct mechanism which begins to dominate the dynamics.²⁹

In this study, the rate coefficients of $\text{N}_2^+ + \text{H}_2\text{O}$ reaction are measured with trapped N_2^+ ions at fixed 100 K and a coaxial H_2O molecular beam with variation beam temperatures from 300 K to 450 K. Using a trapped ion cloud in conjunction with a molecular beam, the relative reactant energy can be easily varied and the effects of non-equilibrium energetics amongst the degrees of freedom directly investigated. The reaction is also used to test our CoMB-RET instrument.

4.2. Experimental

A coaxial molecular beam ring electrode trap (CoMB-RET) instrument is used in the system. The N_2^+ reactant ions are produced by electron impact in a U-shaped radio-frequency trap in the ion source chamber with a N_2 pressure of approximately 1.7×10^{-3} torr. In the storage source, N_2^+ ions are relaxed via charge transfer collisions to the ground electronic state thermalized to the 400 K source temperature. The ions exiting the trap pass through a 90° DC quadrupole bender which separates the ion stream from the effusive gas exiting the source. The ions are then focused into a double quadrupole which is operated in the RF only mode since ion source conditions used now present only N_2^+

ions. The ion beam is then turned another 90° in a second DC quadrupole bender bringing it coaxial with the RET trap axis and the axis of the molecular beam.

Ions are injected into the RET at low energy (<0.1 eV) by dropping the entrance guard ring potential. After a 1 ms loading time, the voltage on the trap entrance is increased. The RET is mounted on the end of a thermally regulated liquid He cryostat and continuous buffer gas admitted to the trap cools to the 100 K wall temperature as do the ions through buffer gas collisions. The use of N₂ buffer in this study provides for extremely efficient ion cooling through resonant electron exchange compared to He buffer. Ion storage times in excess of 10 s have been realized limited only by the background impurities within the trap cell.

The ions in the trap are exposed to the transiting H₂O molecules from a skimmed effusive molecular beam. The beam source nozzle consists of a 30 mm long 0.5 mm internal diameter tube mounted onto the end of a second thermally regulated liquid He cryostat, and is backed with 20 torr of water vapor. The beam expands into the beam chamber and is skimmed 20 mm downstream via a 0.5 mm orifice conical skimmer. The beam passes through a beam buffer chamber and is skimmed a second time at a distance 300 mm from the nozzle by a 2 mm diameter flat aperture and becomes coaxial with the trap. The beam passes through the quadrupole bender and enters the ring electrode trap through a 4 mm inside diameter gate lens. The center of the trap lies 450 mm from the source nozzle. As introduced in chapter 2, the molecular beam terminates into the ion source chamber of the RGA and the beam number density is cross calibrated against the observed N₂⁺-H₂O rate at 300 K (both beam source and RET using $k_1 = 2.4 \times 10^{-9} \text{ cm}^3 \text{ s}^{-1}$

¹).³⁰ The beam density of water in the trap in this study ranges between 4.5×10^7 and $8.0 \times 10^7 \text{ cm}^3 \cdot \text{s}^{-1}$ depending upon source nozzle temperature.

Following exposure of the ion cloud to the water beam, the trap exit gate lens is dropped in potential and the remaining reactant and newly born product ions are allowed to enter the quadrupole where they are mass selectively filtered and detected using a fast MCP ion counting system. Ion counts versus trapping exposure time is then used to determine the pseudo-first order N_2^+ reactant ion loss rate, and from the known water density, the rate coefficient.³¹ N_2^+ losing and H_2O^+ increasing at different trapping times is shown in figure 2.13. Figure 2.14 describes the second order rate of H_2O^+ formation.

4.3 Results and Discussion

The water molecules used as neutral reactants in this study depart the beam nozzle effusively. The molecular velocity distribution in the effusive beam is

$$f(v_x) = \sqrt{\frac{m}{2\pi kT}} \exp\left(-\frac{mv_x^2}{2kT}\right) \quad (4.2)$$

and the average H_2O molecule velocity in this work is calculated to be $372 \text{ m} \cdot \text{s}^{-1}$ at 300 K and $456 \text{ m} \cdot \text{s}^{-1}$ at 450 K and it takes 1.37 ms to 1.68 ms for H_2O molecules to travel from the nozzle to the RET. The Einstein A coefficient of H_2O for spontaneous rotational transitions are between 0.003 s^{-1} and 16.01 s^{-1} ,³² therefore the lifetime of H_2O spontaneous rotational emission is higher than 62 ms which is 37 times greater than the time the H_2O molecules take to travel from the beam nozzle to the RET.³³ The

relationship between the Einstein A coefficient and Einstein B coefficient which describes the absorption and stimulated emission between rotational levels is

$$A = \frac{8\pi h \nu^3}{c^3} B \quad (4.3)$$

and the function of the energy density for blackbody radiation³⁴ is

$$\rho_\nu(T) = \frac{8\pi h \nu^3}{c^3} \frac{1}{\exp(h\nu/kT) - 1} \quad (4.4)$$

This result shows that the absorption or the stimulated emission period for rotational transitions of H₂O is greater than 200 ms for any relevant transitions in our temperature window. In this case, water molecules maintain internal thermal equilibrium with the nozzle wall temperature throughout their transit to the RET. The N₂ buffer gas density employed in the RET is below 1.4 x 10¹⁰ cm⁻³ (pressure in the trap 5 x 10⁻⁷ torr) and thus most water molecules on average transit the RET without either wall or buffer gas collisions. Meanwhile the reverse reaction need not be considered owing to the extreme exothermicity of the forward processes. The result being that the ion cloud presents trap equilibrated ion collisions to a water beam with an internal state distribution which is thermal at the water nozzle source temperature.

The collision energy is a weighted mean of the translational beam energy and the random ion cloud thermal energy. The appropriate relative center of mass velocity distribution for a low angular divergence skimmed effusive beam-isotropic gas collision system such as this has been shown to be given by:

$$P(g_0^2) = \{2g_0[\pi(\alpha_1^2 + \alpha_2^2)]^{-1/2}\} \exp\left[-g_0^2/(\alpha_1^2 + \alpha_2^2)\right] \quad (4.5)$$

where g_0 is the relative initial velocity of the ion-molecule collision pair. The quantity

$$\alpha_i = 2km_i/T_i \quad (4.6)$$

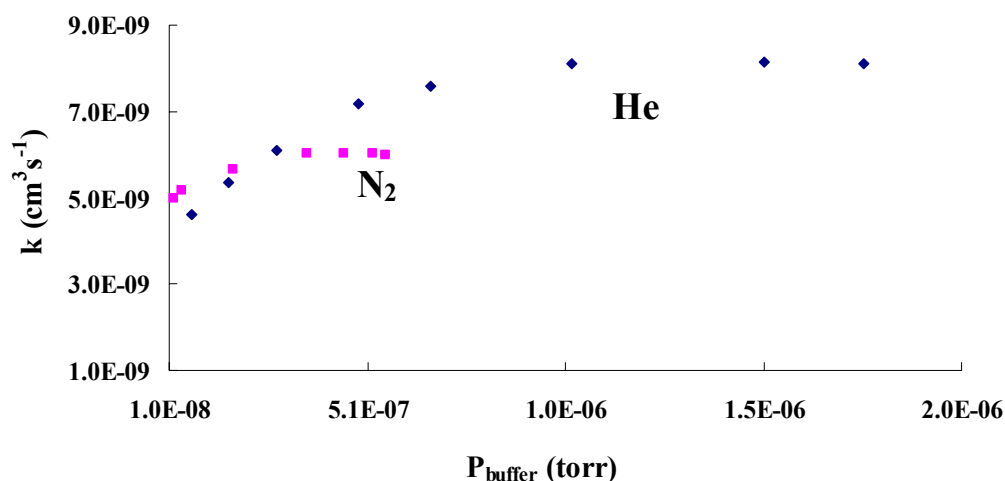
From this, the effective collision temperature is obtained from the moment of the collision energy and is shown to be:

$$T_{eff} = \frac{2\langle E \rangle}{3k} = \frac{m_1T_2 + m_2T_1}{m_1 + m_2} \quad (4.7)$$

The internal temperatures of the water molecules and ions remain independently equilibrated to the nozzle temperature and the RET wall temperature, respectively. Thus by varying the nozzle and trap temperatures, it is possible to broadly control the collision energy for a reactive system over independently determined rotational energy distributions.^{16,35,36,37}

Figure 2.14 shows the result of rate measurements for the N_2^+ ion cloud with the H_2O beam over trapping times from 0.01 s to 3 s. The observed kinetics are clearly first order in water density but do show dependence upon both ion source and RET nitrogen neutral density owing to the presence of internally excited nitrogen ions when the buffer density is low. Thus, the ions are clearly prepared in a variety of internally excited states, which upon exiting the ion source chamber are certainly ro-vibrationally excited. Figure 4.2 shows the result of a study of the dependence of the observed rate coefficients upon various buffer densities.

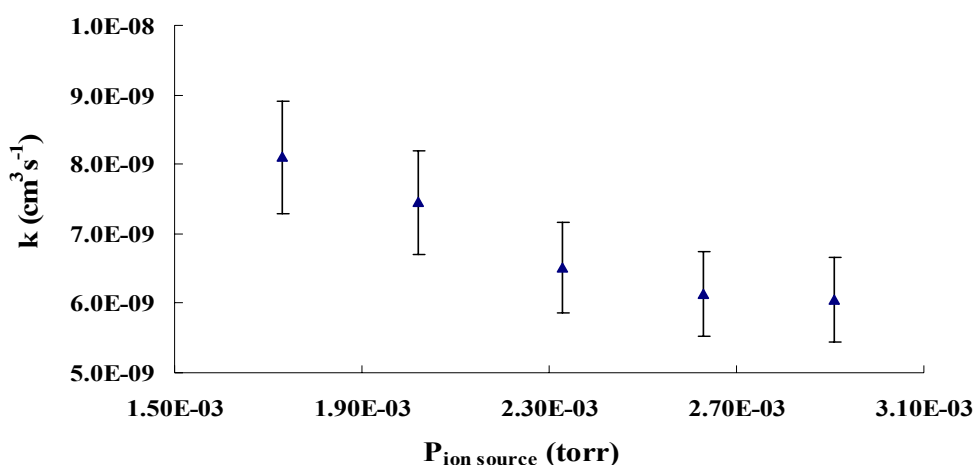
Figure 4.2 Observed rate coefficients in various buffer densities. The N_2^+ temperature is 100 K and the H_2O beam temperature is 380 K. (■) Rate coefficients vs. N_2 trap pressure, (♦) Rate coefficients vs. He trap pressure, both of them with ion source pressure 1.7×10^{-3} torr.



It is seen that the buffer in the RET rapidly translationally cools the injected ions to the 100 K trap wall condition leading to an increase in rate coefficient consistent with the known inverse temperature dependence of this reaction. Cooling saturation or equilibration as measured by the rate coefficient of reaction (4.1), is observed when the collision frequency between nitrogen buffer and ions exceeds approximately 0.2 s. However it is seen that in the case of He buffer in the RET, the rate coefficient extrapolates at high density to values 30% higher than those for nitrogen cooled ions. This indicates that the He cooled ions represent a distribution of internal states not fully equilibrated to the trap temperature but which are equilibrated using N_2 . The known rate of vibrational relaxation ($v > 0 \rightarrow v = 0$) of N_2^+ (v) by N_2 is to be $5 \times 10^{-10} \text{ cm}^3 \text{s}^{-1}$, at trap pressure greater than 5×10^{-7} torr (100K) of N_2 , the quenching rate is about 200 times faster than the rate of N_2^+ and H_2O reaction³⁸, ensuring reaction of whole vibrationally

equilibrated N_2^+ with H_2O under the employed beam densities. This is confirmed when the rate is measured with 1×10^{-6} torr of He in the RET, over a series of measurements where the ion source N_2 density is increased. These data are shown in Figure 4.3 demonstrating the relaxation of the rate coefficient to that observed for similar densities of N_2 in the RET.

Figure 4.3 Rate coefficient measurement at constant He buffer in the RET and variable ion source N_2 pressure



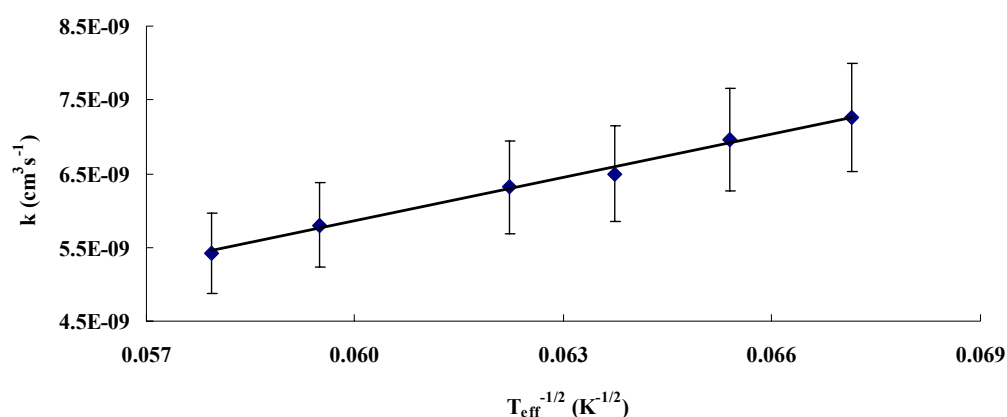
Since the rf ion trap source has an externally measured temperature of approximately 400 K, the internal temperature of the ions exiting the source at the highest source pressures should not drop below this value. The He in the RET should effectively cool the translational (and presumably rotational) degrees of freedom, but the internal vibrations likely remain at the ion source condition. The fact that the N_2 source pressure (with high RET He pressure) asymptotically relaxes the observed rate to the same values obtained at high RET N_2 pressures, suggest that with high densities of He or N_2 in the trap, translation-rotation is efficiently relaxed but that small variance in the vibrational temperature between 400 K and 100 K is not resulting in significant rate change.

The rate coefficients, with RET N_2 relaxed ion populations, for the reaction at effective collision temperatures, T_{eff} , over a range from 283 K to 384 K are shown in Figure 4.4 and table 4.1. In these measurements, the temperature of the internally equilibrated trapped N_2^+ ions is 100 K while the beam derived water molecules are in the temperature range from 300 K to 425 K.

Table 4.1 Rate coefficients for $\text{N}_2^+ + \text{H}_2\text{O}$ reaction measured at H_2O nozzle temperatures between 300 K and 450 K

H_2O nozzle temperature (K)	Collision temperature (K)	Rate coefficient ($10^9 \text{ cm}^3 \text{ s}^{-1}$)
300	222	7.26
320	234	6.96
340	246	6.50
360	258	6.31
380	270	6.05
400	283	5.80
425	298	5.42

Figure 4.4 Rate coefficient of $\text{N}_2^+ + \text{H}_2\text{O}$ reaction as a function of collision temperature in equation (4.7)



A simple model for ion-dipolar molecule reactions that has been widely employed is the average dipole orientation (ADO) collision rate model from the work of Su & Bowers.

This capture model has been introduced in chapter 1 and the resulting thermal capture rate constant for ion-dipolar molecule collision is

$$k_{ADO} = 2\pi e \left(\frac{\alpha}{\mu} \right)^{1/2} + C \left(\frac{2\pi e \mu_D}{\mu} \right) \left(\frac{2}{\pi kT} \right)^{1/2} \quad (4.9)$$

Thus, this capture treatment leads to a complex collision rate coefficient which is linearly proportional to the square root of the temperature. The rate coefficients seen in Figure 4.4 are seen to vary linearly with the inverse square root of the collision temperature^{18,39} consistent with such a capture model. The details of the kinematics of this reaction are beyond the scope of this communication, but with this mass combination and the fact that the N_2^+ ions are significantly translationally colder than water, this excellent correlation with simple water temperature (and beam velocity) is not surprising. The quantitative fit to any of the models is not meaningful at this point however, as the form of Equation 4.7 represents a simple one dimensional model on collision energy which cannot differentiate between the non-equilibrium nature of this study. In other words, the excellent agreement with a form linear in $T^{-1/2}$ seen here suggests that the range of the variable space (T_1 , T_2 , and the internal temperatures) is not sufficient to differentiate more precise models. However, this study well isolates the one translational energy variable and the observed excellent correlation with that variable is uncontestable. This opens the way for further study of both the specific dynamical variables in similar ion-molecule reactions as well reaction systems in natural non-equilibrium environments such as the interstellar medium.^{40,41}

ADO theory assumes that the reaction is dominated by long-range intermolecular forces and when the ion moves to a certain distance from the molecule which is beyond the centrifugal barrier, the collision always proceeds with unit efficiency. The rotationally adiabatic capture and centrifugal sudden approximation (ACCSA) theory of D.C.Clary and coworkers is based on a quantum level micro-canonical capture model combining the ADO assumptions with rotationally adiabatic capture. Rotationally adiabatic capture assumes that as the ion moves toward the molecule, the initial rotational state j stays on its own adiabatic potential energy curve and no tunneling through the centrifugal barrier occurs as the reaction proceeds. In the ACCSA model the ADO rate coefficient formula is determined to be accurate for each rotational state j . The constant c in ADO theory becomes a function of j decreasing as j increases. As a result, small values of j will show a stronger temperature dependence and this will be reflected in the inverse temperature dependence of the ACCSA rate coefficient.^{42,43,44} In application, it is found that the ADO theory and ACCSA models predict similar rate coefficients above room temperature but at low temperature, usually below 200 K, the rate coefficient calculated by ACCSA has steeper dependence on temperature than ADO theory. In addition, the experiment shows that the ACCSA model works very well for strongly exothermic reaction at low temperature but not as good for slightly endothermic reaction. In the present reaction, though the temperature of N_2^+ ions is held at a low value (100 K), only the H_2O temperature changes and in a range at or above 300 K. It is then not surprising that the simpler ADO model still adequately describes the rate coefficient. The exoergicity of the $\text{N}_2^+ + \text{H}_2\text{O}$ reaction is 2.76 eV and it is in the range where ACCSA theory works well. In

this case, it is found that even with the energy of N_2^+ ions being low, as the rotational and translational energy of the molecular dipole is much higher, the rate coefficient appears to manifest none of the additional temperature sensitivity predicted by ACCSA. Perhaps only when the rotational state of both N_2^+ ions and H_2O are lower than 200 K, will the rate coefficient have steeper dependence on temperature and using our instrument we can explore this in future reaction studies.

4.4 Conclusion

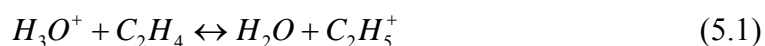
The charge transfer rate coefficient of the $\text{N}_2^+ + \text{H}_2\text{O}$ reaction is determined as a function of water temperature for ions stored in a ring electrode trap. With the temperature of N_2^+ ions held at 100 K, the water beam temperature is varied from 300 K to 450 K. The result shows that the total energy of the dipolar H_2O molecules affects the rate coefficients in a way consistent with the predictions of simple capture models. Different buffer gases nitrogen and helium are used respectively in the trap to cool the N_2^+ ions to 100 K and the ground ro-vibrational energy states. Parent nitrogen buffer gas is observed to be a much more efficient internal relaxant than helium buffer in this reaction owing to the availability of a near resonant electron transfer relaxation mechanism. Such observations should be carefully taken into account when studying low energy ions under conditions where non-equilibrium internal energy distributions may persist.

CHAPTER 5 $C_2H_4 + H_3O^+ \leftrightarrow C_2H_5^+ + H_2O$ PROTON TRANSFER EQUILIBRIUM REACTION

5.1 Introduction

Proton-transfer reactions of simple molecules play significant roles in dense interstellar clouds, as they can effectively produce neutral molecules.⁴⁵ Rate coefficient determination for proton transfer is important in modeling complex chemistry in the interstellar medium (ISM) and the studies of the relative proton affinity between different acids.⁴⁶ H_3O^+ , H_2O , C_2H_4 and $C_2H_5^+$ are all detected in the ISM and are essential intermediates in the production of complicated oxygenated organic molecules.

The endothermic proton transfer equilibrium reaction



has been well studied in the past.^{47,48,49,50} In the present study, a coaxial molecular beam radio frequency ring electrode trap is applied to measure the forward and reverse rate coefficients of this endothermic reaction, with molecular beam and ion temperatures varied independently from 300 K to 450 K and from 25 K to 350 K, respectively. From these data, the thermodynamics of equilibrium (5.1) in the low temperature window can be determined and are compared to past studies.

The results also have significant implications to the reaction mechanism at low collision temperatures. There are two common types of reaction mechanism in gas phase

ion-molecule reactions: direct collision through stripping dynamics at high collision energy (more than several electron volts) and complex-mediated reaction through long-range attraction when the collision energy is lower than 1 eV.^{51,52} The results of the present study strongly support a long-lived complex mechanism, where all degrees of freedom in both reactants participate equally as energy baths in driving the endothermic proton transfer from H_3O^+ to ethylene molecule.

5.2 Experimental

A coaxial molecular beam — ring-electrode trap (CoMB-RET) that has been specifically designed to minimize trap interactions with ion-source gas or background beam molecule contamination is used in this study.

The reactant ions H_3O^+ are produced by electron impact in a U-shaped radio-frequency trap with an H_2O vapor pressure of approximately 5×10^{-5} torr. Trajectories of the ions exiting the ion source are bent 90° by a dc quadrupole bender, which separates the ion stream from the effusive gas exiting the source. The ions are then focused into a double quadrupole ion guide/mass selector. The mass selected ion beam is then turned another 90° , bringing it to a coaxial alignment with both the RET axis and the molecular beam.

Ions at low energy (<0.1 eV) are injected into the RET, which is mounted on the end of a thermally regulated liquid He cryostat, used to vary the trap temperature between 20 K and 450 K. Buffer gas admitted to the trap equilibrates to the defined wall temperature,

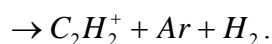
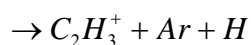
as do the ions through buffer gas collisions. Buffer cooling is used to equilibrate the stored ions with the thermal conditions of the trap walls. After ions are cooled and most of the He buffer is pumped out of the RET, the reaction between stored ions and neutral molecules in the chopped molecular beam starts which takes from several hundred milliseconds to a few seconds (usually < 5 s). Following the reaction period, the remaining reactant and newly created product ions are allowed to enter the quadrupole analyzer, where they are accelerated, mass-selectively filtered and detected using a fast micro-channel plate (MCP) ion counting system.

The ethylene nozzle consists of a 50 mm long, 0.5 mm internal-diameter tube mounted onto the end of a second thermally regulated cryostat. The stagnation pressure of C_2H_4 is (65 ± 1) torr. The beam passes through a 0.5 mm orifice conical skimmer (Beam Dynamics, Inc.) mounted 20 mm downstream and then skimmed a second time, 300 mm downstream from the nozzle, using a 2 mm diameter flat aperture, and becomes coaxial with the trap. A regulated shutter is placed in the beam path in front of the second skimmer. The shutter is opened after the stored ions in the RET have been cooled and kept open for a desired time depending on the reaction period in the RET. The molecular beam terminates in the chamber of a residual gas analyzer (RGA; Stanford Research Systems 200) which is used to calibrate the number density of the molecular beam.

5.3 Result and discussion

5.3.1 Beam number density calibration

In order to determine the ethylene beam number density in the RET, the reaction $\text{Ar}^+ + \text{C}_2\text{H}_4$ with a known rate coefficient ($k_2 = 1.10 \times 10^{-9} \text{ cm}^3 \cdot \text{s}^{-1}$ at 300 K⁵³) is used



Product ions C_2H_2^+ , C_2H_3^+ and C_2H_4^+ are all observed at the detector and secondary product ions C_2H_5^+ and C_3H_5^+ created from collisions between initial product ions C_2H_2^+ , C_2H_4^+ and neutral molecule C_2H_4 are also detected.^{53,54,55} The growth of the sum of all the observed product ions as well as the loss of Ar^+ ions are used to get a self consistent determination of ethylene beam number density.

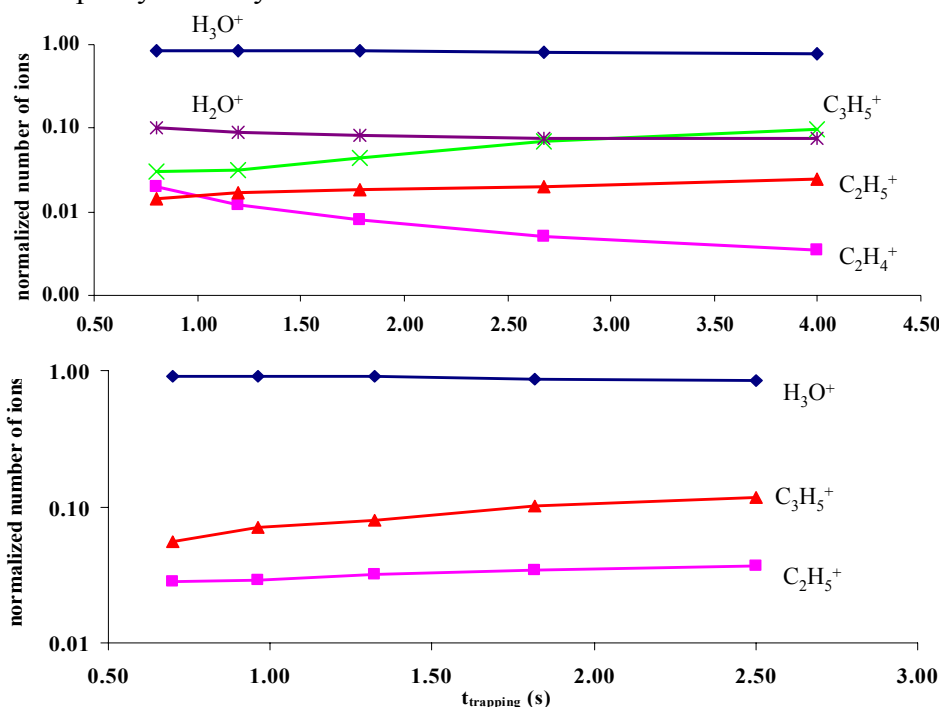
The number density of ethylene in the RET is calibrated to be $2.5 \times 10^9 \text{ cm}^{-3}$ at 300 K and is inversely proportional to the square root of beam temperature.

Molecular dimers are easily formed at low molecular beam temperatures ($< 220 \text{ K}$)⁵⁶, however, at 300 K and higher beam temperatures, the ethylene dimer fraction in the beam is less than 0.01% and the effect of dimers on the calibration reaction and subsequent proton transfer equilibrium studies is insignificant.

5.3.2 Measurement of forward rate coefficient $\text{H}_3\text{O}^+ + \text{C}_2\text{H}_4$

To measure the rate coefficient of forward reaction $\text{H}_3\text{O}^+ + \text{C}_2\text{H}_4$, it has to make sure in the very beginning that no H_2O^+ ions are there in the system as when H_2O^+ ions collide with C_2H_4 molecules, there is fast charge transfer reaction with rate coefficient $(1.55 \pm 0.04) \times 10^{-9} \text{ cm}^3 \cdot \text{s}^{-1}$. Figure 5.1 shows the reactant and product ions changing with trapping time with and without H_2O^+ contaminations in the system.

Figure 5.1 Reactant and product ions varied with reaction time with and without H_2O^+ impurity in the system



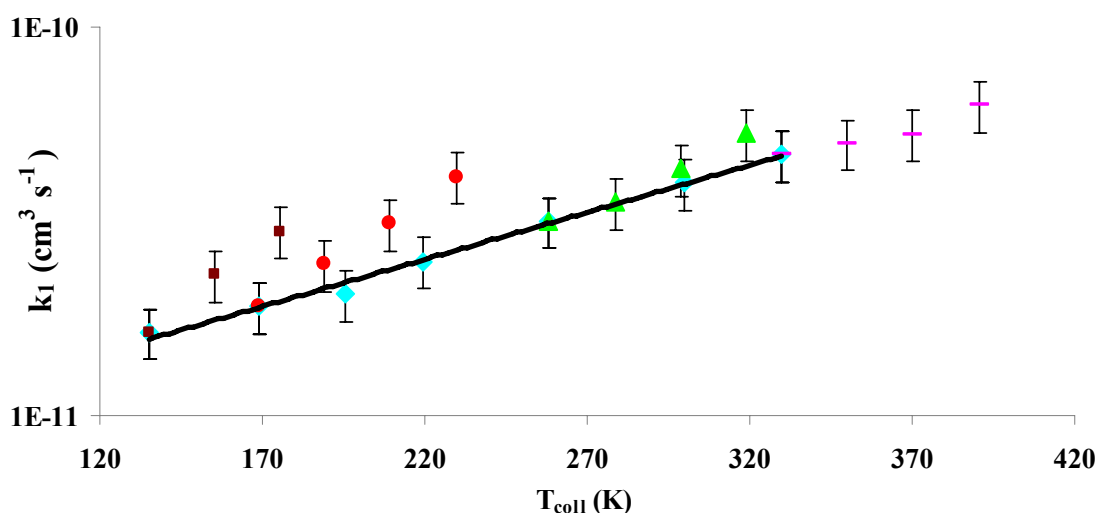
The top one has 10% H_2O^+ ions in the reaction system and the by-product C_2H_4^+ ions together with C_3H_5^+ product ions are observed which will strongly affect the rate coefficient measurements. By baking the RET and the whole vacuum system at 350 K for three days, as shown in the bottom figure, no H_2O^+ contaminations and the related C_2H_4^+ by-product are detected in the reaction system anymore.

Figure 5.2 shows the observed rate coefficient of proton transfer reaction $\text{H}_3\text{O}^+ + \text{C}_2\text{H}_4$ at different collision temperatures. The center of mass collision temperature is defined as

$$T_{\text{coll}} = \frac{m_{\text{ion}}T_{\text{beam}} + m_{\text{beam}}T_{\text{ion}}}{m_{\text{ion}} + m_{\text{beam}}} \quad (5.3)$$

where m_{ion} is the mass of H_3O^+ , T_{beam} is trap temperature, m_{beam} is the mass of C_2H_4 and T_{ion} is beam temperature.

Figure 5.2 The observed rate coefficient for $\text{H}_3\text{O}^+ + \text{C}_2\text{H}_4$ forward reaction at different collision temperatures. (♦) Rate coefficient of $\text{H}_3\text{O}^+ + \text{C}_2\text{H}_4$ reaction when beam temperature stays at 300 K and trap temperature varied from 23 K to 350 K. (■) Rate coefficient of $\text{H}_3\text{O}^+ + \text{C}_2\text{H}_4$ reaction when ion temperature maintained at 23 K and trap temperature varied from 300 K to 450 K. (●) Rate coefficient of $\text{H}_3\text{O}^+ + \text{C}_2\text{H}_4$ reaction when ion temperature stays at 80 K and trap temperature varied from 300 K to 450 K. (▲) Rate coefficient of $\text{H}_3\text{O}^+ + \text{C}_2\text{H}_4$ reaction when ion temperature is 230 K and trap temperature varied from 300 K to 450 K. (□) Rate coefficient of $\text{H}_3\text{O}^+ + \text{C}_2\text{H}_4$ reaction when ion temperature maintained at 350 K and trap temperature varied from 300 K to 450 K.



As shown in Figure 5.2, by varying trap and beam temperatures independently, rate coefficients can be determined at equivalent collision temperatures, but different degrees

of excitation of the ion and neutral molecule degrees of freedom. At a beam temperature of 300 K, the rate coefficients at different trap temperatures defined a smooth monotonic function; however, the rate coefficients have quite different beam temperature dependence at fixed trap temperatures.

Therefore, collision temperature alone does not account for the energy brought to bear on the endothermic barrier by the two reactants with different internal degrees of freedom. A new temperature should be defined for the reaction system to account statistically for the internal and external energies contributed in a collision. We assume complete equilibration of internal and external degrees of freedom for each specific reactant, which implies that the ion motions are described by the trap wall temperature, while the nozzle temperature completely describes the motion of the neutrals in the effusive beam (no expansive cooling). For the 10 atom collision system, $\text{H}_3\text{O}^+ + \text{C}_2\text{H}_4$, there are 27 degrees of freedom (DOF) in the center of mass frame. There are 3 center of mass translational DOF whose energy moment is given by T_{coll} in Equation (5.3). The H_3O^+ ion has 9 internal DOF (3 rotational, 6 vibrational) while C_2H_4 has 3 rotational and 12 vibrational DOF. Independent of energy spacing, each DOF brings an average of $1/2 K T_i$ to the collision over the ensemble average appropriate to a rate coefficient measurement. Here, T_i is the temperature appropriately describing the energy distribution of the specific DOF.

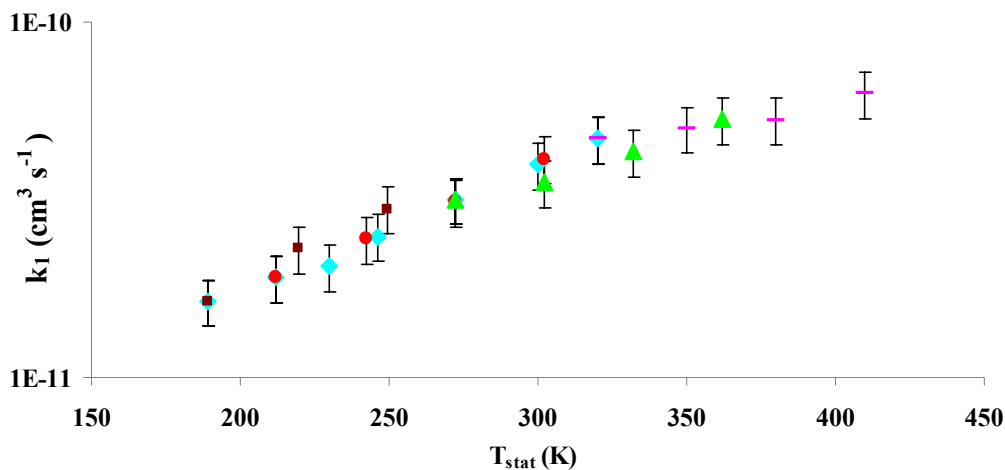
In this case, we can define a reaction temperature, T_{react} , describing the total internal energy moment of the $\text{H}_3\text{O}^+ \cdot \text{C}_2\text{H}_4$ collision pair.

$$T_{\text{react}} = \left(\frac{3}{27}\right) \cdot T_{\text{coll}} + \left(\frac{9}{27}\right) \cdot T_{\text{trap}} + \left(\frac{15}{27}\right) \cdot T_{\text{beam}} \quad (5.4)$$

where T_{coll} is the collision temperature defined in Equation (5.3). The second and third terms in Equation (5.4) represent the internal temperature contribution of the H_3O^+ ions and C_2H_4 , respectively.

If we compare rate coefficients for Reaction (1) against T_{react} we obtain the relationship shown in Figure 5.3. Here, we see that independent of energy source, be it collisional, internal to the ion or internal to the neutral, we find a common relationship within experimental error. This strongly suggests complete equilibration of energy in the $\text{H}_3\text{O}^+ \cdot \text{C}_2\text{H}_4$ collision complex as the system surmounts the endothermic barrier.

Figure 5.3 The observed rate coefficient for $\text{H}_3\text{O}^+ + \text{C}_2\text{H}_4$ forward reaction at defined statistical temperatures. (♦) Rate coefficient of $\text{H}_3\text{O}^+ + \text{C}_2\text{H}_4$ reaction when beam temperature stays at 300K and trap temperature varied from 23K to 350K. (■) Rate coefficient of $\text{H}_3\text{O}^+ + \text{C}_2\text{H}_4$ reaction when ion temperature maintained at 23K and trap temperature varied from 300K to 450K. (●) Rate coefficient of $\text{H}_3\text{O}^+ + \text{C}_2\text{H}_4$ reaction when ion temperature stays at 80K and trap temperature varied from 300K to 450K. (▲) Rate coefficient of $\text{H}_3\text{O}^+ + \text{C}_2\text{H}_4$ reaction when ion temperature is 230K and trap temperature varied from 300K to 450K. (□) Rate coefficient of $\text{H}_3\text{O}^+ + \text{C}_2\text{H}_4$ reaction when ion temperature maintained at 350K and trap temperature varied from 300K to 450K.



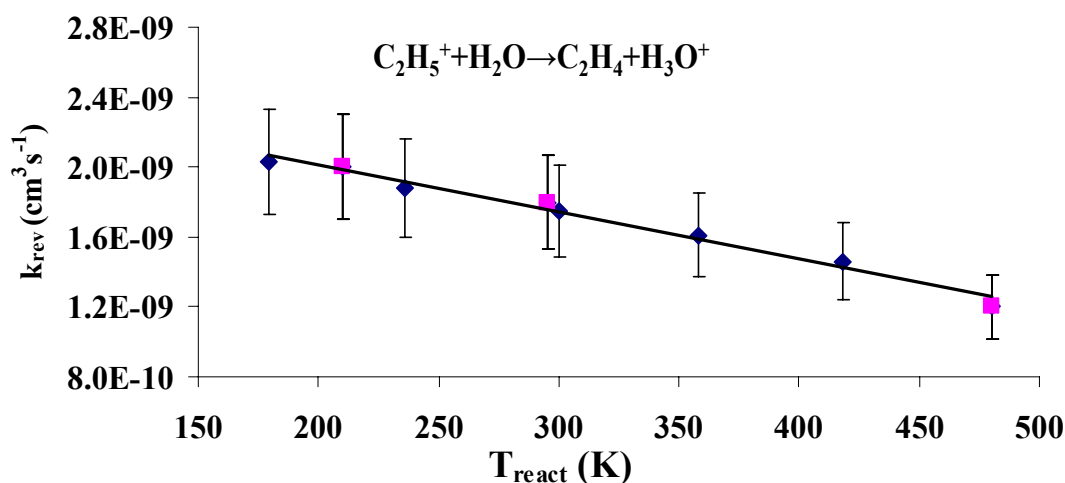
5.3.3 Measurement of reverse reaction, $\text{C}_2\text{H}_5^+ + \text{H}_2\text{O}$ and the Van Hoff plot

The reverse reaction in the equilibrium reaction (5.1) is a fast exothermic proton transfer whose rate coefficient was measured at several reaction temperatures. In this context, the appropriate reaction temperature for k_{-1} is given by

$$T_{-1} = \left(\frac{3}{27}\right)T_{coll} + \left(\frac{6}{27}\right)T_{beam} + \left(\frac{18}{27}\right)T_{trap} \quad (5.5)$$

This new data is shown in Figure 5.4, together with the data from the previous study by McIntosh and co-workers.⁵⁰

Figure 5.4 Rate coefficient of $\text{H}_3\text{O}^+ + \text{C}_2\text{H}_4$ reverse reaction. (♦) Data in our study from temperature range 180 K to 300 K. (■) Previous study by McIntosh and co-workers in the temperature range from 210 K to 480 K.

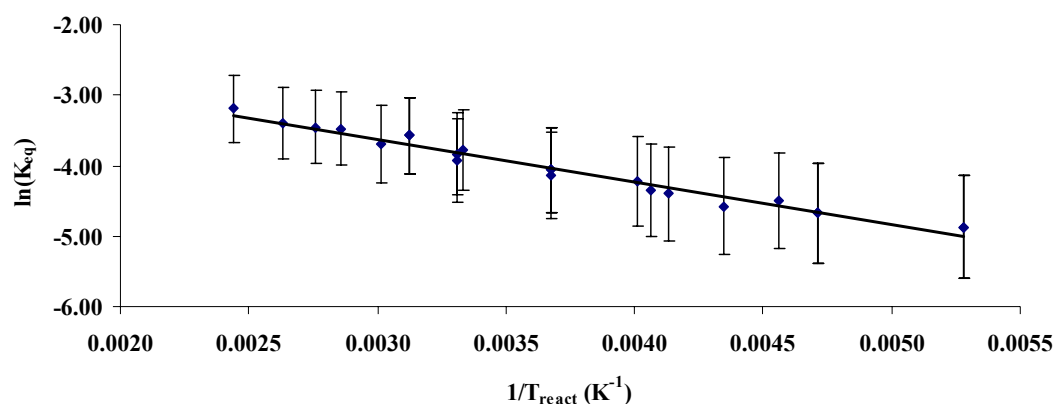


The combined dataset is found to be very well fit by a common relationship (using appropriate temperatures for the independent studies) given by

$$k_{-1} \text{ (cm}^3 \text{ s}^{-1}\text{)} = 2.55 \times 10^{-9} - 2.69 \times 10^{-12} T \quad (5.6)$$

which is slightly inversely temperature dependent, consistent with the polarity of H_2O . We can use this fit to the experimental data for k_{-1} , given in Equation (5.6), to determine the equilibrium constant $K_{\text{eq}}(T_{\text{react}})$ for each temperature, T_{react} for which k_{-1} was measured. The relationship between $K_{\text{eq}}(T_{\text{react}})$ and $1/T_{\text{react}}$, in a typical Van't Hoff relationship, allows determination of the enthalpy, ΔH_r° , entropy, ΔS_r° and ΔG° for Reaction (5.1), as shown in Figure 5.5.

Figure 5.5 The Van Hoff plot for $\text{C}_2\text{H}_4 + \text{H}_3\text{O}^+ \leftrightarrow \text{C}_2\text{H}_5^+ + \text{H}_2\text{O}$ equilibrium reaction



From the slope and intercept of the relationship we determine in the temperature window 180 K to 450 K, $\Delta H = (5.1 \pm 0.5) \text{ kJ}\cdot\text{mol}^{-1}$ and $\Delta S = (-15.0 \pm 0.9) \text{ J}\cdot\text{mol}^{-1}\cdot\text{K}^{-1}$. The values determined in this work compare favorably with past determinations as shown in Table 5.1.

Table 5.1 Comparison of the experimental enthalpy ΔH , entropy ΔS and free standard energy ΔG at 300 K for equilibrium reaction $\text{C}_2\text{H}_4 + \text{H}_3\text{O}^+ \leftrightarrow \text{C}_2\text{H}_5^+ + \text{H}_2\text{O}$

	ΔH ($\text{kJ}\cdot\text{mol}^{-1}$)	ΔS ($\text{J}\cdot\text{mol}^{-1}\cdot\text{K}^{-1}$)	$\Delta G_{300\text{K}}$ ($\text{kJ}\cdot\text{mol}^{-1}$)
Bohme D.K. ^a	5.8 ± 5.0	-9.6 ± 18.8	7.5 ± 0.8
McIntosh B.J. ^b	10.4	4.2	9.6
Collyer S.M. ^c	17.1	9.2	14.2
McMahon T.B. ^d	13.8 ± 2.1	-5.0 ± 4.2	15.5 ± 0.8
Our work	5.1 ± 0.5	-15.0 ± 0.9	9.6 ± 0.8

^aRef (49), ^bRef (50), ^cRef (48), ^dRef (47)

The present work significantly constrains the determination of the thermo-chemistry for this reaction and has significantly reduced the error and better defined the optimal values to be employed in future modeling of environments incorporating this reaction.

5.4 Conclusion

Using a coaxial molecular beam ring electrode trap reaction method, the proton transfer equilibrium reaction $\text{C}_2\text{H}_4 + \text{H}_3\text{O}^+ \leftrightarrow \text{C}_2\text{H}_5^+ + \text{H}_2\text{O}$ was studied. The temperatures of both molecular beam and ion trap were controlled independently and reaction temperature defined as a degree of freedom weighted average of the energy modes brought to the reaction complex. It is verified that the forward proton transfer reaction $\text{H}_3\text{O}^+ + \text{C}_2\text{H}_4$ behaves statistically, as all available energy is equally available and therefore randomized within the reaction complex as it surmounts the barrier. The enthalpy ΔH_r° and entropy ΔS_r° of the equilibrium reaction (5.1) are calculated to be ΔH_r°

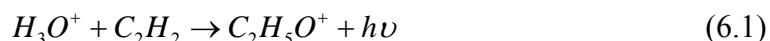
$= (5.1 \pm 0.5) \text{ kJ}\cdot\text{mol}^{-1}$ $\Delta S_r^\circ = (-15.0 \pm 0.9) \text{ J}\cdot\text{mol}^{-1}\cdot\text{K}^{-1}$ respectively. Besides in reasonable agreement with previous studies, these values are better defined with higher accuracy and precision through this investigation.

CHAPTER 6 $\text{H}_3\text{O}^+ + (\text{C}_2\text{H}_2)_2$ REACTION

6.1 Introduction

Production of oxygenated organics in the interstellar medium (ISM) represents the first step towards the abiotic generation of molecules critical to life. The production mechanisms are important for understanding the plethora of complex organics now known to exist in the ISM^{57,58} as well as on other planetary bodies beyond Earth. Acetaldehyde, CH_3CHO , is ubiquitous in the ISM and has been detected in a variety of environments since it was first observed in 1973. These environments include hot cores, dark clouds, and regions of star formation.^{59,60}

Radiative association plays a significant role in the gas phase synthesis of molecular ions in dense interstellar clouds and planetary atmospheres.⁶¹⁻⁶⁵ The radiative association reaction between H_3O^+ and C_2H_2 monomer is considered as one of the most important steps for acetaldehyde production in the ISM:



followed by electron recombination to produce CH_3CHO .⁶⁰ Protonated water is one of the most stable forms of oxygen containing molecular ions and understanding its reactive potential with small hydrocarbons present in natural environments is critical.

Herbst and co-workers investigated both radiative and three-body $\text{H}_3\text{O}^+ + \text{C}_2\text{H}_2$ association reactions in 1989.^{65,66} The rate coefficient of reaction (6.1) deduced from their three-body experimental value was $4.75 \times 10^{-13} \text{ cm}^3 \cdot \text{s}^{-1}$ at 50 K, two orders of magnitude

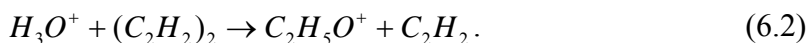
lower than theoretical prediction. Fairley and co-workers studied the three-body $\text{H}_3\text{O}^+ + \text{C}_2\text{H}_2$ association reaction at 300 K using the Canterbury selected ion flow tube (SIFT) system in 1996 and the rate coefficient they measured was consistent with Herbst's result.⁶⁰ To date, there has not been a direct rate coefficient measurement of radiative association for $\text{H}_3\text{O}^+ + \text{C}_2\text{H}_2$. Such direct determination is critical for the refinement of current models and insight into the generation of oxygenated organics in the ISM.

Molecular complexation of organic molecules is the basis for the generation of organic haze on Titan, as well as the possible first steps in the generation of organic condensation clouds in its stratosphere. It has been proposed that molecular dimers, specifically of diacetylene, exist in the dense atmosphere of Titan and may act as red-shifted chromophores.⁶⁷ Such chromophores may extend the photochemically important spectral range into the normal ultraviolet and thereby extend active photochemistry to lower, denser altitudes in the Titan atmosphere. In the low-temperature environment of Titan's atmosphere, molecular dimers and clusters can exist in appreciable concentrations to quite high altitudes. Their potential presence in the ionosphere would allow for new ion-molecule reaction mechanisms for the build up of polyatomic organics in low density binary chemical regimes.

Many weakly bound dimers and higher polymers have been observed in the ISM.^{68,69} Owing to its polarizability, acetylene is one of the simplest organic molecules that readily form clusters. These clusters are important in low-temperature environments because of their inherent reactivity and ability to create larger hydrocarbons in reactions with ions and radicals.⁷⁰

Oxygen in Titan's atmosphere is known to be present in the form of CO (50 ppm), while the reducing nature of the methane-rich atmosphere makes small concentrations of water vapor almost assured. With the high fractional ionization in these media, protonated water is expected to be a significant component of any of these dynamic plasmas. As such, the role of H_3O^+ in the incorporation of oxygen into organic molecules is potentially an important channel in the production of complex pre-biotic organics. Although the majority of reactions of protonated water with organic molecules involve simple proton transfer, removing oxygen from the ion chemistry, the potential for more complex chemistry with molecular clusters is intriguing. In the simplest form, ligand exchange provides a mechanism for the production of oxygen containing organic ions. More profound reactions involving oxygen-carbon bonds can be thermodynamically favorable and may provide a key pathway for covalent oxygen incorporation into organics in rarefied environments. In the case of oxygen containing ion complexes, subsequent ion-electron recombination will also provide possible mechanisms for carbon-oxygen bond formation.

In this study, we report a temperature dependent rate coefficient study for H_3O^+ reactions with C_2H_2 (reaction 6.1) and $(\text{C}_2\text{H}_2)_2$:



Both reactions produce $\text{C}_2\text{H}_5\text{O}^+$. The measurements are carried out in a ring-electrode trap (RET) using collisions between H_3O^+ at a variety of trap temperatures and a coaxial $\text{C}_2\text{H}_2/(\text{C}_2\text{H}_2)_2$ molecular beam with independent variation of beam temperature.

6.2 Experimental

A coaxial molecular-beam ring-electrode trap is employed in this study which has been specifically developed to minimize trap interactions with ion source gas or background beam molecule contaminations.

The H_3O^+ reactant ions are produced from H_2O vapor (5×10^{-5} torr) by electron impact in a U-shaped radio-frequency source trap. The exit lens potential on the source trap is pulsed to ground to produce an ion packet (1 ms duration) of maximal density. These ions pass through a 90° DC quadrupole bender which separates the ion packet from the effusive gas exiting the source. After the bender, ions are focused into a double quadrupole mass guide/selector. After passing another electrostatic lens set, the mass-selected ion beam is then turned another 90° in a second DC quadrupole bender, bringing it coaxial with both the RET axis and the axis of the molecular beam.

Ions from this pulse are injected into the RET at low energy (<0.1 eV) by dropping the entrance guard ring potential. After a 1 ms ion loading period, the potential on the trap entrance is increased. The RET is mounted on the end of a thermally regulated liquid He cryostat, which is used in this study to vary the trap temperature between 25 K and 400 K. Buffer gas admitted to the RET equilibrates to the defined wall temperature, as do the ions through buffer gas collisions. The buffer gas inlet line employs a pulsed valve, which opens 100 ms prior to ion loading for a 3 ms period and is used to admit He buffer. Buffer gas collision is effective in relaxing all degrees of freedom and the internal temperature of ions.^{26,71}

The cooled ions stored in the trap are then exposed to a chopped effusive beam of acetylene, containing C_2H_2 monomers and molecular clusters and reaction takes place. The ion-molecule reaction period is typically regulated from several hundred milliseconds to several seconds. Following a certain amount of reaction period, the electrostatic potential on the trap exit gate lens is dropped and the remaining reactant and newly created product ions are allowed to enter the third quadrupole operated in mass selection mode, where they are accelerated, mass-selectively filtered and detected using a fast micro-channel plate (MCP) ion counting system.

The acetylene molecular beam source nozzle consists of a 40 mm long, 3.2 mm internal-diameter tube terminates at a 1 mm thick wall with a 0.3 mm diameter aperture. This nozzle is mounted onto the end of a second thermally regulated cryostat. The stagnation pressure of C_2H_2 is 51 torr. Under these conditions, the pressure drop across the 1 mm exit plate is very nearly the full 51 torr stagnation condition while the mean free path for neutral collisions in the aperture is 13 μm . The beam passes through a 0.5 mm orifice conical skimmer mounted 20 mm downstream and enters a differentially pumped beam buffer region. It is then skimmed a second time, 300 mm downstream from the nozzle, using a 2 mm diameter flat aperture, and becomes coaxial with the trap.

In order to chop the effusive beam prior to the trap entrance, a regulated shutter is placed in the beam path at the second differential wall which blocks better than 99.9% of all gas flow. The shutter is opened after the ions stored in the trap have been cooled and the He buffer gas is pumped out, allowing the ions to collide with the neutral beam molecules. The shutter is kept open for a time defining the reaction period in the trap. The

center of the trap lies 450 mm away from the beam nozzle. The beam traverses the RET and exits without wall interactions through the 4 mm aperture exit gate lens. The molecular beam terminates in the source chamber of a residual gas analyzer (RGA; Stanford Research Systems 200). The RGA is used to determine beam flux which is then calibrated to the RET neutral beam density using the calibration reaction $N_2^+ + C_2H_2$ rate at 300 K. The acetylene beam density in the RET trap in this study is between 1.41×10^9 and $1.93 \times 10^9 \text{ cm}^{-3} \cdot \text{s}^{-1}$, depending on the nozzle temperatures.

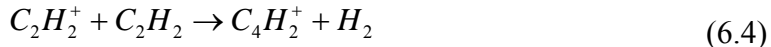
6.3 Result and discussion

6.3.1 Calibration reaction: $N_2^+ + C_2H_2$

The highly exothermic charge-transfer reaction⁷²



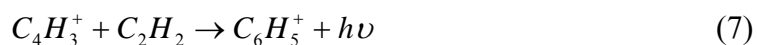
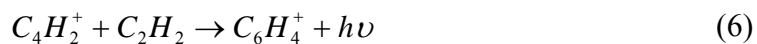
is used to determine the number density of the acetylene beam in the RET. At 300 K, the rate coefficient of this reaction is $5.50 \times 10^{-10} \text{ cm}^3 \cdot \text{s}^{-1}$ and it is expected to be temperature independent. In addition to the primary reaction (3), its products may undergo the following secondary reactions:



The combined rate coefficient for reactions (6.4) and (6.5) is $1.4 \times 10^{-9} \text{ cm}^3 \text{ s}^{-1}$.⁷³⁻⁷⁵ As both of these reactions consume the product ions in reaction (6.3), $C_2H_2^+$, the sum of the

observed $C_4H_2^+$ and $C_4H_3^+$ ion signals, combined with $C_2H_2^+$, is used for determination of the net rate of reaction (6.3).

Rate coefficients of radiative association reactions



are $2.8 \times 10^{-10} \text{ cm}^3 \text{ s}^{-1}$ and $2.0 \times 10^{-10} \text{ cm}^3 \text{ s}^{-1}$, respectively.⁷⁴⁻⁷⁶ In our reaction system, the observed changes in $C_6H_4^+$ and $C_6H_5^+$ signals are small within the noise, and these products are neglected.

The calibration reaction (6.3) was studied at different beam temperatures, as well as by independently varying the ion temperature. One series of measurement was carried out with beam temperatures of 300 K, 250 K, 200 K, 180 K and 160 K, while the ion temperature was set at 300 K. In the other series, the beam temperature was fixed at 160 K, while the ion temperature was varied between 80 K and 300 K. In all of these measurements, the beam stagnation pressure was kept constant at (51 ± 1) torr. Under these conditions, the acetylene partial pressure reading at the RGA remained constant $(1.20 \pm 0.10) \times 10^{-8}$ torr, indicating that the flux of the molecular beam was constant, while its number density varied inversely with the square root of beam temperature.

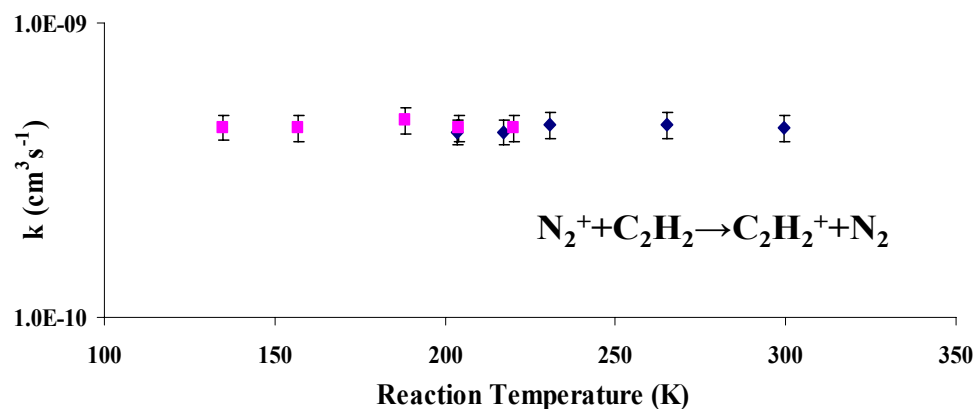
For ion-molecular beam reaction, the reaction rates are examined in regard to the reaction temperature T_{react} , defined in our other studies as

$$T_{\text{react}} = \left(\frac{3}{15}\right)T_{\text{coll}} + \left(\frac{3}{15}\right)T_{\text{ion}} + \left(\frac{9}{15}\right)T_b \quad (6.8)$$

$$T_{coll} = \frac{T_{ion}m_b + T_b m_{ion}}{m_{ion} + m_b} \quad (6.9)$$

where T_b and T_{ion} are molecular beam and ion temperatures, respectively, while m_b and m_{ion} are the corresponding molecular masses. T_{coll} in equation (6.9) represents the relative collision temperature between ions and neutral molecules. For N_2^+ ions, it has 3 internal degrees of freedom and for C_2H_2 molecular, the internal degrees of freedom are 9. Adding the 3 relative collisional degrees of freedom, the total degrees of freedom for the reaction system is 15. As the collisional degrees of freedom are 3 out of the total 15, so the coefficient in front of T_{coll} is 3/15. Similarly, 3/15 and 9/15 are the coefficients for T_{ion} and T_b . The measured rate coefficient of the calibration reaction (6.3) as a function of reaction temperature is plotted in figure 6.1. The result indicates that the rate coefficient of the calibration reaction is indeed temperature independent, supporting this analysis.

Figure 6.1 Rate coefficient of $N_2^+ + C_2H_2$ reaction at different statistical reaction. (♦) Trap temperature is 298 K while beam temperature varied from 160 K to 300 K. (■) Trap temperature varied from 80 K to 300 K while beam temperature varied is 160 K.



From reaction (6.3), the beam density of acetylene in the RET in this study is determined to be 1.41×10^9 molecules·cm⁻³ at a beam temperature of 300 K. In addition, as discussed below, it is found that at a beam temperature of 300 K, there is 0.05% of acetylene dimer in the molecular beam, while at 160 K the dimer fraction increases to 0.6%. The dimer present in the beam is likely to react with N_2^+ to produce $C_4H_3^+$ and $C_4H_2^+$ at a rate coefficient nearing the capture rate, which is of the same magnitude as the rate coefficient of $C_2H_2^+ + C_2H_2$ ion molecule reaction. However, as the dimer fraction in the beam is less than 1.0%, the effect of acetylene dimer in the calibration analysis of beam density is insignificant.

6.3.2 $H_3O^+ + C_2H_2$ and $H_3O^+ + (C_2H_2)_2$ reactions

The $H_3O^+ + C_2H_2$ reaction was studied in our system by independently varying the molecular beam and ion temperatures. Representative results are presented in figures 6.2 and 6.3. Figure 6.2 shows the growth of $C_2H_5O^+$ product ions observed in the trap upon exposure of H_3O^+ ions to a C_2H_2 beam. Figure 6.3 shows the measured second order rate coefficient $k'(T_{\text{react}})$ for product formation based upon acetylene monomer density in the trap at different reactions temperatures. The reaction temperature is defined similar to Equation (6.8) which for the $H_3O^+ + C_2H_2$ reaction must be written as

$$T_{\text{react}} = \left(\frac{3}{21}\right)T_{\text{coll}} + \left(\frac{9}{21}\right)T_{\text{ion}} + \left(\frac{9}{21}\right)T_b \quad (6.10)$$

as the total degrees of freedom for reaction system is 21 this time (collisional : 3, H_3O^+ internal: 9, C_2H_2 internal: 9).

Figure 6.2 The reactant and product ions at different trapping time for $\text{H}_3\text{O}^+ + \text{C}_2\text{H}_2$ component reaction. (♦) H_3O^+ ions (■) $\text{C}_2\text{H}_5\text{O}^+$ ions, trap temperature 80 K, beam temperature 200 K.

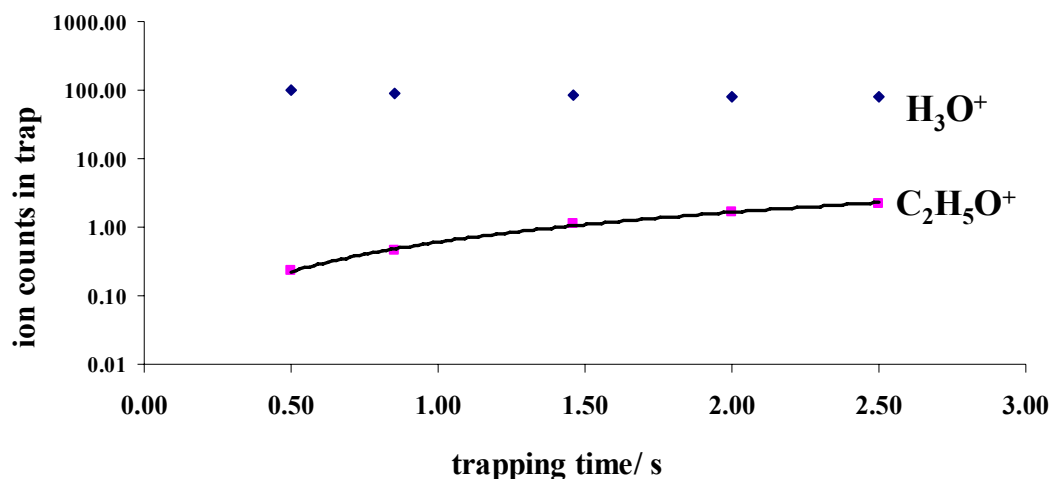
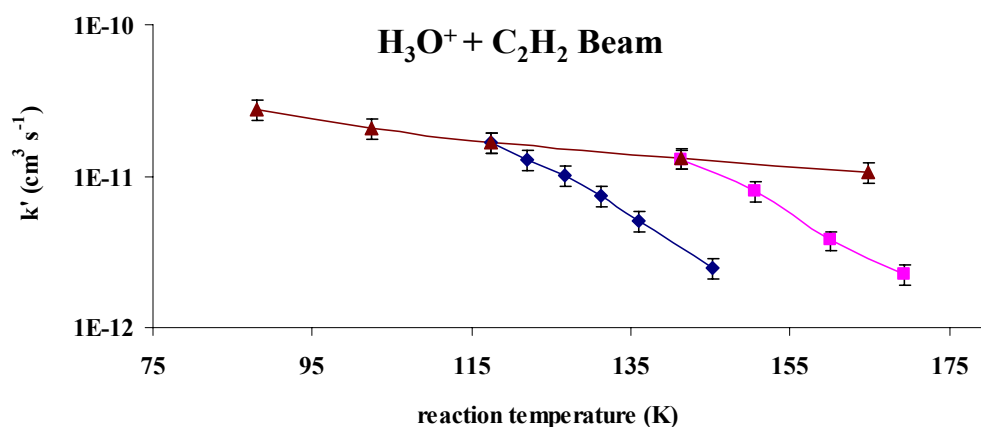


Figure 6.3 Second order rate coefficient measurements based upon acetylene monomer density $k'(T_{\text{react}})$ for $\text{C}_2\text{H}_5\text{O}^+$ product formation in reaction of H_3O^+ with the components of the acetylene beam. (♦) Trap temperature is 80 K while beam temperature varied from 160 K to 220 K. (■) Trap temperature is 125 K while beam temperature varied from 160 K to 220 K. (▲) Trap temperature varied from 25 K to 170 K while beam temperature is 160 K.



As seen in figure 6.3, with a constant molecular beam temperature, the reaction rate shows a slight increase as the ion temperature decreases. However, when the ion

temperature is held constant, the reaction rate increases dramatically with decreasing temperature of the molecular beam. Therefore, the reaction rate exhibits a strong dependence on C_2H_2 beam temperature while being only weakly dependent on the temperature of the ions. Under the present conditions, production of $\text{C}_2\text{H}_5\text{O}^+$ from acetylene could only be accounted for by radiative association.

According to Herbst and Bates, the temperature dependence of rate coefficient for radiative association is given by:

$$k_{ra} \propto T^{-(l/2+\delta)} \quad (6.11)$$

where l is the number of rotational degrees of freedom of all the reactants and δ is a typically small correction factor ($\delta \ll 1$) accounting for the product stabilization step.^{64,77-79} Expression (6.11) well describes the behavior of many known association rate coefficients.

Typically, the limiting values of the exponent b in Equation (6.11) ($b = l/2 - \delta$) are $b < 3$. For the $\text{H}_3\text{O}^+ + \text{C}_2\text{H}_2$ reaction system, the theoretical limit of b is 2.5 (including 3 rotational degrees of freedom for H_3O^+ and 2 for linear C_2H_2 molecule, neglecting δ). If assuming all the $\text{C}_2\text{H}_5\text{O}^+$ products observed in the experimental system are from radiative association reaction (6.1), it is determined that the experimental value of the exponent in Equation (6.10) is around 1 with respect to ion temperature which is a reasonable value if some of the rotational degrees of freedom are not coupled in the reaction. In regard to molecular beam temperature, the observed exponent is near 8.5. This high exponent value cannot be explained through Herbst and Bates' model and appears physically unreasonable by any statistical reaction model.

Attempting to explain the high exponents ($b > 5$) observed in some association reactions, Viggiano found that the assumption of a unit vibrational partition function in Herbst's model in equation (6.11) is not valid in certain temperature ranges and the contribution of reactant vibrational degrees of freedom sometimes cannot be neglected. The temperature-dependent rate coefficient of radiative association reaction in Viggiano's model takes the form:

$$k_{ra} \propto T^{-(l/2+\delta)} \prod_i [1 - \exp(-h\nu_i/kT)]. \quad (6.12)$$

Viggiano's model could explain some of the known association reactions with high exponent values^{80,81} at high temperature range. The vibrational contribution of reactants in radiative association reactions was also discussed by Dunbar.^{82,83} The total internal partition function of acetylene molecule, in the reaction temperature range can be calculated from Herman⁸⁴ and applied to the Viggiano's model. The temperature dependence of the acetylene internal state distribution cannot account for anything near the rate coefficient effect exponent observed.

Therefore, it appears that the $C_2H_5O^+$ products do not derive from radiative association reaction only. A possible additional channel is the reaction of H_3O^+ with acetylene dimer present in the gas flow. What's more, at a trap temperature of 80 K and beam temperature of 160 K, product ions, $C_4H_7O^+$, are observed in the reaction system (near 10% compared to $C_2H_5O^+$ products). The existence of $C_4H_7O^+$ would appear to be due to displacement of C_2H_2 from $(C_2H_2)_3$ supporting the effect of clusters. We hypothesize that $C_2H_5O^+$ products observed at low molecular beam temperatures are due to dimer reaction and that higher order cluster derivatives cannot account for this product.

It is also verified in part 3 of this section that less than 1% of $C_2H_5O^+$ products are created by radiative association reaction.

A quantitative model for acetylene dimer and monomer equilibrium was proposed by Colussi and co-workers⁶⁸ in 1994 based upon spectroscopic observation. In the equilibrium system



the dimer to monomer ratio P_d/P_m is given by the expression

$$P_d / P_m = K_p(T) P_m f_m^2 / f_d, \quad (6.14)$$

where $K_p(T)$ is the equilibrium constant of equation (6.14) in pressure units, P_d is the partial pressure of dimer, P_m is the partial pressure of monomer and f_m and f_d are the fugacity coefficients of monomer and dimer, respectively. For acetylene, $f_m^2/f_d \approx 0.99$.⁶⁸

In Colussi's model, $K_p(T)$ can be simplified as

$$K_p(T) = 6.7T^{-4}Q(z) \cdot \exp(D_0/kT) \quad (6.15)$$

where $K_p(T)$ is in units of atm^{-1} , D_0 is the dimer binding energy, $Q(z)$ is the partition function and z is an adjustable parameter which controls the degrees of coupling of Van der Waals vibrations for C_2H_2 intermolecular stretch.⁶⁸

Before calculating the acetylene dimer fraction P_d/P_m in equation (6.14), from our beam conditions, it is important to verify that the partial pressure of acetylene monomer P_m in the molecular beam is determined by the stagnation condition and does not change significantly during passage through the source nozzle. The pressure drop in the nozzle is completely across the 1 mm thick aperture which takes 2×10^{-7} s for a molecule to transit.

This transit time should be compared to the timescale of dimer dissociation. To estimate the latter, we express the equilibrium constant $K_p(T)$ of equation (6.15) as the association rate coefficient for the monomers producing dimers, k_a , divided by the dimer dissociation rate coefficient, k_d . Using $K_p(T) = k_a/k_d$, the dimer dissociation rate coefficient, k_d , can be calculated from $K_p(T)$ and k_a .

The value of k_a can be estimated using

$$k_a = 145.5 \sigma^5 q \sqrt{D_e^2 / kTm} \quad (6.16)$$

where σ is zero potential radius, D_e is potential well depth and q is collision effectiveness^{85,86} which is

$$q = 0.4 \cdot \exp(-0.6 D_e / kT). \quad (6.17)$$

For acetylene dimer, $\sigma = 0.43\text{nm}$,⁸⁷ while D_e is between 478 cm^{-1} and 610 cm^{-1} .⁸⁸⁻⁹¹ Assuming the mid-range value $D_e = 544\text{ cm}^{-1}$, k_a is calculated using Equation (6.16) to be $4.59 \times 10^{-32}\text{ cm}^6\cdot\text{s}^{-1}$ at 160 K and $6.39 \times 10^{-32}\text{ cm}^6\cdot\text{s}^{-1}$ at 220K. Then, $K_p(T)$ calculated according to Equation (6.15) at different binding energies is between $3.1 \times 10^{-22}\text{ cm}^3$ and $9.3 \times 10^{-21}\text{ cm}^3$ in the experimental temperature range from 220 K to 160 K.

Thus, it can be estimated that in the experimental temperature range from 160 K to 220 K, k_d varies from $5 \times 10^{-12}\text{ cm}^3\cdot\text{s}^{-1}$ to $2 \times 10^{-10}\text{ cm}^3\cdot\text{s}^{-1}$, while the stagnation number density of acetylene dimer is between $2.0 \times 10^{16}\text{ cm}^{-3}$ and $2.5 \times 10^{16}\text{ cm}^{-3}$. As a result, acetylene dimer dissociates with a time constant near 0.5 ms which is three orders of magnitude greater than the nozzle transit time. Therefore, the stagnation dimer fraction is completely transferred to the RET.

As P_m is verified to be the acetylene stagnation pressure, the rate coefficient of $H_3O^+ + (C_2H_2)_2$ reaction can be derived from Colussi's dimer model and the experimental data. In the calculation of the equilibrium constant $K_p(T)$ in equation (6.15), the ab initio value of $D_0 = 404 \text{ cm}^{-1}$ is used while the parameter z for partition function is set to be 0.32, consistent with Colussi's observation. Under this condition, the equilibrium constant $K_p(T)$ of equation (6.15) and dimer fraction P_d/P_m can be obtained and the result is shown in table 1.

Table 6.1 The calculated dimer/monomer equilibrium constant $K_p(T)$, dimer fraction P_d/P_m values at binding energy D_0 equals 404 cm^{-1} while parameter z is 0.32.

$D_0(\text{cm}^{-1})$	K_p &	Temperature (K)					
/Z	P_d/P_m	160	170	180	190	200	220
404/	$K_p(\text{atm}^{-1})$	9.1×10^{-2}	7.2×10^{-2}	5.8×10^{-2}	4.7×10^{-2}	3.9×10^{-2}	2.8×10^{-2}
0.32	P_d/P_m	0.60%	0.48%	0.38%	0.31%	0.26%	0.19%

The rate coefficient k of $H_3O^+ + (C_2H_2)_2$ reaction is deduced from the expression

$$k = \frac{k_1(T_{\text{react}})}{n_d(T_b)} = \frac{k_1(T_{\text{react}})}{n_m(T_b) \times (P_d / P_m)} \quad (6.18)$$

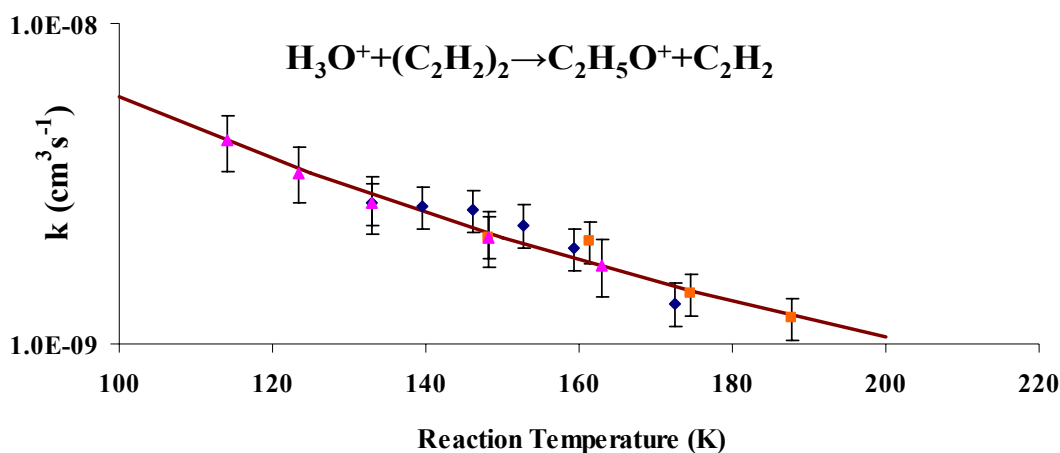
where $k_1(T_{\text{react}})$ is the experimental first order rate coefficient of $C_2H_5O^+$ formation, and $n_m(T_b)$ and $n_d(T_b)$ are the number density of acetylene monomer and dimer at different beam temperatures, respectively. The $H_3O^+ + (C_2H_2)_2$ reaction temperature T_{react} is written as

$$T_{\text{react}} = \left(\frac{3}{33}\right)T_{\text{coll}} + \left(\frac{9}{33}\right)T_{\text{ion}} + \left(\frac{21}{33}\right)T_b \quad (6.19)$$

using 9 internal degrees of freedom for H_3O^+ and 21 for $(C_2H_2)_2$. Adding the 3 relative collisional degrees of freedom, the total degrees of freedom for the reaction system is 33.

The rate coefficient of the $\text{H}_3\text{O}^+ + (\text{C}_2\text{H}_2)_2$ reaction calculated from equation (6.18) at different reaction temperatures is shown in figure 6. The calculated rate coefficient curve is fix as $4.0 \times 10^{-10}(\text{T}_{\text{react}}/300)^{-2.5}$.

Figure 6.4 The rate coefficient defined in equation (6.19) of $\text{H}_3\text{O}^+ + (\text{C}_2\text{H}_2)_2$ reaction versus statistical temperature with the expression of equation (6.20). (♦) Trap temperature is 80 K while beam temperature varied from 160 K to 220 K. (■) Trap temperature is 125 K while beam temperature varied from 160 K to 220 K. (▲) Trap temperature varied from 25 K to 170 K while beam temperature is 160 K.



The result demonstrates that Colussi's dimer model explains the experimental rate observation well and the product $\text{C}_2\text{H}_5\text{O}^+$ is created through dimer reaction. The acetylene dimer rate coefficient is temperature dependent as the acetylene dimer, $(\text{C}_2\text{H}_2)_2$, is known from microwave and infrared spectroscopic studies to have a T-shaped (C_{2v} symmetry) structure^{88,92,93} with a permanent dipole moment of 0.27 D.⁹⁴

6.3.3 Radiative association of H_3O^+ and C_2H_2

The $\text{H}_3\text{O}^+ + \text{C}_2\text{H}_2$ radiative association reaction has been studied by Herbst in 1985, through both theory and experiment. Assuming the structure of product $\text{C}_2\text{H}_5\text{O}^+$ is

CH_3CHOH^+ , which is the most stable isomer, the rate coefficient of radiative association reaction is theoretically calculated as $4.5 \times 10^{-12} \cdot (T/300)^{-1.6}$ in the temperature range from 10 K to 50 K.⁶² However, the rate coefficient deduced from three-body association data is two orders of magnitude lower in the same temperature range with k_{obs} which is $2.7 \times 10^{-14} \cdot (T/300)^{-1.6}$.⁶² To explain the difference between theory and experiment, Herbst concluded that product $\text{C}_2\text{H}_5\text{O}^+$ being formed during the reaction does not lead to the lowest energy isomer, CH_3CHOH^+ .

In our study, at a trap temperature of 80 K and beam temperature 300 K (reaction temperature 187 K), no $\text{C}_2\text{H}_5\text{O}^+$ products were observed. Under these conditions, the beam contains a dimer fraction of only 0.04%, effectively negating contributions of the dimer in any observed product formation. Considering the instrument detection limit for product detection at these beam densities, the rate coefficient of $\text{H}_3\text{O}^+ + \text{C}_2\text{H}_2$ radiative association reaction must be below $1 \times 10^{-13} \text{ cm}^3 \cdot \text{s}^{-1}$ at this temperature. When the reaction temperature is 121 K (beam 160 K, trap 80 K), the rate coefficient calculated from Herbst is $1.2 \times 10^{-13} \text{ cm}^3 \cdot \text{s}^{-1}$. From the discussion above, the plot of the second order rate of $\text{C}_2\text{H}_5\text{O}^+$ formation divided by the acetylene monomer number density is approximately $10^{-11} \text{ cm}^3 \cdot \text{s}^{-1}$. Therefore, only 1% of observed $\text{C}_2\text{H}_5\text{O}^+$ product is produced from $\text{H}_3\text{O}^+ + \text{C}_2\text{H}_2$ radiative association.

In Vigren's study of dark cloud TMC-1 in 2010,⁵⁹ there is a discussion of the rate for $\text{H}_3\text{O}^+ + \text{C}_2\text{H}_2$ radiative association reaction. As mentioned in the paper, if the rate coefficients follows Herbst's deduced experimental value, their model shows a large decrease in the calculated acetaldehyde abundance at TMC-1 for the estimated chemical

age and gas phase chemistry cannot reproduce the observed amount of acetadelhyde in TMC-1. They concluded that the formation of acetaldehyde might be from grain-surface chemistry. Our conclusion that the rate coefficient of $\text{H}_3\text{O}^+ + \text{C}_2\text{H}_2$ radiative association reaction is mostly likely Herbst's experimental value would seem to support a conclusion of purely gas phase production mechanism if the radiative association reaction product can lead to acetaldehyde through electron-ion recombination.

6.4 Conclusion

The reaction between H_3O^+ and acetylene/acetylene dimer was studied using a molecular beam-radio frequency ring electrode trap method. The temperatures of both beam (160 K to 300 K) and trap (20 K to 450 K) were controlled independently and the collision temperature was used to analyze the temperature dependence of the rate coefficient. It is found that the rate coefficient of $\text{H}_3\text{O}^+ + \text{C}_2\text{H}_2$ radiative association reaction is below $1 \times 10^{-13} \text{ cm}^3 \cdot \text{s}^{-1}$ which supports the experimental rate coefficient value of Herbst. The sharp temperature dependence of rate coefficient by varying beam temperature can be explained by the increase of acetylene dimer at lower temperatures and Colussi's dimer model is used in the acetylene dimer calculation. Based on this model, the rate coefficient of the $\text{H}_3\text{O}^+ + (\text{C}_2\text{H}_2)_2$ reaction is determined to behave as $4.0 \times 10^{-10} \cdot (\text{T}_{\text{tran}}/300)^{-2.5}$ in the reaction temperature range 114 K to 187 K.

CHAPTER 7 CONCLUSION

The study of temperature dependent rate coefficient measurement for reactions in the ISM is very important in the research of the existence and the synthesis of molecules in the ISM. CoMB-RET instrument is one of the most significant techniques for reaction coefficient studies at low temperatures and ultra-high vacuum. Ions can be stored in the RET at thermal energy for 50 s which is long enough for the reaction taking place. If the Rf field and DC potential applied to the RET is under the stability limit, the average kinetic energy of ions stored in the RET keeps constant though the instantaneous value changed all the time. Effusive molecular beam is used in the system and the velocity distribution of molecules in the beam follows Boltzmann-Maxwell distribution.

The main improvement done to the CoMB-RET instrument is to control the ion temperature and beam temperature separately in order to find the mechanism of the reaction in more details. To control the ion temperature, pulsed buffer gas is admitted into the RET which equilibrates to the defined trap wall temperature, as do the ions through buffer gas collisions. The defined temperature of the RET is cooled by a regulated liquid He cryostat. Compared to the continuous buffer cooling used before, the cooling efficiency is higher and the ion-molecule reaction can start until the system is pumped down to 10^{-8} torr, therefore, buffer gas will not affect the reaction process. A Chopped molecular beam is applied to the system by putting a shutter in front of the second skimmer of the molecular beam. As soon as the pulsed buffer gas is pumped out and ions in the ring electrode trap are relaxed to the desired low temperature, the shutter is open

and the reaction takes place. The temperature of the molecular beam is controlled by the regulated liquid He cryostat mounted on the beam nozzle. The molecular beam terminates at the RGA at the beam dump chamber which is used to measure the molecular beam flux and to check whether there are contaminations in the system background.

The temperature dependent rate coefficients of three reactions are studied through this instrument. In the $\text{N}_2^+ + \text{H}_2\text{O}$ charge transfer reaction, it is verified that during the ion-molecule collision reaction, the ions internal temperature equilibrates with the trap wall temperature and the molecular beam internal temperature is equal to the beam nozzle temperature. Meanwhile, the ion-molecule center of mass collision temperature can be calculated as $T = (m_1 T_2 + m_2 T_1) / (m_1 + m_2)$. The rate coefficient of the highly exothermic $\text{N}_2^+ + \text{H}_2\text{O}$ reaction is explained by the ADO theory.

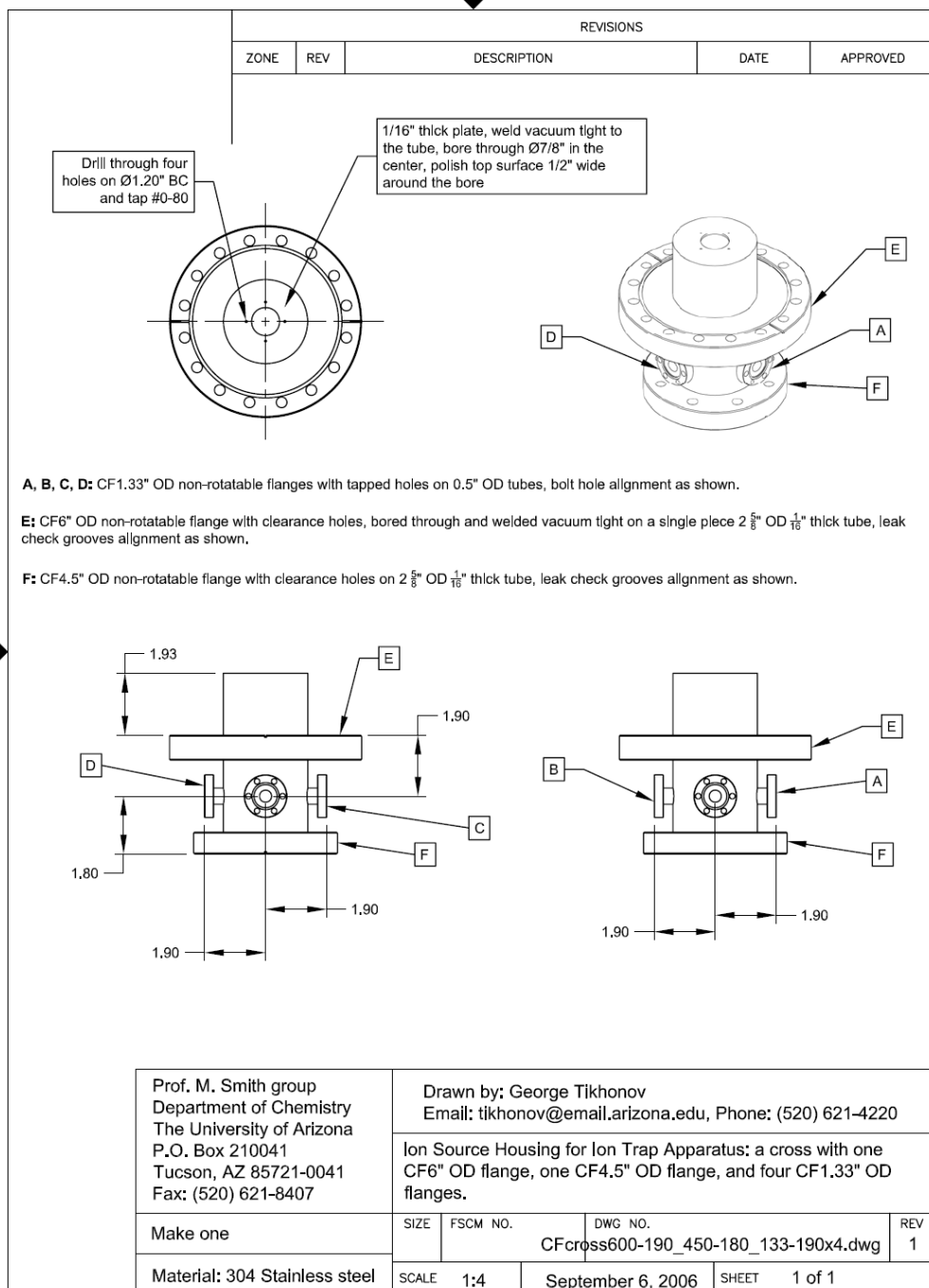
In the $\text{H}_3\text{O}^+ + \text{C}_2\text{H}_4$ proton transfer reaction, rate coefficients at different ion and beam temperatures of both forward and reverse reactions are measured. A statistical reaction temperature which is based on the numbers of degrees of freedom of ion-molecule center of mass collision and the internal degrees of freedom of each reactant is defined which well explains the temperature dependent rate coefficient result for $\text{H}_3\text{O}^+ + \text{C}_2\text{H}_4$ forward endothermic reaction. The enthalpy ΔH_r° and entropy ΔS_r° of the equilibrium reaction $\text{H}_3\text{O}^+ + \text{C}_2\text{H}_4 \leftrightarrow \text{C}_2\text{H}_5^+ + \text{H}_2\text{O}$ are calculated to be $(5.1 \pm 0.5) \text{ KJ} \cdot \text{mol}^{-1}$ and $(-15.0 \pm 0.9) \text{ J} \cdot \text{mol}^{-1} \cdot \text{K}^{-1}$, respectively. They are all in the reasonable range compared to the previous study.

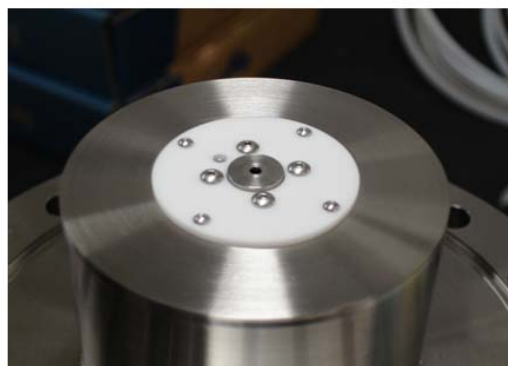
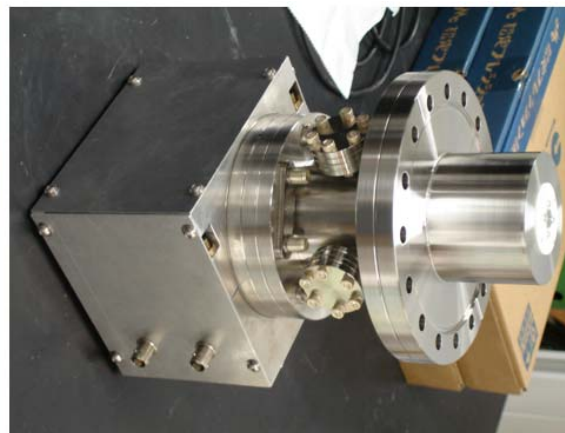
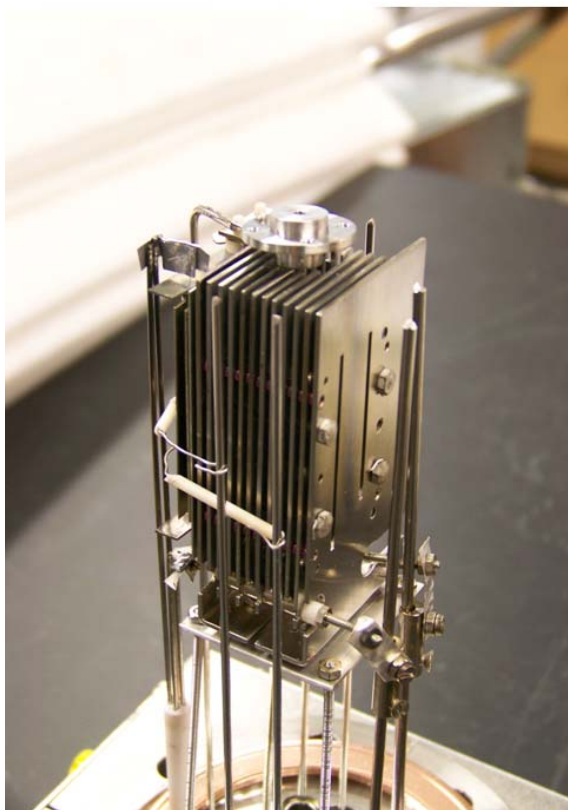
In the study of the $\text{H}_3\text{O}^+ + \text{C}_2\text{H}_2/(\text{C}_2\text{H}_2)_2$ reaction system, the rate coefficient shows steep temperature dependence on molecular beam temperatures. This phenomenon is explained by the dimer fractions in the acetylene beam at different beam temperatures and it is verified that product $\text{C}_2\text{H}_5\text{O}^+$ observed in the system is formed by $\text{H}_3\text{O}^+ + (\text{C}_2\text{H}_2)_2$ dimer reaction. The rate coefficient of the dimer reaction can be written in the expression $4.0 \times 10^{-10} \cdot (T_{\text{tran}}/300)^{-b}$. In this study it is also found that the rate coefficient of $\text{H}_3\text{O}^+ + \text{C}_2\text{H}_2$ radiative association reaction is below $1 \times 10^{-13} \text{ cm}^3 \cdot \text{s}^{-1}$ which supports the experimental rate coefficient value of Herbst.

Appendix

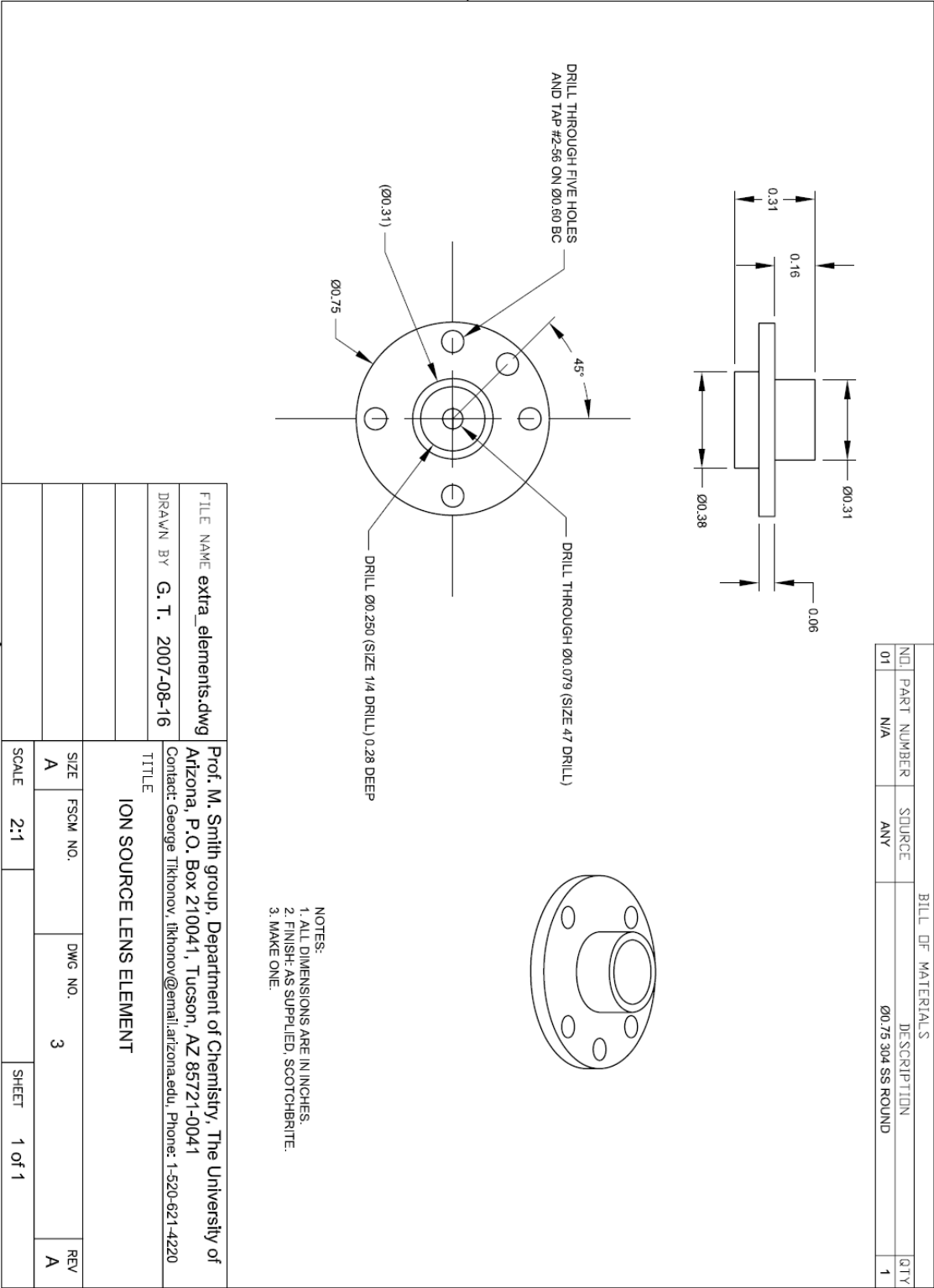
(1) Dimensions of Ion Source

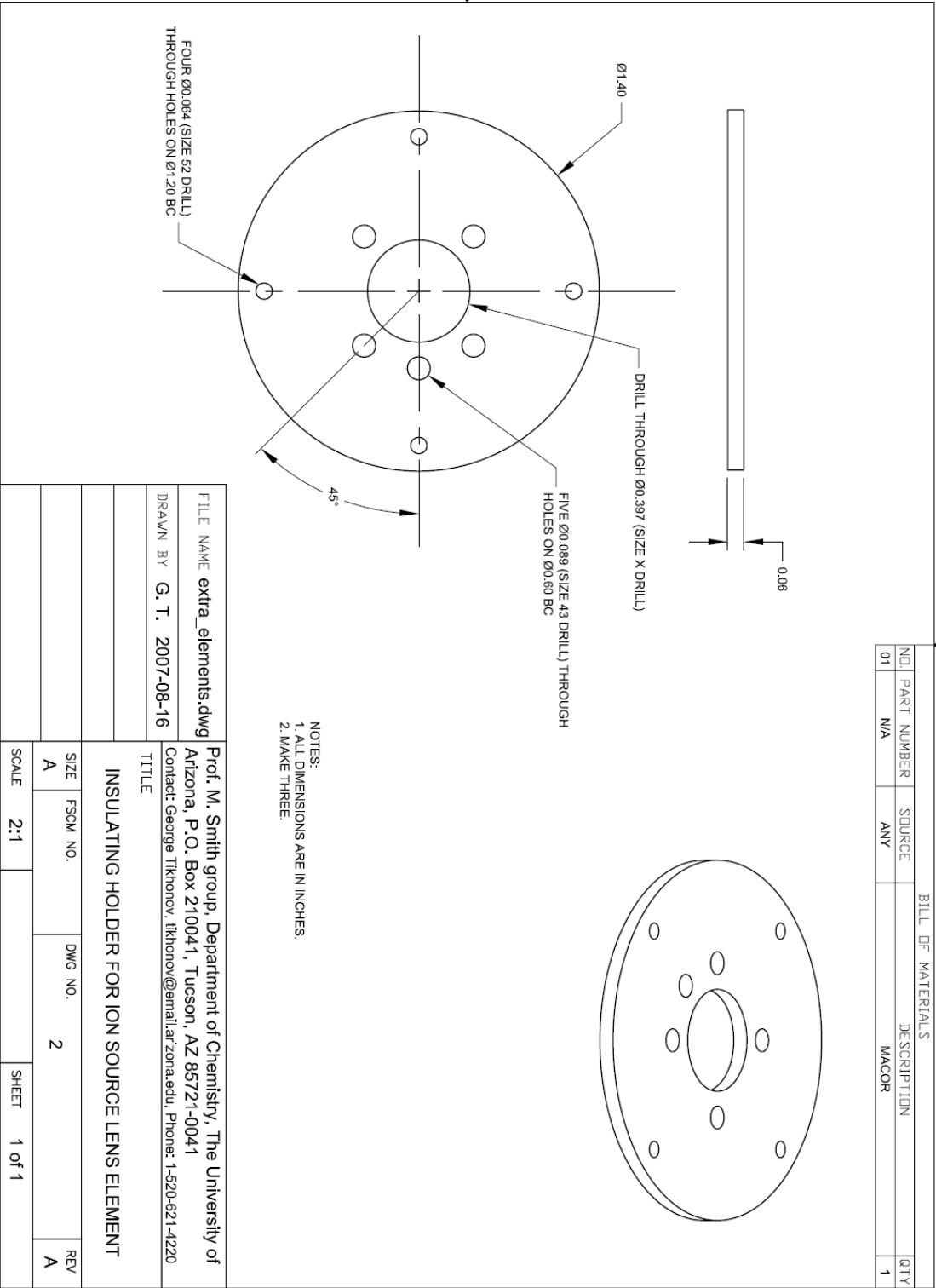
a. Ion source chamber and differential wall

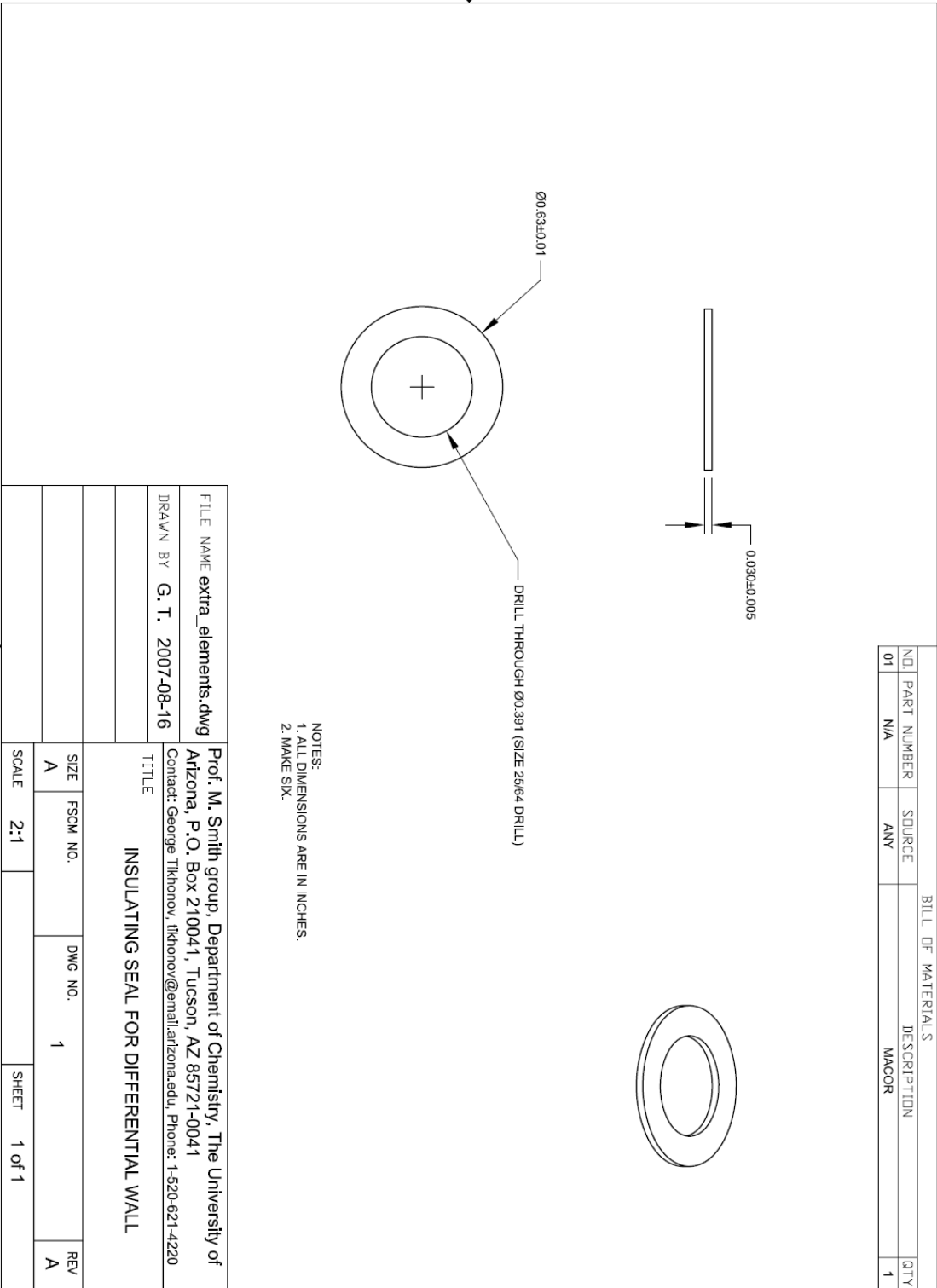




b. ion source exit lens elements

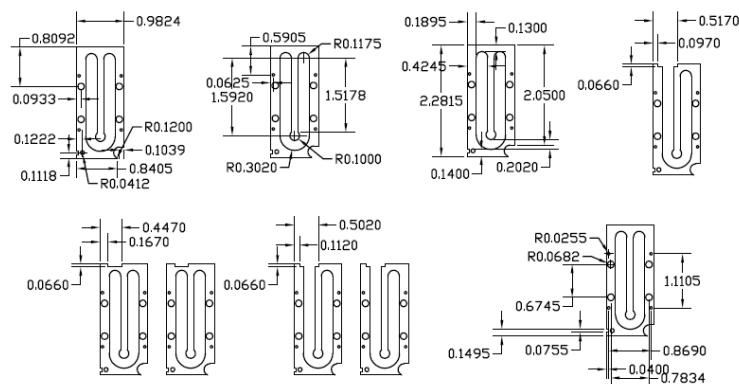




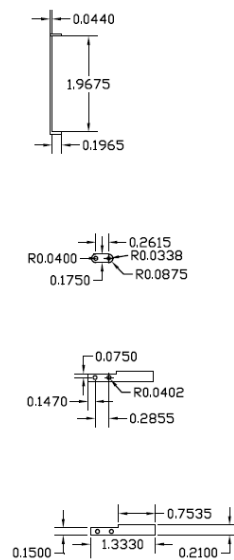


c. Ion source electronic plates

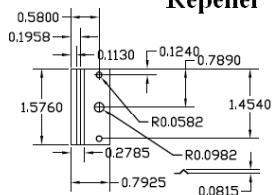
Rf plates



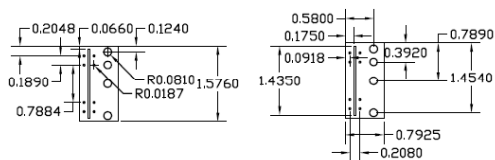
Filament Holder



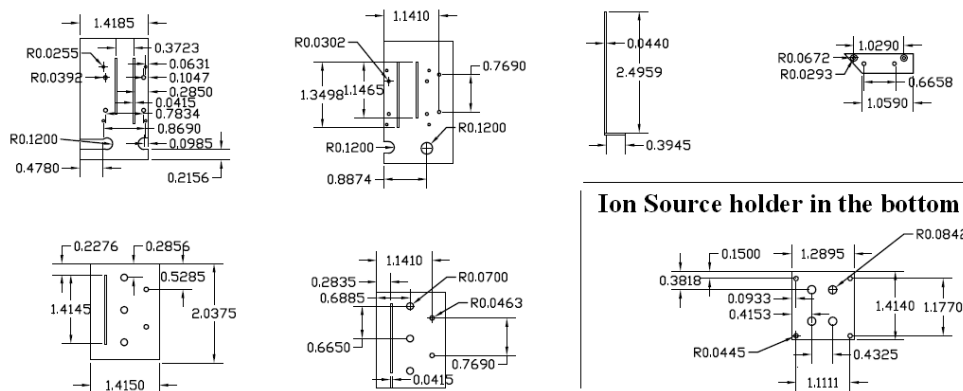
Repeller



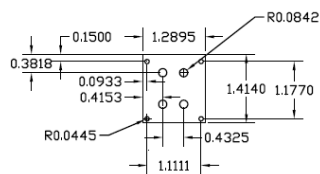
Electron Extraction plate



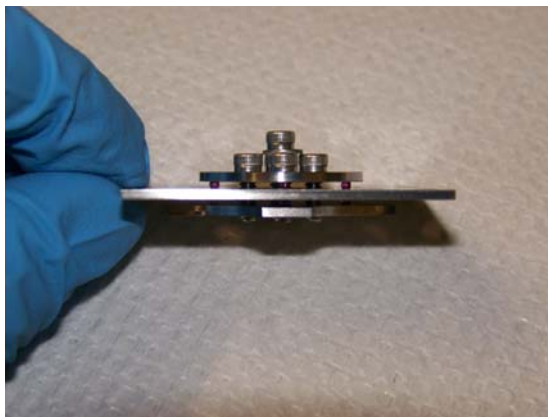
Endplate

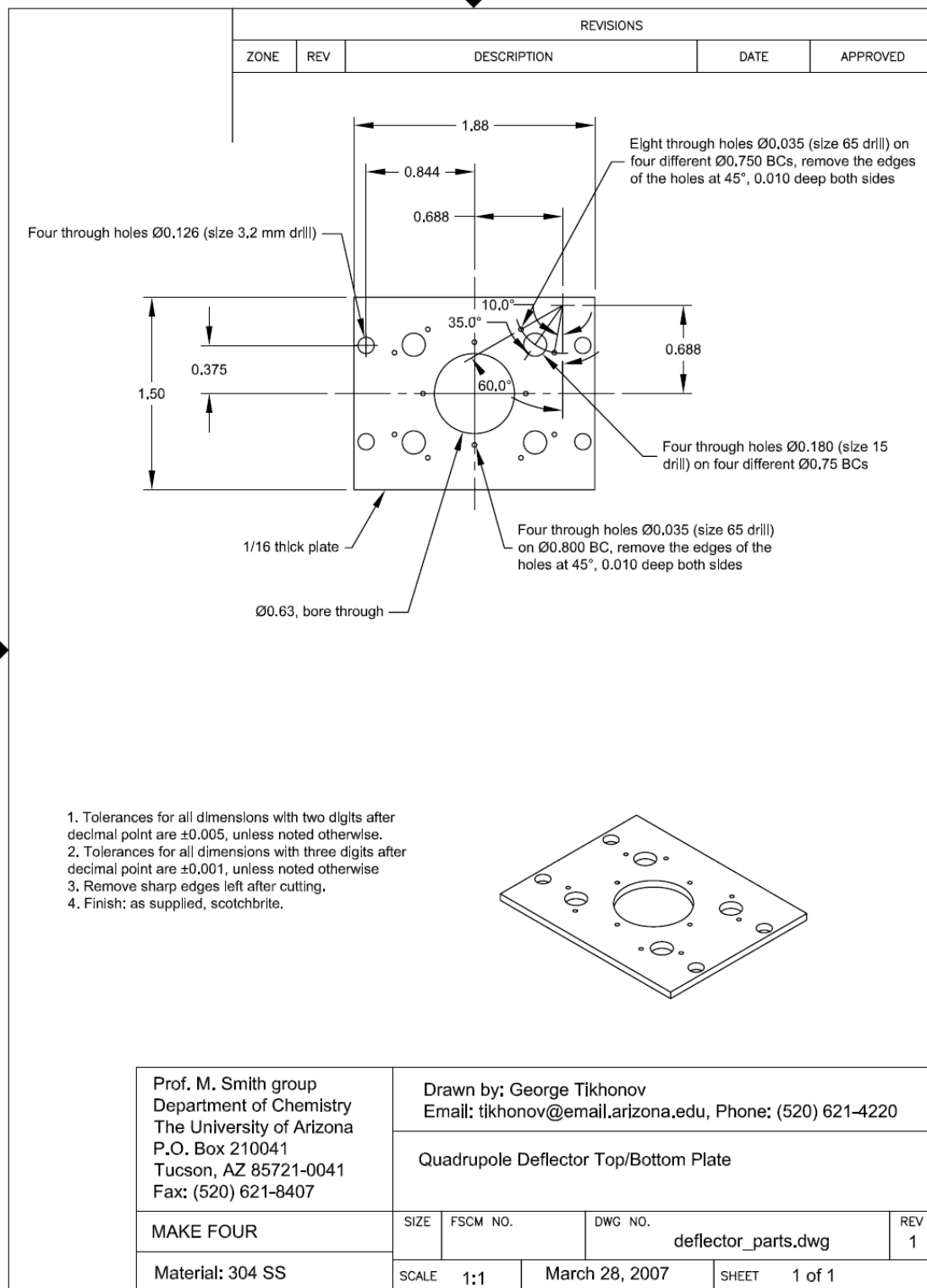


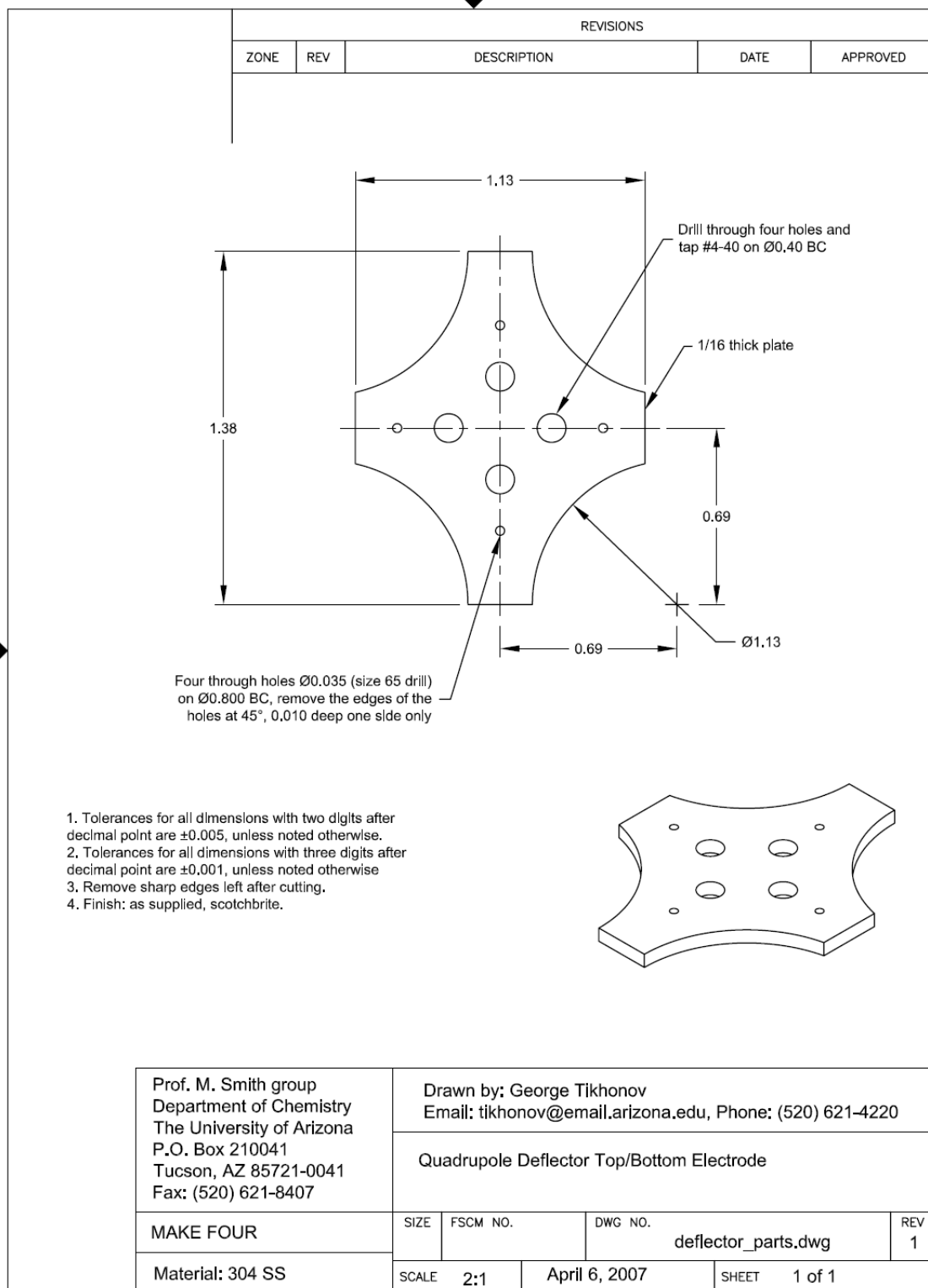
Ion Source holder in the bottom

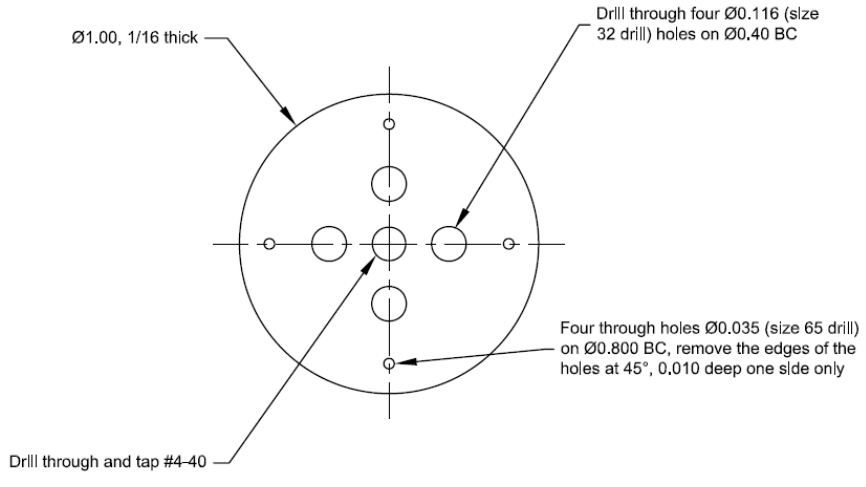
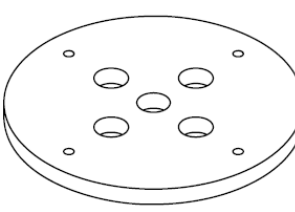


- (2) DC quadrupole bender and quadrupole ion guide/mass selector
a. DC quadrupole bender

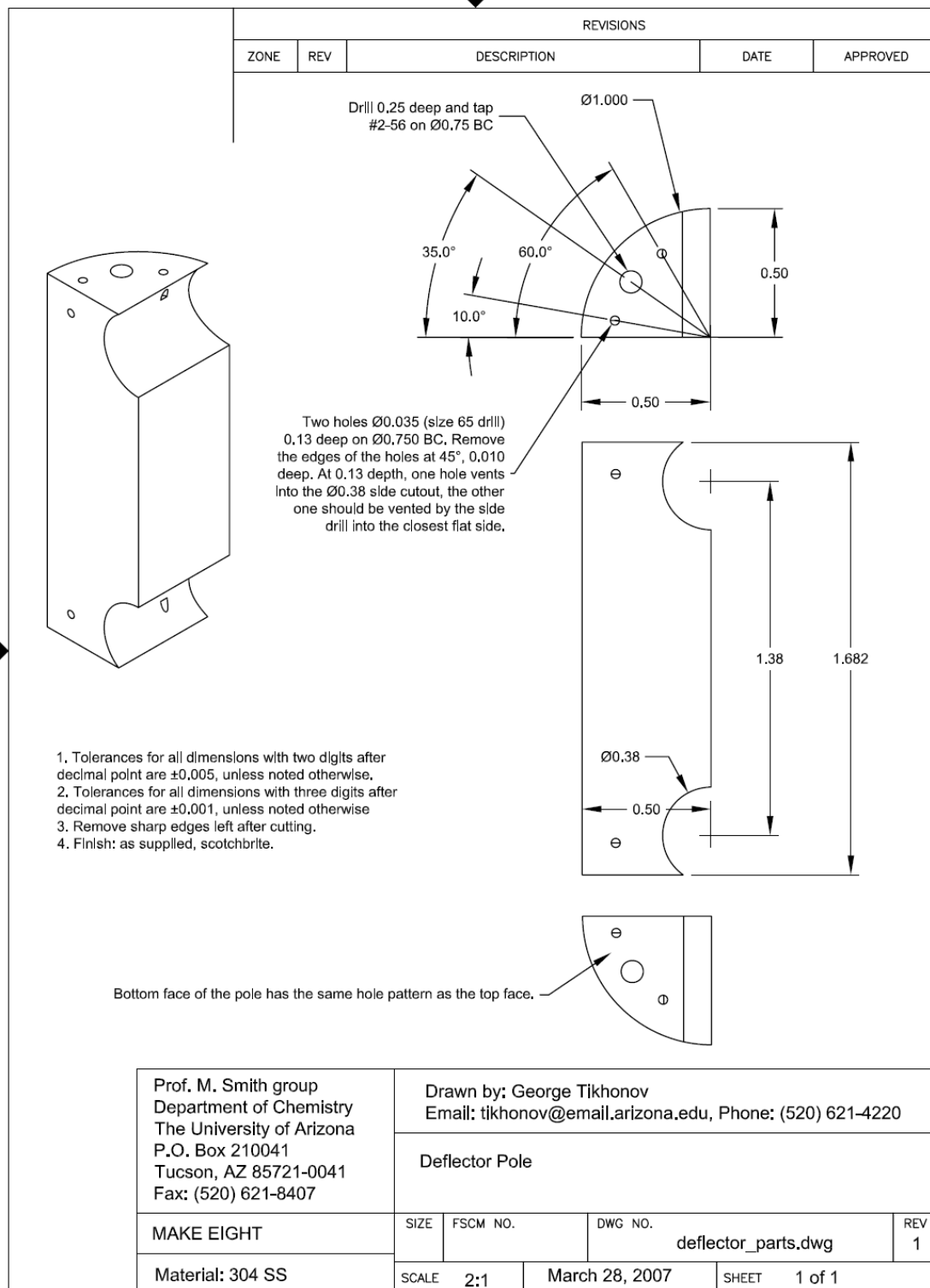






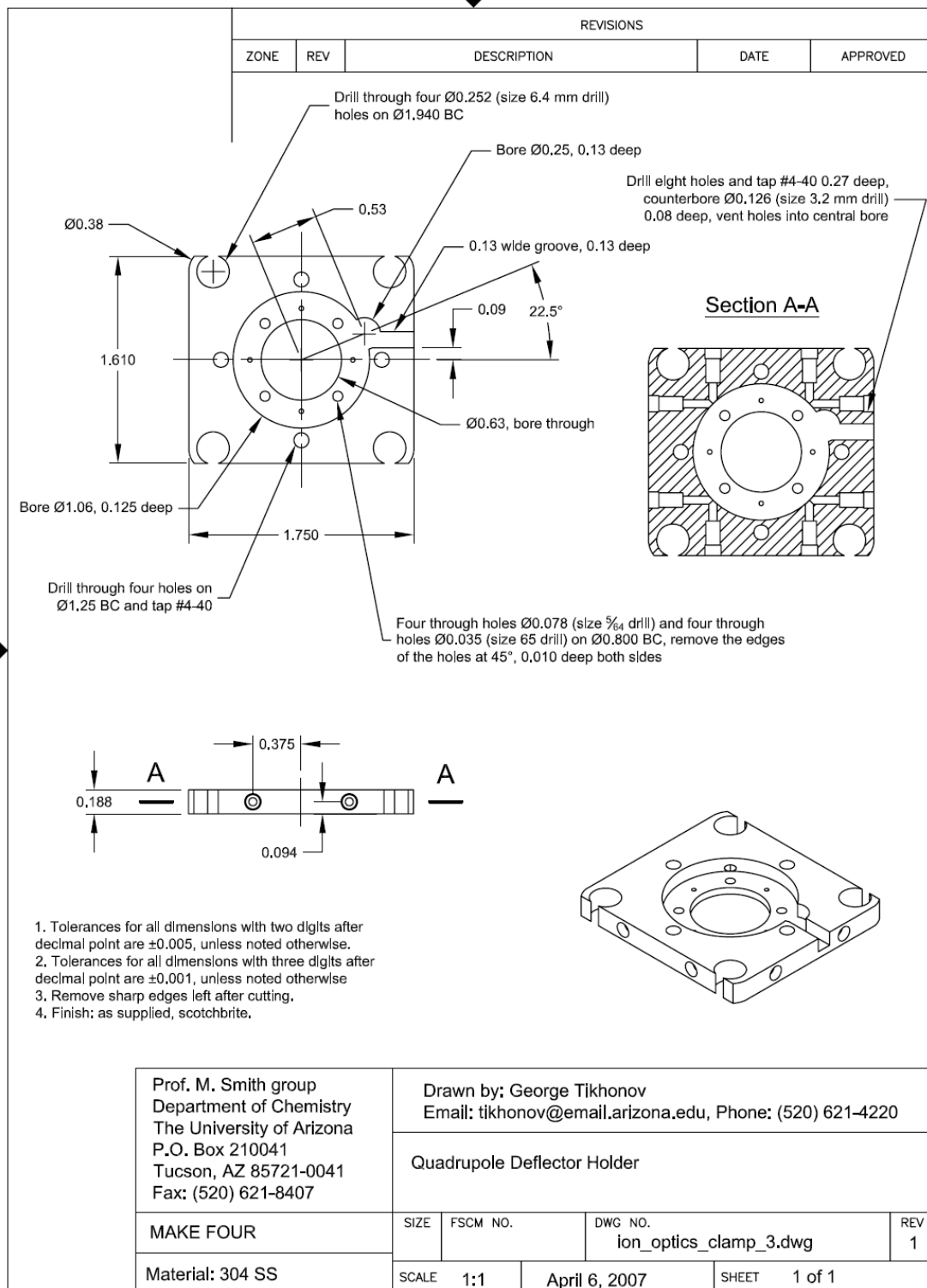
REVISIONS				
ZONE	REV	DESCRIPTION	DATE	APPROVED
<div style="text-align: center;">  <p>Ø1.00, 1/16 thick</p> <p>Drill through four Ø0.116 (size 32 drill) holes on Ø0.40 BC</p> <p>Four through holes Ø0.035 (size 65 drill) on Ø0.800 BC, remove the edges of the holes at 45°, 0.010 deep one side only</p> <p>Drill through and tap #4-40</p> </div> <div style="margin-top: 20px;">  </div> <div style="margin-top: 20px;"> <p>1. Tolerances for all dimensions with two digits after decimal point are ± 0.005, unless noted otherwise.</p> <p>2. Tolerances for all dimensions with three digits after decimal point are ± 0.001, unless noted otherwise.</p> <p>3. Remove sharp edges left after cutting.</p> <p>4. Finish: as supplied, scotchbrite.</p> </div>				

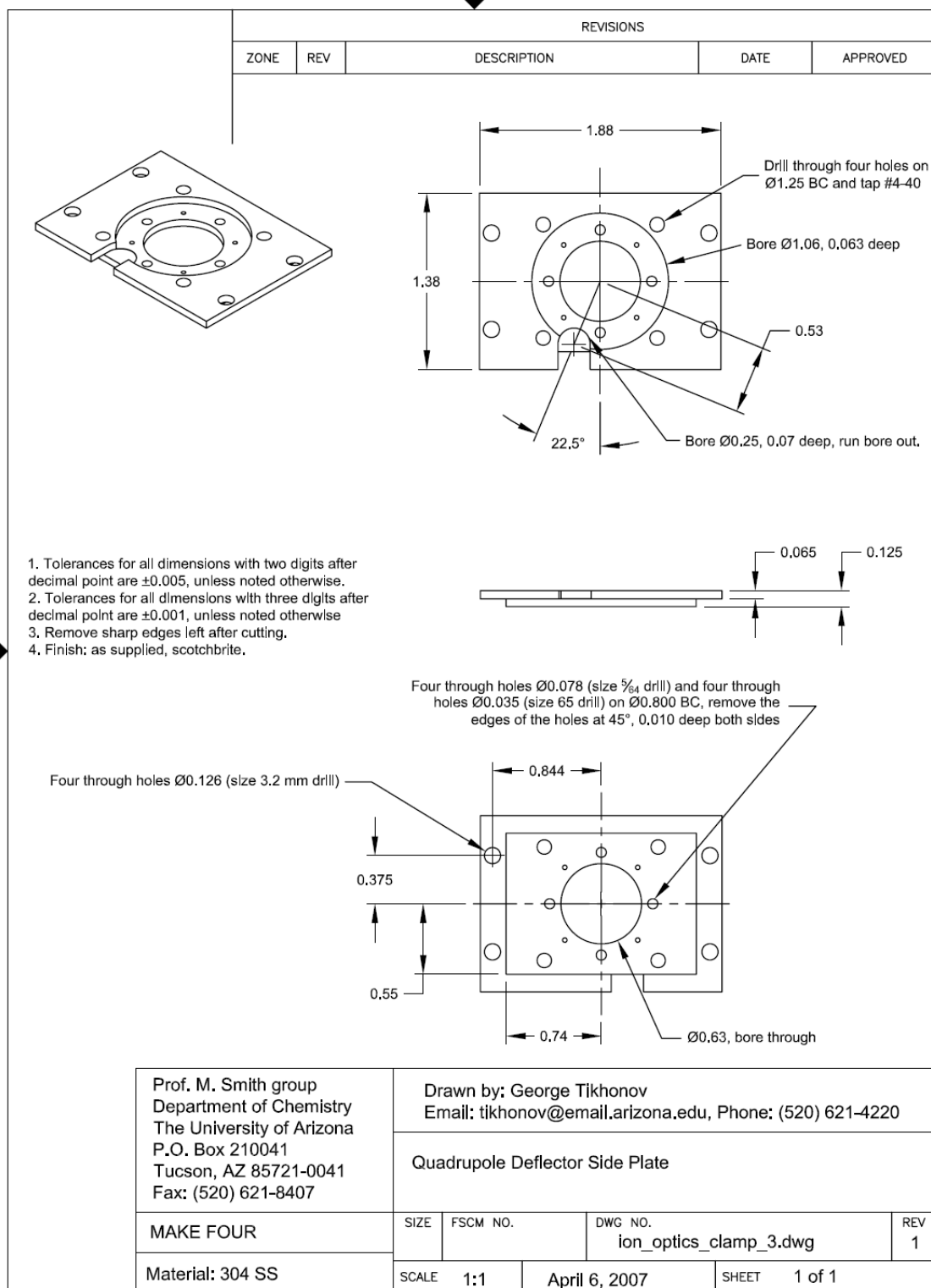
Prof. M. Smith group Department of Chemistry The University of Arizona P.O. Box 210041 Tucson, AZ 85721-0041 Fax: (520) 621-8407		Drawn by: George Tikhonov Email: tikhonov@email.arizona.edu, Phone: (520) 621-4220 Quadrupole Deflector Top/Bottom Electrode Holder		
MAKE FOUR	SIZE	FSCM NO.	DWG NO. deflector_parts.dwg	REV 1
Material: 304 SS	SCALE 2:1	March 28, 2007		SHEET 1 of 1



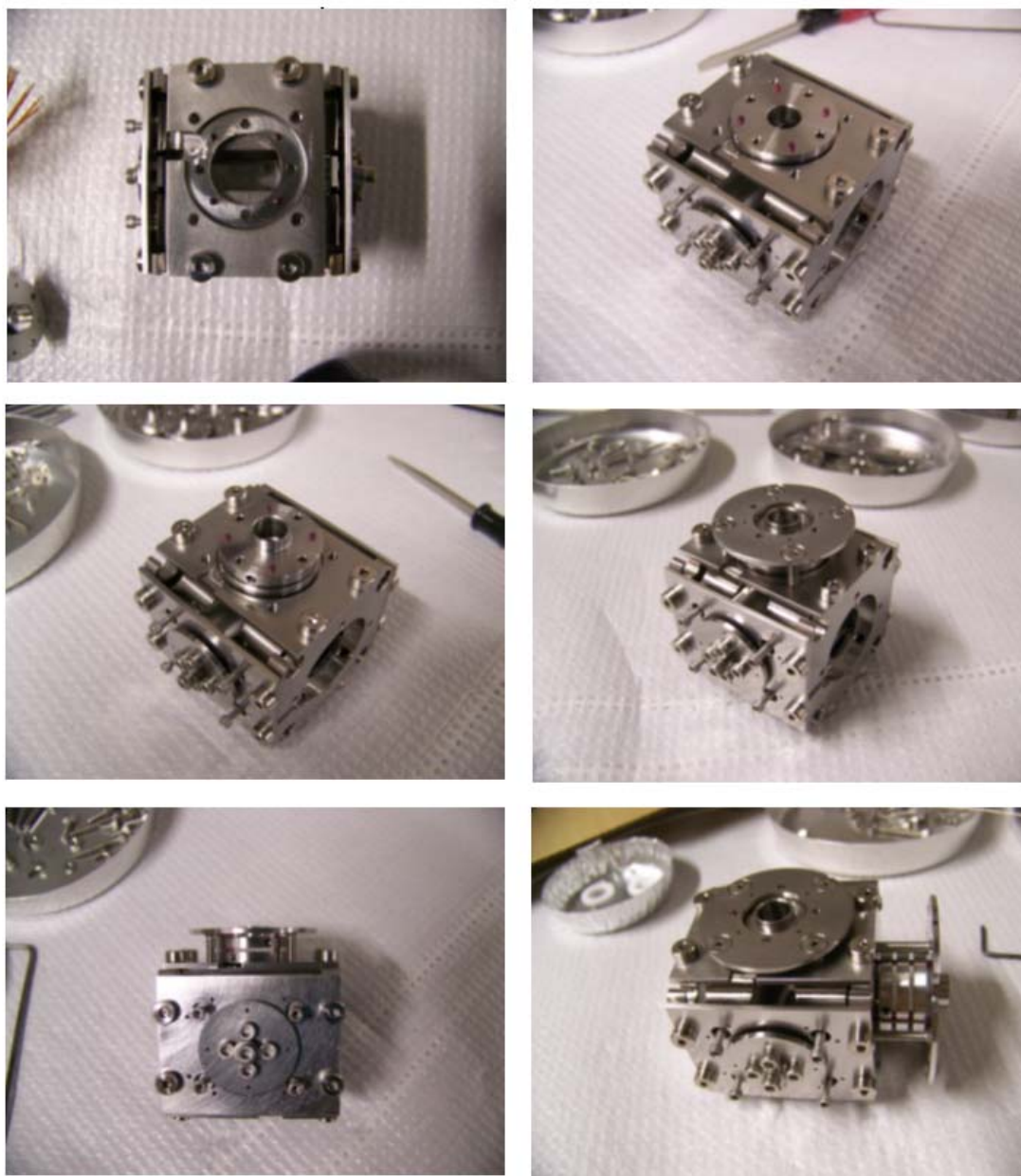
b. Quadrupole bender holder and side plate

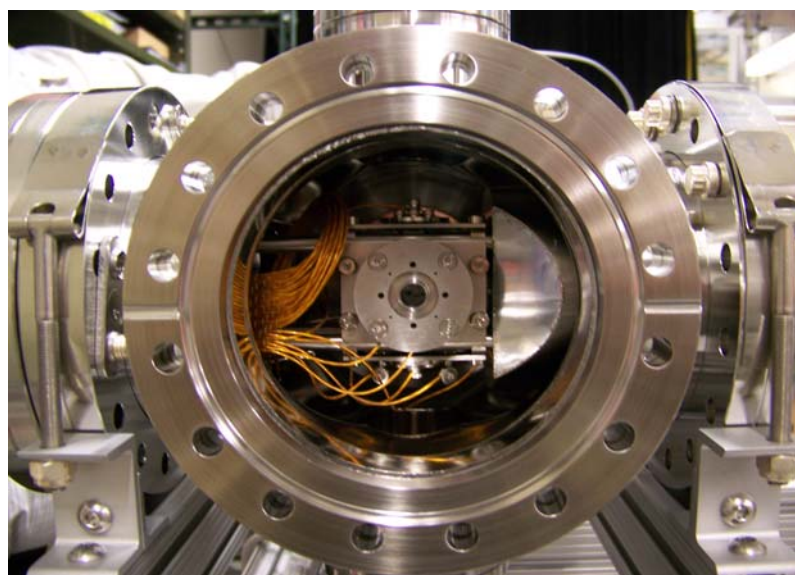
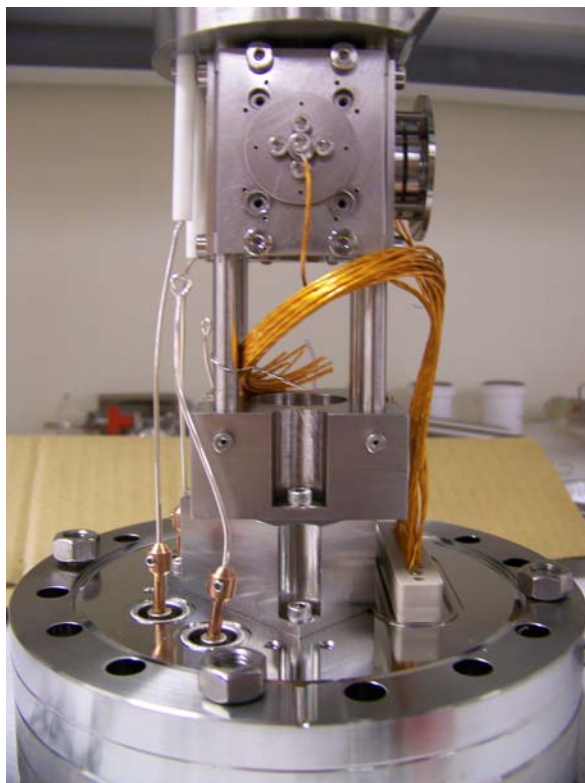


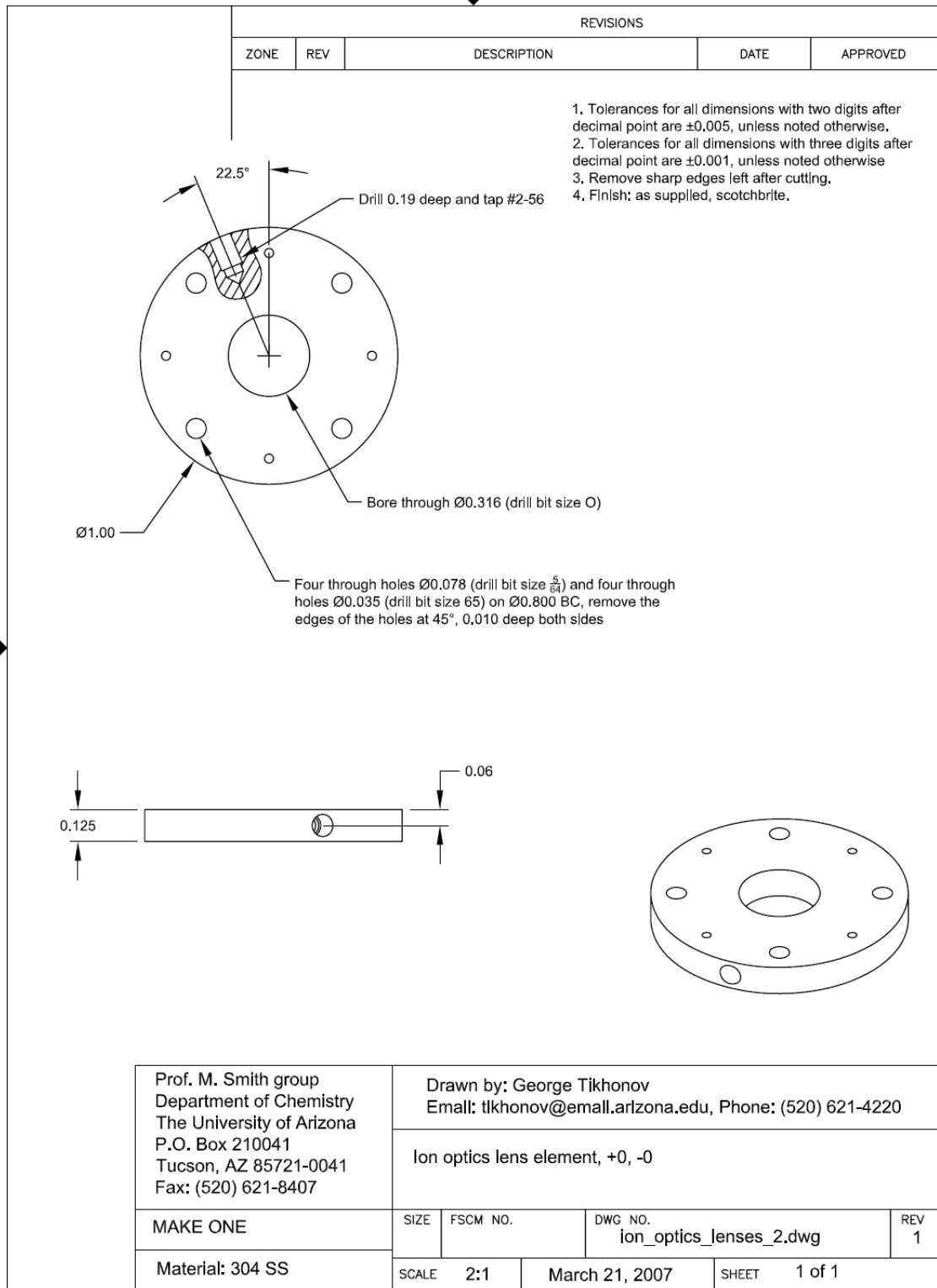


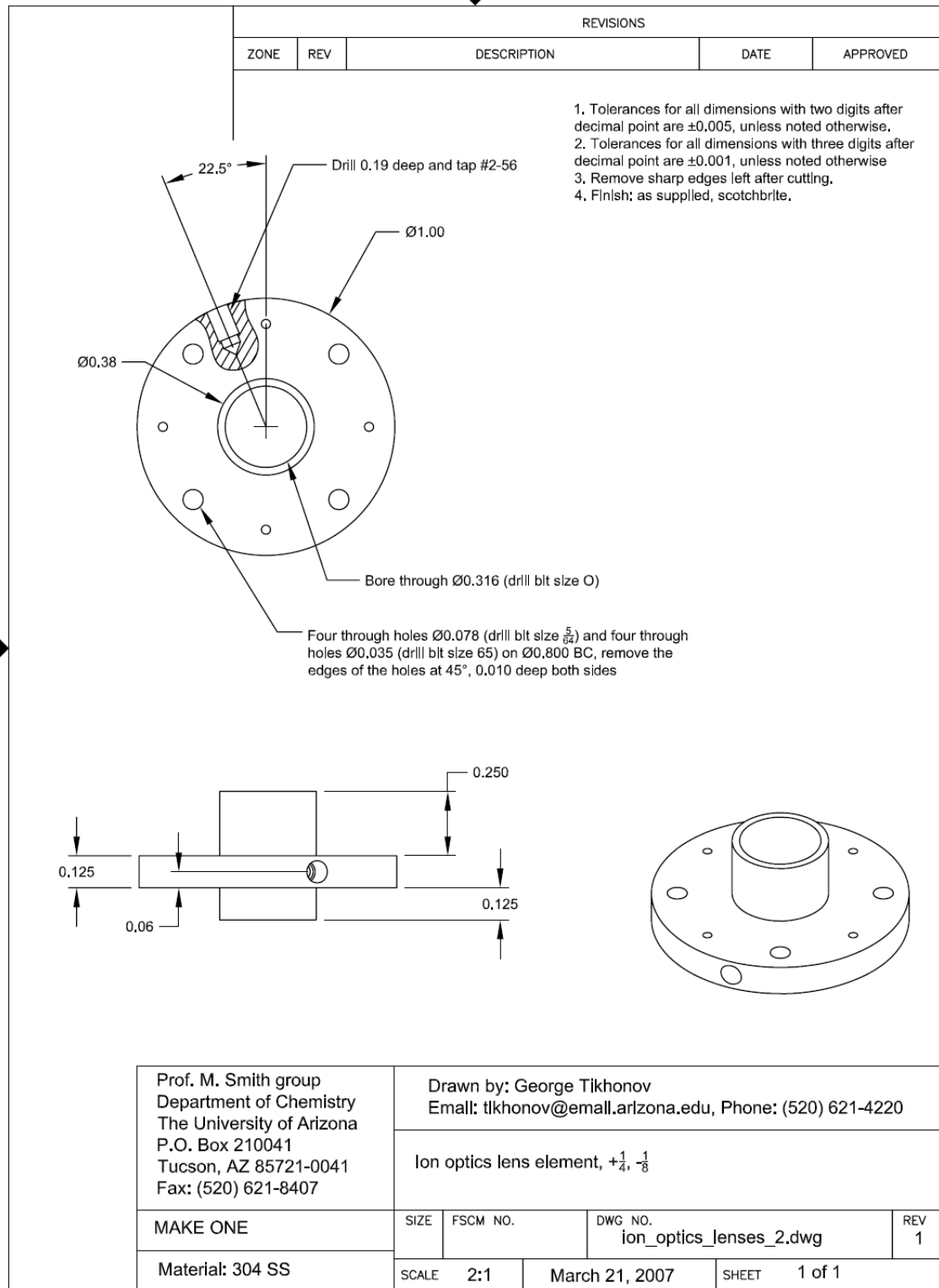


c. Electronic lenses and Ions optic pressure plate









Prof. M. Smith group
Department of Chemistry
The University of Arizona
P.O. Box 210041
Tucson, AZ 85721-0041
Fax: (520) 621-8407

Drawn by: George Tikhonov
Email: tlkhonov@email.arizona.edu, Phone: (520) 621-4220

Ion optics lens element, $+1, -1$

MAKE ONE

SIZE FSCM NO.

DWG NO.
ion_optics_lenses_2.dwg

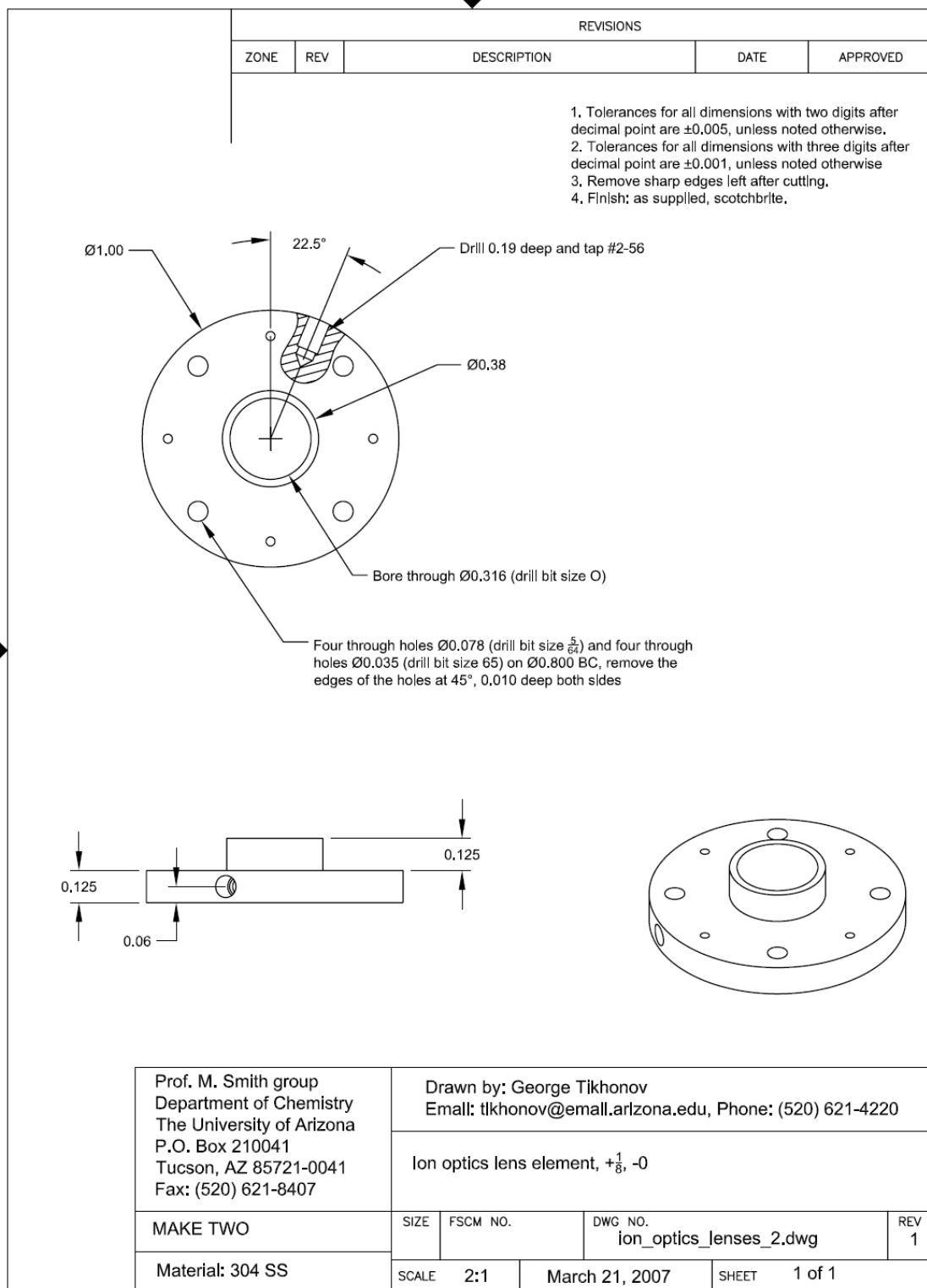
REV
1

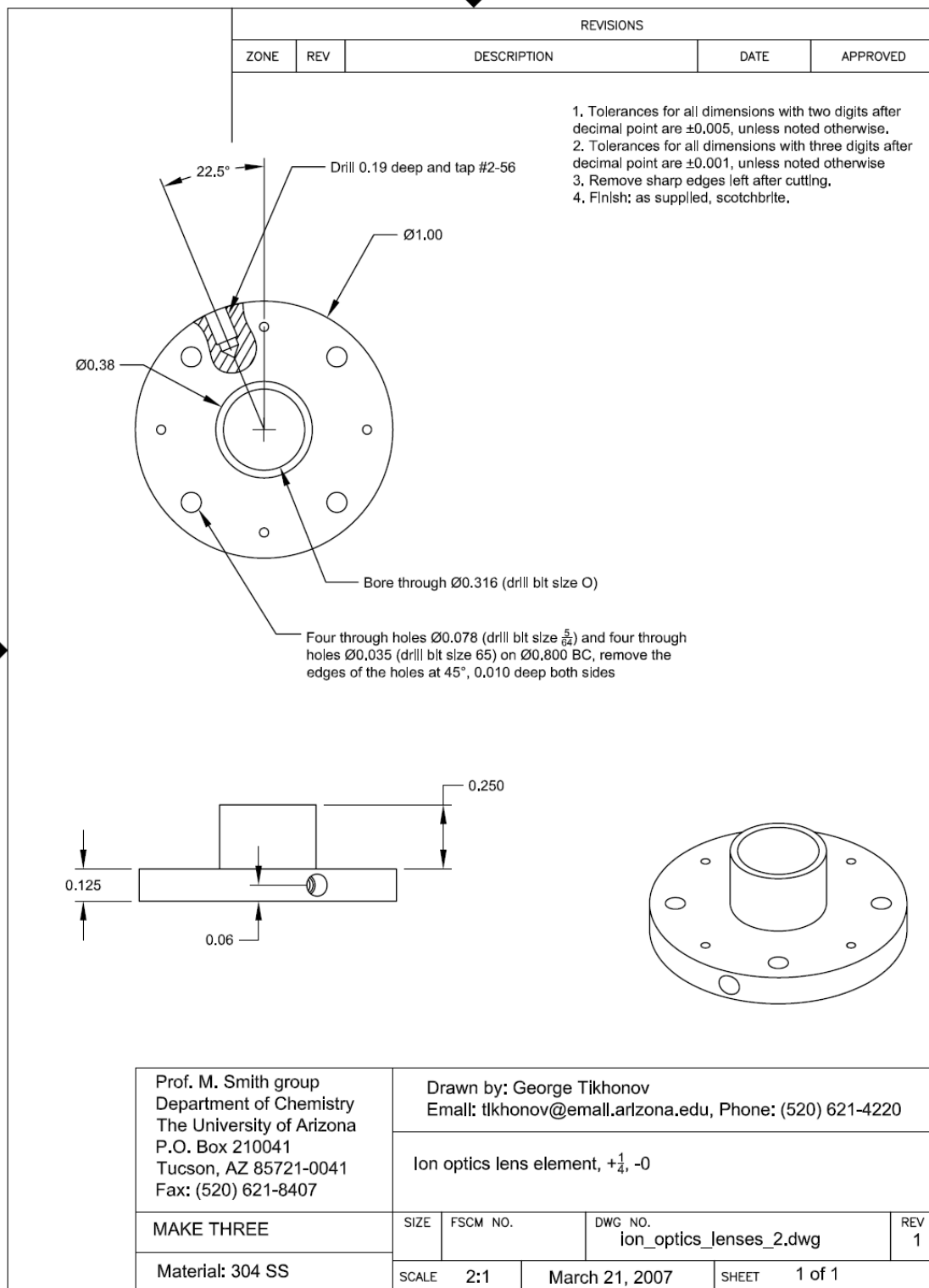
Material: 304 SS

SCALE 2:1

March 21, 2007

SHEET 1 of 1





REVISIONS		ZONE	REV	DESCRIPTION	DATE	APPROVED

22.5°

Drill 0.19 deep and tap #2-56

Ø1.00

Ø0.38

Bore through Ø0.316 (drill bit size O)

Four through holes Ø0.078 (drill bit size $\frac{5}{64}$) and four through holes Ø0.035 (drill bit size 65) on Ø0.800 BC, remove the edges of the holes at 45°, 0.010 deep both sides

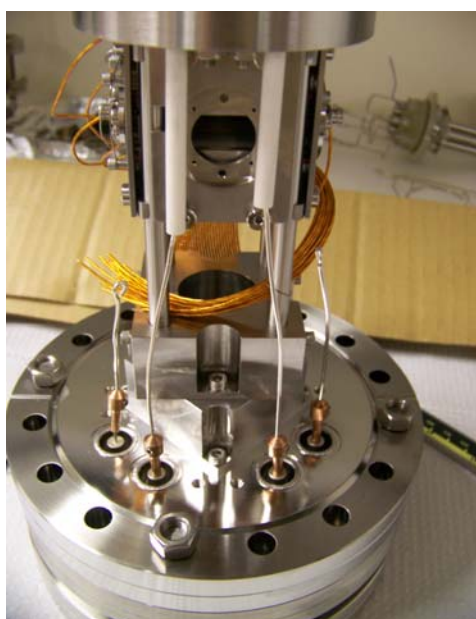
0.125

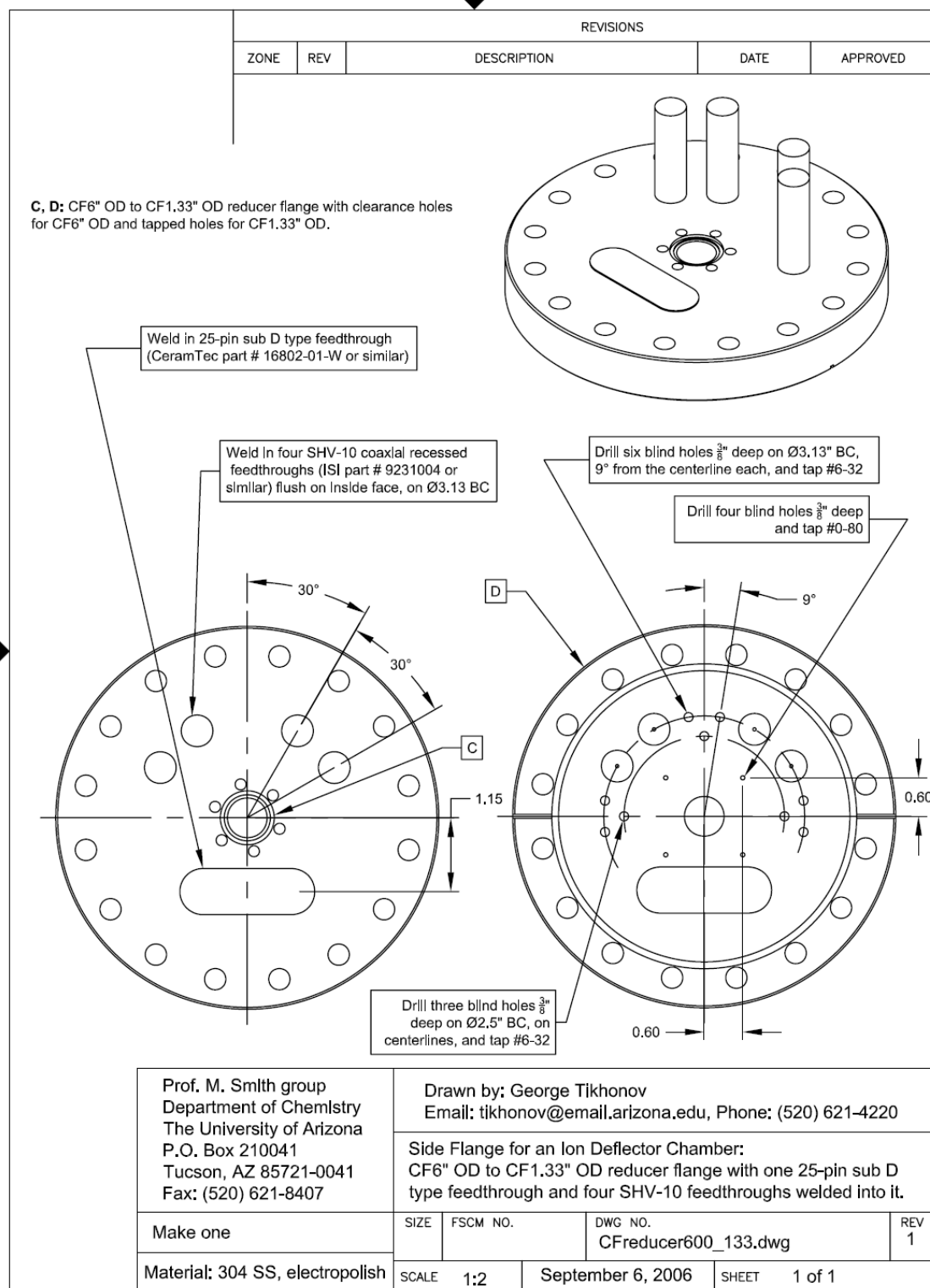
0.06

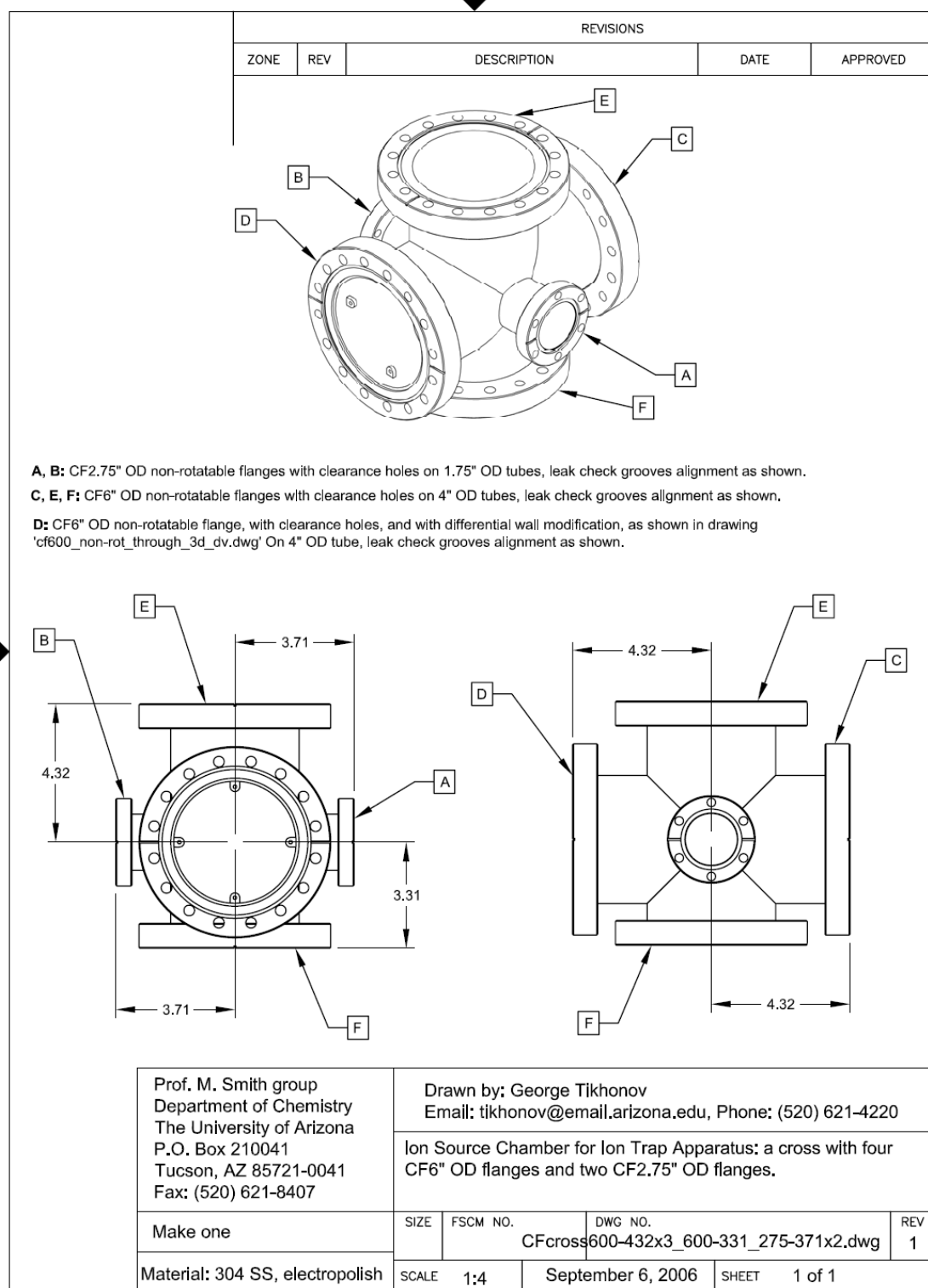
1. Tolerances for all dimensions with two digits after decimal point are ± 0.005 , unless noted otherwise.
2. Tolerances for all dimensions with three digits after decimal point are ± 0.001 , unless noted otherwise.
3. Remove sharp edges left after cutting.
4. Finish: as supplied, scotchbrite.

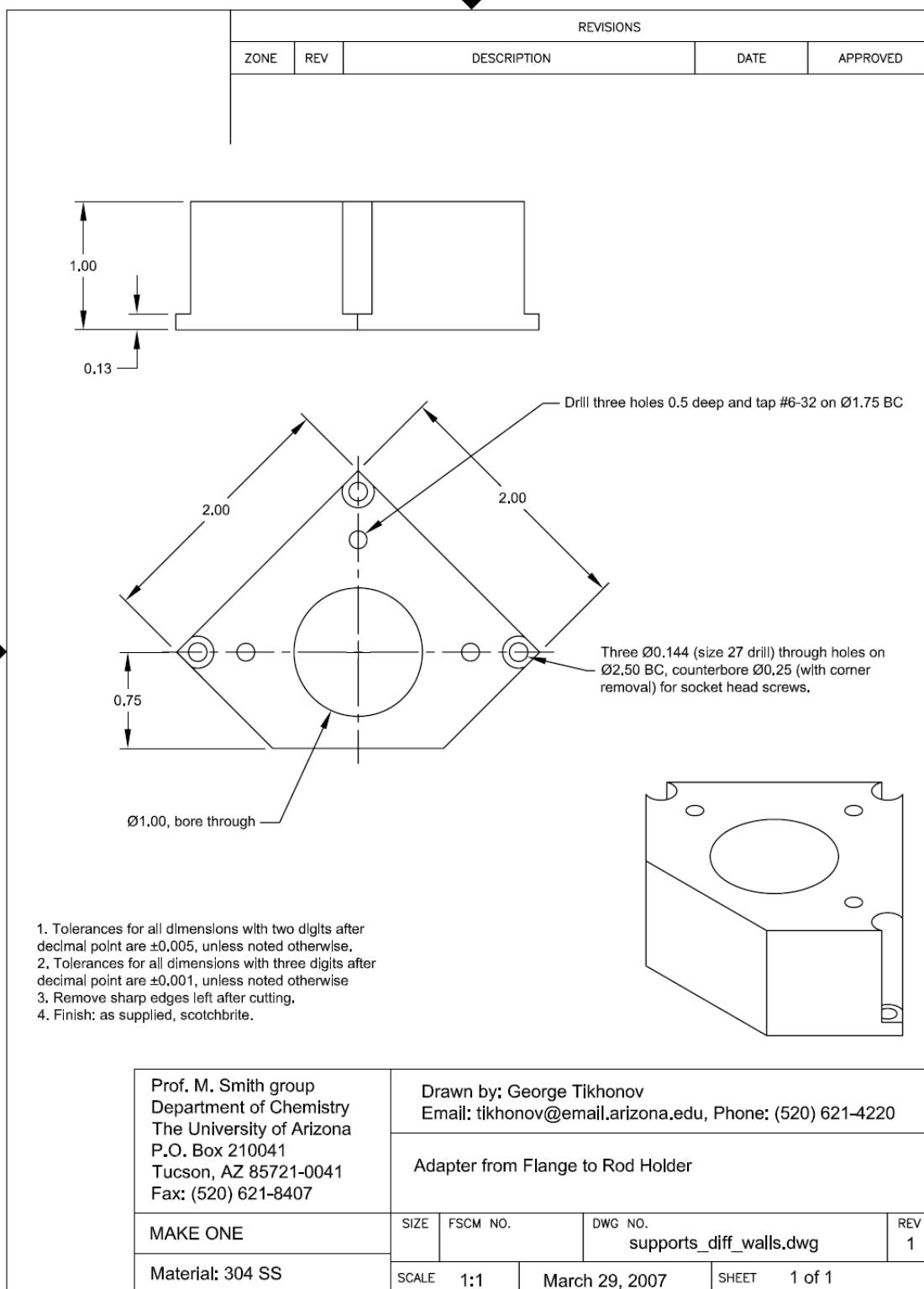
Prof. M. Smith group Department of Chemistry The University of Arizona P.O. Box 210041 Tucson, AZ 85721-0041 Fax: (520) 621-8407	Drawn by: George Tikhonov Email: tlkhonov@email.arizona.edu , Phone: (520) 621-4220		
	Ion optics lens element, $+1\frac{1}{8}$, $-1\frac{1}{8}$		
MAKE TWO	SIZE	FSCM NO.	DWG NO. ion_optics_lenses_2.dwg
Material: 304 SS	SCALE 2:1	March 21, 2007	SHEET 1 of 1

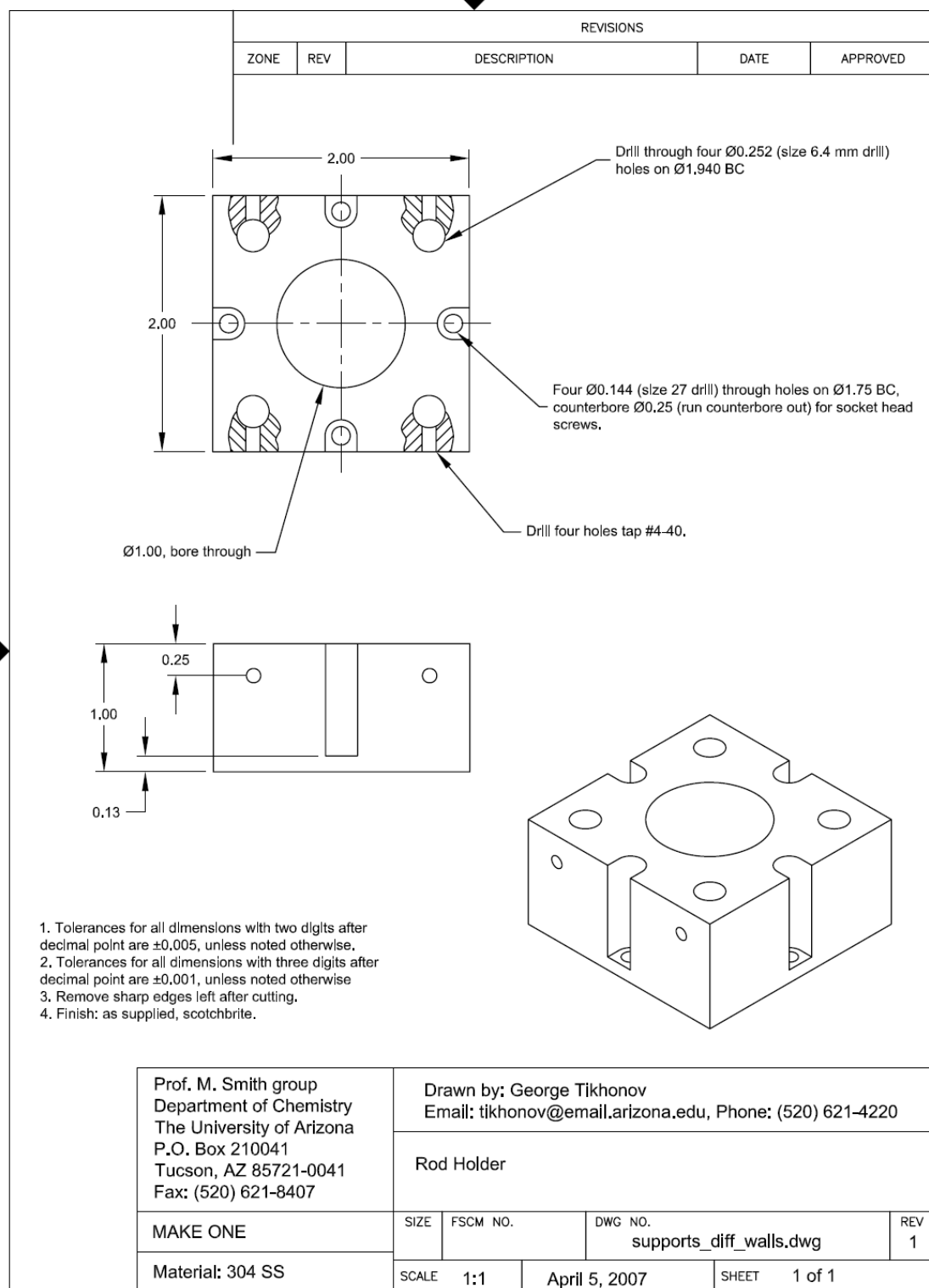
- d. Side flange of ion deflector chamber, support rod and rod holder

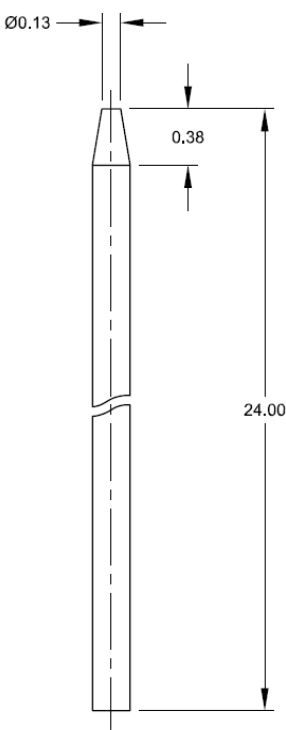






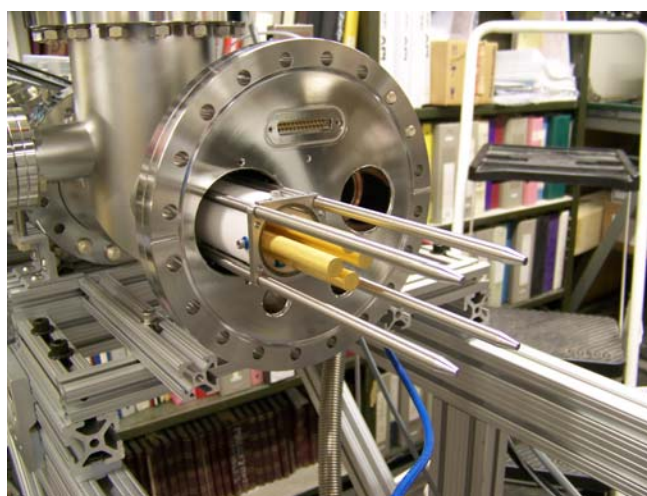




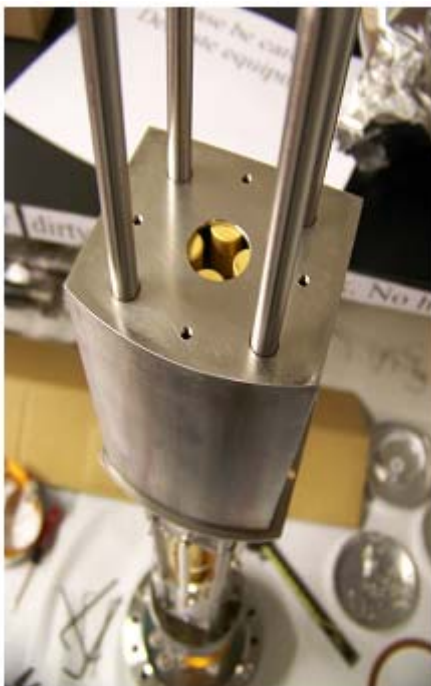
REVISIONS				
ZONE	REV	DESCRIPTION	DATE	APPROVED
<div style="display: flex; justify-content: space-between;"> <div style="width: 40%;">  </div> <div style="width: 55%;"> <ol style="list-style-type: none"> 1. Tolerances for all dimensions with two digits after decimal point are ± 0.005, unless noted otherwise. 2. Tolerances for all dimensions with three digits after decimal point are ± 0.001, unless noted otherwise. 3. Remove sharp edges left after cutting. 4. Finish: as supplied. </div> </div>				
Prof. M. Smith group Department of Chemistry The University of Arizona P.O. Box 210041 Tucson, AZ 85721-0041 Fax: (520) 621-8407		Drawn by: George Tikhonov Email: tikhonov@email.arizona.edu, Phone: (520) 621-4220 Main Support Rod for Ion Guide - modification of supplied precision-ground Ø0.250 304 SS rod (McMaster part # 8934K13)		
MODIFY FOUR		SIZE	FSCM NO.	DWG NO. support_rods.dwg
Material: 304 SS		SCALE 1:1	April 6, 2007	REV 1
		SHEET	1 of 1	

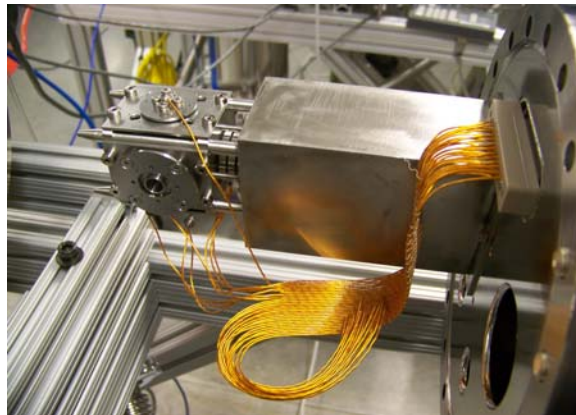
- (3) Quadrupole ion guide/mass selector elements
a. Quadrupole ion guide/mass selector

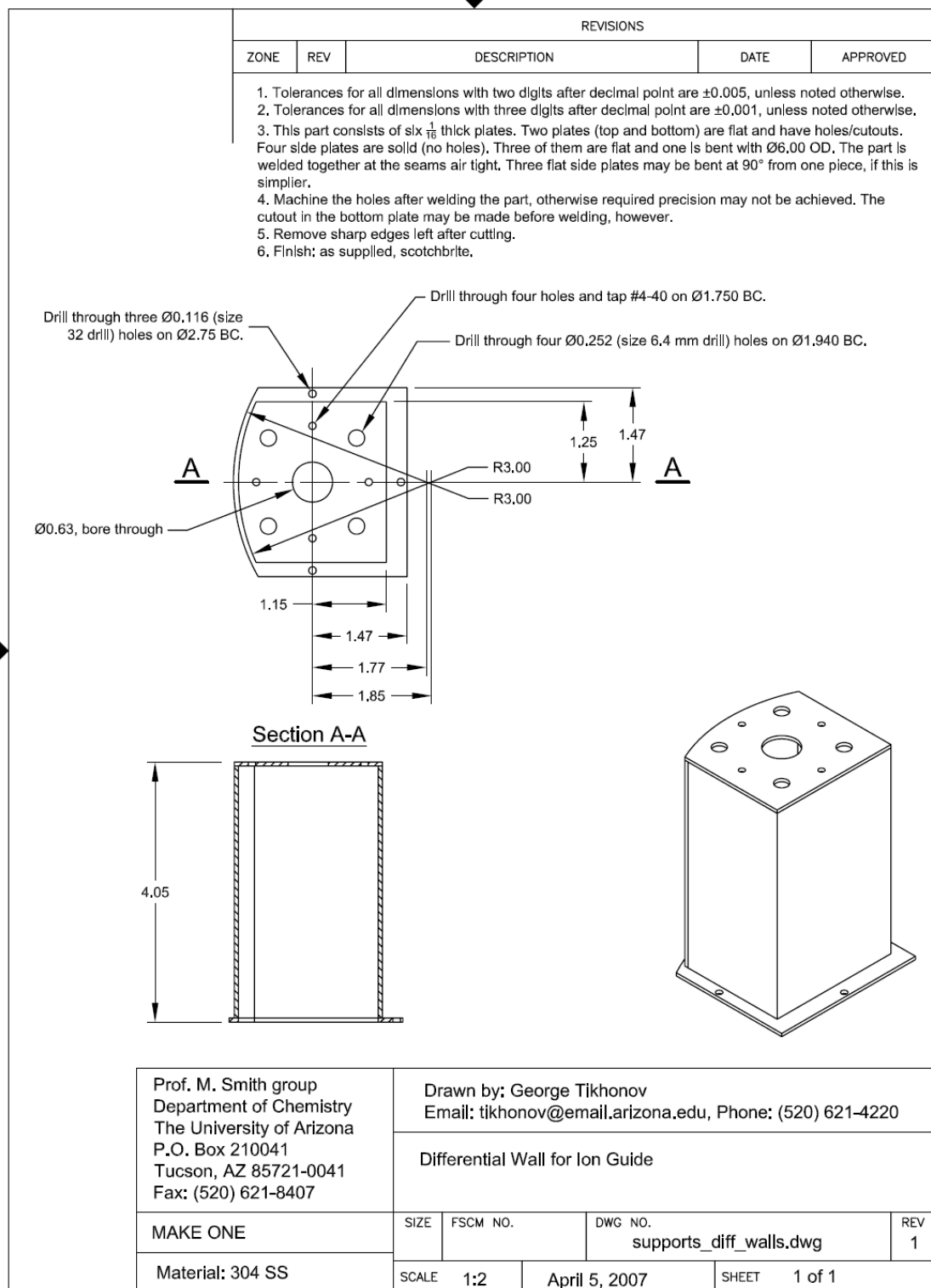


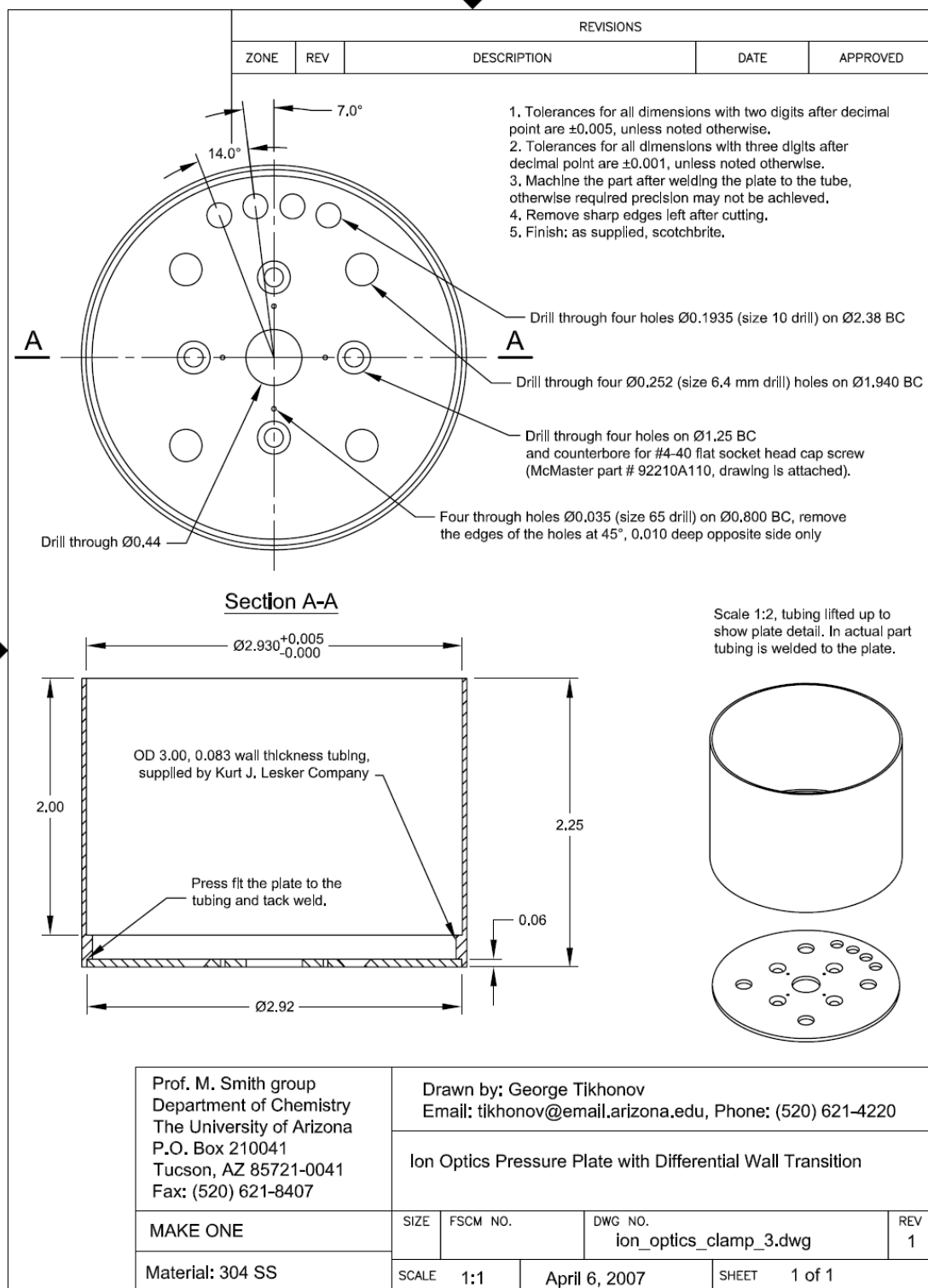


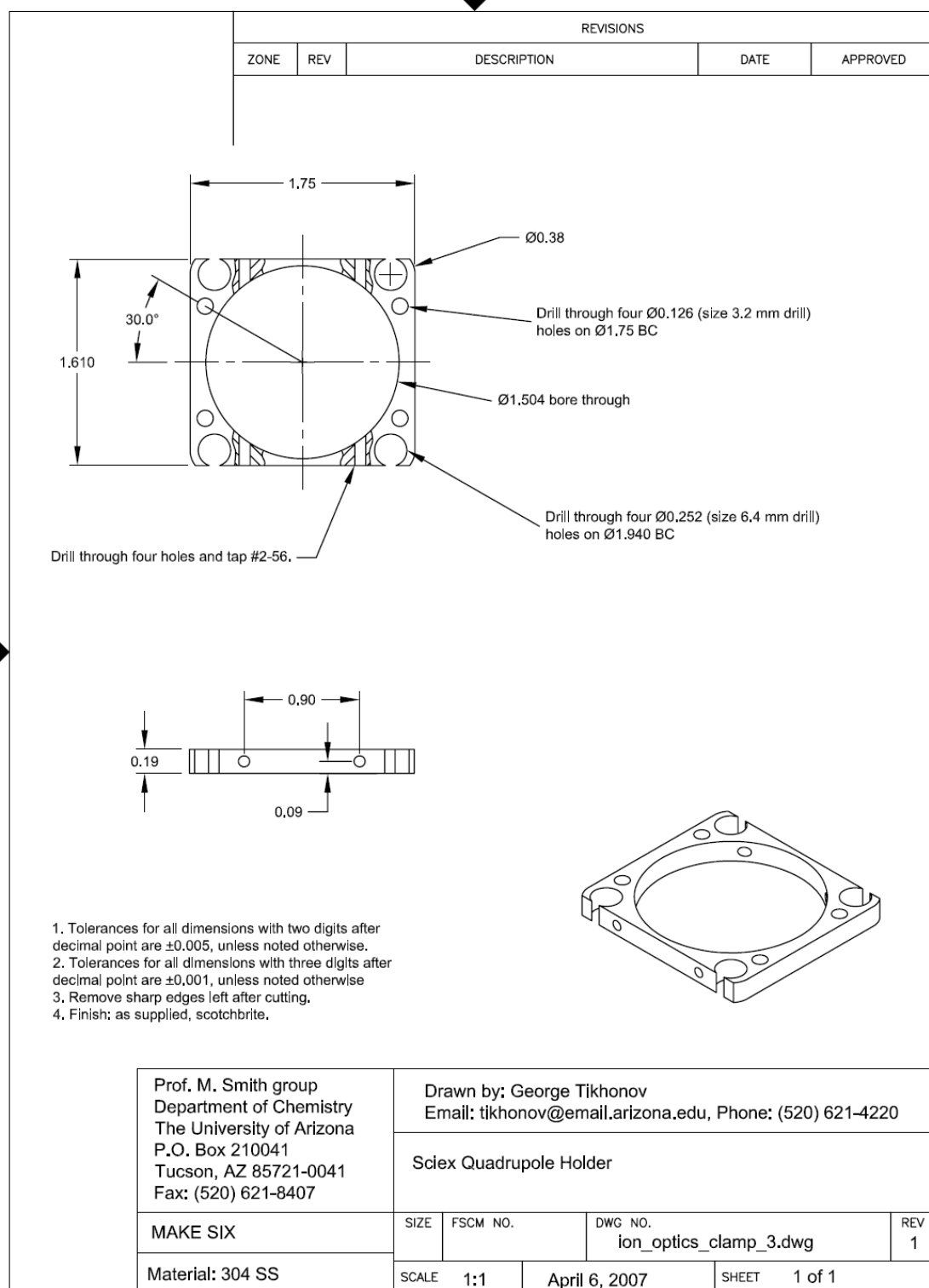
b. quadrupole differential wall and sciex quadrupole holder



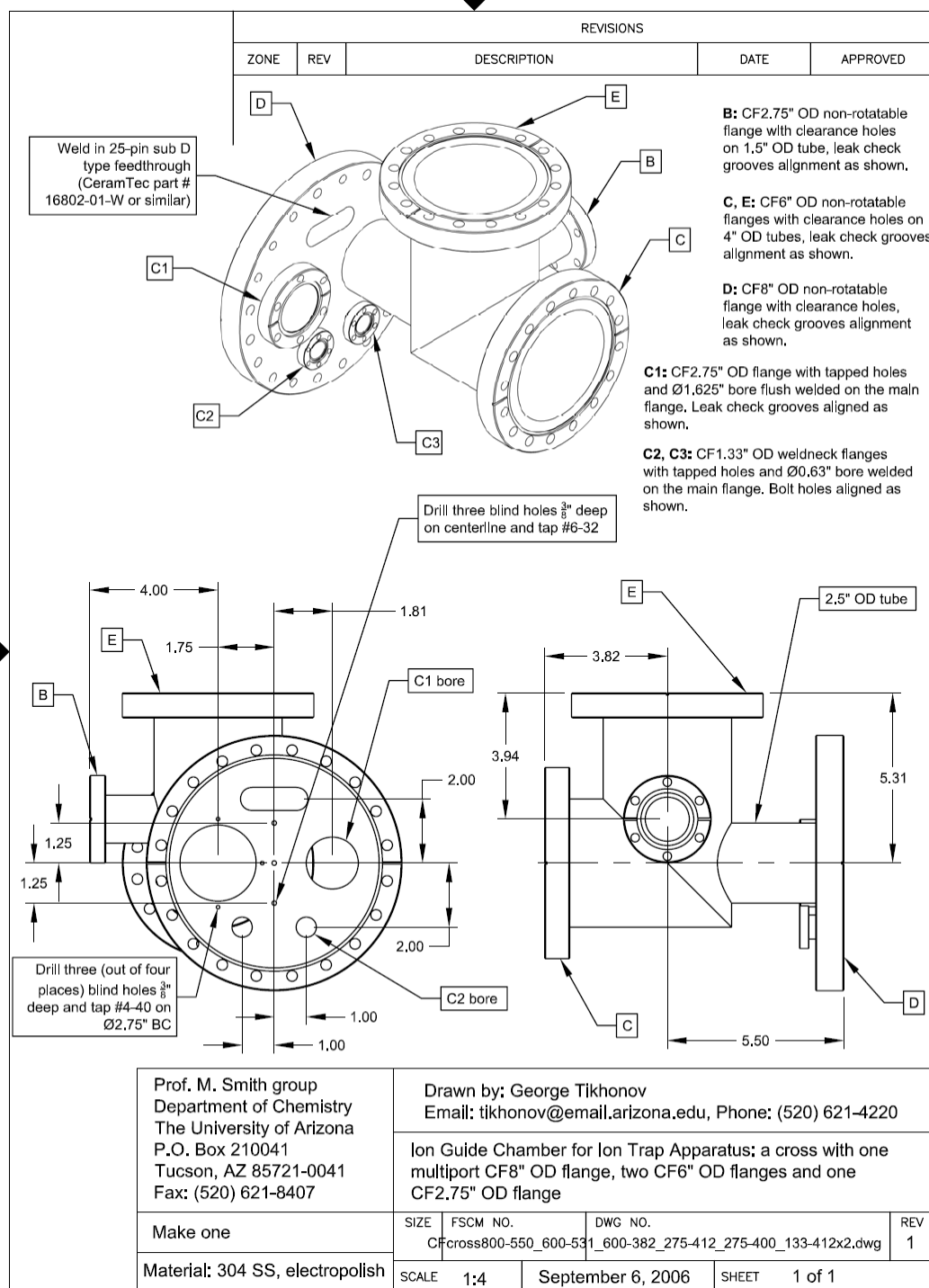






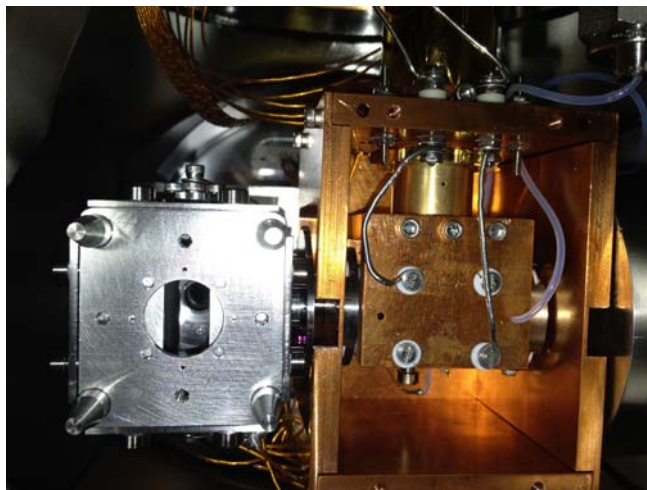
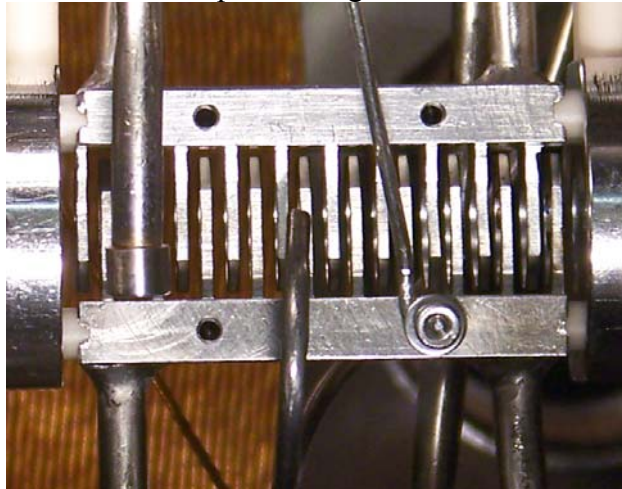


c. Chamber of quadrupole ion guide/mass selector

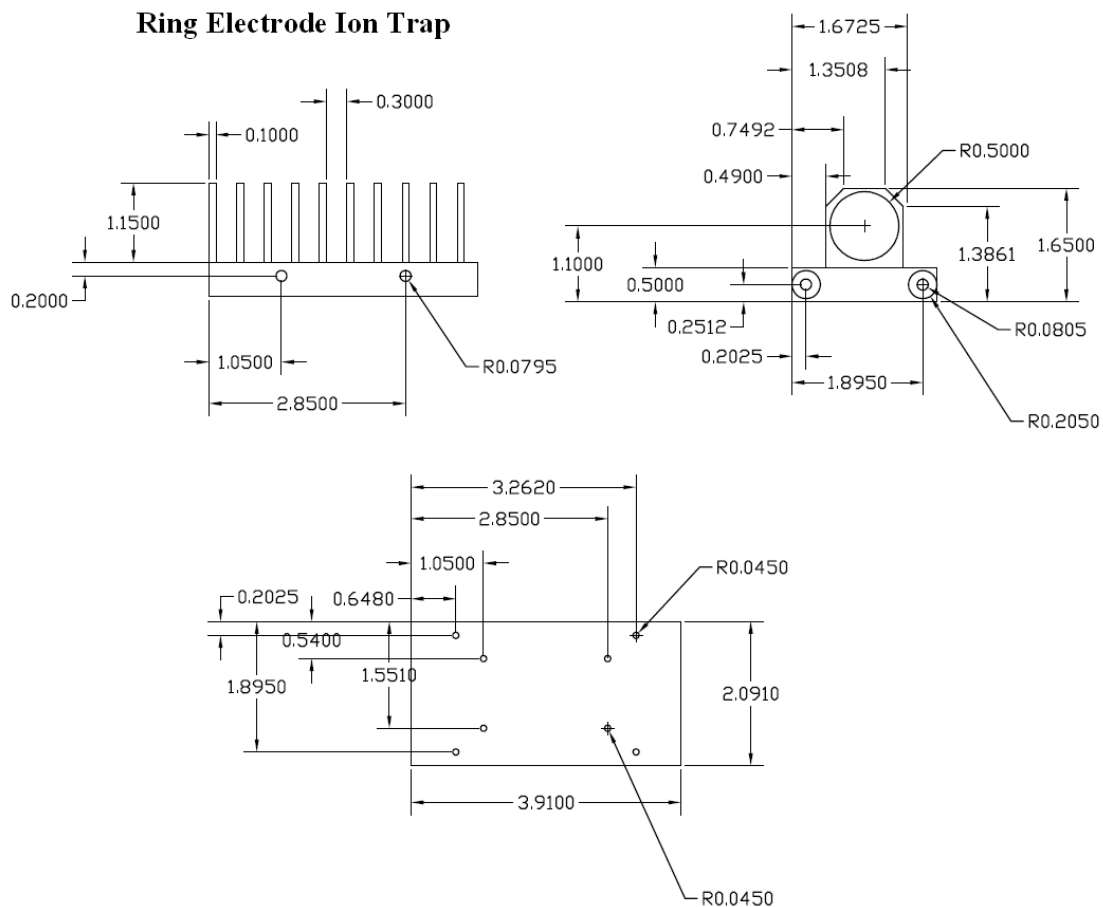


(4) Ring electrode ion trap

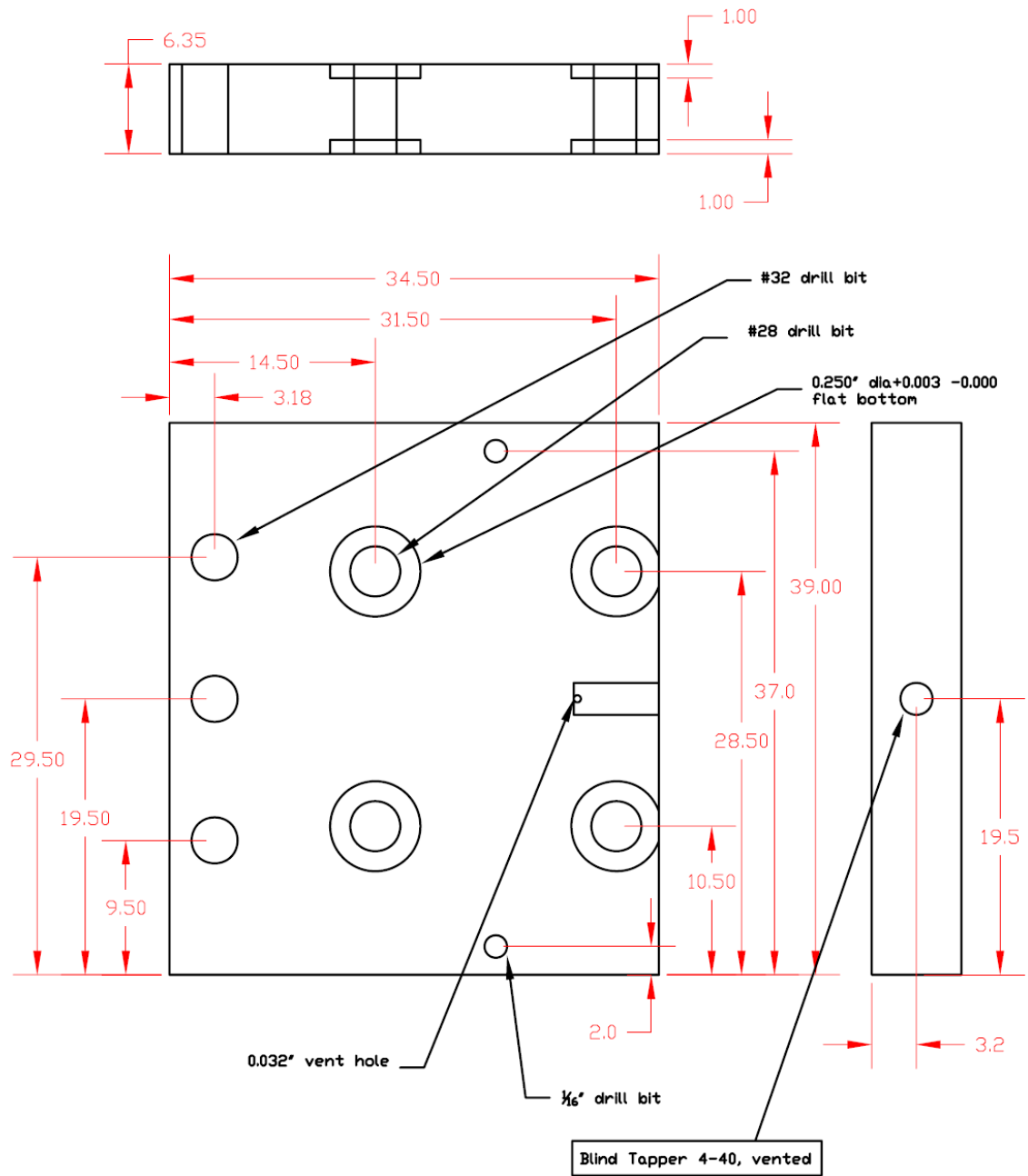
a. Ring electrode and trap mounting walls



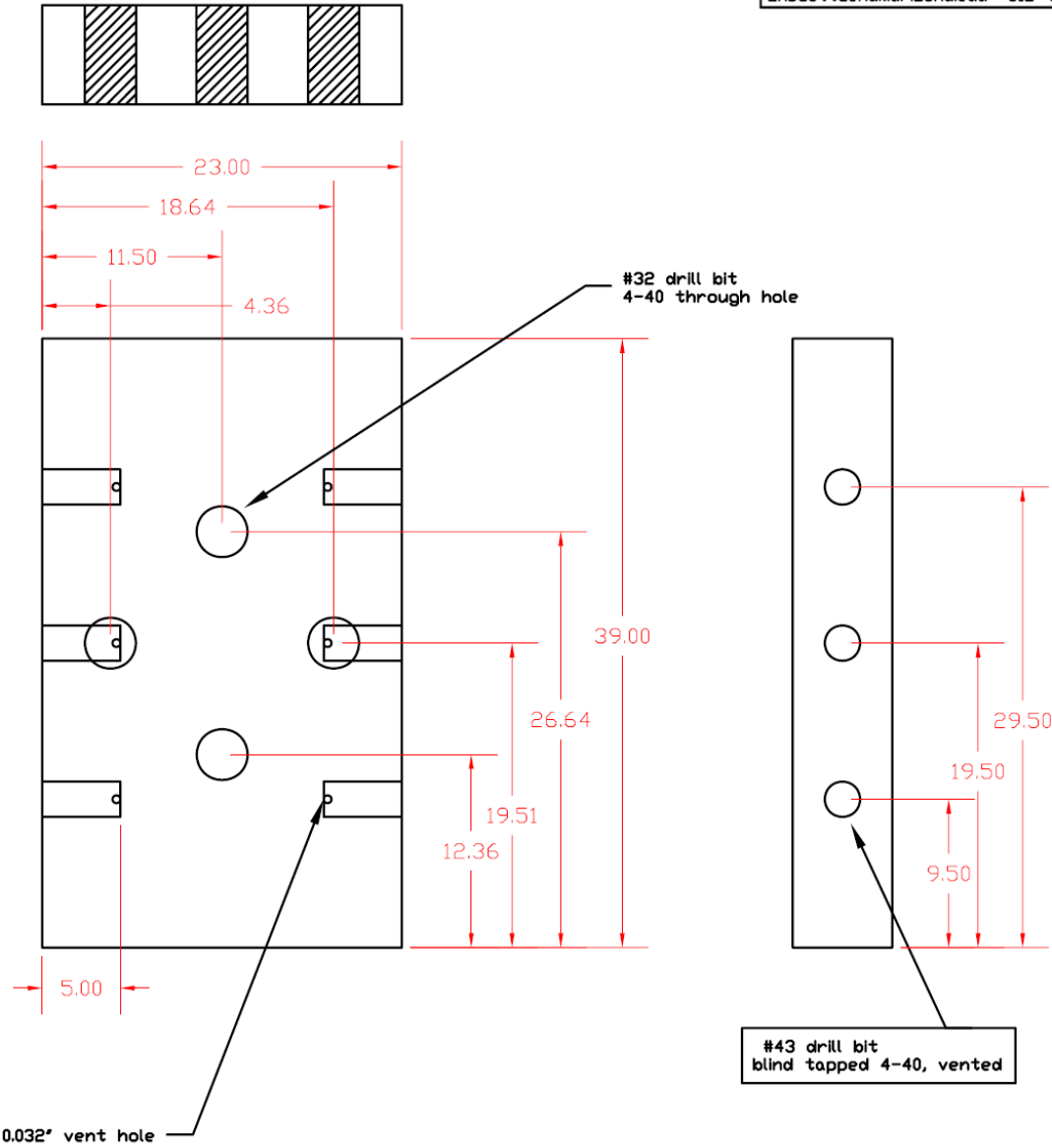
Ring Electrode Ion Trap

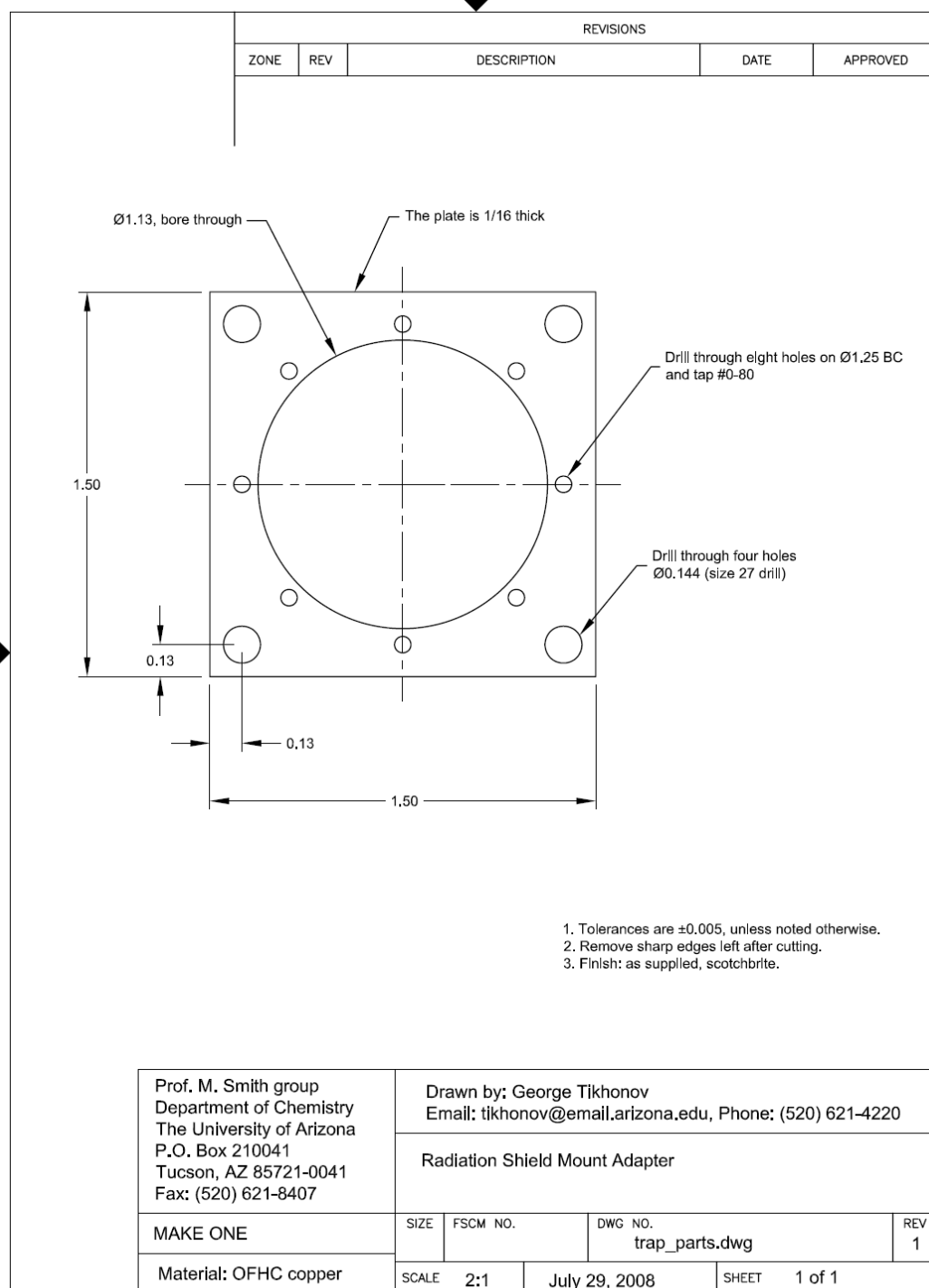


University of Arizona
Zachary Scott Smith Group
3/6/09 mounting walls for RET
1/4" OFHC copper
all measurement in metric unless specified
Uty: 2 tolerance:
zmscott@email.arizona.edu 812-499-1693

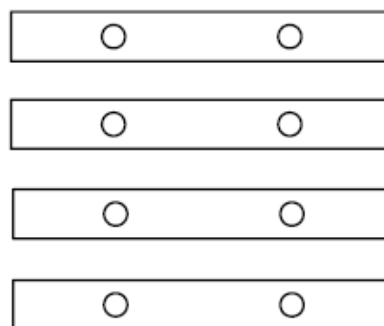
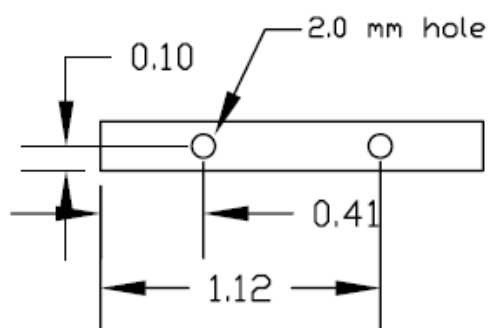


University of Arizona
Zachary Scott Smith Group
3/6/09 base plate for RET
1/4" OFHC copper
all measurement in mm unless specified
Uty: 1
zmscott@email.arizona.edu 812-499-1693

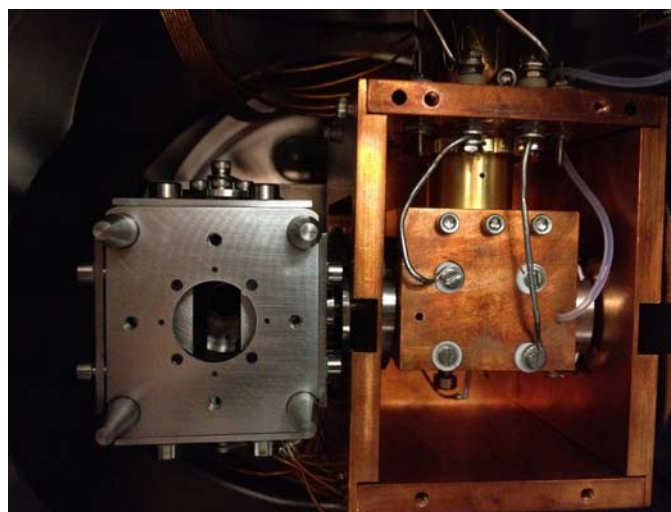
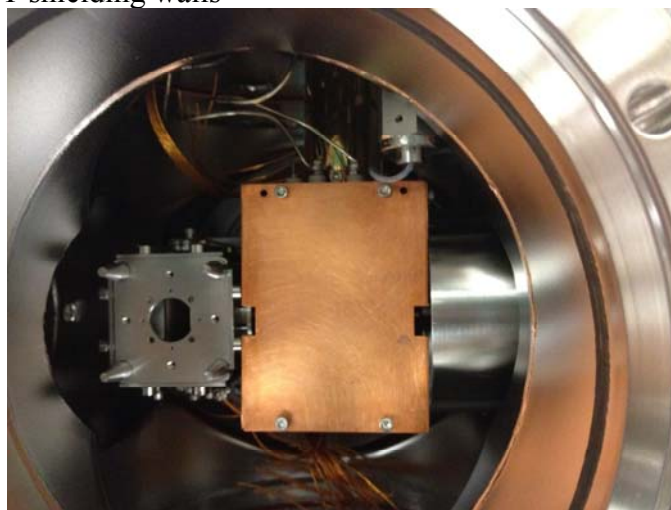




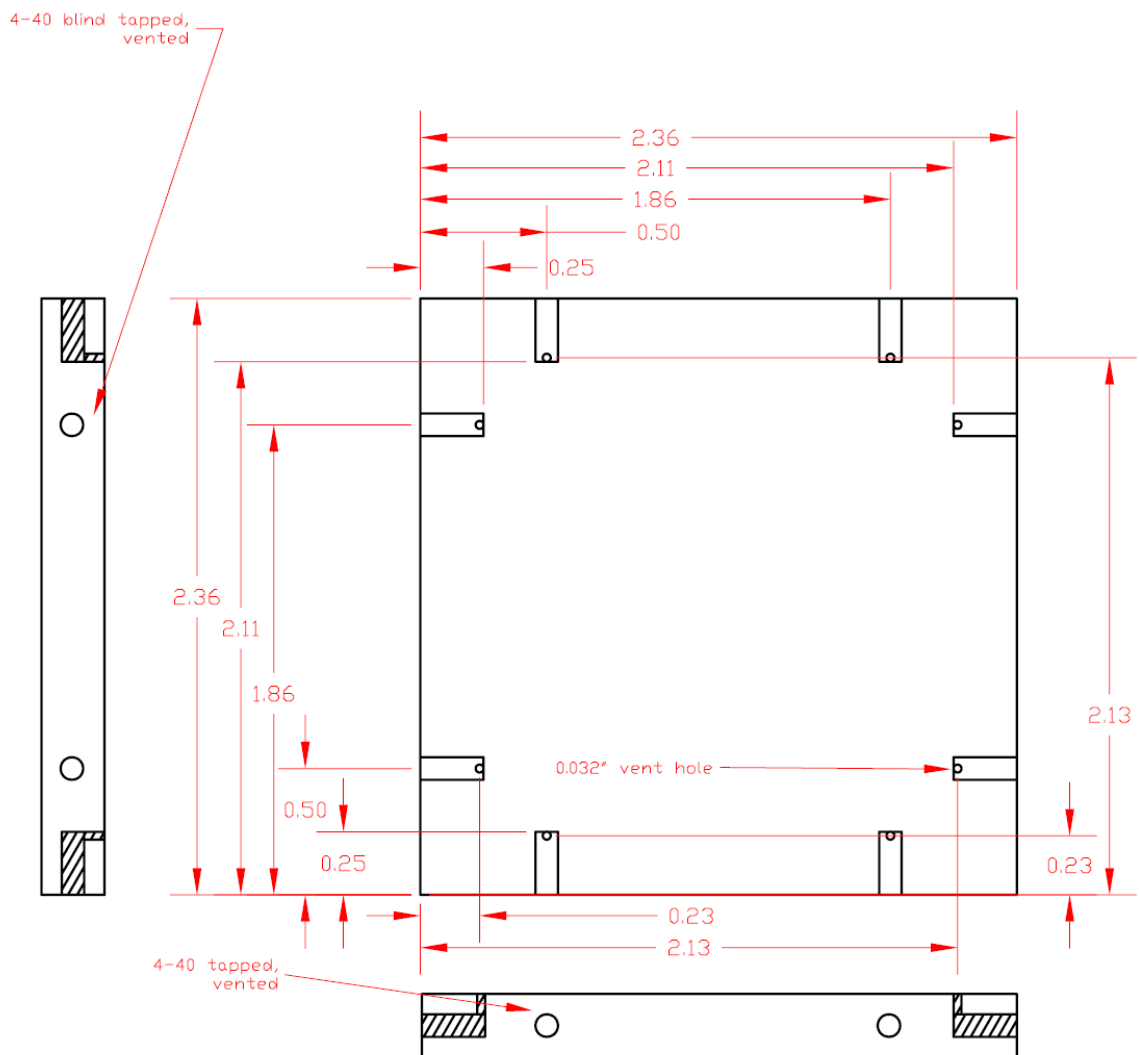
Sapphire Plate for RET



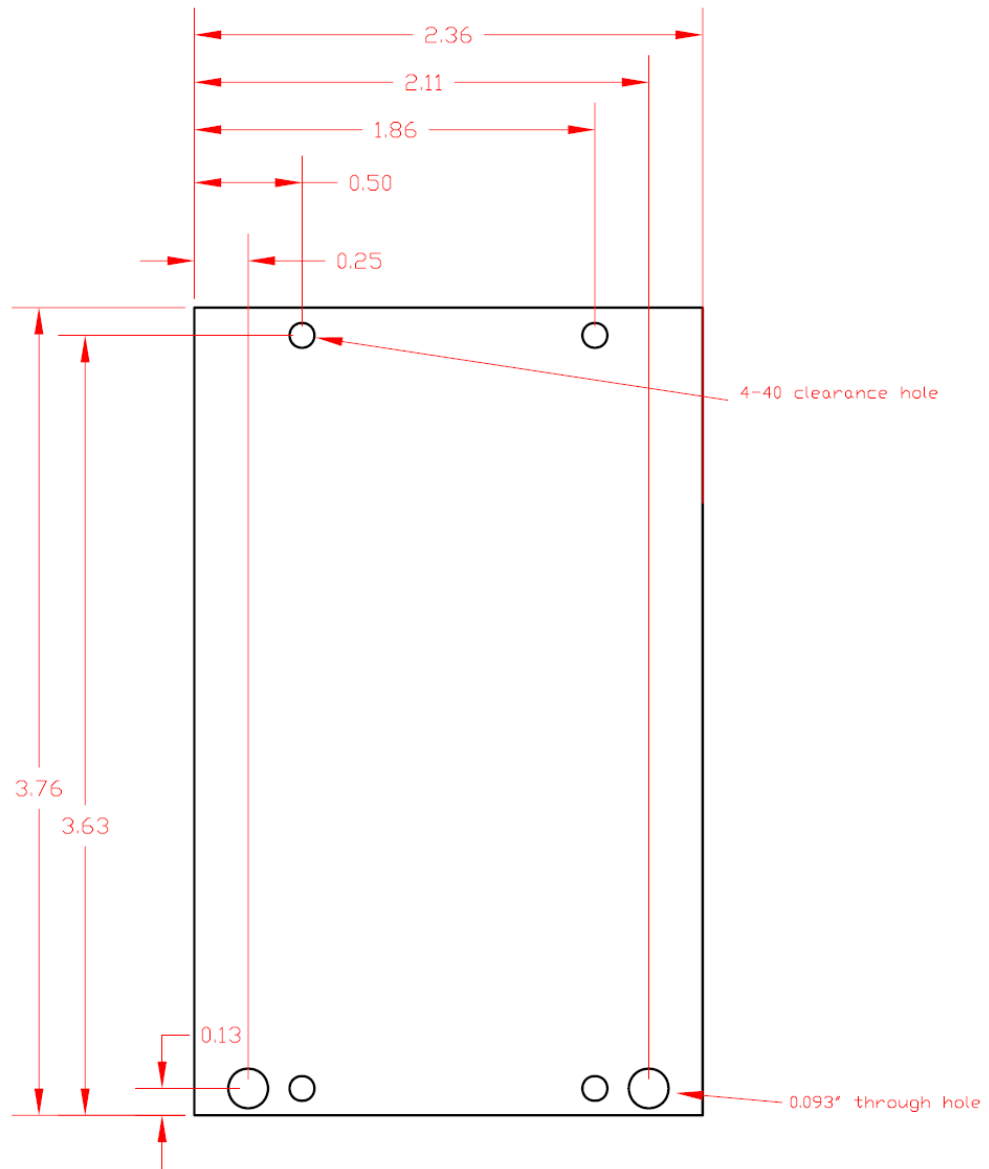
b. RET shielding walls



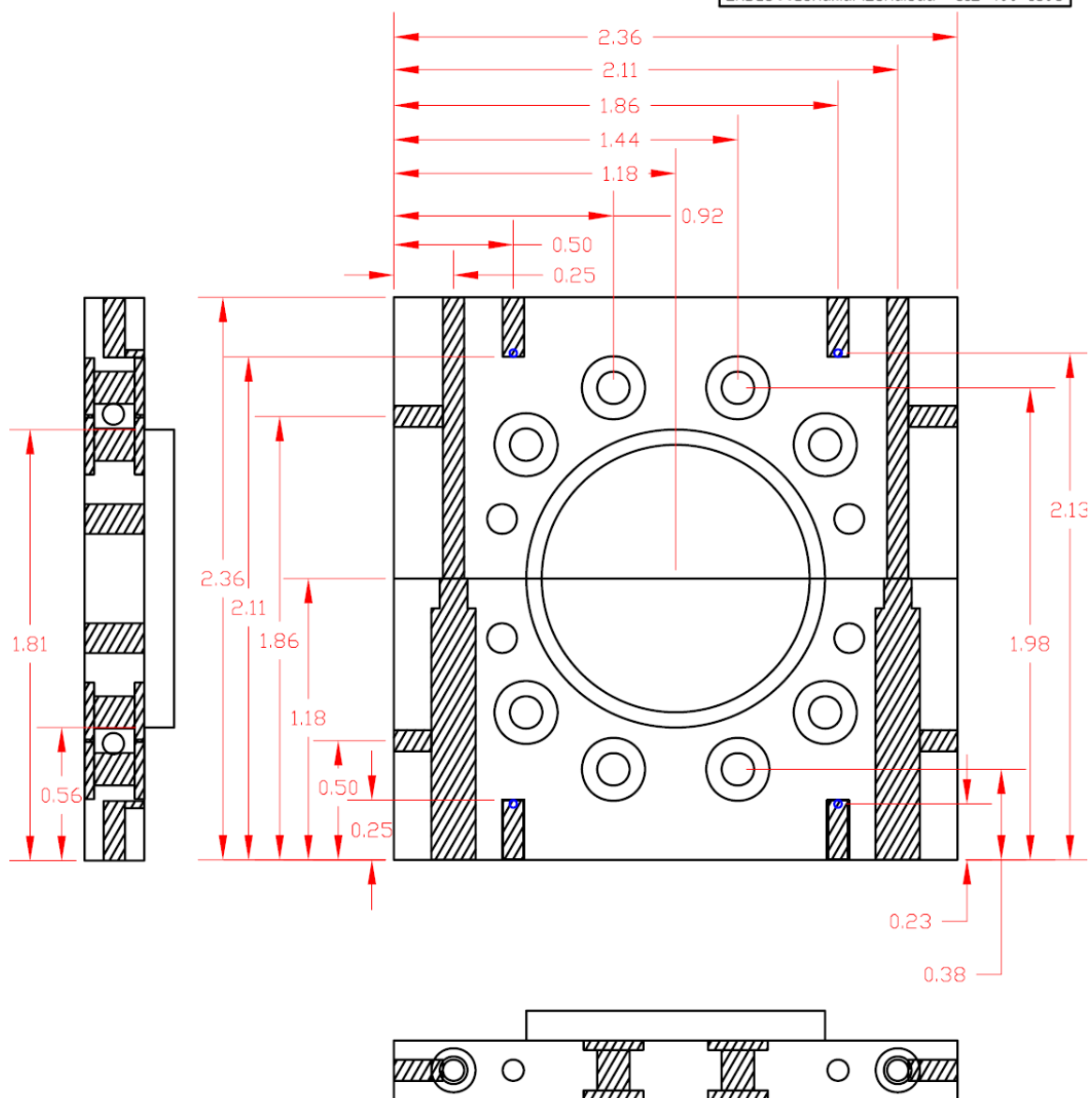
University of Arizona
Zachary Scott Smith Group
3/8/09 bottom plate for trap shield
0.250" DFHC copper
all measurement in inch unless specified
Uty: 1
zmsscott@email.arizona.edu 812-499-1693



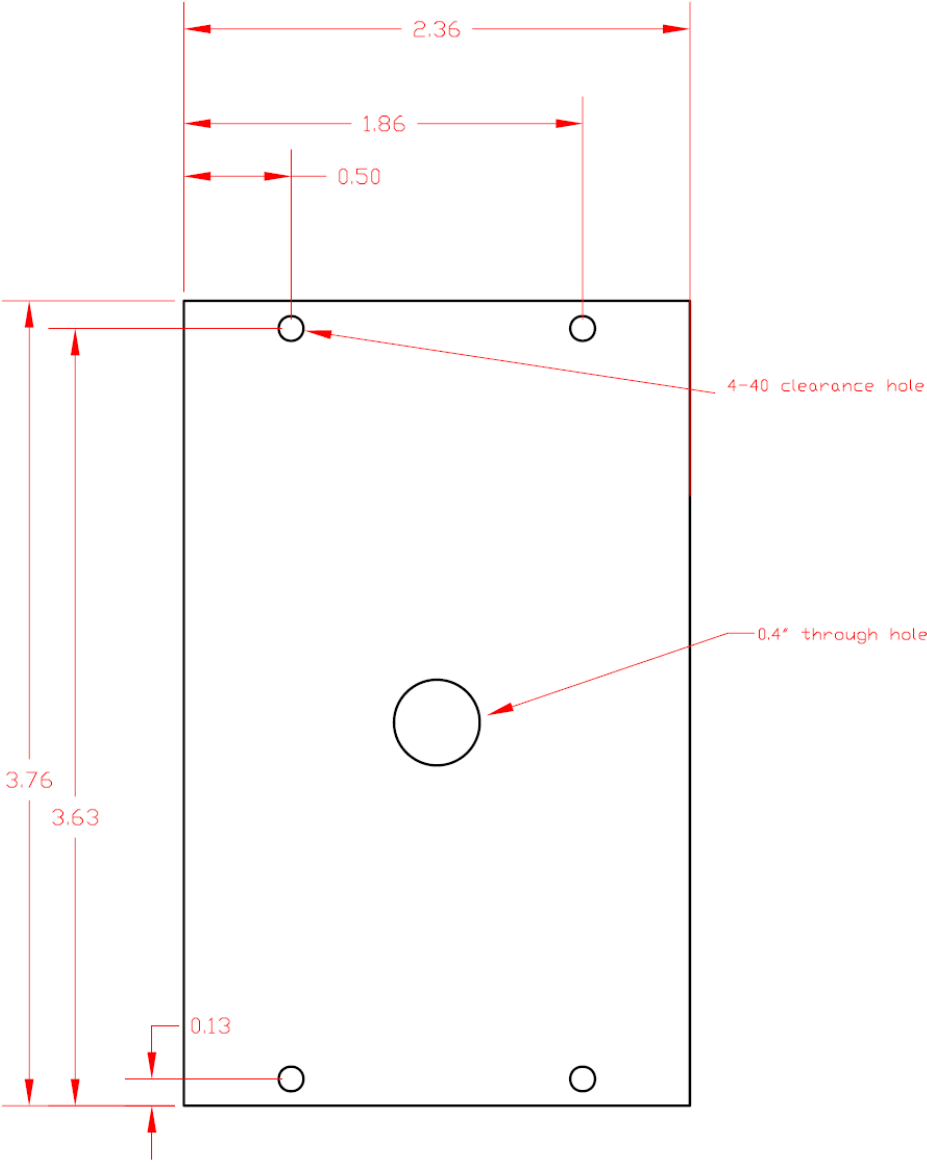
University of Arizona
Zachary Scott Smith Group
3/8/09 off axis wall for trap shield
0.032" OFHC copper
all measurement in inch unless specified
Uty: 2
zmsscott@email.arizona.edu 812-499-1693



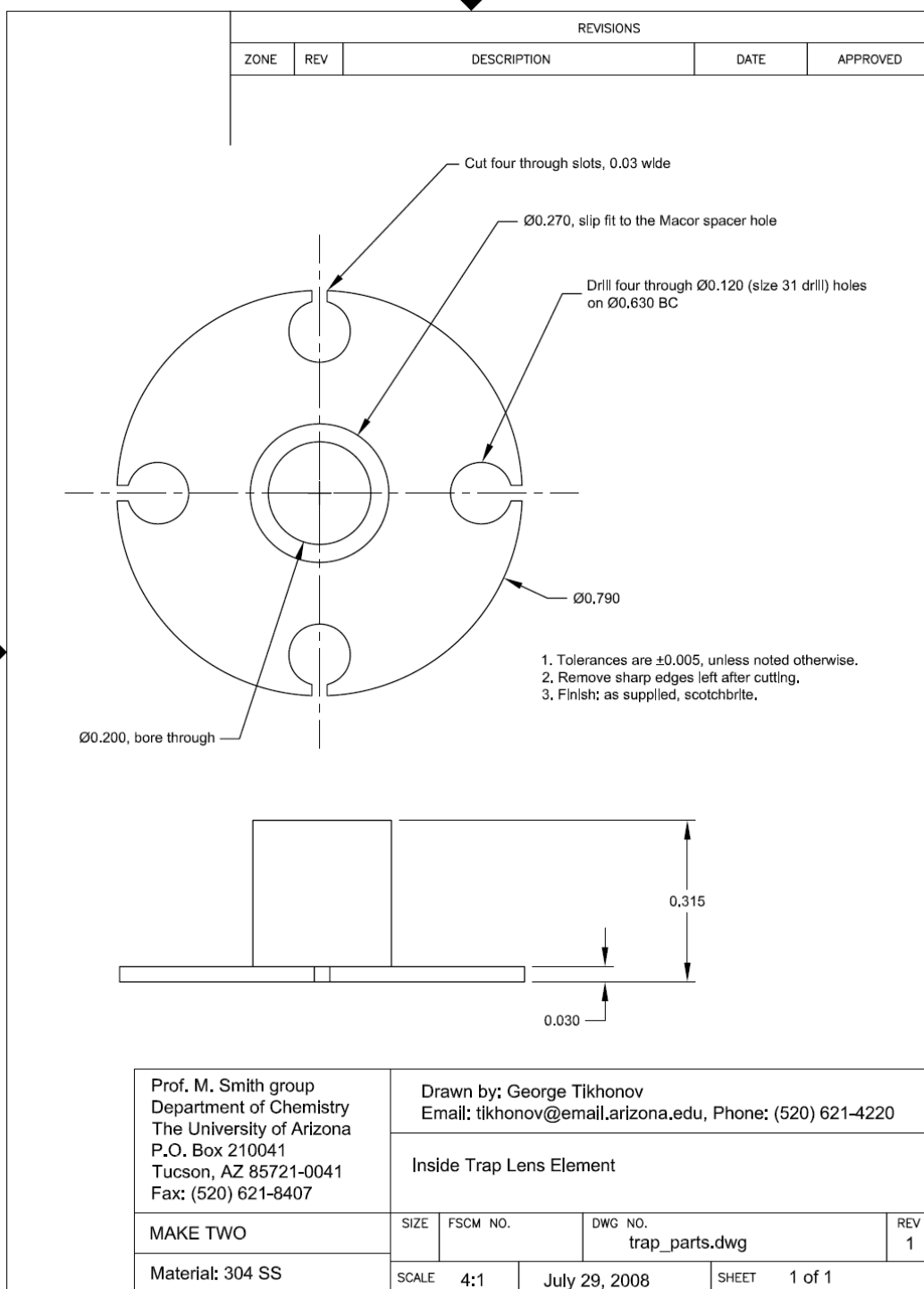
University of Arizona	
Zachary Scott	Smith Group
3/8/09 top plate for trap shield	
3/8" OFHC copper	
all measurement in inch unless specified	
Uty: 1	
zmiscott@email.arizona.edu	812-499-1693

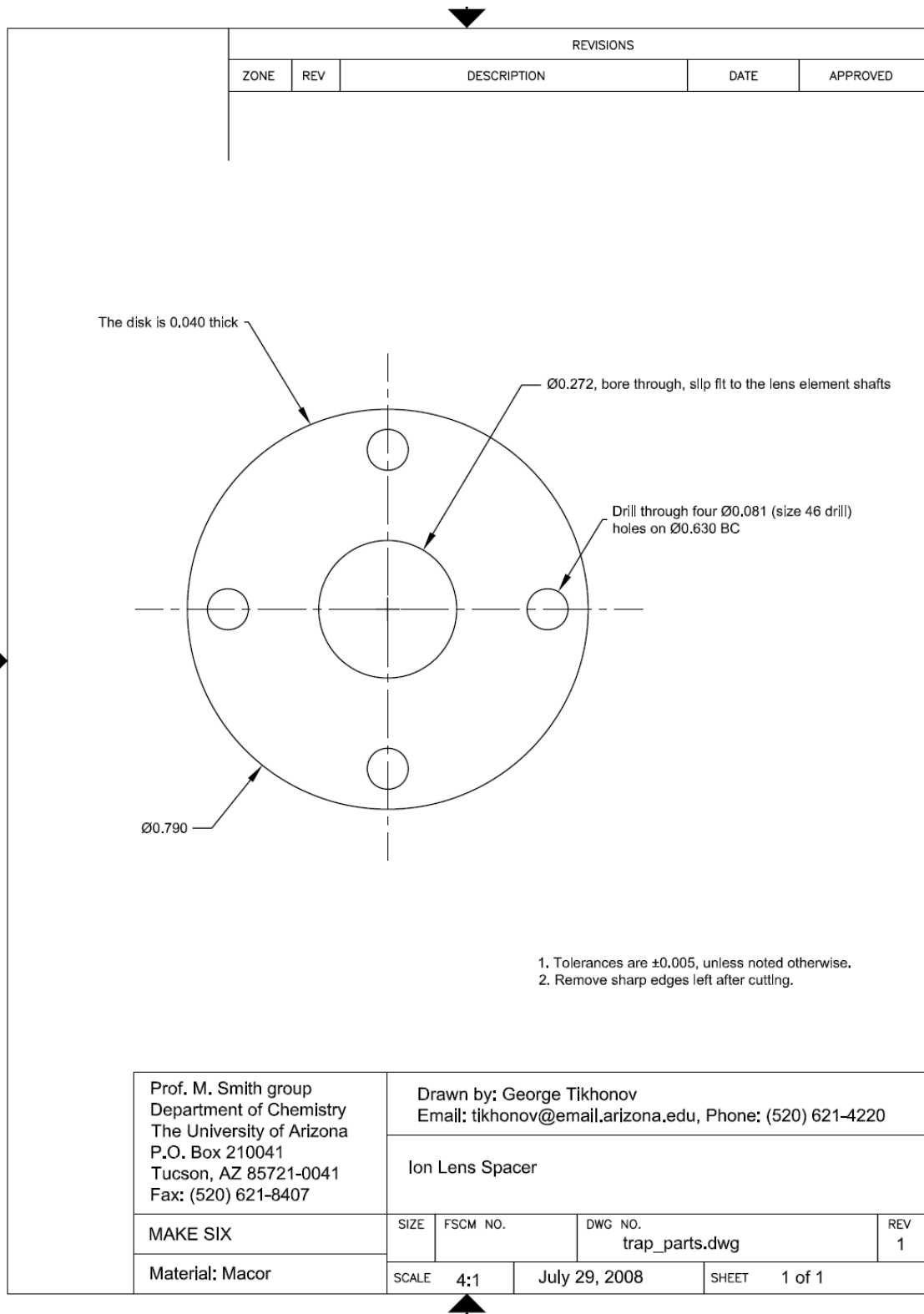


University of Arizona
Zachary Scott Smith Group
3/8/09 on axis wall for trap shield
0.032" OFHC copper
all measurement in inch unless specified
Uty: 2
zmscott@email.arizona.edu 812-499-1693

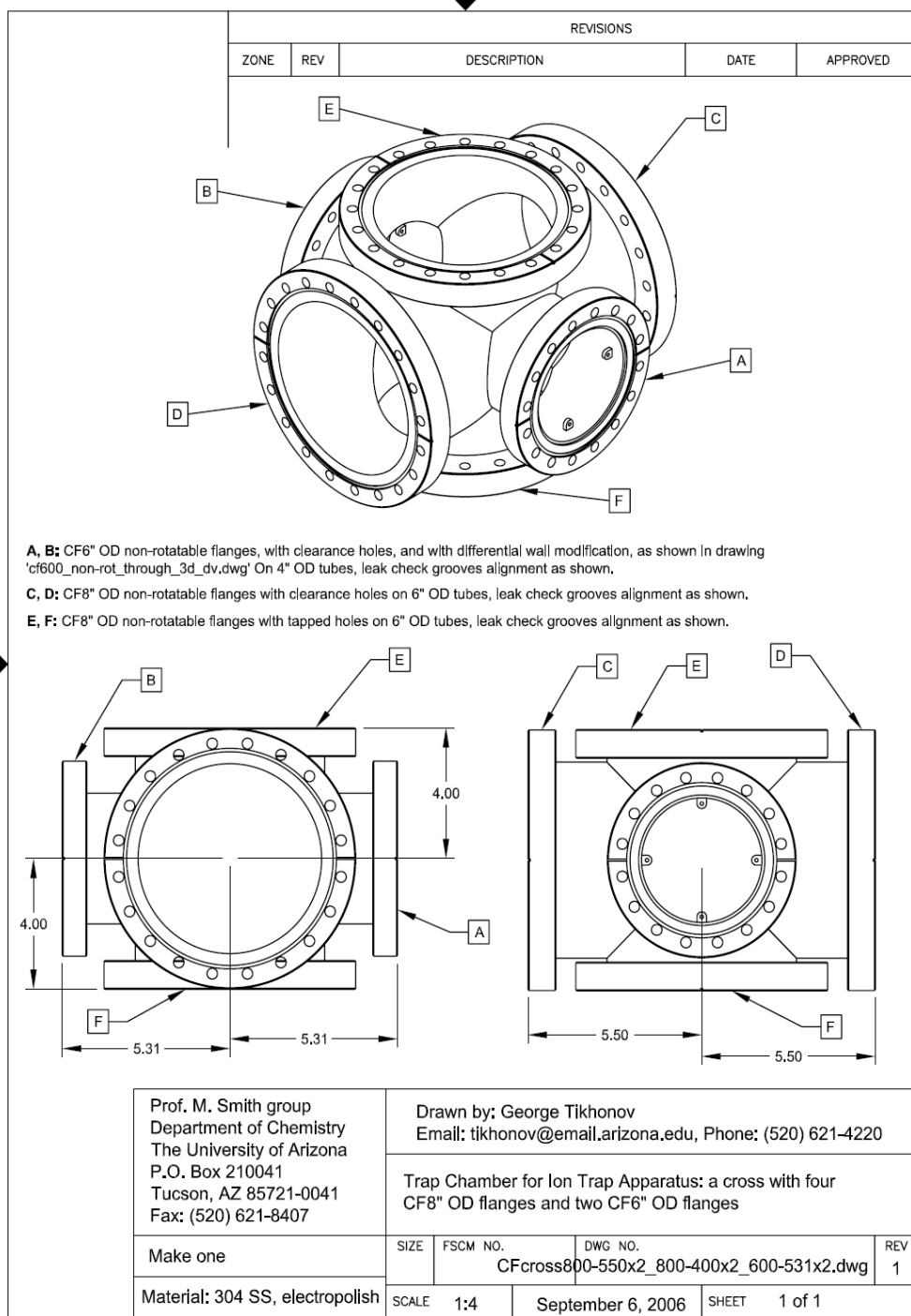


c. Ion entrance/exit lens elements



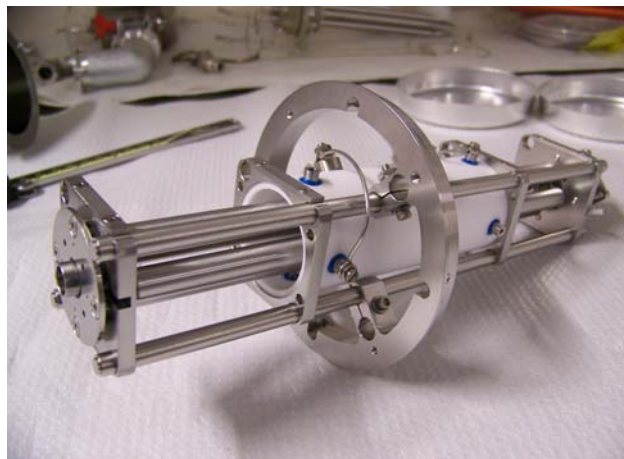
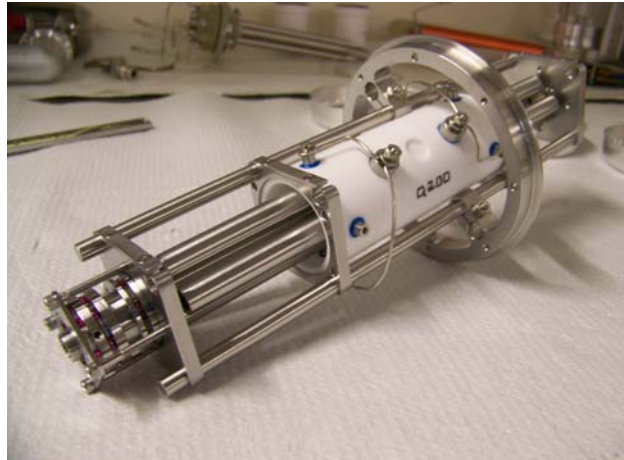


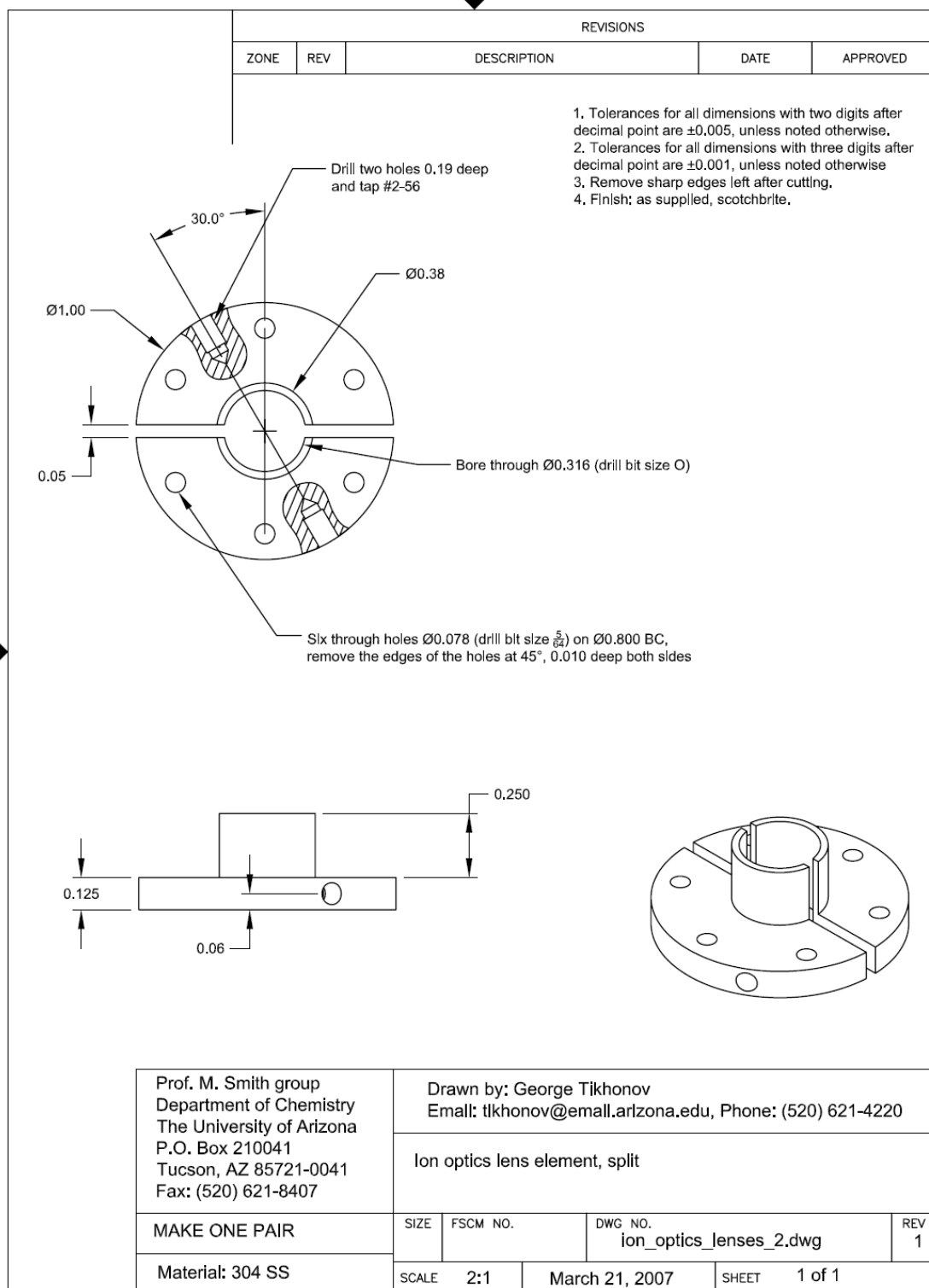
d. Trap chamber

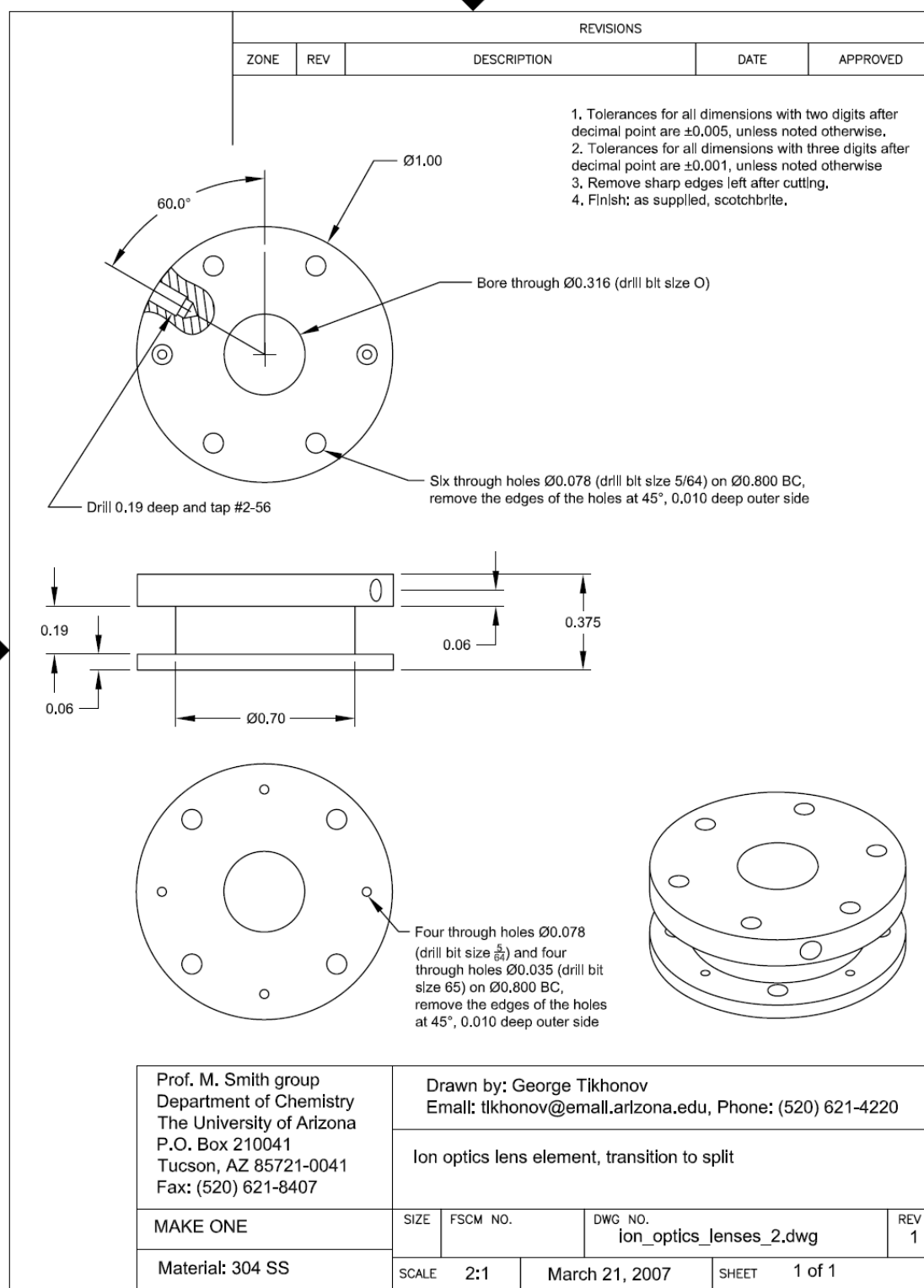


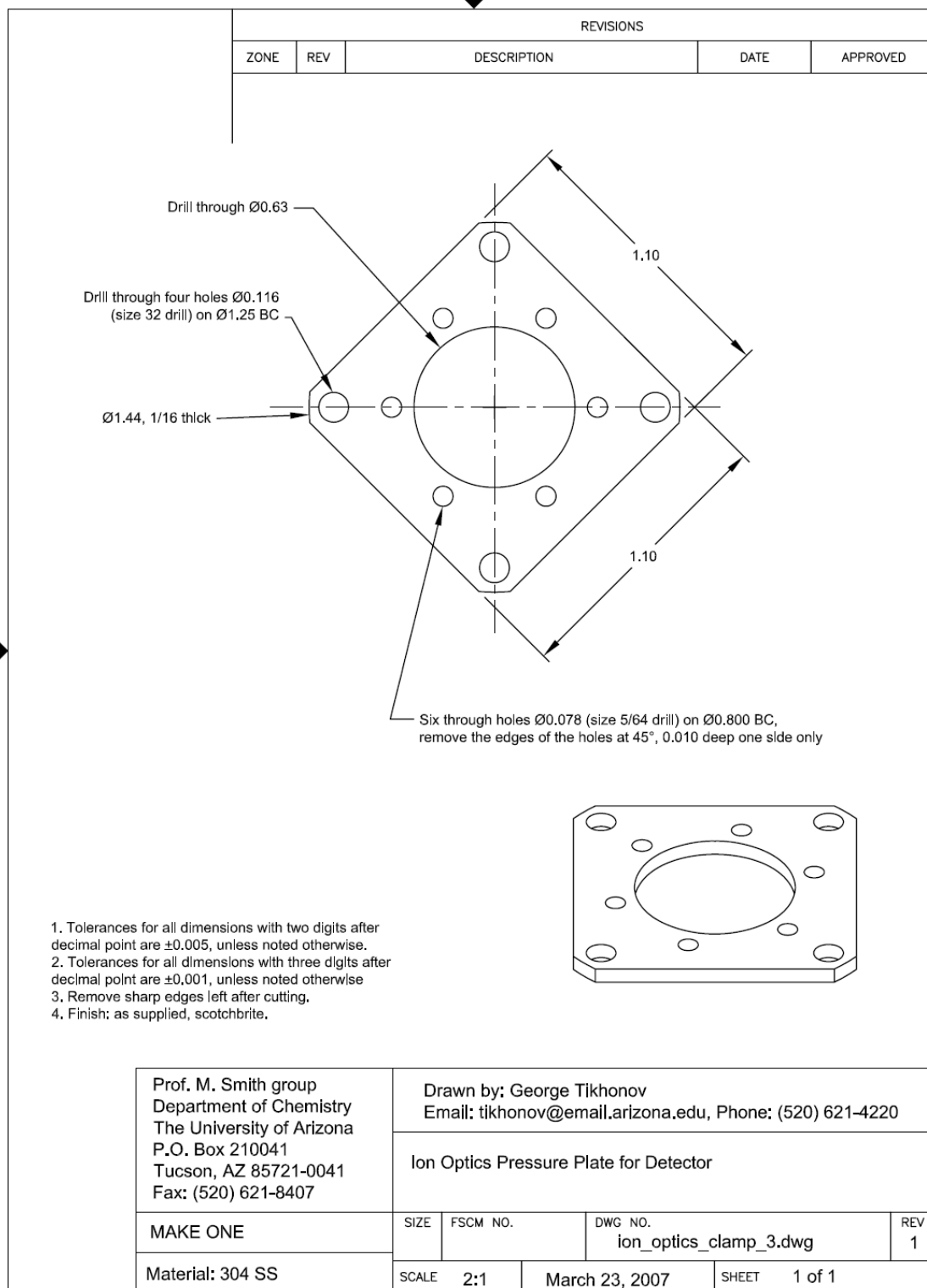
- (5) Quadrupole analyzer (Behind ion trap)
a. Quadrupole, electronic lens and support holder

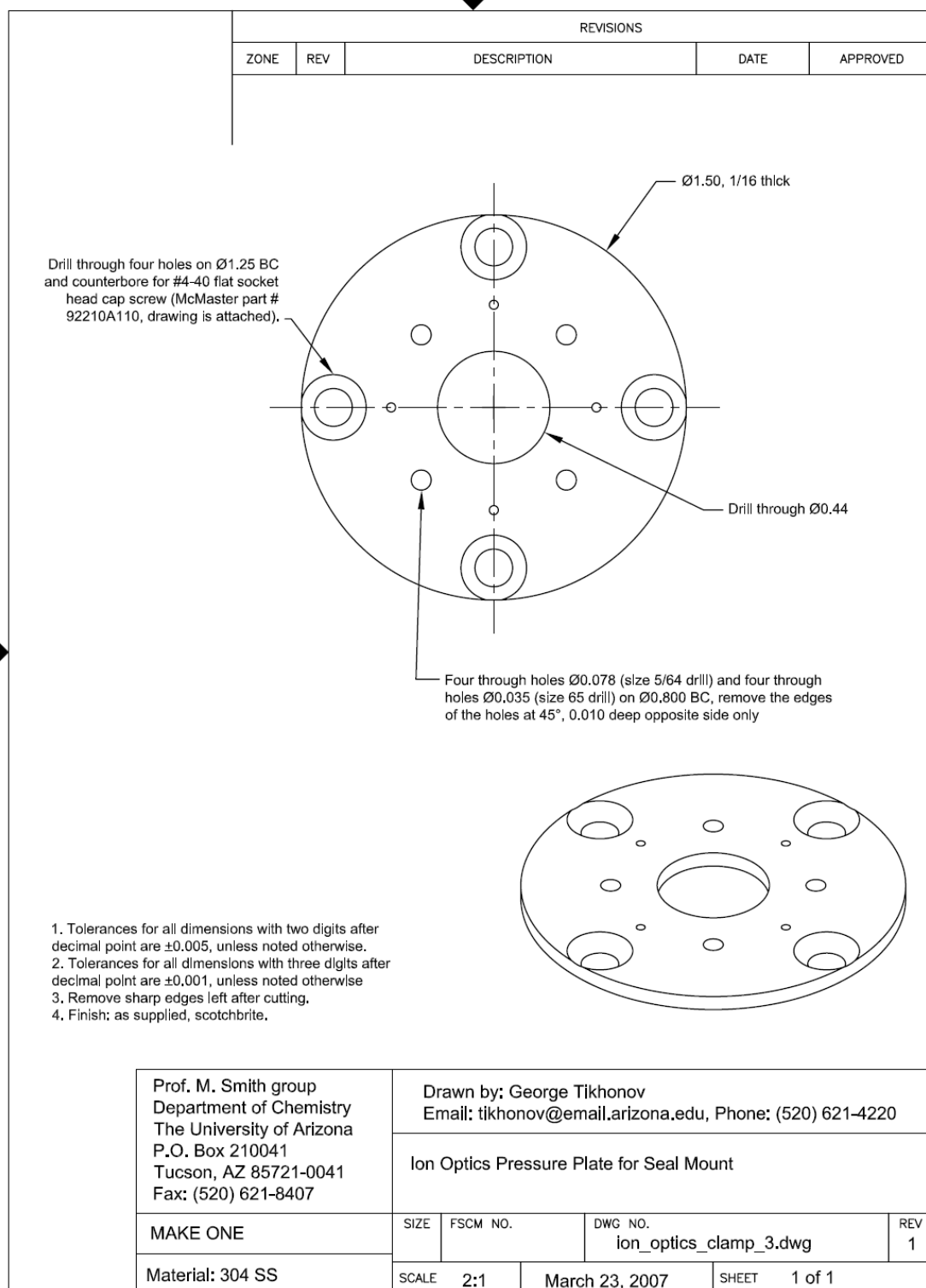


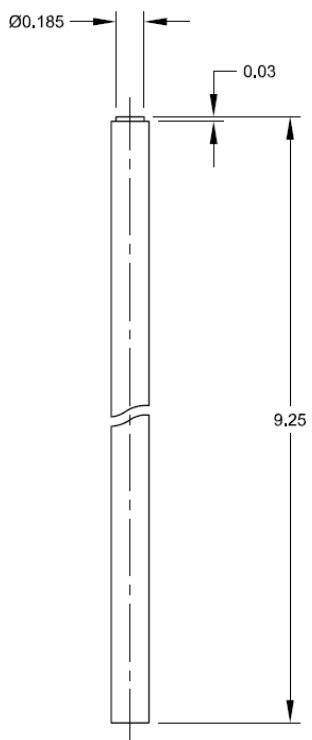
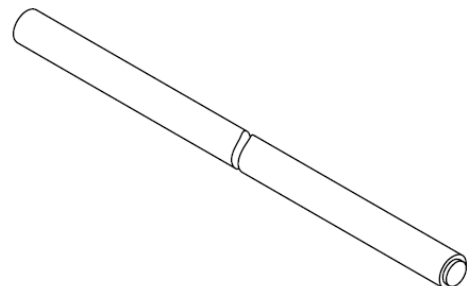




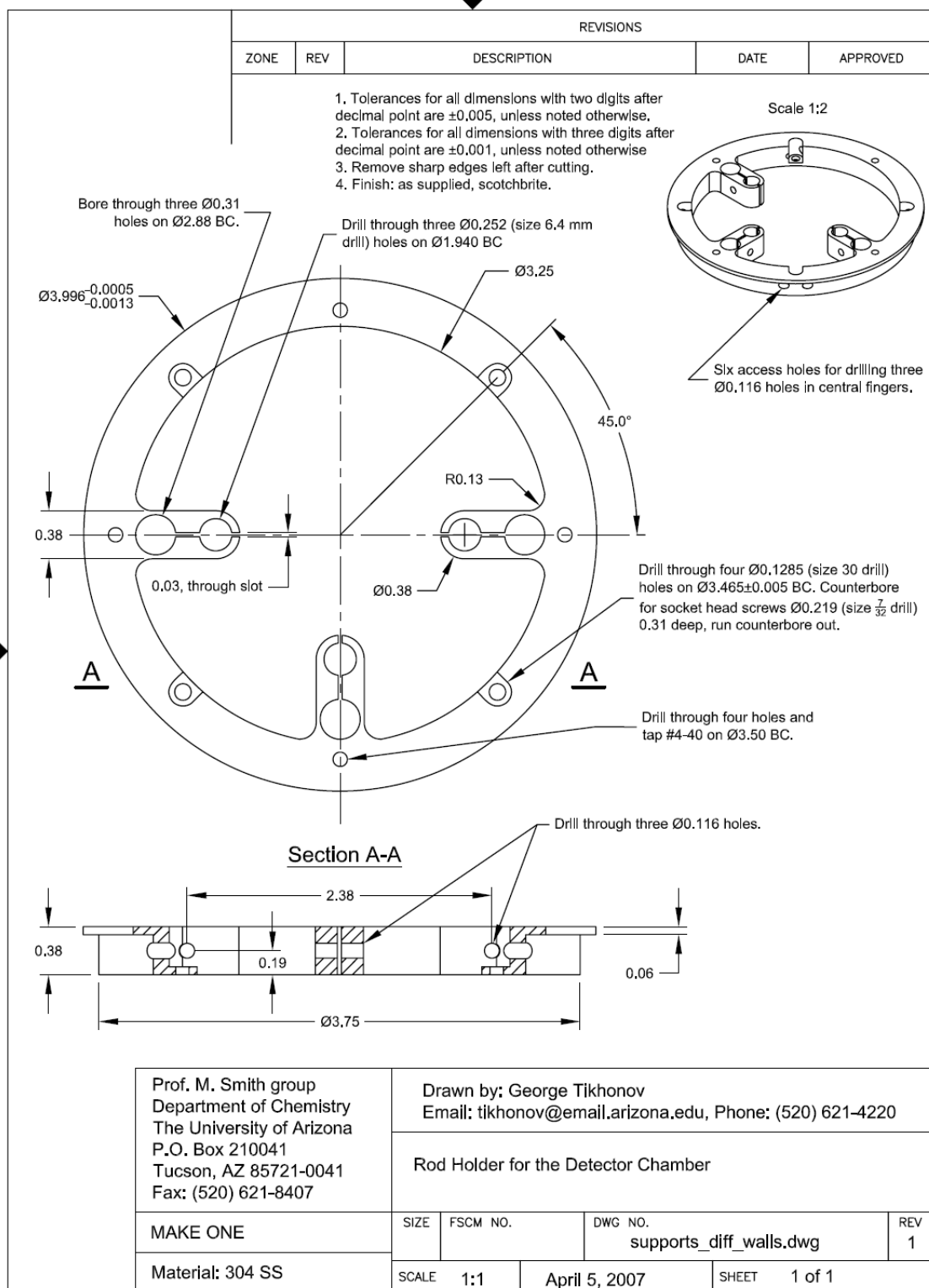




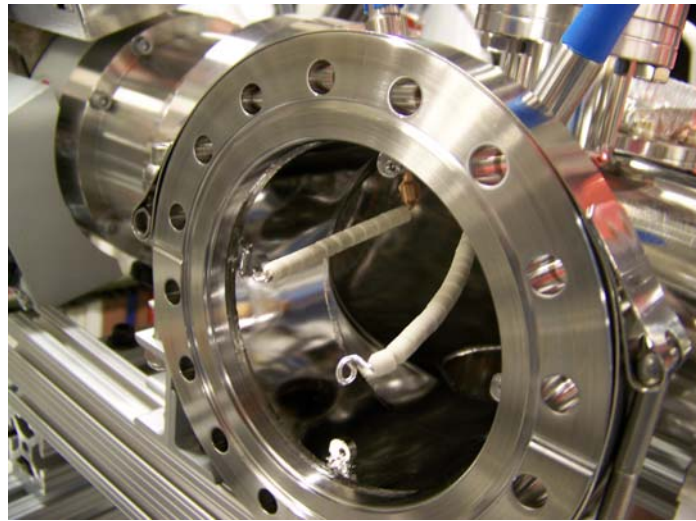
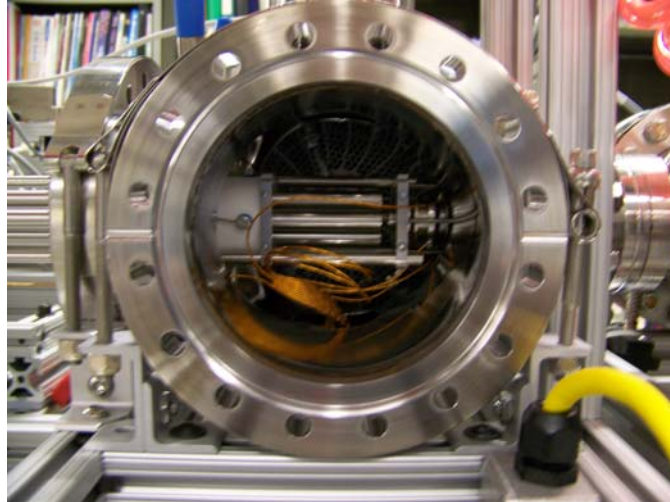


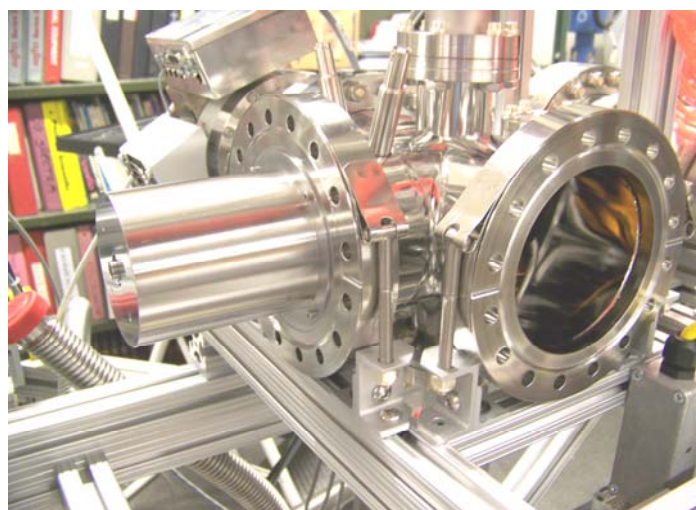
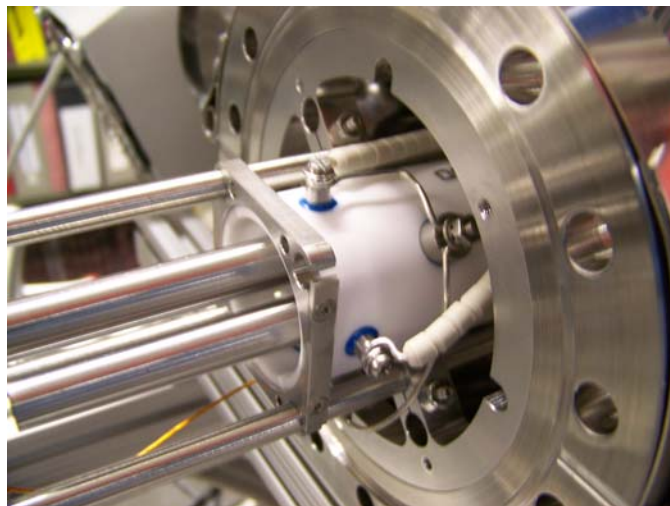
REVISIONS				
ZONE	REV	DESCRIPTION	DATE	APPROVED
<div style="display: flex; justify-content: space-between;"> <div style="width: 40%;">  </div> <div style="width: 55%;"> <p>1. Tolerances for all dimensions with two digits after decimal point are ± 0.005, unless noted otherwise. 2. Tolerances for all dimensions with three digits after decimal point are ± 0.001, unless noted otherwise. 3. Remove sharp edges left after cutting. 4. Finish: as supplied.</p> </div> </div> <div style="text-align: center; margin-top: 50px;">  </div>				

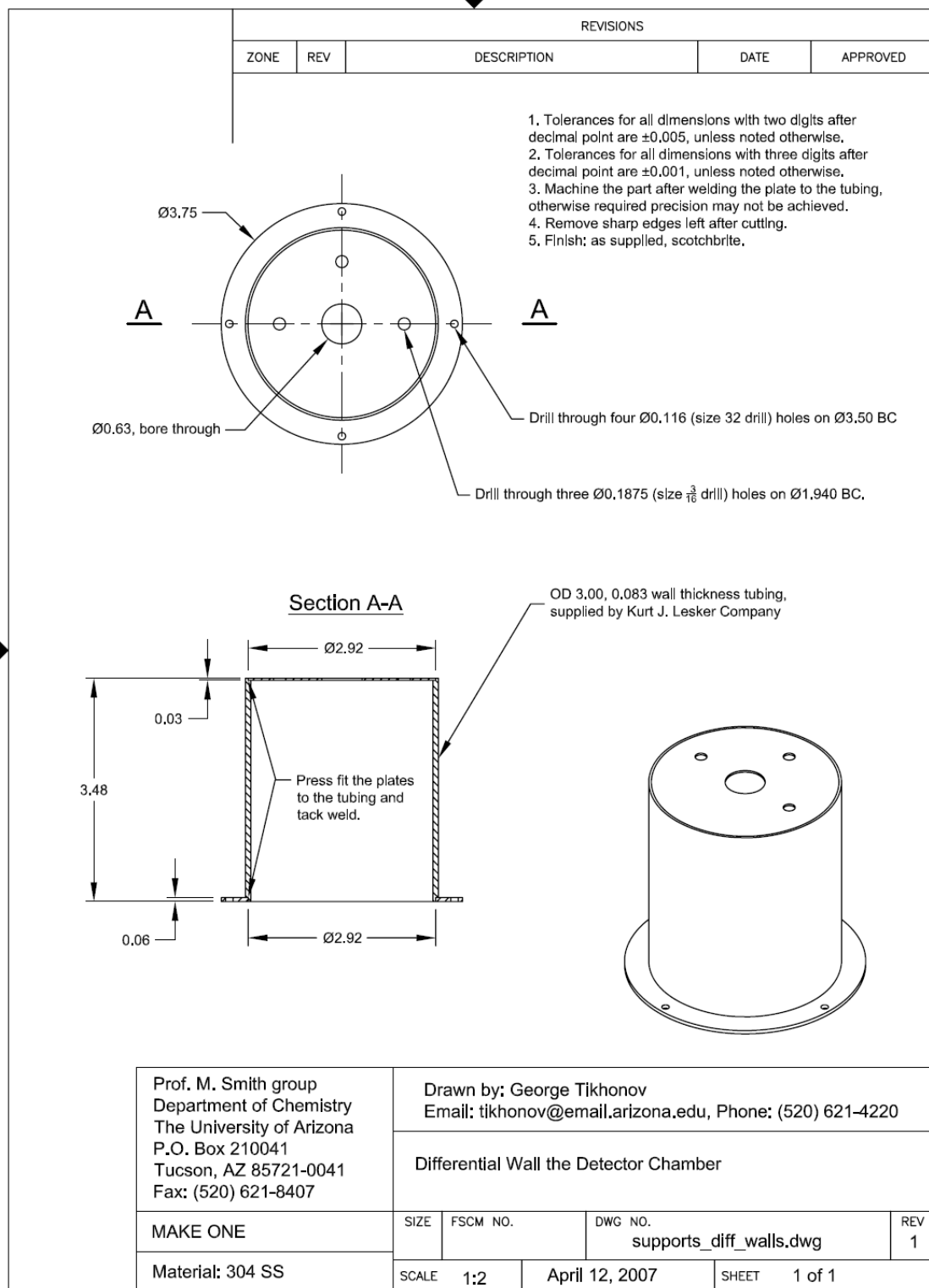
Prof. M. Smith group Department of Chemistry The University of Arizona P.O. Box 210041 Tucson, AZ 85721-0041 Fax: (520) 621-8407	Drawn by: George Tikhonov Email: tikhonov@email.arizona.edu, Phone: (520) 621-4220 Main Support Rod for Detector - modification of supplied precision-ground $\varnothing 0.250$ 304 SS rod (McMaster part # 8934K13)								
MODIFY THREE	<table border="1" style="width: 100%; border-collapse: collapse;"> <tr> <td style="width: 10%;">SIZE</td> <td style="width: 20%;">FSCM NO.</td> <td style="width: 40%;">DWG NO.</td> <td style="width: 30%;">REV</td> </tr> <tr> <td></td> <td></td> <td style="text-align: center;">support_rods.dwg</td> <td style="text-align: center;">1</td> </tr> </table>	SIZE	FSCM NO.	DWG NO.	REV			support_rods.dwg	1
SIZE	FSCM NO.	DWG NO.	REV						
		support_rods.dwg	1						
Material: 304 SS	<table border="1" style="width: 100%; border-collapse: collapse;"> <tr> <td style="width: 15%;">SCALE</td> <td style="width: 25%;">1:1</td> <td style="width: 25%;">April 6, 2007</td> <td style="width: 35%;">SHEET 1 of 1</td> </tr> </table>	SCALE	1:1	April 6, 2007	SHEET 1 of 1				
SCALE	1:1	April 6, 2007	SHEET 1 of 1						

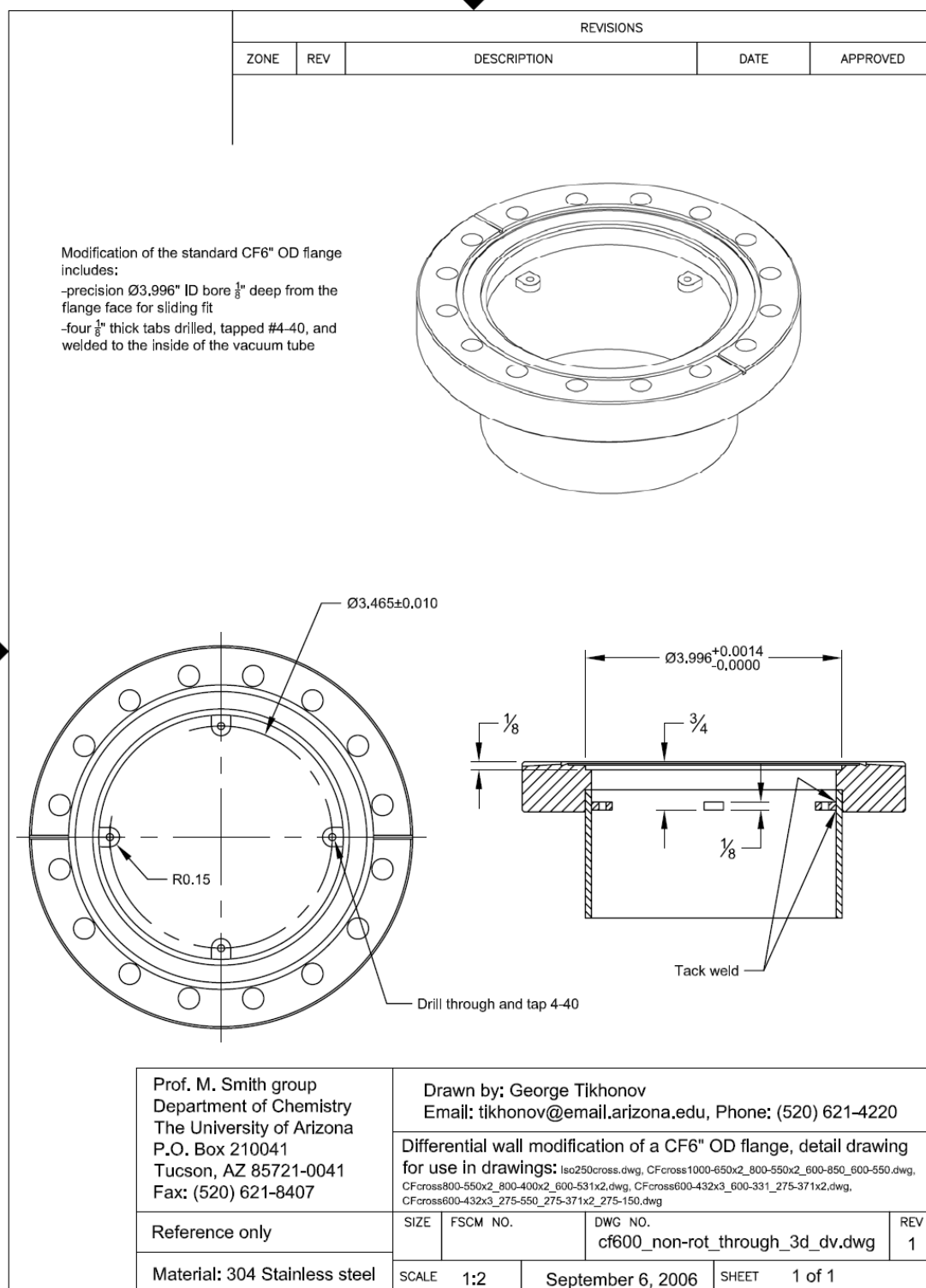


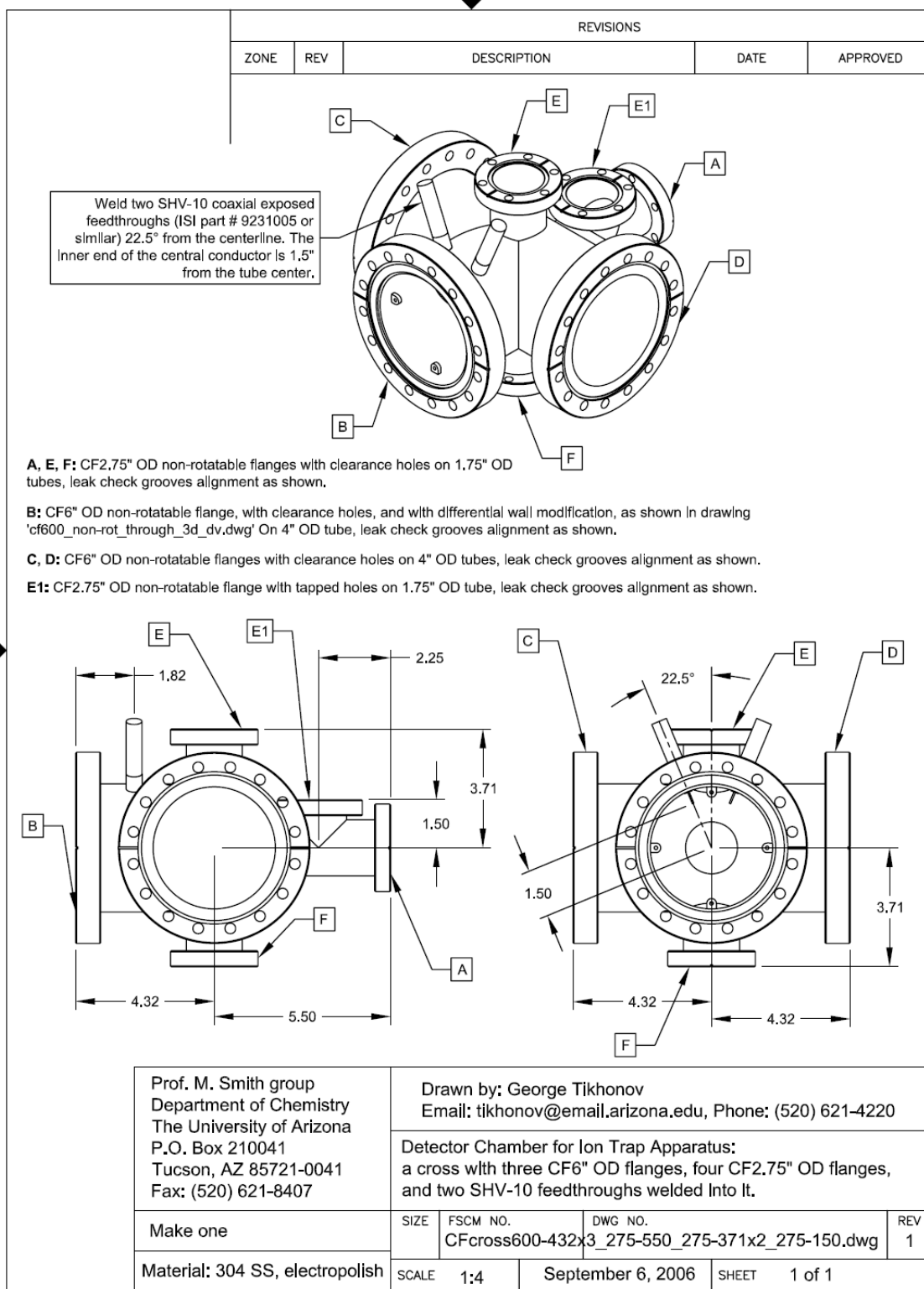
b. Detector chamber and differential wall



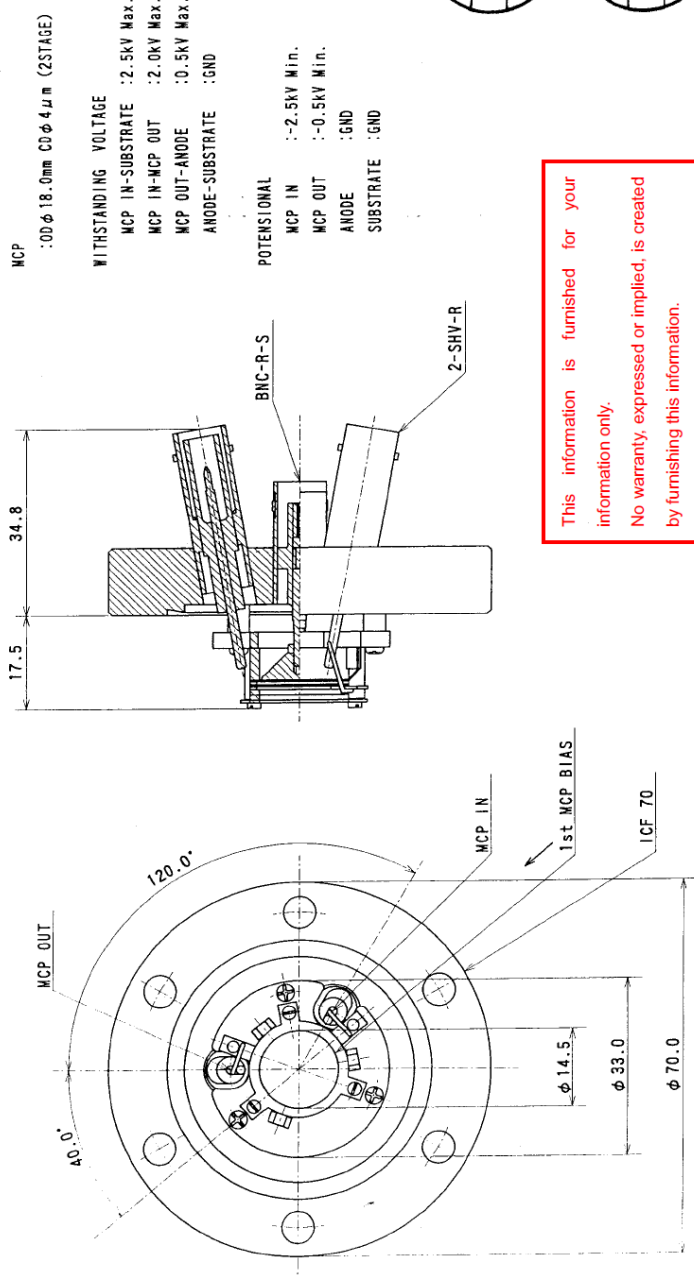









(6) MCP detector

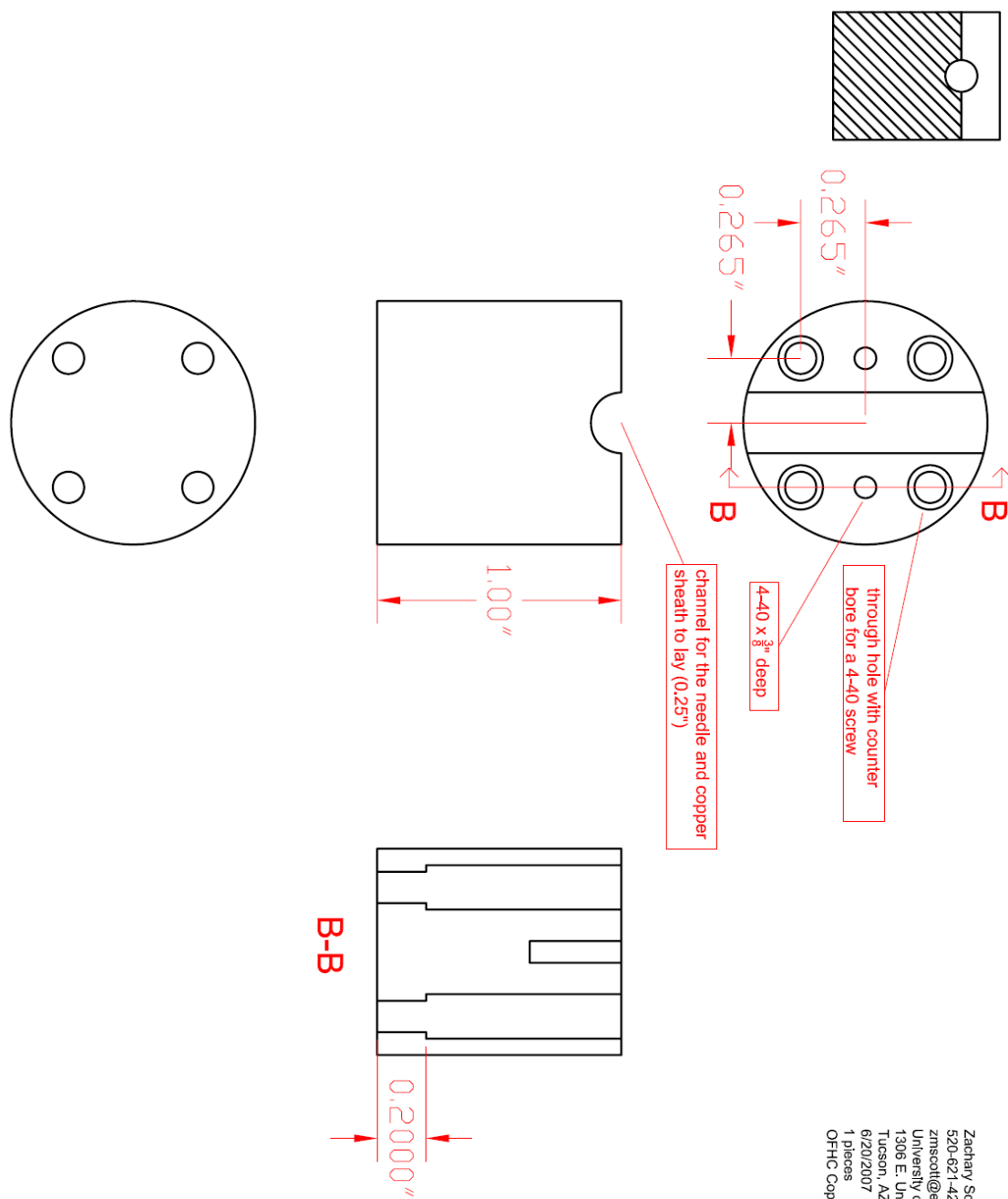


This information is furnished for your information only.
No warranty, expressed or implied, is created by furnishing this information.

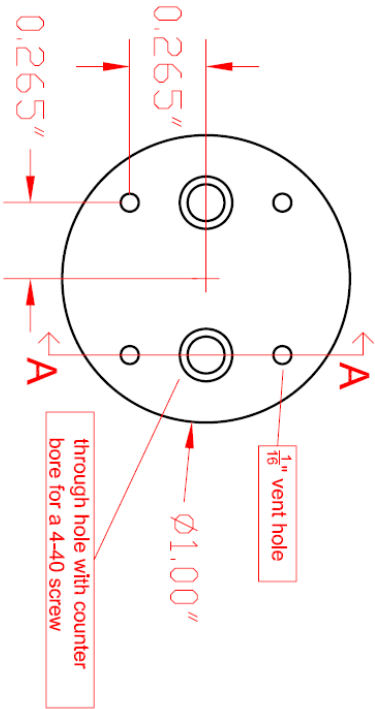
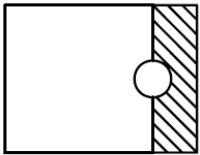
UNIT: mm

GENERAL TOLERANCE 一般公差				ALT	MARK	REASON	SIGN	DATE	MATERIAL 材質	SCALE 尺度		DATE	TITLE 品名			
DIMENSION 区分		A	B										C	F 4655-13X		
≤6	±0.10	±0.20	±0.30							1 / 1		2006.06.12	APPD.承認	CHK.検図	DES.設計	DFT.製図
6<	±0.15	±0.25	±0.50						0°TY. 傾度	FINISH 仕上			N. Nomaki			
30<	±0.25	±0.35	±0.80										SUZUKI			
120<	±0.40	±0.50	±1.40										SUZUKI			
500<	±0.80	±1.00	±2.00						TRTM. 処理	PAINT 塗装			SUZUKI			
											HAMAMATSU PHOTONICS K.K					
											DRAW. No. 図面番号					
											AF2221-A111A					

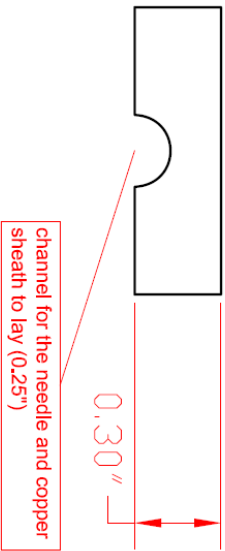
- (7) Molecular beam source
 a. Molecular beam nozzle element



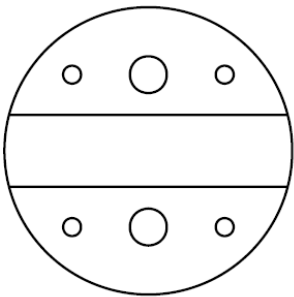
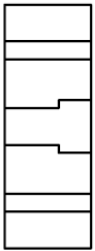
Zachary Scott
 520-621-4220
 zmscott@email.arizona.edu
 University of Arizona
 1306 E. University Blvd.
 Tucson, AZ 85721
 6/20/2007
 1 pieces
 OFHC Copper



Zachary Scott
520-621-4220
zmscott@email.arizona.edu
University of Arizona
1306 E. University Blvd.
Tucson, AZ 85721
6/20/2007
1 pieces
OFHC Copper

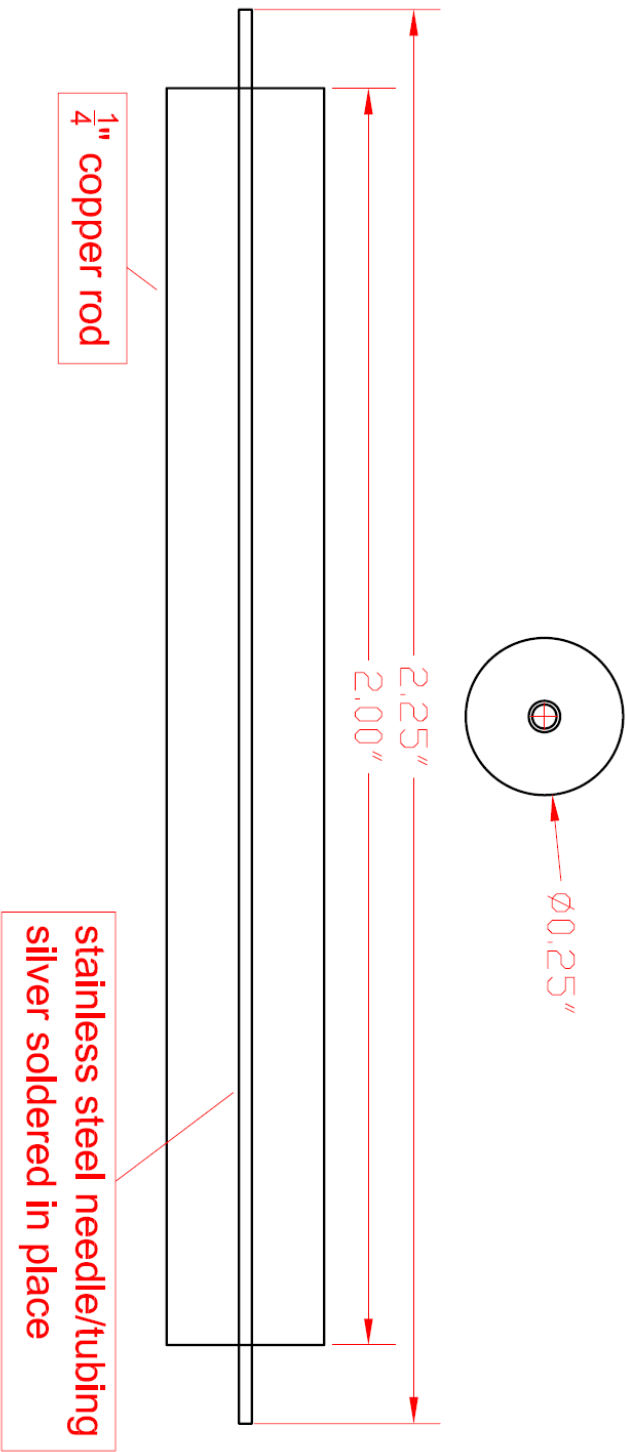


A-A

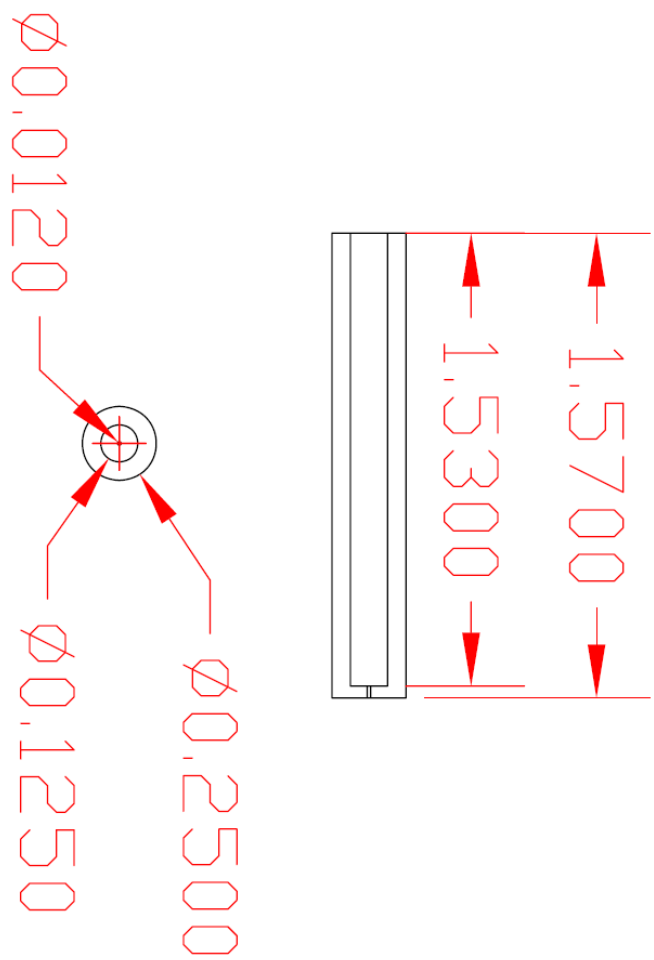


gauge	I.D.	O.D.
T17 316	0.042	0.058
T21 316	0.020	0.032
T24 316	0.012	0.022

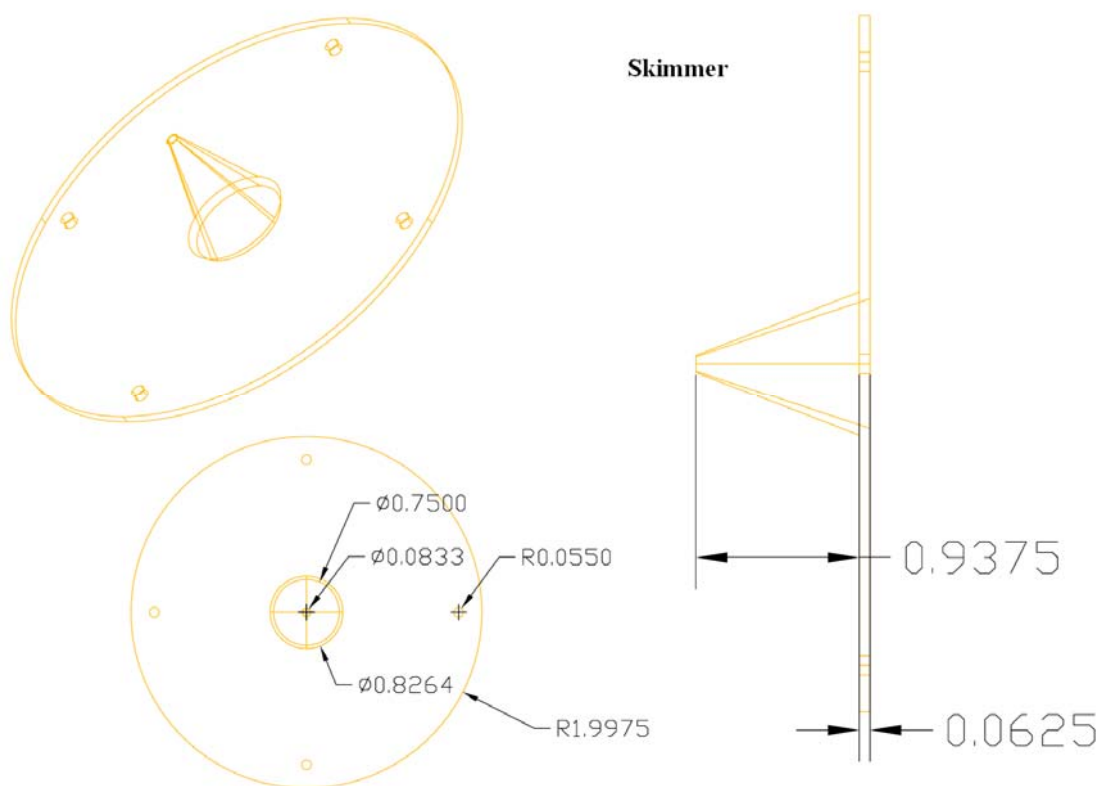
Zachary Scott
520-621-4220
zmscott@email.arizona.edu
University of Arizona
1306 E. University Blvd.
Tucson, AZ 85721
6/20/2007
1 piece for each gauge tubing
18, 21, and 23
OFHC Copper
Stainless steel tubing



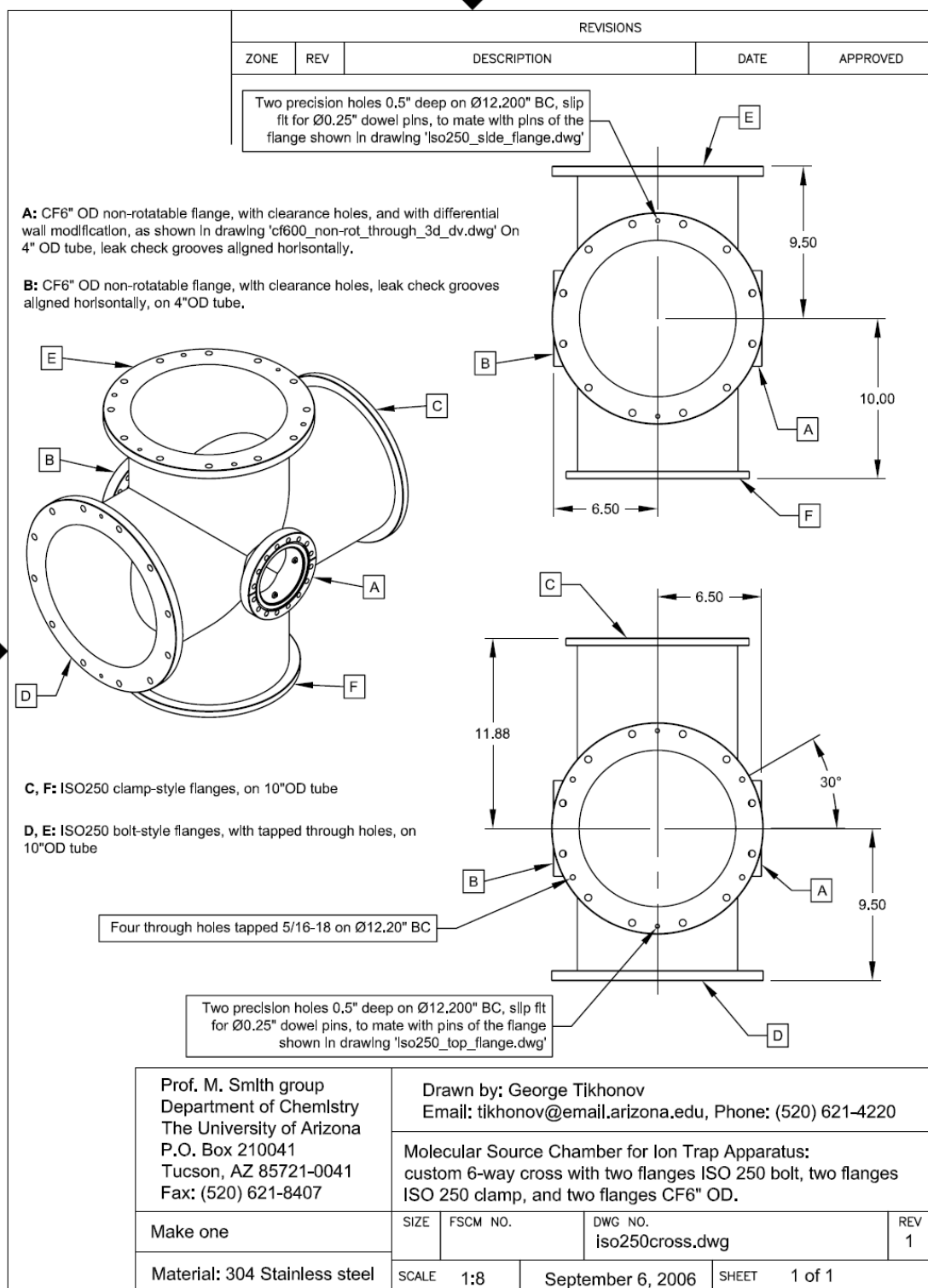
Nozzle for dimer reaction



b. First skimmer of molecular beam



c. Molecular beam source chamber



REVISIONS		ZONE	REV	DESCRIPTION	DATE	APPROVED

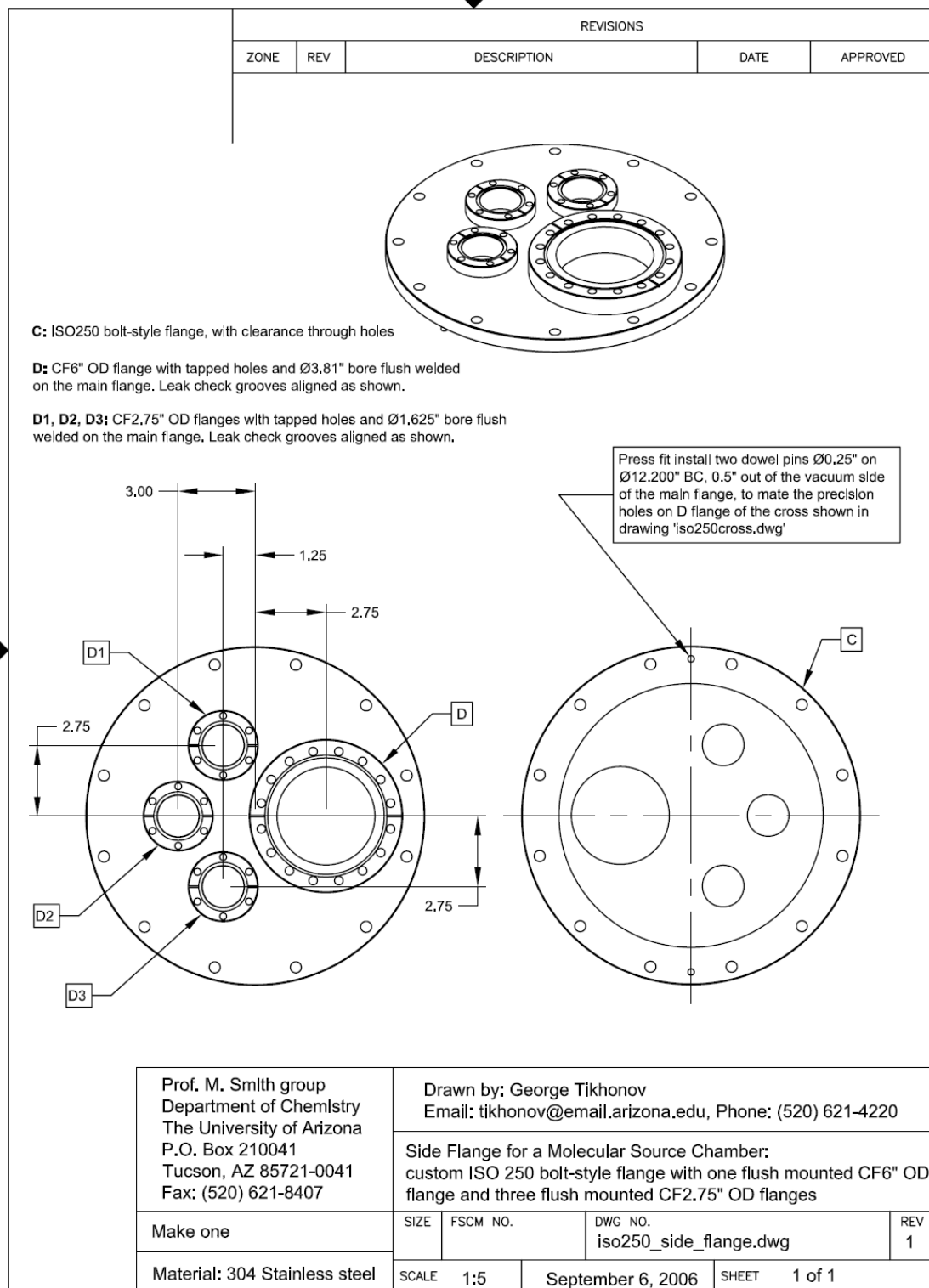
E: CF2.75" OD non-rotatable flange with clearance holes and Ø1.625" bore on Ø1.75" OD tube. Leak check grooves aligned as shown.

E1, E2, E3, E4, E5, E6: CF2.75" OD flanges with tapped holes and Ø1.625" bore flush welded on the main flange, E1 is in the center of the main flange, five others on Ø7" BC (five places out of six total). Leak check grooves aligned as shown.

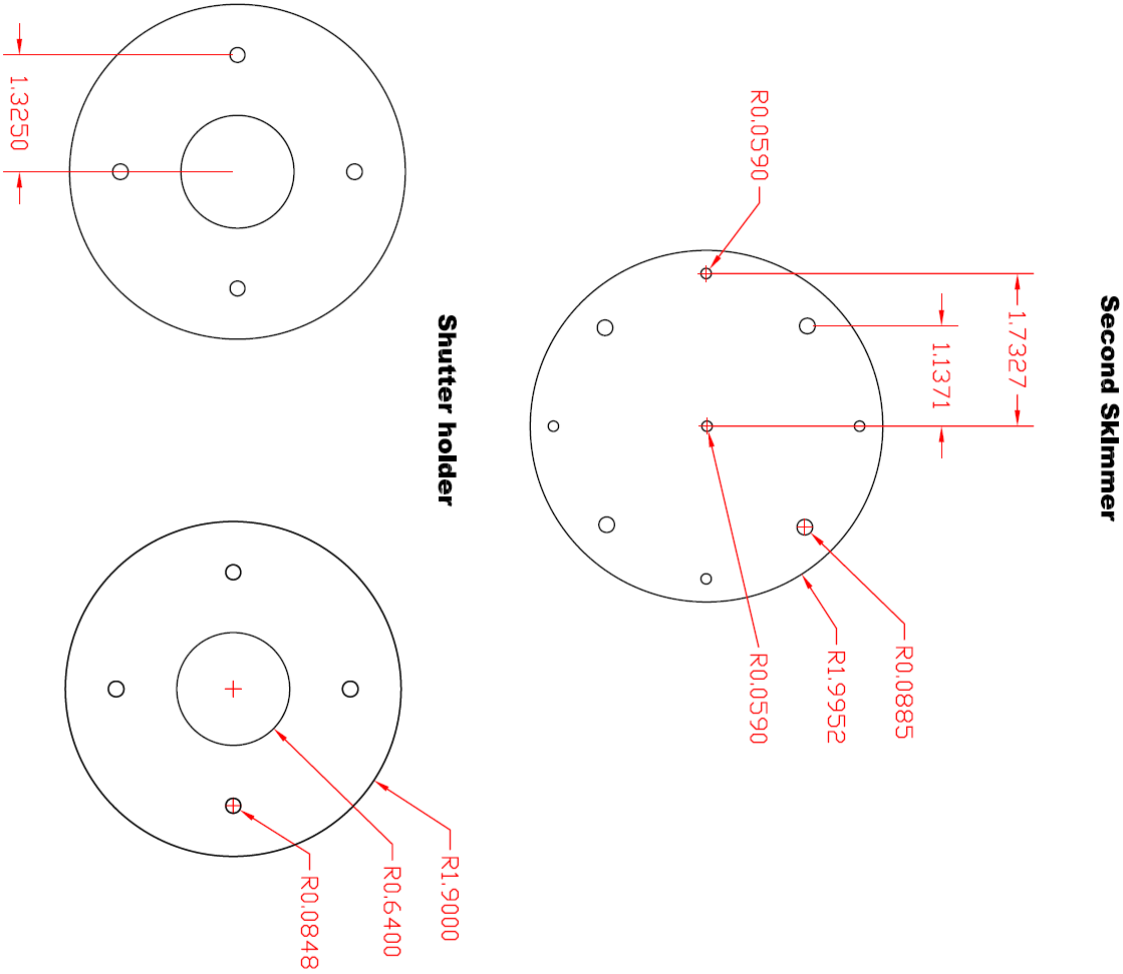
F: ISO250 bolt-style flange, with clearance through holes.

Press fit install two dowel pins Ø0.025" on Ø12.200" BC, 0.5" out of the vacuum side of the main flange, to mate the precision holes on E flange of the cross shown in drawing 'iso250cross.dwg'

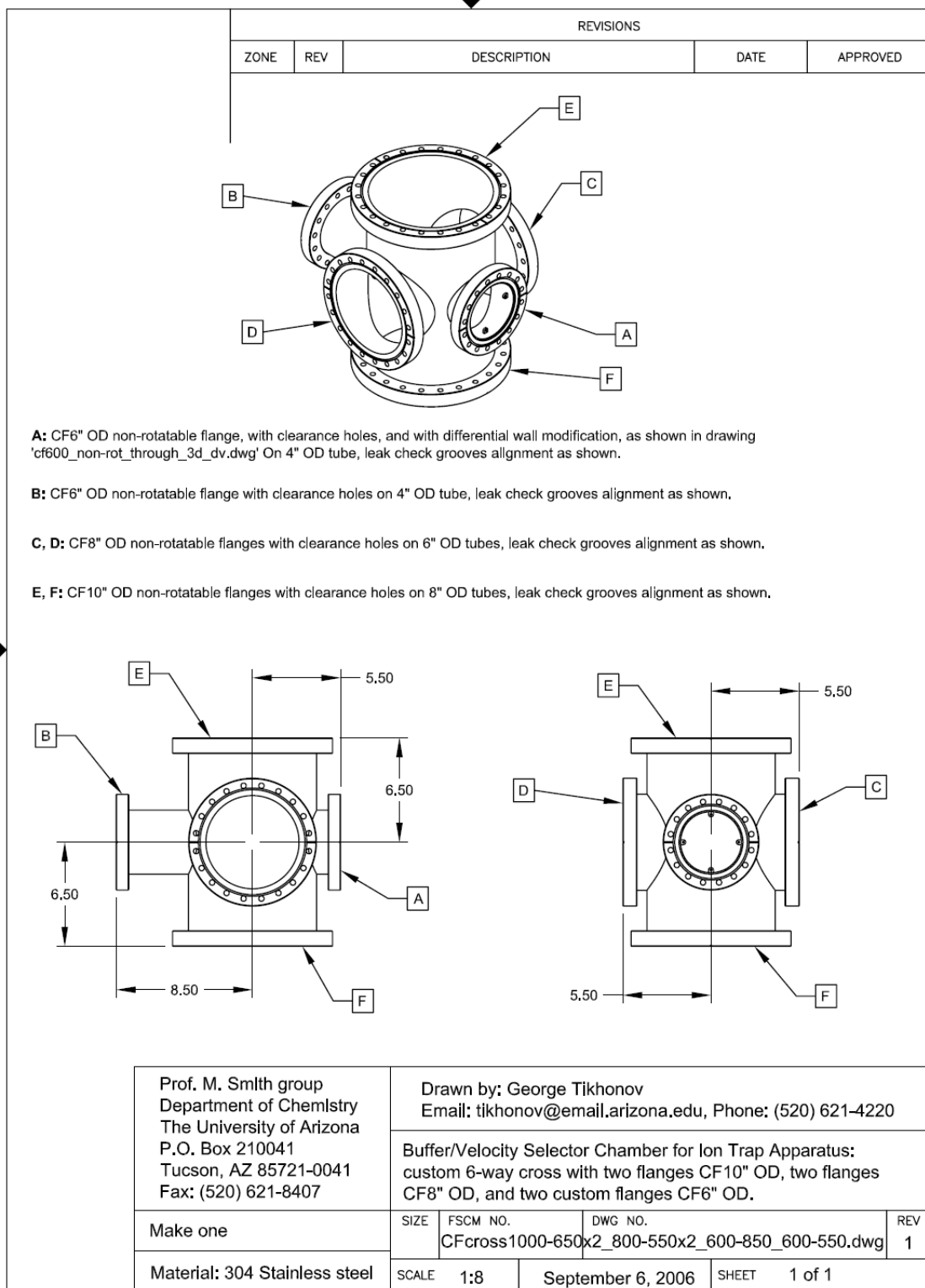
Dimensions: 0.50, 1.75, 4.05, 60°, Ø7.00



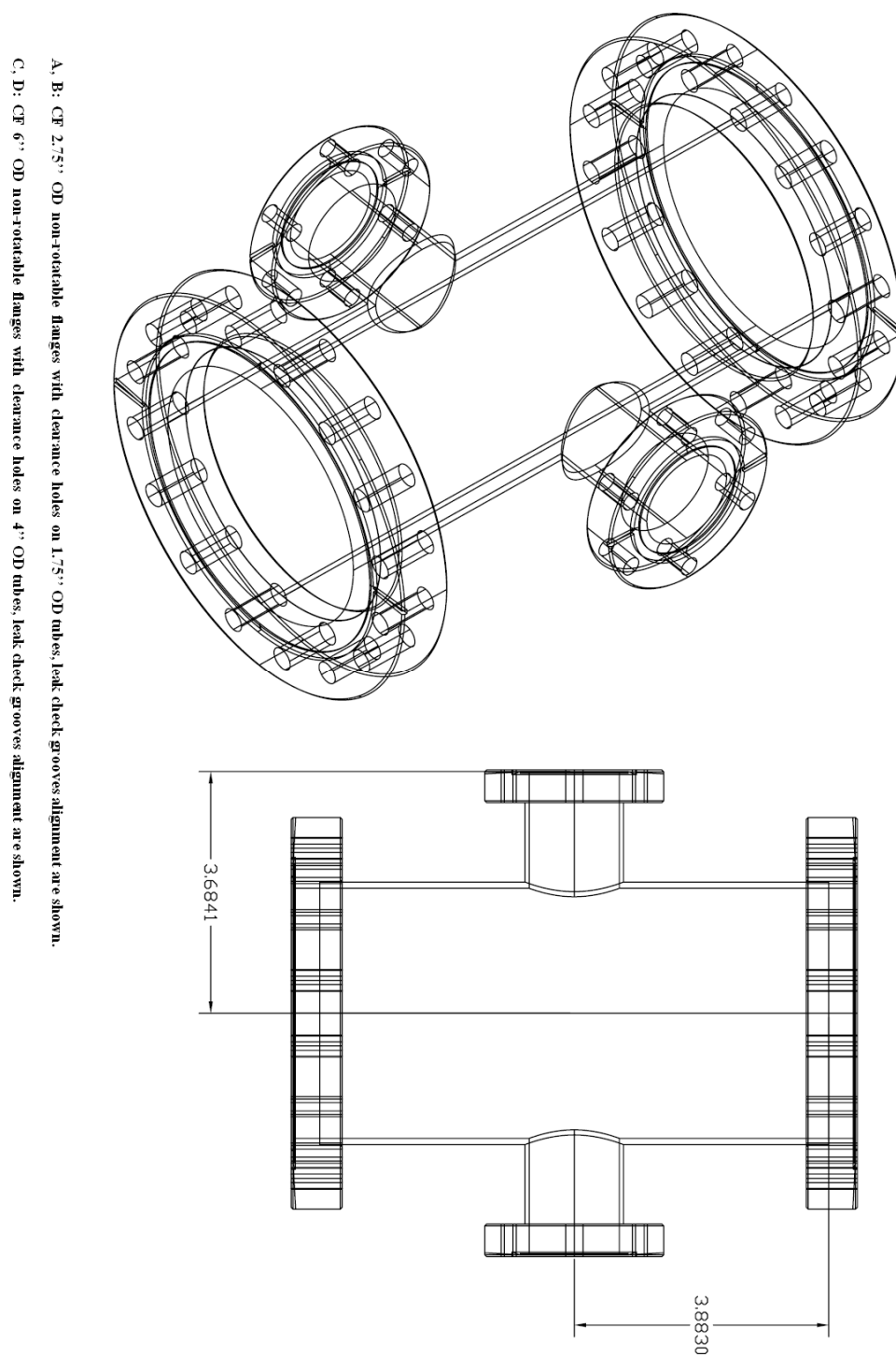
(8) Molecular beam buffer chamber
a. Second skimmer and shutter holder



b. Molecular beam buffer chamber



c. Molecular beam dump chamber



REFERENCES

- ¹ R. Carbo and A. Ginebreda, J. Chem. Educ. **62**, 832 (1985).
- ² W. Klemperer, PNAS. **103**, 12232 (2006).
- ³ V. Wakelam, I. W. M. Smith, E. Herbst, J. Troe, W. Geppert, H. Linnartz, K. Oberg, E. Roueff, M. Agundez, P. Pernot, H. M. Cuppen, J. C. Loison and D. Talbi, Space Sci. Rev. **156**, 13 (2010)
- ⁴ E. Herbst, J. Phys: Conference Series. **4**, 17 (2005).
- ⁵ N. D. Twiddy, Contemp. Phys. **15**, 427 (1974).
- ⁶ A. L. Schmeltekopf, E. E. Ferguson and F. C. Fehsenfeld, J. Chem. Phys. **48**, 2966 (1968).
- ⁷ B. R. Rowe and J. B. Marquette, Int. J. Mass. Spectrom. Ion Processes. **80**, 239 (1987)
- ⁸ J. Heimerl, R. Johnsen and M. A. Biondi, J. Chem. Phys. **51**, 5041 (1969).
- ⁹ N. G. Adams and D. Smith, Int. J. Mass. Spectrom. Ion Phys. **21**, 349 (1976).
- ¹⁰ P. Spanel and D. Smith, Med & Biol. Eng. & Comput. **34**, 409 (1996).
- ¹¹ B. R. Rowe and J. B. Marquette, Int. J. Mass. Spec. Ion Proc. **80**, 230 (1987).
- ¹² M. Hawley, T. L. Mazely, L. K. Randeniya, R. S. Smith, X. K. Zeng and M. A. Smith, Int. J. Mass. Spec. Ion Proc. **97**, 55 (1990).
- ¹³ R. T. McIver, Jr, Rev. Sci. Instrum. **41**, 555 (1970).
- ¹⁴ T. B. McMahon and J. L. Beauchamp, Rev. Sci. Instrum. **43**, 509 (1972).
- ¹⁵ S. Guan and A. G. Marshall, J. Am. Soc. Mass Spectrom. **7**, 101 (1996).
- ¹⁶ D. Gerlich. *Inhomogeneous Rf fields: A versatile tool for the study of processes with slow ions*, in: Ng. C. Y. (ed.); Baer. M. (ed.), *Stated-selected and State-to-state ion-molecular reaction dynamics. Part 1. Experimental. Adv. in Chem Phys. Ser, Vol. LXXXII*. 1992.
- ¹⁷ D. Gerlich and M. A. Smith, Phys. Scr. **73**, c25 (2006).

- ¹⁸ T. Su and M. T. Bowers., *classical ion-molecule collision theory*, in: Bowers, M.T. (ed.), *Gas Phase ion Chemistry vol. 1*, Academic Press, New York, San Francisco, London, 1979, 84-117.
- ¹⁹ W. H. Miller, J. Chem. Phys. **61**, 1823 (1974).
- ²⁰ J. B. Anderson, J. Chem. Phys. **58**, 4684 (1973).
- ²¹ T. Baer and P. M. Mayer, Am. Soc. Mass Spectrom. **8**, 103 (1997).
- ²² T. Su, J. Chem. Phys. **76**, 5183 (1982).
- ²³ V. G. Anicich, J. Phys. Chem. Ref. data. **22**, 1469 (1993).
- ²⁴ W. Umrath (ed.), H. Adam, A. Bolz, H. Boy, H. Dohmen, K. Gogol, W. Jorisch, W. Monning, H. Mundinger, H. Otten, W. Scheer, H. Seiger, W. Schwarz, K. Stepputat, D. Urban, H. Wirzfeld and H. Zenker. Fundamentals of Vacuum Technology. Leybold Vacuum products and reference book 2001/2002.
- ²⁵ Models CIS 100, CIS 200 and CIS 300 closed ion course quadrupole gas analyzer. Operating manual and programming reference. Stanford Research systems, Inc. Revision 1.1. 2000.
- ²⁶ D. Gerlich. *The production and study of ultra-cold molecular ions*, in: Smith, I.W.M. (ed.), *Low Temperatures and cold molecules*, Imperial College Press, 2008, 13-14.
- ²⁷ B. R. Turner and J. A. Rutherford, J. Geophys. Res. **73**, 6751-6758 (1968).
- ²⁸ R. A. Dressler, J. A. Gardner, R. H. Salter, F. J. Wodarczyk and E. Murad, J. Chem. Phys. **92**, 1117 (1990).
- ²⁹ R. A. Dressler, R. H. Salter and E. Murad, J. Chem. Phys. **99**, 1159 (1993).
- ³⁰ V. G. Anicich, J. phys. Chem. Ref. data. **22**, 1469 (1993).
- ³¹ O. Asvany, I. Savic, S. Schlemmer and D. Gerlich, Chem. Phys. **298**, 97 (2004).
- ³² G. Buffa, O. Tarrini, F. Scappini and C. C. Pestellini, Astrophys. J. Suppl. S. **128**, 597 (2000).
- ³³ P. F. Bernath, Chem. Soc. Rev. **25**, 111 (1996).
- ³⁴ P. F. Bernath. *Spectra of atoms and molecules (second edition)*, Oxford University Press, 2005, 7-11.

- ³⁵ P. J. Dagdigian, H. W. Cruse, R. N. Zare, J. Chem. Phys. **62**, 1824 (1975).
- ³⁶ J. A. Kettleborough and K. G. McKendrick, J. Phys. Chem. **95**, 8255 (1991).
- ³⁷ Gerlich, D. *The production and study of ultra-cold molecular ions*, in: *Smith, I.WM. (ed.), Low Temperatures and cold molecules*, Imperial College Press, 2008, 13-14.
- ³⁸ P. R. Kemper and M. T. Bowers, J. chem, phys. **81**, 2634 (1984).
- ³⁹ E. E. Ferguson, Annu. Rev. Phys. Chem. **26**, 17 (1975).
- ⁴⁰ A. A. Viggiano, J. M. Van Doren, R. A. Morris and J. F. Paulson, J. Chem. Phys. **93**, 4761 (1993).
- ⁴¹ R. Marx, G. Mauclaire and R. Deraï, Int. J. Mass Spectrom. Ion Phys. **47**, 155 (1983).
- ⁴² D. C. Clary, J. Chem. Soc. **83**, 139 (1987).
- ⁴³ D. C. Clary, D. Smith and N. G. Adams, Chem. Phys. Lett. **119**, 320 (1985).
- ⁴⁴ D. C. Clary, Chem. Phys. Lett. **232**, 267 (1995).
- ⁴⁵ D. Smith, Chem. Rev. **92**, 1473 (1992).
- ⁴⁶ P. Spanel and D. Smith, Int. J. Mass Spectrom. **181**, 1 (1998).
- ⁴⁷ T. B. McMahon and P. Kebarle, J. Am. Chem. Soc. **107**, 2612 (1998).
- ⁴⁸ S. M. Collyer and T. B. McMahon. J. Phys. Chem. **87**, 909 (1983).
- ⁴⁹ D. K. Bohme and G. I. Mackay, J. Am. Chem. Soc. **103**, 2173 (1981).
- ⁵⁰ B. J. McIntosh, N. G. Adams, and D. Smith, Chem. Phys. Lett. **148**, 142 (1988).
- ⁵¹ D. J. Levandier, D. F. Varley and J. M. Farrar, **97**, 4008 (1992).
- ⁵² H. Palm, C. Alcaraz, P. Millie and O. Dutuit, Int. J. Mass Spectrom. **249- 250**, 31 (2006).
- ⁵³ M. Tsuji, H. Kouno, K. Matsumura, T. Funatsu, Y. Nishimura, H. Obase, H. Kugishima, K. Yoshida, J. Chem. Phys. **98**, 2011 (1993).

- ⁵⁴ M. Hawley, T. L. Mazely, L. K. Randeniya, R. S. Smith, X. K. Zeng, and M. A. Smith, *Int. J. Mass. Spectrom. Ion. Proc.* **97**, 55 (1990).
- ⁵⁵ M. J. McEwan, G. B. Scott, and V. G. Anicich, *J. Mass. Spectrom. Ion. Proc.* **172**, 209 (1998).
- ⁵⁶ B. Yuan, A. M. Sanov and M. A. Smith. In press.
- ⁵⁷ L. M. Ziurys, *Proc. Natl. Acad. Sci. USA.* **103**, 12274 (2006).
- ⁵⁸ W. Klemperer, *Annu. Rev. Phys. Chem.* **62**, 173 (2011).
- ⁵⁹ E. Vigren, M. Hamberg, V. Zhaunerchyk, M. Kaminska, R. D. Thomas, S. Trippel, M. Zhang, I. Kashperka, M. Ugglas, C. Walsh, R. Wester, J. Semaniak, M. Larsson and W. D. Geppert, *Phys. Chem. Chem. Phys.* **12**, 11670 (2010).
- ⁶⁰ D. A. Fairly, G. B. Scott, C. G. Freeman, R. G. A. R. MacLagan, M. McEwan, *J. Chem. Soc., Faraday Trans.* **92**, 1305 (1996).
- ⁶¹ D. Gerlich and S. Horning, *Chem Rev.* **92**, 1509 (1992).
- ⁶² V. Ryzhov and R. C. Dunbar, *Int. J. Mass Spectrom. Ion Proc.* **167/168**, 627 (1997).
- ⁶³ R. C. Dunbar, *Int. J. Mass Spectrom. Ion Proc.* **160**, 1 (1997).
- ⁶⁴ E. Herbst, *Astrophys. J.* **205**, 94 (1976).
- ⁶⁵ E. Herbst, *J. Chem. Soc, Faraday Trans.* **85**, 1655 (1989).
- ⁶⁶ E. Herbst, *Astrophys. J.* **313**, 867 (1987).
- ⁶⁷ T. S. Zwier and M. Allen. *Icarus.* **123**, 578 (1996).
- ⁶⁸ A. J. Colussi, S. P. Sander and R. R. Friedl, *Chem. Phys. Lett.* **178**, 497 (1991).
- ⁶⁹ J. W. V. Storey and A. C. Cheung, *Astrophys. Lett.* **19**, 89 (1987).
- ⁷⁰ P. O. Momoh, A. M. Hamid, S. A. Abrash and M. S. El-Shall, *J. Chem. Phys.* **134**, 204315 (2011).
- ⁷¹ D. Gerlich and G. Borodi, *Faraday Discuss.* **142**, 57 (2009).
- ⁷² E. P. Hunter, S. G. Lisa, Gas phase ion energetics data. In *NIST Chemistry webBook*; W. G. Mallard, P. J. Linstrom., Eds.; NIST Standard Reference Database Number 69;

National Institute of Standards and Technology: Gaithersburg, MD, 1998;
<http://webbook.nist.gov>.

- ⁷³ V. G. Anicich, *J. Am. Soc. Mass. Spectrom.* **15**, 1148 (2004).
- ⁷⁴ V. G. Anicich, A. D. Sen, and W. T. Huntress (Jr), *J. Chem. Phys.* **93**, 7163 (1990).
- ⁷⁵ V. G. Anicich, W. T. Huntress (Jr), M. J. McEwan, *J. Phys. Chem.* **90**, 2446 (1986).
- ⁷⁶ J. S. Knight, C. G. Freeman and M. J. McEwan, *J. Phys. Chem.* **91**, 3898 (1987).
- ⁷⁷ D. R. Bates, *J. Chem. Phys.* **90**, 87 (1989).
- ⁷⁸ N. G. Adams and D. Smith, *Chem. Phys. Lett.* **79**, 563 (1981).
- ⁷⁹ E. Herbst, *J. Chem. Phys.* **70**, 2201 (1979).
- ⁸⁰ A. A. Viggiano, *J. Chem. Phys.* **84**, 244 (1986).
- ⁸¹ A. A. Viggiano, F. Dale and J. F. Paulson, *J. Geophys. Res.* **90**, 7977 (1985).
- ⁸² S. J. Klippenstein, Y. C. Yang, V. Ryzhov and R. C. Dunbar, *J. Chem. Phys.* **104**, 4502 (1996).
- ⁸³ V. Ryzhov, Y. C. Yang, S. J. Klippenstein and R. C. Dunbar, *J. Phys. Chem. A.* **102**, 8865 (1998).
- ⁸⁴ M. Herman, A. Campargue, M. I. E. Idrissi and J. V. Auwera, *J. Phys. Chem. Ref. Data.* **32**, 921 (2003).
- ⁸⁵ C. Winkler, *Chem. Phys. Lett.* **242**, 39 (1995).
- ⁸⁶ E. L. Knuth, *J. Chem. Phys.* **66**, 3515 (1977).
- ⁸⁷ R. G. A. Bone and N. C. Handy, *Thero. Chem. Acta.* **78**, 133 (1990).
- ⁸⁸ S. Karthikeyan, H. M. Lee and K. S. Kim, *J. Chem. Theory. Comput.* **6**, 3190 (2010).
- ⁸⁹ K. Shuler and C. E. Dykstra, *J. Phys. Chem. A.* **104**, 4562 (2000).
- ⁹⁰ I. L. Alberts, T. W. Rowlands and N. C. Handy, *J. Chem. Phys.* **88**, 3811 (1988).
- ⁹¹ C. E. Dykstra, *J. Phys. Chem.* **99**, 11680 (1995).
- ⁹² S. Resende, S and W. B. D. Almeida, *Chem. Phys.* **206**, 1 (1996).

⁹³ H. Takeuchi, J. Comput Chem. **31**, 1699 (2010).

⁹⁴ D. G. Prichard, R. N. Nandi and J. S. Muentner, J. Chem. Phys. **89**, 115 (1988)